Dissertation

submitted to the
Combined Faculty of Natural Sciences and Mathematics
of the Ruperto Carola University Heidelberg, Germany
for the degree of
Doctor of Natural Sciences

Presented by
MSc Jasmin Elena Mangei
born in Heidelberg, Germany
Oral Examination: December 20th, 2021

EXPLORING THERAPEUTIC VULNERABILITIES IN TUMOURS WITH GLI1 ONCOGENE ACTIVATION

Referees:

Prof Dr Karsten Rippe

Prof Dr Peter Lichter

The work and results of the following dissertation were performed and obtained from December 2017 until September 2021 under the supervision of Dr Bernhard Radlwimmer and Prof Dr Peter Lichter in the Division of Molecular Genetics at the German Cancer Research Center (DKFZ), Heidelberg, Germany.

Declaration

I hereby declare that I have written the submitted dissertation “Exploring therapeutic vulnerabilities in tumours with GLI1 oncogene activation” myself and in this process have not used any other sources than those indicated.

I hereby declare that I have not applied to be examined at any other institution, nor have I used the dissertation in this or any other form at any other institution as an examination paper, nor submitted it to any other faculty as a dissertation.

Jasmin Mangei

To my family because without you I wouldn’t be the person I am today.

Summary

Deregulation of oncogene expression is one of the main drivers in tumorigenesis. Genetic alterations, such as gene amplification and structural variation, or epigenetic mechanisms based on the chemical modification of DNA or histones, facilitate the activation of proto-oncogenes that convey growth and survival advantages to the cells. Previously, our group identified focal amplification of the chromosome arm 12q in 14 of 60 glioblastoma patients (23.3 %) of which 4 patients harboured fusion genes with the oncogene GLI Family Zinc Finger 1 (GLI1).

In this study, I investigated the frequency and structure of *GLI1* fusion genes, mechanisms of *GLI1* transcriptional activation, GLI1-dependent tumour cell phenotype, and the potential value of GLI1 as a therapeutic target in precision-oncology in glioblastoma and liposarcoma. Initially, I identified GLI1 fusion genes linked with focal amplification on chromosome arm 12q in three independent glioblastoma cohorts (HIPO016, HIPO043, and TCGA-GB). *GLI1* fusion genes were associated with high expression of *GLI1* and its target genes, such as *HHIP*, *PTCH1*, and *FOXS1*. The boundary of the 12q amplification region often coincided with the GLI1 locus, presumably causing the breakage within the gene and the formation of fusion transcripts. The analysis of sarcoma tumours of the NCT MASTER study revealed high *GLI1* expression in subtypes of osteosarcoma and soft tissue sarcoma. In addition, *GLI1* fusion genes were found in liposarcoma and leiomyosarcoma. Furthermore, the disruption of a CTCF binding site upstream of the *GLI1* locus upregulated the RNA expression of *GLI1* and its target genes and increased cell proliferation. These data suggest that fusion-related genetic and epigenetic mechanisms regulate *GLI1* expression. To explore its oncogenic function, I conducted phenotypic assays with and without GLI1 suppression and observed a reduction in tumour cell proliferation, anchorage-independent growth and increased apoptosis upon shRNA depletion or inhibition with the GLI1 inhibitor GlaB. The downregulation of several DNA repair pathways upon GLI1 depletion suggested that patients with aberrant *GLI1* expression might benefit from combined GLI1 and DNA repair inhibitor therapy. To address this question, I performed a pre-clinical drug combination screen of GLI1 and DNA repair/cell cycle checkpoint inhibitors in glioblastoma and liposarcoma cell lines. In the primary screen, I tested inhibitors individually to identify effective and selective drugs of which the most promising candidates were tested in combination in the subsequent secondary screen. Both glioblastoma and liposarcoma showed high sensitivities to the SHH inhibitor JK184 and the GLI1 inhibitor GlaB. Synergistic effects were observed when GLI1 inhibitors were combined with inhibitors of the ATR/CHK1 axis, i.e., the CHK1 inhibitor LY2606368 or the ATR inhibitor Berzosertib. The independent validation of the screening results in cellular assays showed an increased effect of the combination treatment compared to the single agents on short- and long-term tumour cell proliferation. I furthermore confirmed the reduction in tumour growth upon treatment with GlaB and LY2606368 in a glioblastoma cerebral organoid model.

In conclusion, these data suggest that concurrent targeting of the SHH/GLI1 and ATR/CHK1 axes provides a possible precision-therapy approach for tumours with high *GLI1* expression.

Zusammenfassung

Die Fehlregulierung der Onkogenexpression ist einer der wesentlichen Treiber bei der Tumorentstehung. Genetische Veränderungen, wie z.B. Genamplifikation und strukturelle Variationen, oder epigenetische Mechanismen basierend auf chemischer DNA- oder Histonmodifizierung, ermöglichen die Aktivierung von Proto-Onkogenen, die wiederum den Zellen einen Wachstumsvorteil und ein erhöhtes Überleben verleihen. In vorangehenden Studien konnte unsere Arbeitsgruppe eine fokale Amplifikation des Chromosomenarms 12q in 14 von 60 Glioblastompatienten (23,3 %) nachweisen, von denen vier Patienten Fusionsgene mit dem Onkogen GLI, Zinkfinger 1 der GLI-Familie (GLI1), hatten.

In dieser Studie untersuchte ich die Häufigkeit und Struktur von *GLI1* Fusionsgenen, die Mechanismen der transkriptionellen *GLI1*-Aktivierung, den GLI1-abhängigen Tumorzellphänotyp sowie den möglichen Nutzen von GLI1 als therapeutischen Ansatzpunkt in der zielgerichteten Therapie von Glioblastom- und Liposarkomtumoren. Zunächst identifizierte ich in drei unabhängigen Glioblastomkohorten (HIPO016, HIPO043 und TCGA-GB) *GLI1*-Fusionsgene, die mit fokaler Amplifikation innerhalb des Chromosomenarms 12q verbunden waren. *GLI1*-Fusionsgene waren mit einer hohen Expression von *GLI1* selbst sowie seinen Zielgenen wie z.B. *HHIP*, *PTCH1* und *FOXS1* assoziiert. Die Grenze der amplifizierten 12q-Region fiel oft mit dem GLI1-Genlokus zusammen, was vermutlich zum Bruch innerhalb des Gens sowie zur Bildung der Fusionstranskripte führte. In der Analyse von Sarkomtumoren aus der NCT MASTER-Studie zeigten Osteosarkom- und bestimmte Weichteilsarkomsubtypen eine hohe *GLI1*-Expression, wobei *GLI1*-Fusionsgene zusätzlich in Liposarkom- und Leiomyosarkom-Tumoren auftraten. Außerdem bewirkte der Verlust einer CTCF-Bindungsstelle vor dem *GLI1*-Lokus eine Hochregulierung der *GLI1* RNA-Expression und seiner Zielgene sowie eine Zunahme der Zellproliferation. Diese Daten legen nahe, dass genetische und epigenetische Mechanismen, die durch Fusionsgene bedingt sind, die GLI1-Expression kontrollieren. Um die onkogene Funktion von GLI1 genauer zu untersuchen, führte ich phänotypische Experimente mit und ohne GLI1-Hemmung durch und konnte eine Verringerung der Zellproliferation, des verankerungsunabhängigen Wachstums sowie eine Zunahme der Apoptose nach shRNA-Knockdown oder der Inhibition mit dem GLI1-Inhibitor GlaB feststellen. Die Herunterregulierung mehrerer DNA-Reparaturwege nach Verlust der *GLI1* Expression deutet darauf hin, dass Patienten mit anomaler GLI1-Expression von einer Kombinationstherapie aus GLI1- und DNA-Reparaturinhibitoren profitieren könnten. Um dieser Frage nachzugehen, führte ich ein präklinisches Medikamentenkombinationsscreening aus GLI1 und DNA-Reparatur-/Zellzyklus-Kontrollpunkt-Inhibitoren in Glioblastom- und Liposarkomzelllinien durch. Im Primärscreen habe ich die Inhibitoren einzeln getestet, um wirksame und selektive Wirkstoffe zu identifizieren, von denen die vielversprechendsten Kandidaten im anschließenden Sekundärscreen in Kombination getestet wurden. Sowohl Glioblastom- als auch Liposarkommodelle zeigten hohe Sensitivitäten gegenüber dem SHH-Inhibitor JK184 und dem GLI1-Inhibitor GlaB. Synergistische Effekte wurden beobachtet, wenn GLI1-Inhibitoren mit Inhibitoren der ATR/CHK1-Achse, wie z.B. dem CHK1-Inhibitor LY2606368 oder dem ATR-Inhibitor Berzosertib, kombiniert wurden. Die unabhängige Validierung der Screening-Ergebnisse in zellulären Assays belegte einen zusätzlichen Effekt bei der Kombinationsbehandlung auf die kurz- und langfristige Tumorzellproliferation im Vergleich zu den Einzelwirkstoffen. Darüber hinaus bestätigte ich ein verringertes Tumorwachstum unter Behandlung mit GlaB und LY2606368 in einem Glioblastommodell in zerebralen Organoiden.

Zusammenfassend legen diese Daten nahe, dass die gleichzeitige Behandlung mit Inhibitoren der SHH/GLI1- und ATR/CHK1-Achsen einen möglichen Therapieansatz für Tumore mit hoher *GLI1* Expression darstellt.

Contents

1 Introduction 23
1.1 Oncogenes and cancer 23
1.1.1 Mechanisms of oncogene activation 23
1.1.2 Oncogenes as therapeutic targets 32
1.2 GLI Family Zinc Finger 1 and Hedgehog/GLI signalling 33
1.2.1 Canonical HH/GLI signalling 34
1.2.2 Oncogenic HH/GLI signalling 35
1.2.3 Therapeutic targeting of GLI1 36
1.3 Glioblastoma 36
1.4 Sarcoma 38
1.5 Drug combinations in cancer therapy 39
1.6 Aims of the study 40
2 Materials and Methods 41
2.1 Materials 41
2.1.1 Cell lines 41
2.1.2 Cell culture reagents 41
2.1.3 Chemicals and Reagents 42
2.1.4 Antibiotics and Inhibitors 43
2.1.5 Buffers and Solutions 45
2.1.6 Antibodies 45
2.1.7 Plasmids 46
2.1.8 Oligonucleotide sequences 47
2.1.9 Kits 48
2.1.10 Consumables 49
2.1.11 Equipment and Devices 49
2.1.12 Databases and Software 51
2.2 Methods 53
2.2.1 Cell lines and culture conditions 53
2.2.2 Generation of spheroid cultures 53
2.2.3 DNA FISH 53
2.2.4 Lentivirus production 54
2.2.5 ShRNA cloning and knockdown 55
2.2.6 Reverse transcription quantitative PCR 56
2.2.7 Western Blotting analysis 56
2.2.8 Development of CTCF CRISPR/Cas9 KO cell lines 57
2.2.9 CTCF chromatin immunoprecipitation 57
2.2.10 CTCF ChIP-qPCR 58
2.2.11 Click-iT cell proliferation assay 59

2.2.12 Cell viability assay 59
2.2.13 Cell proliferation assay 59
2.2.14 Cell apoptosis assay 60
2.2.15 Soft agar assay 60
2.2.16 γH2AX foci staining after irradiation 61
2.2.17 RNA sequencing 61
2.2.18 Drug Screening 62
2.2.19 Toxicity studies of cerebral organoids 65
2.2.20 Drug treatment studies of GLICO models 65
2.2.21 Bioluminescent imaging of GLICO models 66
2.2.22 EdU labelling and cell viability staining of GLICO models 66
2.2.23 Embedding, cryosectioning, and immunofluorescent staining of organoid tissue 66
2.2.24 Statistical analysis 67

3 Results 69

3.1 Genetic alterations of *GLI1* in glioblastoma 69
3.1.1 *GLI1* fusion genes frequently occur in 12q-amplified tumours and are associated with strong overexpression 69
3.1.2 Identification and validation of *GLI1* fusion transcripts in glioblastoma tumours of the HIPO016 cohort 71
3.1.3 Amplification boundary coincides with *GLI1* breakpoint in fusion-positive tumours 73
3.1.4 GLI1 target gene expression is upregulated in fusion-positive tumours of the HIPO016 cohort 75
3.1.5 Detection of *GLI1* genomic rearrangements in additional glioblastoma cohorts 76
3.2 Genetic alterations of *GLI1* in sarcoma 79
3.3 Comparison of *GLI1* fusion frequency and implications for further study 81
3.4 Epigenetic alteration by CTCF binding site disruption controls *GLI1* expression 81
3.5 *In vitro* phenotypic analysis of GLI1 in glioblastoma and liposarcoma cell models 84
3.5.1 Characterisation of glioblastoma and liposarcoma cell lines 84
3.5.2 GLI1 knockdown and inhibition affects cell proliferation, anchorage-independent growth, and apoptosis 85
3.5.3 RNA sequencing reveals downregulation of DNA repair pathways upon GLI1 knockdown 89
3.5.4 GLI1 inhibition causes DNA repair deficiency upon irradiation-induced DNA damage 91
3.6 Preclinical combination screening of GLI1 and DNA repair inhibitors 93
3.6.1 Screen setup 93
3.6.2 Primary drug screen identifies drugs with high sensitivity and selectivity as single agents 94
3.6.3 Secondary screen identifies synergistic drug combinations of GLI1 and DNA repair inhibitors 98
3.6.4 Validation of drug screening results 100

4 Discussion 107

4.1 Oncogenic activation of GLI1 in 12q-amplified glioblastoma and sarcoma tumours 107

4.2 Validation of GLI1 as a therapeutic target in glioblastoma and sarcoma cell models 111

4.3 GLI1 as a regulator of the DNA damage response and glycosylation 113

4.4 Identification of novel drug combinations in a preclinical drug screening 115

4.5 Combined targeting of GLI1 and the ATR/CHK1 axis as a potential treatment for patients with aberrant GLI1 activity 116

5 Conclusion 119

6 References 121

A Supplementary Information 141

B Publications 161

C Acknowledgements 163

List of Figures

Figure 1: Cytogenetics of gene amplification. 25

Figure 2: Mechanisms of gene fusion formation. 27

Figure 3: Frequency and classification of gene fusions across different tumour types. 29

Figure 4: Oncogene activation by alterations of the TAD structure. 32

Figure 5: Functional domains and motifs in GLI proteins. 33

Figure 6: Canonical Hedgehog signalling pathway in the primary cilium. 34

Figure 7: Hedgehog signalling activation as a driver of cancer hallmarks. 35

Figure 8: Patient information of HIPO016 cohort. 69

Figure 9: 12q amplification and *GLI1* expression in the HIPO016 cohort. 70

Figure 10: Experimental validation of *GLI1* fusion transcripts found in the HIPO016 cohort. 72

Figure 11: CNV plots based on 450k/EPIC methylation array analyses of patient tumours with *GLI1* fusion transcripts. 74

Figure 12: Expression of GLI1 target genes is upregulated in fusion-positive tumours. 75

Figure 13: *GLI1* fusion events and RNA expression in the TCGA-GB cohort. 77

Figure 14: *GLI1* expression levels in glioblastoma tumours of the HIPO043 cohort. 78

Figure 15: *GLI1* expression and amplification in sarcoma tumours. 80

Figure 16: CTCF binding sites locate in proximity of the *GLI1* locus. 82

Figure 17: CRISPR/Cas9 CTCF binding site disruption changes expression levels and cell proliferation. 83

Figure 18: Characterisation of glioblastoma and liposarcoma cell lines. 85

Figure 19: ShRNA knockdown of GLI1 decreases cell proliferation in glioblastoma and liposarcoma cell lines. 86

Figure 20: GLI1 inhibition impairs cell proliferation and anchorage-independent growth and induces apoptosis. 88

Figure 21: Differentially expressed genes in glioblastoma and liposarcoma cell lines. 89

Figure 22: GLI1 inhibition impairs DNA repair efficiency. 92

Figure 23: Screen setup of GLI1 and DNA repair inhibitors. 93

Figure 24: Inhibitor dose responses in cell lines with high GLI1 expression. 95

Figure 25: Drug sensitivity scoring identifies selective drugs in glioblastoma and liposarcoma cell models. 97

Figure 26: Correlation of IC_{50} values in 384-well format and 1536-well format. 98

Figure 27: Drug interaction profiles across GLI1/SHH and DNA repair inhibitor combinations. 99

Figure 28: Additive effects in T778 and LN308 cells upon combination treatment with GlaB and LY2606368. 100

Figure 29: Inhibition of long- and short-term proliferation in LN308 cells upon combination treatment with GlaB and LY2606368. 101

Figure 30: Evaluation of toxicity effects in cerebral organoids upon drug treatment. 103

Figure 31: Inhibitor treatment study in LN308 GLICO model. 105

List of Tables

Table 1: List of cell lines used in this work. 41
Table 2: List of cell culture reagents used in this work. 41
Table 3: List of chemicals and reagents used in this work. 42
Table 4: List of antibiotics, pharmaceutical drugs and inhibitors used in this work. 43
Table 5: List of buffers and solutions used in this work. 45
Table 6: List of primary antibodies used in this work. 45
Table 7: List of secondary antibodies used in this work. 46
Table 8: List of fluorescently conjugated antibodies used in this work. 46
Table 9: List of commercial plasmids used in this work. 46
Table 10: List of generated plasmids used in this work. 47
Table 11: List of shRNA sequences used in this work. 47
Table 12: List of sgRNA sequences used in this work. 47
Table 13: List of qPCR primers used in this work 48
Table 14: List of commercial kits used in this work. 48
Table 15: List of consumables used in this work. 49
Table 16: List of equipment and devices used in this work. 49
Table 17: List of databases used in this work. 51
Table 18: List of software used in this work. 51
Table 19: DNA probe preparation for DNA FISH. 54
Table 20: Covaris S2 sonication settings for chromatin fragmentation of T778 cells 58
Table 21: Seeding densities for cell lines used in this study. 63
Table 22: Compound concentration ranges used in the secondary screen. 64
Table 23: *GLI1* fusion transcript prediction in patients of the HIPO016 cohort using the confFuse and Arriba software. 71
Table 24: Genomic rearrangements with GLI1 in TCGA and HIPO043 glioblastoma cohorts. 76
Table 25: Detected genomic rearrangements with *GLI1* in the HIPO028 sarcoma cohort. 79
Table 26: KEGG pathway analysis of differentially expressed genes identifies common DNA repair pathways downregulated in liposarcoma and glioblastoma cell lines. 90
Table 27: KEGG pathway analysis of differentially expressed genes identifies common metabolic pathways upregulated in liposarcoma and glioblastoma cell lines. 90

Abbreviations

5PL	Five-parametric logistic
7-AAD	7-Aminoactinomycin D
ACTB	β-actin
ADH7	Alcohol dehydrogenase 7
AFH	Angiomatoid fibrous histiocytoma
Amp	Ampicillin
ASA	Angiosarcoma
ASPS	Alveolar soft-part sarcoma
ATO	Arsenic trioxide
BCA	Bicinchoninic acid
BSA	Bovine serum albumin
CCND1	Cyclin D1
CCS	Clear cell sarcoma
CCSK	Clear cell sarcoma of the kidney
CDK	cyclin-dependent kinase
CDK4	Cyclin Dependent Kinase 4
CFS	Chromosome fragile site
ChIP	Chromatin immunoprecipitation
ChIP-seq	Chromatin immunoprecipitation and sequencing
CHORD	Chordoma
CML	Chronic myeloid leukaemia
CNS	Central nervous system
CRISPR	Clustered regularly interspaced short palindromic repeats
CSA	Chondrosarcoma
CSC	Cancer stem cells
CTCF	CCCTC-binding factor
DDLS	Dedifferentiated liposarcoma
DDR	DNA damage response
dDSS	Differential drug sensitivity scoring
DFSP	Dermatofibrosarcoma protuberans
DM	Double minute
DMEM	Dulbecco’s modified eagle medium
DSB	Double-strand break
ecDNA	Extrachromosomal DNA
EdU	5-ethynyl-2-deoxyuridine
EGFR	Epidermal growth factor receptor
EHE	Epithelioid hemangioendothelioma
ERBB2	Erb-B2 Receptor Tyrosine Kinase 2
ES	Epithelioid sarcoma
ESS	Endometrial stromal sarcoma

EWS	Ewing sarcoma
FCS	Fetal calf serum
FDCS	Follicular dendritic cell sarcoma
FISH	Fluorescence *in situ* hybridisation
FITC	Fluorescein isothiocyanate
FMS	Fibromyxoid sarcoma
FOXS1	Forkhead Box S1
FPKM	Fragments per kilobase per million mapped fragments
FS	Fibrosarcoma
GAPDH	Glyceraldehyde 3-phosphate dehydrogenase
GB	Glioblastoma
G-CIMP	Glioma CpG island methylator phenotype
GCTB	Giant cell tumour of bone
GIST	Gastrointestinal stromal tumour
GlaB	Glabrescione B
GLI1	GLI Family Zing Finger 1
GSC	Glioma stem cells
GSEA	Gene set enrichment analysis
hEGF	Human epidermal growth factor
HG	High-grade
HH	Hedgehog
HHIP	Hedgehog interacting protein
HRP	Horseradish peroxidase
HSR	Homogeneously staining region
ICGC	International Cancer Genome Consortium
IDH	Isocitrate dehydrogenase
IMT	Inflammatory myofibroblastic tumour
IQR	Interquartile range
LB	Luria-Bertani
LG	Low-grade
LGG	Low grade glioma
LMO	Leiomyoma
LMS	Leiomyosarcoma
LS	Liposarcoma
MDM2	Mouse double minute 2
MEL (CUT)	Cutaneous melanoma
MFS	Myxofibrosarcoma
MGMT	O6-methylguanine methyl transferase
MIT	Massachusetts Institute of Technology
MLS	Myxoid liposarcoma
MOI	Multiplicity of infection
MPNST	Malignant peripheral nerve sheath tumour

MRT	Malignant rhabdoid tumour
MRT	Malignant rhabdoid tumour
NA	Not available
NaOH	Sodium hydroxide
NOS	Not otherwise specified
NS	Not significant
NSCLC	Non-small cell lung cancer
OS	Osteosarcoma
OS	Overall survival
PB	Polybrene
PCAWG	Pan-Cancer Analysis of Whole Genomes
PDGFRA	Platelet-derived growth factor receptor A
PE	Phycoerythrin
PECOMA	Perivascular epithelioid cell sarcoma
PEI	Polyethylenimine
PFS	Progression-free survival
PLS	Primary lung sarcoma
PNET	Primitive neuroectodermal tumor
PTCH1	Patched 1
PVNS	Pigmented villonodular synovitis
RCT	Round cell tumour
rhFGF	Recombinant human basic fibroblast growth factor
RMS	Rhabdomyosarcoma
RNA-seq	RNA sequencing
RPS18	Ribosomal protein S18
RT	Room temperature
RTK	Receptor tyrosine kinase
RT-qPCR	Real-time quantitative PCR
SCS	Spindle cell sarcoma
SEF	Sclerosing epithelioid fibrosarcoma
SFT	Solitary fibrous tumour
sgRNA	Single guide RNA
shRNA	Short hairpin RNA
SS	Synovial sarcoma
TAD	Topologically associating domain
TCGA	The Cancer Genome Atlas
TF	Transcription factor
TIGF	Transcription-induced gene fusions
TMZ	Temozolomide
TP53	Tumour suppressor protein 53
TSS	Transcription start site
UPS	Undifferentiated pleomorphic sarcoma

USARC	Undifferentiated sarcoma
VEGF	Vascular endothelial growth factor
WDLS	Well-differentiated liposarcoma
WES	Whole-exome sequencing
WGBS	Whole-genome bisulfite sequencing
WHO	World Health Organisation
WT	Wildtype

1 Introduction

1.1 Oncogenes and cancer

Cancer development is a multi-step progressive process in which several genetic and epigenetic aberrations manifest in a normal cell leading to its malignant transformation [1]. These alterations can be inherited in the germline, predisposing a person to develop a particular type of cancer, but more commonly are gained in somatic cells. In this case, a healthy cell acquires a series of alterations that accumulate over time and ultimately lead to uncontrolled cell growth, evasion from immunosurveillance, inhibition of cell differentiation and formation of new blood vessels to provide nutritional supply to the cell. If undetected and unhindered, tumour cells can eventually spread to other parts of the body, forming tumour metastases. Genetic studies in different types of cancers have identified only a small subset of genes associated with a high propensity for cancer [2]. These cancer-related genes can be subdivided into three classes, oncogenes, tumour suppressor genes, and non-coding RNAs. Non-coding RNAs are a major transcriptional output in the human genome and are not translated into proteins. In recent years, they have gained attention as essential regulators of various cellular processes with either activating or suppressing function, and their deregulation has been associated with human diseases, including cancer [3-5]. Oncogenes and tumour suppressor genes encode for proteins with opposing functions. Tumour suppressor genes typically inhibit cell division, control DNA damage repair, induce apoptosis, and suppress metastasis. The inactivation or loss of these genes can induce the onset or progression of tumour development [6]. In contrast, oncogenes frequently are involved in developmental processes, accelerate cell division, impede cell death, and inhibit cell differentiation. They commonly function as transcription factors, signal transducers, growth factor receptors, chromatin remodelers, or apoptosis regulators and their overexpression or activation is involved in tumorigenesis [7-11].

1.1.1 Mechanisms of oncogene activation

The activation of oncogenes can be driven by spontaneous or environmentally induced genetic and epigenetic mechanisms to proto-oncogenes that are otherwise normal genes. These include activating mutations in coding and regulatory regions, structural variations such as DNA copy number amplification or fusion gene formation, and chemical modifications of nucleic acids, histones, and non-histone proteins [12, 13].

1.1.1.1 Point mutations

Point mutations change the DNA sequence of a gene’s coding region or its regulatory region [14, 15]. While non-synonymous mutations within the coding region of a gene can alter the structure of the protein and lead to a hyperactive gene product, mutations in the regulatory region of the gene can modify transcriptional regulation and lead to elevated activity. The number of coding mutations differs across different types of cancer as well as across tumours of a given malignancy but it has been shown that mutations enrich within driver genes [16-18]. Activating non-synonymous mutations in proto-oncogenes are frequent drivers in tumorigenesis. The most notable examples are mutations within the kinase domain of the *BRAF* and *RAS* proto-oncogene families, which result in a constitutively active protein and uncontrolled stimulation of the signalling cascade [19]. *BRAF* mutations are common in melanoma, thyroid cancer, and some paediatric brain tumours; mutated RAS oncogenes (*KRAS*, *HRAS*, *NRAS*) are frequently found in lung, colon, pancreas and hematologic cancers [20, 21].

1.1.1.2 Gene amplification

Gene amplification is a common event in many human cancers and results from copy number variation of a DNA segment that can span small chromosomal regions of only a few kb up to whole chromosomes or even the whole genome [22, 23]. Independent of the overall size of the amplified region, the expression of individual genes included in the amplicon is often increased concomitantly with the gene copy number change (gene-dosage effect). Amplified regions can be mapped by either chromosome banding and fluorescence in situ hybridisation (FISH) or analysed at a higher resolution by copy number variation arrays and sequencing techniques [24, 25]. Sequencing techniques additionally allow determining whether these structural variations occur at clonal or subclonal frequencies, thereby approaching whether the amplification occurred during early or late tumour stages [26, 27]. The amplified DNA can be present in extrachromosomal structures (ecDNA), as tandem repeats in cytologically visible homogenously staining regions (HSR), or distributed randomly in the genome [23]. Analyses of normal and cancer cells from different tumours showed that oncogene amplification on ecDNA is widespread amongst cancer types but rarely found in normal cells [28]. Characteristically, these cancer-associated ecDNA particles are > 1 Mb in size, contain one or more genes and regulatory regions, lack centromeres and can form pairs of chromatin bodies that are called double minute chromosomes (DM) (Figure 1) [29, 30]. EcDNA can re-integrate into chromosomal DNA such as near telomeres, thereby further promoting genome instability [31]. As ecDNA is unequally segregated between daughter cells during cell division, the daughter cell receiving more copies of the ecDNA can gain a selective advantage through the relatively higher expression of the ecDNA-resident oncogene compared to other tumour cells. This process has been proposed to accelerate intratumoral heterogeneity and contribute to tumour evolution [32].

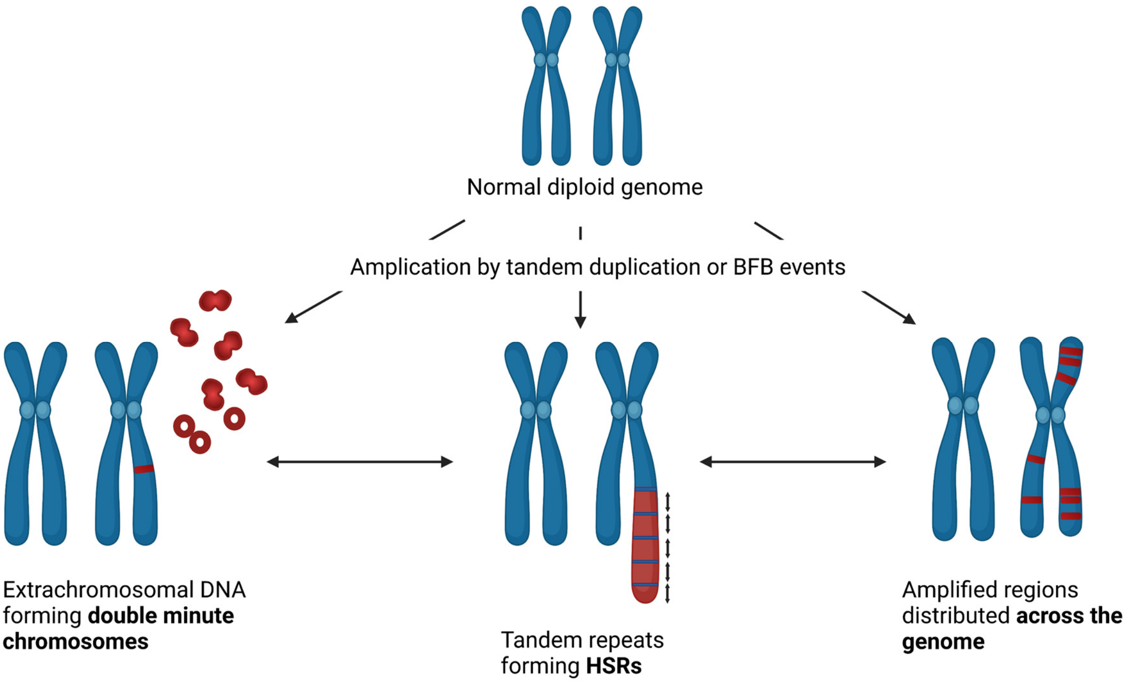

Figure 1: Cytogenetics of gene amplification. DNA amplification resulting from tandem duplication or breakage-fusion-bridge events can be organized in various forms in the genome, such as ecDNA forming double minute chromosomes, in tandem arrays forming homogenously staining regions, or can be interspersed at various locations across the genome. The location of amplified DNA is a dynamic process, and ecDNA can re-integrate into the genome and vice versa. Figure created with BioRender.com based on a similar schematic representation in Albertson D, 2006 [22].

Gene amplification is initiated by genomic instability and double-strand breaks and will only be propagated to daughter cells if the cells can pass cell cycle checkpoints. In the process of gene duplication, cellular repair mechanisms are required to re-connect two DNA ends and ensure genome integrity and cell division. Several DNA repair pathways are available to somatic cells that differ mechanistically. While some depend on sequence homology between the two sequences of the sister chromatids, others promote error-prone non-homologous end-joining, often causing microdeletions at the fusion point [33, 34]. Several mechanisms have been proposed by which oncogenes become duplicated in cancer genomes, including tandem duplications and breakage-fusion-bridge events [35].

Tandem duplication occurs when genetic material is exchanged between separated sites in two sister chromosomes by homologous recombination, annealing, or transposition [36]. Remodelling of the junction region reduces the size of the duplicated region and is often selectively favoured.

Breakage-fusion-bridge (BFB) events can be initiated with a chromosome losing a telomere end by either telomere shortening or unrepaired DNA break. The chromosome replicates during the cell cycle, forming two sister chromatids without telomeres that fuse at their ends. When the chromosomes are pulled to opposite spindle poles during anaphase, a bridge is formed that can break at any site, resulting in one daughter cell receiving a chromosome with an inverted terminal duplication and the other one a terminal deletion. As telomeres are absent in both daughter cells, many BFB cycles consecutively occur in subsequent mitotic events, promoting a drastic increase in copy number of the unstable chromosome and contributing to intratumoral genetic heterogeneity [37, 38].

Certain hotspots and whole chromosomes in cancer genomes are more frequently subjected to duplication than others [39]. For example, while small chromosomes are more prone to whole-chromosome loss, chromosomes 7, 12, and 20 are often duplicated and selectively favoured during tumorigenesis [40]. Chromosomal amplifications frequently include known oncogene loci, including *MYC*, *RAS*, *CCND1*, *ERBB2*, *MDM2*, and *EGFR*, and are associated with increased cancer risk [23, 41]. The amplification of *ERBB2*, for example, is used as a diagnostic tool in breast cancer, correlating with aggressive tumour growth and poor prognosis in these tumours [42, 43]. Moreover, *MDM2* is amplified in many sarcomas and binds to the tumour suppressor protein p53, interfering with tumour growth regulation [44, 45].

1.1.1.3 Gene fusions

Gene fusions are formed when two independent genes fuse to form a single hybrid gene. Several mechanisms have been described to cause the formation of gene fusions, including inter- and intrachromosomal rearrangements and aberrant transcriptional mechanisms affecting alternative splicing [46].

Formation of gene fusions

Structural chromosome rearrangements occur when DNA double-strand breaks are repaired by re-joining and reassembling the fragments in a different order than initially present (Figure 2) [23, 47]. These genetic alterations can either result in balanced or imbalanced structural rearrangements. In inversion or translocation events, the rearrangements are balanced, meaning that only the relative locations of DNA segments are varied on the rearranged chromosome, without any gain or loss of genetic material. Deleting or duplicating DNA segments, ranging from single nucleotides to whole chromosomes, results in imbalanced structural rearrangements. DNA fragments that are excised during deletion events are acentric and will be lost during cell division. Extra copies of DNA gained in duplication events often result in tandem duplications with the segments located directly adjacent to one another. Another genetic mechanism resulting in the formation of gene fusions is chromothripsis, a shattering event of one or a few chromosomes that leads to breakage of the confined regions into many DNA fragments and subsequent inaccurate reassembly [48, 49]. Recent studies show that around 50 % of all cancers are affected by chromothriptic events [50, 51]. Chromoplexy is a similar phenomenon first described in prostate cancer cells, involving DNA segments from multiple chromosomes. It can occur several times in tumour evolution and, compared to the hundreds of clustered genomic breakpoints in chromothripsis, chromoplexy results in fewer unclustered rearrangements [52, 53]. The function of genes affected by rearrangements can get disrupted either by the formation of fusion genes, or transcriptional deregulation, frequently resulting in gene overexpression that can contribute to the malignant transformation of a healthy cell.

Transcription-induced gene fusions (TIGFs) mostly occur in adjacent genes located on the same DNA strand (*cis*-TIGFs) but have also been described for distal genes (*trans*-TIGFs) [54-56]. In *cis*-TIGFs, two consecutive genes are transcribed as read-through. Subsequent alternative splicing by either retaining or skipping individual exons causes the formation of novel gene transcripts. Structural rearrangements such as the deletion of intermediate DNA regions often precede this process and bring otherwise far apart genes in vicinity, favouring transcriptional read-through and the formation of TIGFs [57].

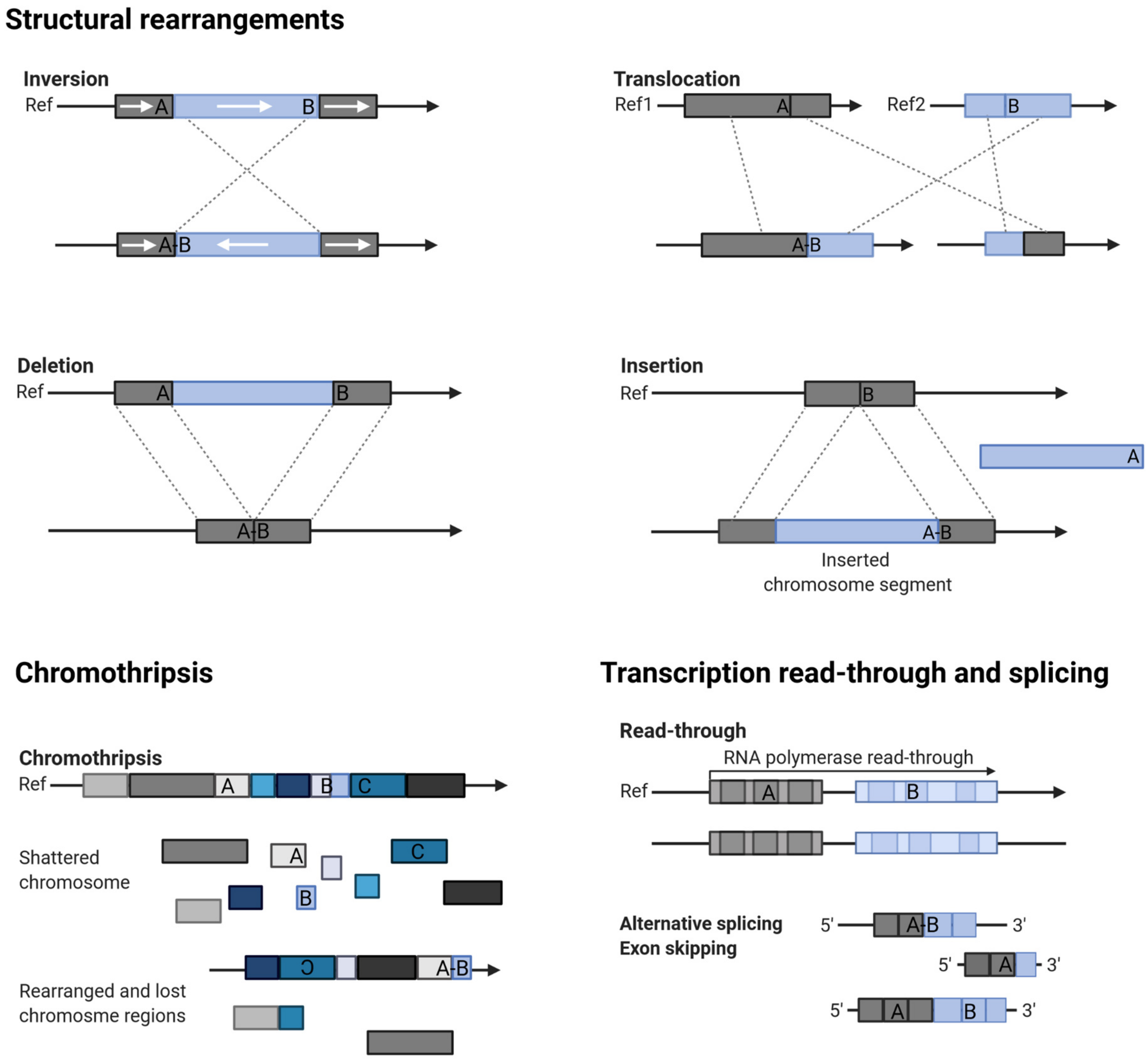

Figure 2: Mechanisms of gene fusion formation. Gene fusions can originate from (1) structural rearrangements of chromosomal regions such as translocations (chromosome regions are transferred intra- or interchromosomally), inversions (flipping of chromosomal regions), deletions (loss of intervening DNA connects two originally distant genes) or insertions (integration of a DNA fragment from a distant site), (2) chromothripsis (catastrophic event, causing the shattering of a chromosome and random rearrangement of chromosome fragments) or (3) transcription read-through and splicing (non-structural rearrangement mechanisms by which neighbouring genes are transcribed together and mRNA molecules are spliced together by retaining or skipping of exons. A and B symbolize affected genes, A-B represents the resulting fusion gene. Figure created with BioRender.com.

Gene fusions in cancer

Many gene fusions have been identified as strong driver mutations in different types of cancer, providing an essential understanding of the disease mechanisms. Since the detection of the Philadelphia chromosome and the *BCR-ABL* fusion gene in chronic myeloid leukaemia (CML) as the first-ever described cancer-associated fusion protein, thousands of other chromosome aberrations have been identified as somatic mutations in cancer [58-60]. Due to advances in genome and transcriptome profiling, the number of reported gene fusions steeply increased in the last decade as sequencing technologies enabled the unbiased detection of fusions without prior knowledge of the cytogenetic information of the malignant cell. Several cross-entity studies have been reported that systematically investigated the landscape of gene fusions and their implications for tumour phenotype, diagnosis, and treatment [61-63]. In a study by Yoshihara and colleagues, 4,366 primary adult neoplasms across 13 different histotypes from the TCGA network were analysed, identifying more than 8,600 tumour-specific fusion pairs [62]. The prevalence of gene fusions differed across tumour types, with the highest frequencies observed in lung squamous cell carcinoma (LUSC), prostate adenocarcinoma (PRAD), and bladder urothelial carcinoma (BLCA). The majority of fusion transcripts were associated with copy number variations such as DNA amplification or deletion events. In contrast, tumour types with overall low frequency (acute myeloid leukaemia and thyroid carcinoma) were characterised by a high frequency of balanced interchromosomal fusions (Figure 3). In line with these results, the Pan-Cancer Analysis of Whole Genomes (PCAWG) Consortium of the International Cancer Genome Consortium (ICGC) and The Cancer Genome Atlas (TCGA) recently analysed matched transcriptome and genome data of 1,188 samples from 27 tumour types and identified more than 3,500 fusion events with only a few (approximately 5 %) occurring in more than one sample across several tumour types [61]. 82 % of detected gene fusions were associated with structural variants. In some fusion transcripts, structural variation of the promoter regions resulted in the fusion of the UTR region of one gene with the coding sequence of another gene [61].

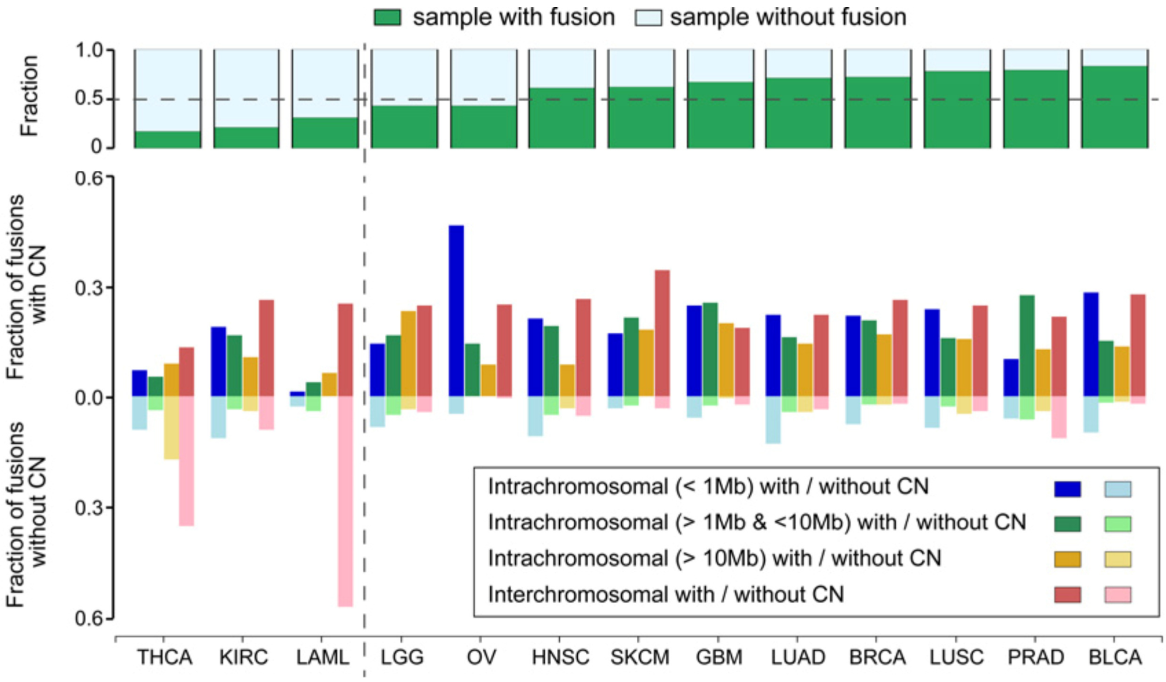

Figure 3: Frequency and classification of gene fusions across different tumour types. Samples were analysed by the TCGA network, including 4366 primary tumour samples from 13 tissue types. Top: Overall prevalence of patients with detected fusion transcripts in 13 malignancies identifies tumour types with overall low frequency of fusion transcripts, including thyroid carcinoma, clear cell carcinoma, and acute myeloid leukaemia. The highest fraction of samples with fusion transcripts was identified in bladder urothelial carcinoma. Bottom: Fusion transcript classification in inter- and intrachromosomal translocations with and without the presence of a DNA copy number alteration that is within 100 kb of the junction point. THCA, thyroid carcinoma; KIRC, kidney renal clear cell carcinoma; LAML, acute myeloid leukaemia; LGG, brain lower grade glioma; OV, ovarian serous cystadenocarcinoma; HNSC, head and neck squamous cell carcinoma; SKCM, skin cutaneous melanoma; GBM, glioblastoma multiforme; LUAD, lung adenocarcinoma; BRCA, breast invasive carcinoma; LUSC, lung squamous cell carcinoma; PRAD, prostate adenocarcinoma; BLCA, bladder urothelial carcinoma. Abbreviations based on TCGA nomenclature, not WHO classification. Figure modified from Yoshihara et al., 2015 [62].

Pathogenetic impact of gene fusions

While a clear link to tumour phenotype has been described for some gene fusions, the cellular consequences of many predicted gene fusions have yet to be elucidated [60]. Pathogenetically, the formation of gene fusions can have different impacts on the gene partners, including transcriptional deregulation, formation of chimeric proteins with a distinct function, gene truncations, and passenger mutations.

In the first case, the transcription of an otherwise normal gene positioned at the breakpoint is changed by either exchanging the promoter region or locating it upstream of a transcriptional control element that is active in the target tissue. Many such fusion events result in oncogene activation through the relocation of a proto-oncogene to an active promoter or enhancer site. Expression analysis of highly recurrent oncogenes involved in fusions, such as *EGFR*, *ERBB2*, and *RET*, showed an increase in expression compared to samples without fusions [63].

Gene translocations creating hybrid proteins with altered functions have been described in many types of cancer and include but are not limited to kinases, transcription factors, and chromatin remodelers [46, 63]. The formation of the chimeric BCR-ABL protein, for example, results in an abnormal ABL tyrosine kinase activity in CML [64]. Furthermore, different ALK fusions in non-small cell lung cancer (NSCLC) and paediatric brain tumours cause the constitutive activation of the receptor tyrosine kinase ALK and its downstream signalling pathways [65-67].

Chromosome rearrangements that result in gene truncations are often associated with the inactivation of tumour suppressor genes by forming out-of-frame gene fusions or deleting important protein domains [6, 68, 69]. However, they can also contribute to oncogenic activation. The loss of intrinsic control elements, microRNA binding sites, or the deletion of autoinhibitory domains and translocation signals can result in the constitutive activation of oncogenes with transforming capacity. For example, the *FGFR3-TACC3* fusion in glioblastoma looses the binding site for miR-99a and thereby escapes its negative regulation, leading to increased FGFR3 protein expression [70, 71]. *SLC45A3-BRAF* fusion-positive prostate cancer cells have lost the autoinhibitory region of BRAF, and its retaining kinase domain becomes constitutively active [72].

The fast-growing number of detected gene fusions have raised the question of their tumorigenic potential. Even though many fusions are clear pathogenic drivers in different neoplasia, the vast majority of gene fusions are passenger mutations and arise as consequences of genetic instability, a characteristic of many types of cancer. As tumours evolve, their genome becomes unstable and accumulate chromosome aberrations, including gene fusions that can increase their invasive and metastatic potential [23, 73].

1.1.1.4 Epigenetic changes

The complexity of tumorigenesis cannot be explained by genetic changes alone but also involves epigenetic modifications that affect the expression of genes without changing the nucleotide sequence [74]. Several mechanisms are known to affect the epigenome in cancer cells and are likely to cooperate during tumorigenesis. DNA methylation, histone modifications, small noncoding microRNA, and chromosome topological organisation are prominent examples amongst them.

DNA methylation of promoter regions can regulate cancer gene expression by silencing the transcription of TSGs or permitting oncogene expression by DNA hypermethylation and hypomethylation, respectively [75, 76]. Changes in DNA methylation patterns of upstream enhancer sites or in gene bodies have also been described to correlate with gene expression levels of the associated gene [77, 78]. Additionally, a strong correlation of gene-body hypermethylation and the activation of many homeobox oncogenes was found in a pan-cancer analysis of several types of solid tumours [78]. Especially in recent years, DNA methylation has gained increasing clinical relevance for tumour sub-classification, as a prognostic marker and to predict the efficacy of targeted therapies [79-81].

Histone modifications are associated with either transcriptional repression or activation [82]. Methylation and acetylation of specific lysine residues on histone proteins affect chromatin structure and nucleosome positioning, thereby regulating the transcriptional machinery's access to coding sequences [83]. For example, the loss of polycomb mark H3K27me3 from bivalent promoters has been associated with the activation of several cancer-promoting genes in colon cancer [84] and mutations in amino acids K27 and G34 of histone H3.3 affect global DNA methylation, defining distinct epigenetic subgroups in paediatric glioblastoma [80].

Small non-coding microRNAs are single-stranded RNAs of 21-23 nucleotides that target complementary mRNA sequences and control their translation into proteins [85]. Their dysregulation in malignant tissues can cause the activation of otherwise dormant proto-oncogenes. For example, the microRNA let-7 interacts with members of the *RAS* family and other important oncogenes such as *c-MYC*, *HMGA*, *JAK* and *STAT3*, inhibiting the activation of their molecular pathways [86-88]. In line with this tumour suppressing function, let-7 expression is downregulated in several types of cancers, including non-small cell lung cancer and colon cancer [89, 90].

Analyses of the structural organisation of the genome revealed that gene regulation occurs by long-range interactions between regulatory elements and their target genes, and changes in topological organisation can lead to altered gene expression in disease [91, 92]. Enhancers and insulators physically connect with their target promoters by chromosomal looping, forming so-called topologically associating domains (TADs) [93]. CTCF is an important mediator in this process as it binds to specific sites at the boundary of TADs and folds the chromatin into such domains. Disruptions of chromosome domains by local TAD boundary disruption or genomic rearrangements can alter the genome architecture and communication between promoters and their regulatory regions, and lead to the deregulation of gene expression patterns within the TADs [94] (Figure 4). For instance, the methylation of CTCF binding sites in IDH^{mut} glioma tumours results in partial inactivation of TAD boundaries, triggering the expression of the *PDGFRA* oncogene by enhancers located outside of the normal *PDGFRA* TAD [95]. In medulloblastoma tumours, structural variation and genomic rearrangements on chromosome 9 juxtapose the *GFI1* oncogene family proximal to active enhancer elements and drive oncogenic activation [96].

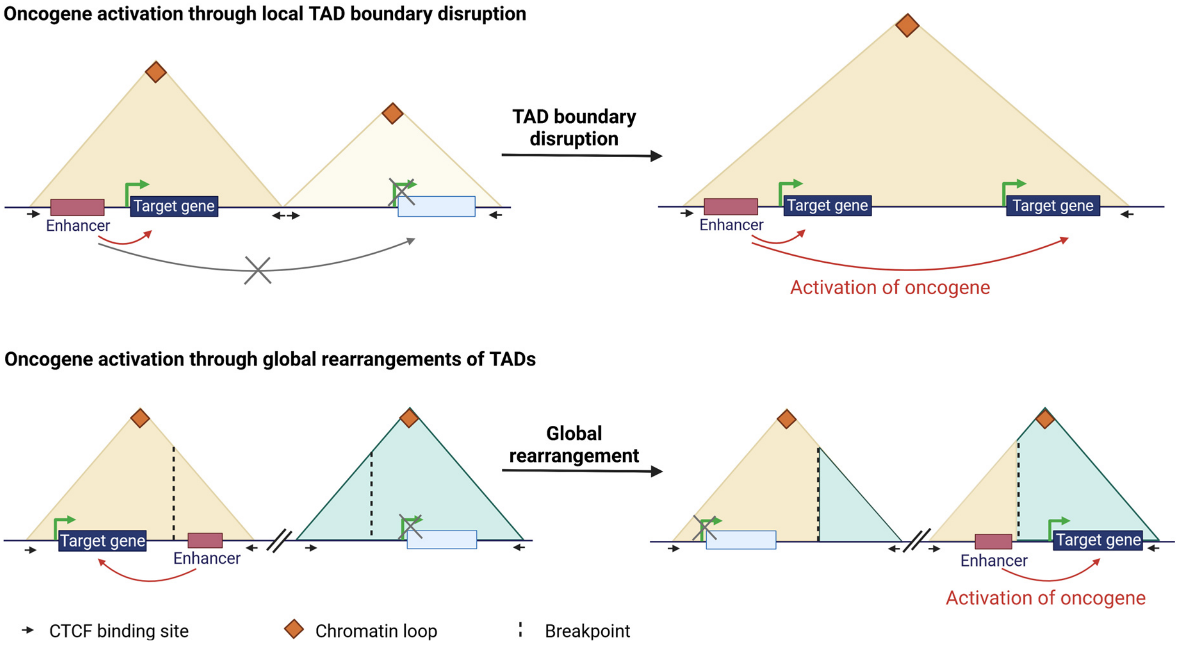

Figure 4: Oncogene activation by alterations of the TAD structure. Changes in genome topology can change the transcriptional regulation and activation of genes by modifying the interaction with regulatory regions. Top: Disruption of a CTCF binding site by either mutation or epigenetic inactivation can disturb local TAD boundaries and affect gene regulation in the two flanking TADs. In this example, two compartments fuse, allowing the interaction and activation of an oncogene by the enhancer locating in the same functional TAD after the fusion. Bottom: Breakpoints within TADs can cause the breakage and fusion of TADs creating new sets of topological domains without affecting the boundaries. Oncogenes in affected domains can get in contact with new sets of regulatory elements, activating oncogenic expression. Figure created with BioRender.com based on a similar schematic representation in Valton & Dekker, 2016 [92].

1.1.2 Oncogenes as therapeutic targets

The correlation of oncogenic gene fusions and amplifications with tumour subtypes and cancer-specificity demonstrates their clinical relevance and indicates them as attractive targets for precision cancer treatment.

Gene fusions are used for cancer classification, screening, and treatment stratification. As such, *TMPRSS2-ERG* fusions serve as a biomarker for a distinct subtype of prostate cancer, and its detection in urine samples has proven helpful as a complement to prostate-specific antigen (PSA) levels in diagnostic screening and risk stratification [97, 98]. The discovery of imatinib, which blocks the kinase activity of the tumorigenic BCR-ABL1 fusion protein, has revolutionised the treatment of CML and other malignancies and was the first therapeutic intervention targeting the product of a gene fusion [99, 100]. Since then, several other fusion-gene targeting drugs gained FDA approval, including crizotinib and ceritinib for *ALK* fusion-positive NSCLC, while others are in preclinical testing or Phase I and II clinical trials [101-103].

Oncogenic proteins resulting from gene amplification or deregulated expression can be targeted by small-molecule inhibitors or, if present on the cell surface, by monoclonal antibodies. For example, breast cancer and gastric/oesophagal cancer patients with tumours harbouring *ERBB2* amplification are treated with trastuzumab and/or pertuzumab, monoclonal antibodies against the product of this oncogene [104, 105].

1.2 GLI Family Zinc Finger 1 and Hedgehog/GLI signalling

The GLI Family Zinc Finger 1 (GLI1) protein, also known as the glioma-associated oncogene homolog 1, is a member of the Kruppel family of zinc finger proteins and a transcription factor initially identified as an amplified gene in a human malignant glioma [106, 107]. Together with the two other members of the *GLI* family, GLI2 and GLI3, it serves as the central effector protein downstream of the Hedgehog (HH) signalling pathway, which is tightly controlled during embryonic development and tissue patterning and is critical in adult tissue homeostasis, regeneration, and healing [108-110]. As a transcription factor, it regulates specific target genes involved in cellular proliferation, cell fate determination, stemness, and cellular survival. While GLI1 exclusively exerts activating function through its C-terminal transcription activation domain, GLI2 and GLI3 also contain a repressor domain at their N-terminus and can act as transcriptional repressors [111]. In addition to the formation of activator and repressor protein forms, GLI activity is negatively regulated by internal degron sequences (D_n, D_c) that account for continuous proteasomal degradation of GLI proteins (Figure 5) [112].

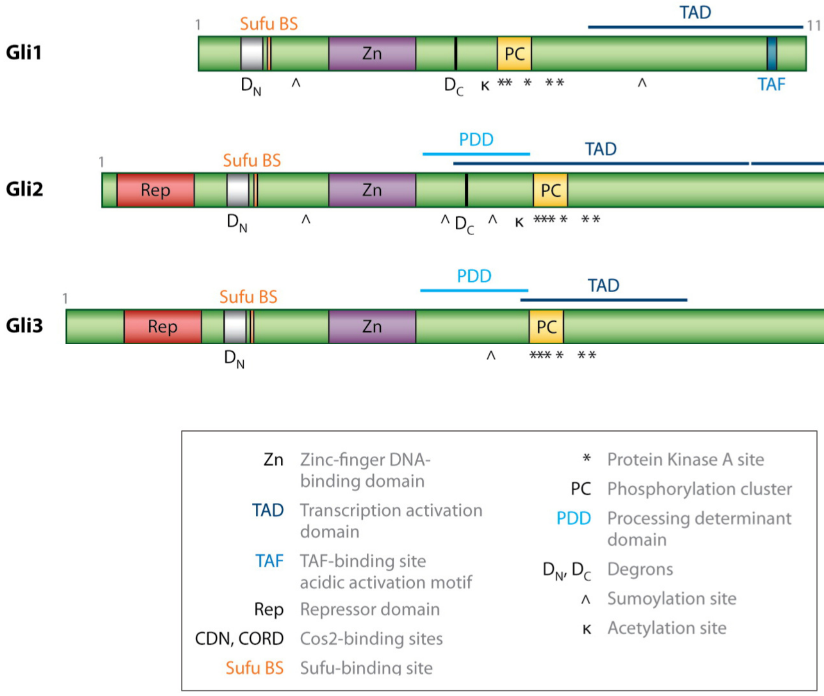

Figure 5: Functional domains and motifs in GLI proteins. Several protein domains are conserved between the three *GLI* family members, GLI1, GLI2, and GLI3. One major difference is the N-terminal repressor domain that is only present in GLI2 and GLI3. While GLI1 only acts as a transcription activator through its C-terminal transcription activation domain (TAD), GLI2 and GLI3 additionally have an N-terminal repressor domain by which they mediate transcriptional repression. Figure modified from [113].

1.2.1 Canonical HH/GLI signalling

The Hedgehog/GLI signalling pathway is coordinated within the primary cilium, which is present in only a few cell types but most commonly in epithelial cells, and depends on extracellular stimuli. In the unstimulated state, the pathway is actively repressed by the unliganded Patched 1 (PTCH1) receptor that precludes the G-protein coupled receptor-like Smoothened receptor (SMO) from entering the cilium. The GLI transcription factors are bound in a protein complex at the tip of the cilium by SUFU Negative Regulator Of Hedgehog Signaling (SUFU) and kinesin-family protein 7 (Kif7). They are sequestered and phosphorylated by PKA, casein kinase 1 (CK1), and glycogen synthase kinase-3 (GSK-3β), and subsequently either processed into N-terminal transcriptional repressor forms (GLI3-R and to a lesser extent GLI2-R) or targeted for degradation (GLI1 and GLI2). Upon binding of one of the HH ligands, IHH, SHH, or DHH, SMO is derepressed and can access the primary cilium, where it represses SUFU and releases GLI1 for activation by proteolytic cleavage. In this form, GLI1 can be transported out of the cilium and translocate to the nucleus where it binds to its consensus sequence (5'-GACCACCCA-3') and activates the transcription of its target genes, including *Cyclin D*, *Cyclin E*, *MYC*, *PTCH1*, *PTCH2*, and *HHIP*. In addition, GLI1 also regulates its transcription as a positive feedback mechanism to further amplify the Hh signal response (Figure 6) [108, 113-115].

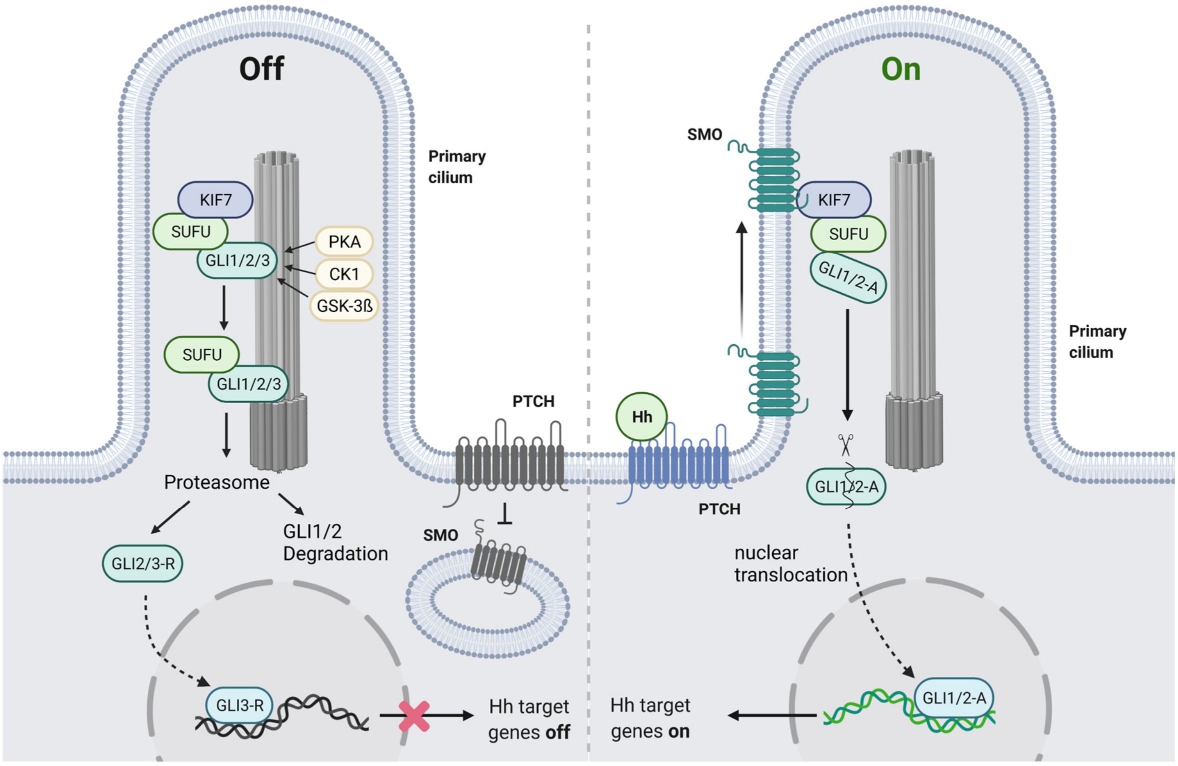

Figure 6: Canonical Hedgehog signalling pathway in the primary cilium. Left: Off-state: GLI transcription factors are either degraded in the proteasome or act as a transcriptional repressor. Right: On-state: GLI transcription factors act as activators by translocating to the nucleus and switching on target gene expression. Figure created with BioRender.com.

1.2.2 Oncogenic HH/GLI signalling

In terminally differentiated healthy tissue, *GLI1* expression levels are low. However, an increased expression level of *GLI1* and persistent activation of HH/GLI signalling has been associated with many types of human cancers, promoting numerous cellular activities that are linked with the hallmarks of cancer, including proliferation, survival, angiogenesis, metastasis, escape from immunosurveillance, chemotherapeutic resistance, metabolic rewiring, genomic instability, tumour-promoting inflammation, and stem cell renewal (Figure 7) [116, 117]. For example, upregulated *GLI1* expression causes uncontrolled cell proliferation and escape from cell death through downregulation of p53, transcriptional upregulation of D-type cyclins, *CCND1* and *CCND2*, and *BCL2* regulation [118-120]. Uncontrolled GLI1 activity has been found in basal cell carcinoma (BCC) [121], SHH-driven medulloblastoma [122], glioma [106, 123], sarcoma [124], non-small cell lung cancer [125], and cancers of the esophagus [126] and bladder [127]. Aberrant GLI1 activation can occur either via SMO-dependent or SMO-independent mechanisms. Loss-of-function mutations in *PTCH1* or gain-of-function mutations in *SMO* cause ligand-independent constitutively active HH/GLI signalling in BCC [128, 129], while mutations in SUFU have been attributed to medulloblastoma tumorigenesis [130, 131]. In addition, SMO-independent non-canonical activation mechanisms of HH signalling have been described, including genomic amplification of *GLI2* in medulloblastoma, aberrant expression by transcriptional or epigenetic deregulation, or the cross-talk with several other oncogenic signalling pathways [116, 131]. Amongst these are the RAS/MEK/ERK, PI3K/AKT, JAK/STAT pathways, and epigenetic modifiers such as BRD4 [115, 116, 132-135].

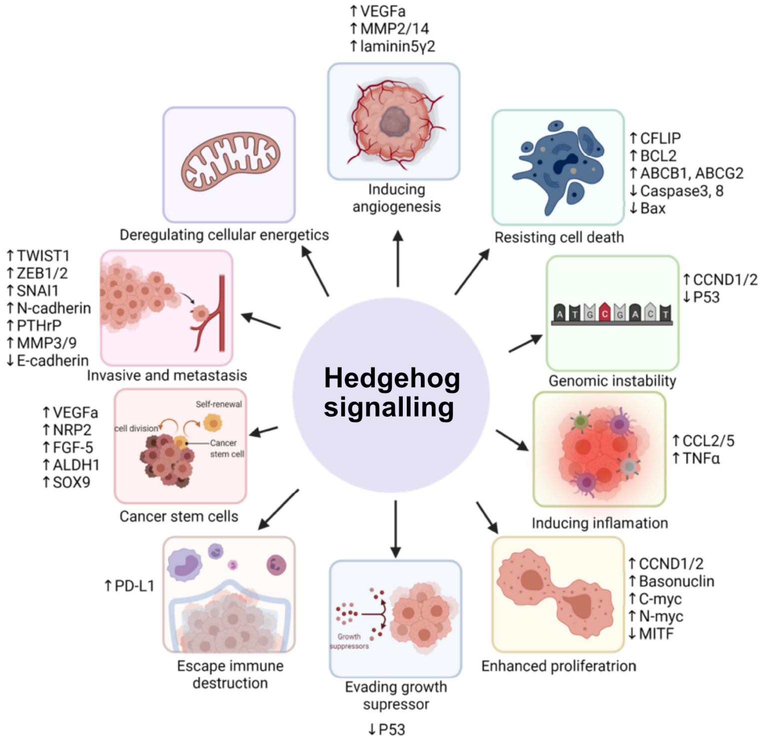

Figure 7: Hedgehog signalling activation as a driver of cancer hallmarks. Aberrant Hedgehog signalling is closely associated with the promotion of numerous hallmarks of cancers, including sustained proliferation, survival, angiogenesis, metastasis, metabolic rewiring, genomic instability, tumour-promoting inflammation, acquisition of cancer stem cell-like traits, and chemotherapeutic resistance through the regulation of several key genes involved. The figure was taken from [116].

1.2.3 Therapeutic targeting of GLI1

The effects of HH/GLI signalling on various key molecular mechanisms makes it an attractive cancer therapy target. To date, most efforts have been focused on targeting the canonical HH pathway and its upstream regulators like SMO [136-139]. Several SMO inhibitors have gained FDA approval for the treatment of BCC and medulloblastoma. However, clinical trials with these compounds in other solid tumours have failed, most likely due to the compensatory activity of non-canonical pathway activation [140]. This, as well as the development of SMO inhibitor resistances, illustrates that direct targeting of GLI1 represents a promising strategy to block canonical and non-canonical HH-driven tumour growth. Even though several promising GLI1 antagonists have been developed in the preclinical setting, most of these inhibitors are pharmacologically not suitable for clinical application. GANT61 and its derivative GANT58, for example, reduce the DNA binding capacity of GLI1 by binding between its zinc finger domains but are rapidly hydrolysed to an inactive form [141-143]. Arsenic trioxide (ATO), an FDA-approved compound for the treatment of acute promyelocytic leukaemia, has been shown to interfere with GLI activity by directly binding to GLI proteins and enhancing their degradation [144, 145]. However, it has not been studied in clinical trials for medulloblastoma or glioma due to its low potency in blood-brain-barrier permeability [146]. One promising new compound to overcome these limitations is GlabrescioneB (GlaB), an isoflavone naturally found in the seeds of *Derris glabrescens*. It inhibits the transcriptional activity by preventing GLI1 binding to DNA and has shown an antitumour effect in BCC and medulloblastoma *in vitro* and *in vivo* [147, 148].

1.3 Glioblastoma

Glioblastomas are the most common malignant tumours of the central nervous system and are classified by the World Health Organisation (WHO) as grade IV of histological malignancy [149, 150]. The tumours are mainly located in the cerebral hemispheres of the brain, and around 90 - 95% of glioblastoma are primary tumours diagnosed *de novo*. The less common secondary glioblastoma are morphologically identical to primary tumours but arise from lower-grade diffuse astrocytoma (WHO grade II), anaplastic astrocytoma (WHO grade III), or oligodendroglioma (WHO grade II). The incidence of glioblastoma is 3.22 per 100,000 adults per year accounting for 14.6 % of all brain tumours and central nervous system neoplasms [149]. Glioblastoma occurrence varies by sex and age with a 1.58 times higher incidence in men and a median age at diagnosis of 65. The prognosis of glioblastoma patients to date is still very poor as the median survival after diagnosis is only 12.6 months and the 5-year overall survival is 6.8 % [149]. Patients are treated in a multimodal approach with maximal surgical resection followed by radiotherapy (60 Gy) with concomitant temozolomide (TMZ) chemotherapy [151]. TMZ treatment efficiency depends on the O6-methylguanine methyltransferase (MGMT) status of the tumour. If *MGMT* is hypomethylated and expressed in the tumour, it can remove the O6-methylguanine modifications induced by TMZ, resulting in therapy resistance [152, 153]. Furthermore, the high intra- and intertumoural heterogeneity of glioblastoma constitute a particularly challenging clinical problem [154].

The dismal prognosis, lack of efficient treatment strategies, and the emergence of therapy resistance highlight the importance of a better understanding of glioblastoma biology. Better patient stratification and individualised treatment strategies are required to combat the complexity of this lethal tumour disease. Advances in sequencing technologies and data analyses in the last two decades have shed light on glioblastoma molecular characteristics and enabled the classification of glioblastoma tumours into molecular subgroups, updating previous histological classification approaches [155]. Up to now, several classification regimes have been proposed based on transcriptional or epigenetic features [80, 81, 156, 157]. Initially, the Cancer Genome Atlas (TCGA) network classified glioblastoma into four distinct subtypes, based on unsupervised clustering of transcription profiles, referred to as proneural, neural, mesenchymal and classical [156]. Another classification approach by Noushmehr and colleagues defined three distinct glioblastoma subgroups based on the tumours' DNA methylation profile [81], with one subgroup having a glioma CpG island methylator phenotype (G-CIMP) with cancer-specific hypermethylation at a large number of CpG loci strongly associated with *IDH1* mutations [81]. In a further refinement of DNA methylation-based glioblastoma classification by Sturm et *al.*, adult glioblastoma tumours were classified into four subgroups, IDH1, RTKI/PDGFRA, Mesenchymal (MES), and RTKII/Classical, with distinct methylation patterns accompanied with differences in mutational patterns, expression profiles, copy number aberrations and patient age [80]. The classification of glioblastoma tumours into distinct subtypes based on their molecular profiles enabled the identification of core signalling pathways that are deregulated in these tumours. Even though glioblastoma classification is still under discussion and a dynamic process, patient stratification is an important first step towards the development of specific treatment modalities in glioblastoma. As subtype-driven aberrations have been shown to differ in their responses to chemotherapeutic treatment, it is of special need to further characterise patient subgroups in more detail and to explore therapeutic options that are tailored for distinct genetic aberrations [156].

Several hotspots of frequent structural variation have been described in glioblastoma, including chromosome 7 amplification, chromosome 10 deletion, EGFR amplification co-occurring with homozygous deletions of *CDKN2A*, and amplification of chromosome 12. Analyses of the somatic landscape in glioblastoma from the TCGA network identified structural variation in chromosome arm 12q in 26 % (11/42) of whole genomes, frequently associated with fusion transcripts, including the *MDM2* and *CDK4* oncogenes [157]. Subsequent studies identified this region as a breakpoint-enriched region (BER) with a shattered chromosome pattern, suggesting local chromosomal instability, present in 5 % of *IDH* wildtype glioblastoma and associated with worse survival [158]. While *TP53* mutations were significantly fewer in these tumours possibly due to TP53 degradation by MDM2, the potential impact of other genes within the 12q14-15 BER such as *GLI1* was not the subject of this study.

After the initial detection as an amplified gene in human glioma, *GLI1* amplification has been repeatedly described in a small subset of gliomas [159, 160]. In a platelet-derived growth factor

(PDGF)–induced glioma model, activated GLI1 was found in the perivascular niche, associated with an SHH-producing microenvironment of stromal cells, including astrocytes, endothelial cells, and pseudopalisade cells [161]. Moreover, SHH expression correlated with tumour grade, with higher SHH expression in high-grade gliomas. In addition to its suggested function in tumorigenesis, the Hedgehog pathway and other developmental pathways, including NOTCH and WNT, have been attributed to the maintenance of glioma stem cells (GSCs), and their deregulation can contribute to chemotherapy resistance [162]. The suppression of the HH pathway was also shown to enhance the cytotoxic effects of TMZ and attenuate glioblastoma growth [163, 164].

1.4 Sarcoma

Sarcomas are a heterogeneous group of malignancies that fall into two main subgroups according to their anatomical location – sarcomas of soft tissue and sarcomas of the skeleton [165]. These tumours are most frequently found in extremities but can develop at almost any anatomic site. The incidence of sarcomas is much higher in children, accounting for 21 % of all solid tumours compared to 1 % in adults. The 2020 WHO classification describes more than 70 histological subtypes for now [166]. However, advances in sequencing technologies are increasingly enabling sarcoma classification based on molecular profiles, superseding the current histological classification and further drastically increasing the number of subtypes [79, 167, 168].

Soft-tissue sarcomas comprise around 70 – 80 % of all sarcomas with an incidence of 4.71 cases per 100,000 people according to the RARECAREnet data, a cancer registry in 27 European countries [169, 170]. The treatment of soft-tissue sarcomas and their sensitivity to systemic therapy options strongly depend on the sub-classification of the tumour. Localised tumours are treated by radiotherapy and chemotherapy after maximal surgical resection. Doxorubicin and the alkylating agent ifosfamide have been used over decades as a standard in systemic therapy in advanced staged soft-tissue sarcoma. However, recent advances in the understanding of the underlying molecular pathologies shifted the focus more towards the development of tailored therapy approaches for different histological subtypes [171]. Sarcoma tumours highly depend on somatic copy number aberrations with the MDM2-p53 and the p16-CDK4-RB1 pathways frequently affected. The overall mutational burden is low, and few genes (*TP53*, *ATRX*, *RB1*) are recurrently mutated across sarcoma subtypes [172]. Amplification and high expression of GLI1, with frequent co-amplification of the cell-cycle oncogenes *CDK4* and *MDM2*, has been reported in paediatric and adult sarcomas [173-175]. Furthermore, *GLI1* upregulation was reported in vincristine-resistant rhabdomyosarcoma and Ewing sarcoma [176]. And individual case reports identified *GLI1* fusion genes in soft-tissue sarcoma [177].

Liposarcomas (LS) are the most frequent type of soft-tissue sarcoma, accounting for 15 - 20 % [166]. They display adipocytic differentiation and can be subgrouped into well-differentiated LS (WDLS), dedifferentiated LS (DDLS), myxoid LS (MLS), and pleomorphic LS (PLS) [178]. WDLPS have a good prognostic outcome after complete surgical excision with only low metastatic potential.

In contrast, DDLS are more aggressive with high local and metastatic potential. Both types share morphologic and genetic features often co-existing in one tumour with DDLS focal outgrowth from a WDLS precursor lesion [178]. WDLS and DDLS are characterised by highly recurrent amplifications in chromosome region 12q13-15, containing known cell-cycle oncogenes *CDK4* and *MDM2*. These two genes are used as diagnostic markers for WDLS/DDLS as MDM2 amplification occurs in all DDLS patients, and *CDK4* is co-amplified in the majority of patients (92 %) [124, 172, 179].

1.5 Drug combinations in cancer therapy

Personalised treatments targeting tumour drivers have successfully been used as specific and effective approaches in cancer therapy. Nevertheless, the inactivation of a target frequently is insufficient to achieve tumour regression [180-182]. The complexity and genomic instability of the tumour often compensate for the loss of the primary target function by acquiring additional genetic mutations that ultimately result in drug resistance and tumour relapse [183]. It is therefore well recognised that simultaneous targeting of multiple molecular mechanisms and pathways in a tumour cell is more effective than single-agent treatment [184]. Multidrug therapy is generally less toxic and has fewer side effects, as different pathways are targeted, requiring lower drug dosages due to synergistic and additive interactions of the combined drugs [184]. This therapy approach is particularly useful for the treatment of cancers that frequently become resistant to therapy or for which targeted therapies have failed.

Among these are glioblastomas that frequently develop resistance to standard of care therapy as *EGFRvIII* amplification, mismatch repair deficiency, and upregulated *MGMT* expression confer resistance to radiation and temozolomide treatment [152, 185]. Several small-molecule inhibitors are in preclinical and clinical development for glioblastoma therapy and are being tested in combination with radio- or chemotherapy [186]. A combination of the MDM2 antagonist nutlin3a and temozolomide, for example, showed enhanced antitumor activity by activation of the p53 pathway [187]. Radiosensitising effects have been observed in the combination of radiotherapy with PARP inhibitors by a prolonged G2/M block and reduction in glioma stem cell proliferation [188, 189].

Several combination therapies have also been reported for sarcoma treatment. For example, the MAID regimen combines mesna, adriamycin (doxorubicin), ifosfamide, and dacarbazine, and is used for the treatment of advanced or metastatic soft-tissue sarcoma [190, 191]. Furthermore, unresectable leiomyosarcoma tumours that progressed after doxorubicin treatment, respond to the combination of gemcitabine and docetaxel [192, 193]. Potential new combination treatment was described for Ewing sarcoma tumours, with vincristine and YK-4-279, a small-molecule inhibitor, targeting the ESW-FLI fusion protein in these tumours [194].

1.6 Aims of the study

Owing to extensive advances in sequencing technologies in the last decades, it becomes more and more a standard in clinical practice to generate a comprehensive multi-omic tumour profile, improving treatment decisions based on a patient’s molecular portrait. Even though these advances enabled the development of many effective targeted therapies, many types of cancer are still difficult to treat because little is known about the underlying biology of the tumours. Glioblastoma and sarcoma tumours are amongst these tumours, as both entities represent a very heterogeneous group of tumours.

In prior work, our group identified *GLI1* fusion genes that were associated with focal amplification on chromosome arm 12q and resulted in strong *GLI1* overexpression. These initial data indicated GLI1 as a potential target for precision-oncology therapy.

In the present work, I studied the mechanism, phenotypic consequences, and targetability of GLI1 in glioblastoma and sarcoma tumours with 12q amplification. My specific aims were to:

1. determine the frequency of *GLI1* amplification and fusion gene formation in glioblastoma and sarcoma tumours,
2. identify potential genetic and epigenetic mechanisms of *GLI1* transcriptional activation,
3. characterise the phenotypic consequences of GLI1 suppression,
4. and explore therapy options for *GLI1*-overexpressing cancers.

2 Materials and Methods

2.1 Materials

2.1.1 Cell lines

Table 1: List of cell lines used in this work.

Cell Line	Supplier
771-3G iPSCs	provided by Dr Lena Kutscher (B062, DKFZ Heidelberg)
HEK293T	ATCC, Manassas, VA, USA
LN229	ATCC, Manassas, VA, USA
LN308	provided by Dr Himanushu Soni (B067, DKFZ Heidelberg)
T449	provided by Dr Priya Chudasama (B390, DKFZ Heidelberg)
T778	provided by Dr Priya Chudasama (B390, DKFZ Heidelberg)
U3037	HGCC, Uppsala, Sweden
U3071	HGCC, Uppsala, Sweden

2.1.2 Cell culture reagents

Table 2: List of cell culture reagents used in this work.

Reagent	Supplier
2-Mercaptoethanol	Life Technologies GmbH, Carlsbad, CA, USA
Accutase	Sigma Aldrich, Munich, Germany
Ascorbic Acid	Sigma Aldrich, Munich, GmbH
B-27 Supplement, minus vitamin A (100X)	Life Technologies GmbH, Carlsbad, CA, USA
B-27 Supplement, with vitamin A	Life Technologies GmbH, Carlsbad, CA, USA
Dimethyl sulfoxide	Sigma Aldrich, Munich, Germany
DMEM/F12 Medium	Thermo Fisher Scientific, Waltham, MA, USA
DMEM/F12 MEdium with HEPES	Thermo Fisher Scientific, Waltham, MA, USA
Dulbecco's Modified Eagle's Medium - High Glucose	Thermo Fisher Scientific, Waltham, MA, USA
Dulbeccos's Phosphate Buffer Solution (DPBS)	Thermo Fisher Scientific, Waltham, MA, USA
Fetal Calf serum (FCS)	Merck Millipore, Darmstadt, Germany
GlutaMAX supplement	Life Technologies GmbH, Carlsbad, CA, USA
HBSS (with Ca^{2+}, Mg^{2+})	Sigma Aldrich, Munich, GmbH

Reagent	Supplier
hEGF	Thermo Fisher Scientific, Waltham, MA, USA
hr-insulin	Sigma Alrich, Munich, Germany
Iscove's Modified Dulbecco's Medium	Thermo Fisher Scientific, Waltham, MA, USA
Laminin (from mouse Engelbreth-Holm-Swarm sarcoma)	Sigma Aldrich, Munich, Germany
L-Glutamine	Thermo Fisher Scientific, Waltham, MA, USA
MEM Non-Essential Amino Acids Solution (100X)	Life Technologies GmbH, Carlsbad, CA, USA
N2 (50X)	Life Technologies GmbH, Carlsbad, CA, USA
Neurobasal medium	Thermo Fisher Scientific, Waltham, MA, USA
Opti-MEM I Reduced Serum Medium	Thermo Fisher Scientific, Waltham, MA, USA
Penicillin/Streptomycin (10000 U/ml, 100 µg/ml)	Thermo Fisher Scientific, Waltham, MA, USA
Polyethylenimine (PEI)	Polysciences Europe GmbH, Hirschberg an der Bergstraße, Germany
poly-L-Lysine	Sigma Aldrich, Munich, Germany
rhFGF	Biomol GmbH, Hamburg, Germany
Trypsin EDTA solution (0.5 %)	Sigma Aldrich, Munich, Germany

2.1.3 Chemicals and Reagents

Table 3: List of chemicals and reagents used in this work.

Chemical	Supplier
AgeI-HF	New England Biolabs, Ipswich, MA, USA
BamHI-HF	New England Biolabs, Ipswich, MA, USA
BsmBI-HF	New England Biolabs, Ipswich, MA, USA
Bovine serum albumin	New England Biolabs, Ipswich, MA, USA
cOmplete Mini, EDTA free	Sigma-Aldrich, Munich Germany
D-Luciferin, potassium salt	BioVision Inc, Milpitas, CA, USA
DNaseI solution (1000 U/ml)	Stemcell Technologies, Vancouver, Canada
Dynabeads Protein G	Thermo Fisher Scientific, Waltham, MA, USA
EcoRI-HF	New England Biolabs, Ipswich, MA, USA
Ethanol	Thermo Fisher Scientific, Waltham, MA, USA
Formamide	Carl Roth, Karlsruhe, Germany
Gelatine	Sigma-Aldrich, Munich Germany
Glycine	Sigma-Aldrich, Munich, Germany
Goat serum	Life Technologies GmbH, Carlsbad, CA, USA

Chemical	Supplier
Isopropanol	Thermo Fisher Scientific, Waltham, MA, USA
Methanol	Thermo Fisher Scientific, Waltham, MA, USA
NuPAGE 4-12 % bis-Tris 1.5 mm x 10-well	Life Technologies GmbH, Carlsbad, CA, USA
NuPAGE 4-12 % bis-Tris 1.5 mm x 15-well	Life Technologies GmbH, Carlsbad, CA, USA
NuPAGE 4X LDS sample buffer	Life Technologies GmbH, Carlsbad, CA, USA
NuPAGE MOPS SDS Running Buffer 20X	Life Technologies GmbH, Carlsbad, CA, USA
NuPAGE Sample Reducing Agent (10X)	Life Technologies GmbH, Carlsbad, CA, USA
Papain	Stemcell Technologies, Vancouver, Canada
Paraformaldehyde (PFA)	Sigma-Aldrich, Munich, Germany
Pierce ECL Plus Western Blotting Substrate	Thermo Fisher Scientific, Waltham, MA, USA
Pierce ECL Western Blotting Substrate	Thermo Fisher Scientific, Waltham, MA, USA
Polybrene	Sigma-Aldrich, Munich Germany
Precisor High-Fidelity DNA Polymerase	BioCat GmbH, Heidelberg, Germany
primaQUANT cybr 2X SYBRGreen Mastermix	Steinbrenner Laborsysteme GmbH, Wiesenbach, Germany
ProLong Gold antifade mounting	Thermo Fisher Scientific, Waltham, MA, USA
Propidium Iodide solution (1.0 mg/ml)	Sigma-Aldrich, Munich Germany
Quick Ligase	New England Biolabs, Ipswich, MA, USA
RIPA Lysis Buffer	Sigma-Aldrich, Munich Germany
SeaPlaque Agarose	FMC BioProducts, Philadelphia, PA, USA
Spectra Multicolor Broad Range Protein Ladder	Thermo Fisher Scientific, Waltham, MA, USA
Spectra Multicolor High Range Protein Ladder	Thermo Fisher Scientific, Waltham, MA, USA
Stbl3, chemically competent E.coli	Life Technologies GmbH, Carlsbad, CA, USA
Sucrose	Sigma-Aldrich, Munich Germany
T4 PNK	New England Biolabs, Ipswich, MA, USA
Triton X-100	Sigma Aldrich, Munich, Germany
Whole milk powder	Carl Roth, Karlsruhe, Germany

2.1.4 Antibiotics and Inhibitors

Table 4: List of antibiotics, pharmaceutical drugs and inhibitors used in this work.

Reagent	Supplier
Ampicillin	Carl Roth, Karlsruhe, Germany
ATO	Hölzel Biotech, Cologne, Germany
AZD0156	Hölzel Biotech, Cologne, Germany

Reagent	Supplier
AZD6738	provided by Prof Dr Marc Remke, Paediatric Neuro-Oncogenomics, DKTK, UKD Düsseldorf
Belotecan	Hölzel Biotech, Cologne, Germany
Berzosertib	Hölzel Biotech, Cologne, Germany
BMS-833923	provided by Prof Dr Marc Remke, Paediatric Neuro-Oncogenomics, DKTK, UKD Düsseldorf
CC-115	Hölzel Biotech, Cologne, Germany
Colcemid	Sigma Aldrich, Munich, Germany
Doxorubicin	provided by Prof Dr Marc Remke, Paediatric Neuro-Oncogenomics, DKTK, UKD Düsseldorf
Etoposide	provided by Prof Dr Marc Remke, Paediatric Neuro-Oncogenomics, DKTK, UKD Düsseldorf
GANT58	Hölzel Biotech, Cologne, Germany
GANT61	Hölzel Biotech, Cologne, Germany
GDC-0575	Hölzel Biotech, Cologne, Germany
Geneticin (G418 Sulfate)	Thermo Fisher Scientific, Waltham, MA, USA
GlabrescioneB	manufactured and provided by Prof. Bruno Botta, Sapienza Universita, Rome, Italy
Hygromycin B	Life Technologies GmbH, Carlsbad, CA, USA
Irinotecan	provided by Prof Dr Marc Remke, Paediatric Neuro-Oncogenomics, DKTK, UKD Düsseldorf
JK184	provided by Prof Dr Marc Remke, Paediatric Neuro-Oncogenomics, DKTK, UKD Düsseldorf
Kanamycin	Sigma Aldrich, Munich, Germany
LY2606368	Hölzel Biotech, Cologne, Germany
Methoxyamine	Biozol Diagnostica, Eching, Germany
MK-1775	provided by Prof Dr Marc Remke, Paediatric Neuro-Oncogenomics, DKTK, UKD Düsseldorf
MK-8776	Hölzel Biotech, Cologne, Germany
Nedisertib	Hölzel Biotech, Cologne, Germany
Olaparib	provided by Prof Dr Marc Remke, Paediatric Neuro-Oncogenomics, DKTK, UKD Düsseldorf
Pamiparib	provided by Prof Dr Marc Remke, Paediatric Neuro-Oncogenomics, DKTK, UKD Düsseldorf
Puromycin	Merck Millipore Darmstadt, Germany
Veliparib	provided by Prof Dr Marc Remke, Paediatric Neuro-Oncogenomics, DKTK, UKD Düsseldorf

2.1.5 Buffers and Solutions

Table 5: List of buffers and solutions used in this work.

Buffer	Composition
1X Transfer buffer	25 mM Tris, 200 mM glycine, 20 % methanol, pH 8.8
1X TRIS buffered saline (TBS)	150 mM NaCl, 10 mM Tris, pH 7.5
20X Saline-sodium citrate (SSC) buffer	3 M NaCl, 0.3 M Sodium Citrate
Blocking buffer (DNA FISH)	4X SSC + 3 % BSA pH 7.3
Blocking buffer (WB)	5 % milk/BSA in TBS - 0.1 % Tween-20
ChIP Elution Buffer	10 mM Tris-HCl pH 8.0, 0.1 mM EDTA, 1 % SDS
ChIP Wash Buffer	10 mM Tris-HCl pH 8.1, 200 mM NaCl, 1 mM EDTA pH 8.0, 0.5 mM EGTA, pH 8.0
Detection buffer (DNA FISH)	4X SSC + 1 % BSA pH 7.3
Farnham Lysis Buffer	5 mM HEPES pH 8.0, 85 mM KCl, 0.5 % NP-40
LB (Luria Bertani) medium	0.5 % (w/v) NaCl, 1 % (w/v) Tryptone, 0.5 % (w/v) yeast extract
LB Agar	0.5 % (w/v) NaCl, 1 % (w/v) Tryptone, 0.5 % (w/v) yeast extract, 1.6 % (w/v) Agarose
Organoid dissociation buffer	125 U/ml papain, 12.5 U/ml DNase I in HBSS (with Ca^{2+}, Mg^{2+})
Papain activation buffer	1.1mM EDTA, 0.067mM mercaptoethanol, 5.5mM cysteine-HCl in 99.5 ml ddH_2O
Shearing Buffer	0.1 % SDS, 1 mM EDTA, 10 mM Tris pH 8.1
TBS-T	TBS 1X, 1:1000 (v/v) Tween-20
Wash A buffer (DNA FISH)	50 % formamide, 2X SSC buffer, pH 7.0
Wash B buffer (DNA FISH)	0.5X SSC buffer, pH 7.0
Wash C buffer (DNA FISH)	4X SSC buffer, 0.1 % Tween-20, pH 7.3

2.1.6 Antibodies

Table 6: List of primary antibodies used in this work.

Target	Dilution	Cat. No, Supplier
53BP1 (H300)	1:1000	Sc-22760, Santa Cruz, Dallas, TX, USA
CTCF	1 µg per 10^6 cells	61932, Active Motif, Carlsbad, CA, CA, USA
GFP	1:1000 (WB)	AB011-EV, Biocat, Heidelberg, Germany
GLI1	1:1000	2553S, Cell Signaling Technology, Danvers, MA, USA

Target	Dilution	Cat. No, Supplier
Rb IgG control	1 µg per 10^6 cells	#02-6102, Thermo Fisher Scientific, Waltham, MA, USA
SOX2	1:250 (IF)	AB5603, Merck Millipore, Darmstadt, Germany
ß-tubulin (DM1A)	1:5000	Sigma Aldrich, Munich, Germany
TUBB3, clone TUJ1	1:1000 (IF)	801201, BioLegend, San Diego, CA
V5-tag (D3H8Q)	1:1000	13202S, Cell Signaling Technology, Danvers, MA, USA
γH2AX	1:1000 (IF)	Abcam, Cambridge, United Kingdom
γH2AX (S139), clone JBW301	1:1000 (WB) 1:200 (IF)	05-636, Merck Millipore, Darmstadt, Germany

Table 7: List of secondary antibodies used in this work.

Target	Dilution	Cat. No, Supplier
anti-mouse IgG Alexa Fluor Plus 488	1:1000	A-32723, Invitrogen, California, USA
anti-mouse IgG HRP-linked	1:5000	7076S, Cell Signaling Technology, Danvers, MA, USA
anti-rabbit IgG Alexa Fluor 488	1:1000	A-11034, Invitrogen, California, USA
anti-rabbit IgG Alexa Fluor 647	1:1000	A-21245, Invitrogen, California, USA
anti-rabbit IgG HRP-linked	1:5000	7074S, Cell Signaling Technology, Danvers, MA, USA

Table 8: List of fluorescently conjugated antibodies used in this work.

Target	Dilution	Cat. No, Supplier
V5 Tag (TCM5), PE	0.25 µg/test	12-6796-42, Life Technologies GmbH, Carlsbad, CA, USA

2.1.7 Plasmids

Table 9: List of commercial plasmids used in this work.

Plasmid	Cat. No, Supplier
lentiCRISPRv2 puro	#98290, Addgene, Cambridge, USA
MISSION pLKO.1 puro non-mammalian shRNA control	SHC002, Sigma Aldrich, Munich, Germany
pLenti CMV GFP puro	658-5, Addgene, Cambridge, USA

Plasmid	Cat. No, Supplier
pLenti PGK V5-LUC Neo	W623-2, Addgene, Cambridge, USA
pLKO.1 puro	#10878, Addgene, Cambridge, USA
pLKO.1 puro CMV TurboGFP	SHC003, Sigma Aldrich, Munich, Germany
pMD2.G	#12259, Addgene, Cambridge, USA
pRL-TK	Promega, Madison, WI, USA
psPAX2	#12260, Addgene, Cambridge, USA

Table 10: List of generated plasmids used in this work.

Plasmid	Use
lentiCRISPRv2 CTCF-BS_1/2/3-puro	CRISPR/Cas9 disruption of CTCF binding sites
pLKO.1 shGLI1-1/2/3 puro	shRNA-mediated GLI1 knockdown

2.1.8 Oligonucleotide sequences

Table 11: List of shRNA sequences used in this work.

Target	Sequence	Targeting site
GLI1_sh1	CGTGAGCCTGAATCTGTGTAT	GLI1 exon 7
GLI1_sh2	GCTCAGCTTGTGTGTAATTAT	GLI1 exon 12
GLI1_sh3	CATCCATCACAGATCGCATTT	GLI1 3’ UTR
shNT	CAACAAGATGAAGAGCACCAA	na

Table 12: List of sgRNA sequences used in this work.

Target	Sequence	Targeting site
CTCF_BS_1	GGCACGGCACTGCCACATGG	chr12:57453074-57453093
CTCF_BS_2	TGTGTGAGAACGGCCAGCAG	chr12:57459250-57459269
CTCF_BS_3	TCTCTGCAGTGTCCAGCAGA	chr12:57462840-57462859

Table 13: List of qPCR primers used in this work.

Target	Forward Sequence	Reverse Sequence
CDK4	CATCGTTCACCGAGATCTGA	CCAACACTCCACATGTCCAC
RPS18	ATCCCTGAAAAGTTCCAGCA	CCCTCTTGGTGAGGTCAATG
GAPDH	CAACAGCCTCAAGATCATCAG	ATGGACTGTGGTCATGAGTC
ß-actin	GTTACACCCTTTCTTGACAAA	GTCACCTTCACCGTTCCAGTT
PTCH1	AATGGGTCCACGACAAAGCCGACTA	TCCCGCAAGCCGTTGAGGTAGAAAG
CTCF_BS-2_ChIP	CTCTAGCTGCTCTTCCAGGC	GTTCCCCAGCTCTTCTGCTT
hH19-ICR_ChIP_Fwd	TGTGGATAATGCCCGACCTGAAGATCTG	ACGGAATTGGTTGTAGTTGTGGAATCGGAAGT
NegCtrl_ChIP	GAGCTCTAAGGGAGGCTCCA	CATCATGGTGTCCTCACAGG
GLI1 ex.1-2	CCAGCGCCCAGACAGAG	GGCTCGCCATAGCTACTGAT
GLI1 ex.7-8	AGCGTGAGCCTGAATCTGTG	CAGCATGTACTGGGCTTTGAA

2.1.9 Kits

Table 14: List of commercial kits used in this work.

Kit	Supplier
CellTiterGlo® 3D Viability Assay	Promega, Madison, WI, USA
CellTiterGlo® Viability Assay	Promega, Madison, WI, USA
Click-iT EdU Alexa Fluor 488 Flow Cytometry Assay Kit	Life Technologies GmbH, Carlsbad, CA, USA
Click-iT EdU Alexa Fluor 647 Flow Cytometry Assay Kit	Life Technologies GmbH, Carlsbad, CA, USA
FITC Annexin V Apoptosis Detection Kit with 7-AAD	BioLegend, San Diego, CA, USA
Pierce BCA Protein Assay	Thermo Fisher Scientific, Waltham, MA, USA
QIAGEN Plasmid Maxi Kit	Qiagen, Hilden, Germany
QIAGEN Plasmid Mini Kit	Qiagen, Hilden, Germany
QIAquick Gel Extractions Kit	Qiagen, Hilden, Germany
QIAquick PCR Purification Kit	Qiagen, Hilden, Germany
QuantiTect Reverse Transcription Kit	Qiagen, Hilden, Germany
Qubit® RNA HS Assay Kit	Thermo Fisher Scientific, Waltham, MA, USA
Quick Ligation Kit	New England Biolabs, Ipswich, MA, USA
RNase-Free DNase Set	Qiagen, Hilden, Germany
RNeasy Mini kit	Qiagen, Hilden, Germany

2.1.10 Consumables

Table 15: List of consumables used in this work.

Consumable	Supplier
0.22 µm Millex 4mm Durapore PVDF filters	Merck Millipore, Darmstadt, Germany
0.45 µm Millex 4mm Durapore PVDF filters	Merck Millipore, Darmstadt, Germany
96-well plate black	Greiner Bio-One GmbH, Kremsmünster, Austria
96-well plate white	Greiner Bio-One GmbH, Kremsmünster, Austria
Cell culture flasks and multi-well plates	Sarstedt GmbH, Nürnbrecht, Germany
Cell culture flasks and multi-well plates for adherent cells	BD Biosciences, Heidelberg, Germany
CometSlides	R&D Systems, Minneapolis, MN, USA
Einweg-Zählkammer C-Chip	Biochrom, Berlin, Germany
Eppendorf® Safe-Lock microcentrifuge tubes (1.5 mL, 2.0 mL)	Eppendorf, Hamburg, Germany
FACS tubes	Becton, Dickinson and Company (BD), Franklin Lakes, NJ, USA
Falcon® tubes (50 and 15 mL)	BD Biosciences, Heidelberg, Germany
Nunc® Cryo tubes	Sigma Aldrich, Munich, Germany
Pipette tips (10 µl, 20 µl, 100 µl, 200 µl, 1000 µl)	VWR International GmbH, Darmstadt, Germany
Polyvinylidene fluoride (PVDF) transfer membrane	Merck Millipore, Darmstadt, Germany
Superfrost PLUS slides	Thermo Fisher Scientific, Waltham, MA, USA
Ultracentrifuge tubes 14,0 ml PA thin-walled	Herolab, Heidelberg, Germany
Vakuum Filtration 500 “rapid” – Filtermax	BD Biosciences, Heidelberg, Germany
White 1536-well microtiter plates	Corning, New York, NY, USA
White 384-well microtiter plates	Corning, New York, NY, USA

2.1.11 Equipment and Devices

Table 16: List of equipment and devices used in this work.

Instrument	Supplier
Agilent 2100 BioAnalyzer	Agilent Technologies Inc., Santa Clara, CA, USA
Azure c200 Gel Imaging System	Azure Biosystems, Dublin, CA, USA
BD FACS Aria Fusion-3	BD Biosciences, Heidelberg, Germany
BD FACS Canto TM II	BD Biosciences, Heidelberg, Germany
BD FACS LSR Fortessa	BD Biosciences, Heidelberg, Germany
Beckman Ultracentrifuge with SW41 rotor	Beckman Coulter GmbH, Krefeld, Germany

Instrument	Supplier
Centrifuge Heraeus Sepatech Varifuge 3.0R	M&S Laborgeräte GmbH, Wiesloch, Germany
D300e Drug Dispenser	Tecan, Crailsheim, Germany
DeltaVision Core microscope	Applied Precision Inc., Issaquah, WA, USA
DynamagTM magnet	Thermo Fisher Scientific, Waltman, MA, USA
EC250-90 Electrophoresis Power Supply	Cambridge Scientific Products, Watertown, MA, USA
Eppendorf Thermomixer comfort	Eppendorf, Hamburg, Germany
Forma Steri-Cycle CO2 incubator	Thermo Fisher Scientific, Waltham, MA, USA
Gammacell 40 Exactor	Best Theratronics, Ottawa, Canada
Heracell 150i incubator	Thermo Fisher Scientific, Waltham, MA, USA
Heraeus Fresco 17 Centrifuge	Thermo Fisher Scientific, Waltham, MA, USA
Heraeus Varifuge 3.0 Centrifuge	Thermo Fisher Scientific, Waltham, MA, USA
HiSeq 2000 v4	Illumina Inc., San Diego, CA, USA
IVIS Lumina LT Series III	Perkin Elmer, Waltham, MA, USA
Leica CM1860 UV cryomicrotome	Leica Microsystems, Wetzlar, Germany
Leica TCS SP8 confocal microscope	Leica Microsystems, Wetzlar, Germany
MasterCycler EP Gradient S	Eppendorf, Hamburg, Germany
Mini-PROTEAN 3 Cell	BioRad, Hercules, CA, USA
Mithras LB 940 plate reader	Berthold Technologies, Bad Wildbad, Germany
MultiDrop Combi Reagent Dispenser	Thermo Fisher Scientific, Waltham, MA, USA
NanoDrop ND-2000c spectrometer	NanoDrop, Wilmington, NC, USA
NanoDrop® ND-2000C Spectrophotometer	NanoDrop, Wilmington, DE, USA
PIPETBOY acu 2	Integra Biosciences, Biebertal, Germany
Pipettes (2 µl, 20 µl, 100 µl, 200 µl, 1000 µl)	STARLAB International GmbH, Hamburg, Germany
Quantstudio5	Thermo Fisher Scientific, Waltham, MA, USA
Qubit 2.0 Fluorometer	Invitrogen, Karlsruhe, Germany
Rotina 380R Centrifuge	Hettich Zentrifugen, Tuttlingen, Germany
Sky Line Orbital Shaker	ELMI North America, Newbury Park, CA, USA
Spark MultiMode microplate reader	Tecan, Crailsheim, Germany
Steri-Cycle CO2 Cell Culture Incubator	Thermo Fisher Scientific, Waltham, MA, USA
Tube Roller	STARLAB International GmbH, Hamburg, Germany
Vi-CELL XR 2.03	Beckman Coulter GmbH, Krefeld, Germany
Voyager 300 8-channel pipette	Integra Biosciences, Biebertal, Germany
Water Bath GFL Type 1002	GFL Gesellschaft für Labortechnik mbH, Burgwedel, Germany
Water Bath Julabo SW-20C	Julabo, Seelbach, Germany

Instrument	Supplier
XCell SureLock Mini-Cell Electrophoresis System	Thermo Fisher Scientific, Waltham, MA, USA
Zeiss Axio Imager M2 microscope	Carl Zeiss AG, Jena, Germany
Zeiss Axio Vert.A1 microscope	Carl Zeiss AG, Jena, Germany
Zeiss Axioplan2 Imaging microscope	Carl Zeiss AG, Jena, Germany

2.1.12 Databases and Software

Table 17: List of databases used in this work.

Database	Supplier, Internet Address
CTCFBSDB 2.0	Yan Cui's Lab, University of Tennessee, Knoxville, TN, USA [195, 196]
GeneCards (Human Genes Database) 5.3	Weizmann Institute of Science, Rehovot, Israel http://www.genecards.org/
JASPAR, 8th release (2020)	University of Copenhagen, Denmark; Centre for Molecular Medicine and Therapeutics, Vancouver, Canada; MRC London Institute of Medical Sciences, London, United Kingdom; Centre for Molecular Medicine Norway, Oslo, Norway; (http://jaspar.genereg.net/) [197]
PubMed	National Institute of Health, Bethesda, USA (http://www.ncbi.nlm.nih.gov/pubmed)
R2 Genomics	Academic Medical Center, Amsterdam, Netherlands (https://r2.amc.nl)
UCSC Genome Browser GRCh38/hg38 Assembly	UCSC, Santa Cruz, CA, USA (http://genome.ucsc.edu)

Table 18: List of software used in this work.

Software	Version	Supplier
Affinity Designer	1.8.3.641	Serif (Europe) Ltd., Nottingham, United Kingdom
BD FACS Diva	6.1.3	BD Biosciences, San Jose, USA
BioRender	2021	Free trial (https://biorender.com)
EndNote	x9	Thomson ResearchSoft, Carlsbad, CA, USA
FlowJo	v.10.7.0	FlowJo, LLC., Ashland, USA
GraphPad Prism	9.0.0	GraphPad Software, San Diego, USA
IGV Genome Browser	2.6	Open Source, Broad Institute, Cambridge, USA

Software	**Version**	**Supplier**
ImageJ	1.51n	Open Source, National Institute of Health, Bethesda, USA
INTAS ChemoStar	v60+	INTAS Science Imaging Instruments GmbH, Göttingen, Germany
Living Image	4.7	PerkinElmer, Waltham, MA, USA
Metafer4	V3.1.3	MetaSystems Hard & Software GmbH, Altlussheim, Germany
Microsoft Excel/PowerPoint/Word	2016	Microsoft, Redmond, USA
QuantStudio Design and Analysis Software	v1.5.1	Thermo Fisher Scientific, Waltham, MA, USA
R	3.6.1	Open Source, R Foundation
RStudio	1.2.1335	Open Source, R Foundation
SnapGene	5.1.5	GSL Biotech LLC, San Diego, USA

2.2 Methods

2.2.1 Cell lines and culture conditions

Human glioblastoma LN308 and LN229 cell lines were cultured in DMEM medium supplemented with 10 % FBS and 1 % P/S. U3071 and U3037 cell lines were grown as adherent cultures on laminin-coated flasks in a 1:1 mix of DMEM/F12 and Neurobasalmedium (each supplemented with 2 mM L-glutamine + 1 % P/S) with 1X B-27, 1X N2, 10 ng/ml hEGF and 10 ng/ml rhFGF. For the laminin coating of culture ware, laminin was diluted in PBS to 10 µg/ml and the culture surface was covered with minimal volume of solution. Culture ware was incubated for 30 min – 1 h at 37 °C. Excess laminin was removed and plates were washed twice with PBS. Cells were added to the culture ware without drying to prevent disruption of the laminin structure. Liposarcoma cell lines T778 and T449 were cultured in RPMI 1640 medium supplemented with 10 % FBS and 1 % P/S. HEK293T cells were maintained in IMDM + 10 % FBS + 2 mM L-glutamine + 1 % P/S. Adherent cell lines were passaged at 80 – 90 % cell confluency by detaching and dissociating the cells with 0.5 % trypsin. For passaging U3037 and U3071 cultures, cells were detached with Accutase. All cell lines were kept in a 5 % CO_2 humidified incubator at 37 °C.

2.2.2 Generation of spheroid cultures

To generate LN308 spheroid culture, adherent cells were transferred to ultra-low attachment plates and grown in a 1:1 mix of DMEM/F12 and Neurobasal A medium (each supplemented with 2 mM L-glutamine + 1 % P/S) with 1X B-27, 1X N2, 10 ng/ml hEGF and 10 ng/ml rhFGF. Spheres were formed after 10 - 14 days of culture. Dead cells were removed from the culture and the growth medium was replaced every 72 h.

2.2.3 DNA FISH

Cytogenetic DNA FISH analysis was used to visualise gene amplification status in different cell lines. Cells were seeded overnight on SuperFrost microscopy slides in a QuadriPERM plate. For metaphase synchronisation, cells were washed once with PBS and incubated overnight with 10 µM colcemid. To prepare samples for FISH staining, the following steps were carried out in staining cuvettes. Slides were rinsed once with PBS and dehydrated in an ascending alcohol series of 70 %, 90 %, and 100 % ethanol for 5 min each at RT. Afterwards, proteins were digested by incubating the samples in 10 µg pepsin in 0.01 M hydrochloric acid solution (HCl) for 3 min in a 37 °C water bath. After washing once with PBS for 5 min, samples were fixed in 1 % PFA for 5 min on ice and washed again for 10 min with PBS. Samples were dehydrated in a second ascending alcohol series of 70 %, 90 %, and 100 % ethanol for 5 min each at RT and air-dried at RT. Digoxigenin- and streptavidin-labelled DNA probes were prepared on ice according to Table 19 and precipitated for 30 min at - 80 °C.

Table 19: DNA probe preparation for DNA FISH.

Component	Amount per slide
DNA probe	10 µl locus probe 1.5 µl centromere probe
Human Cot-DNA	7 µl
Salmon sperm	0.7 µl
NaAc 3 M	0.96 µl (1/20 volume fraction)
100 % EtOH, non-denatured	50.4 µl (2.5X volume)

After precipitation, the sample was centrifuged for 20 min at 13,000 rpm in a prechilled tabletop centrifuge and the supernatant was carefully removed. The sample was washed with 400 µl 70 % non-denatured EtOH, centrifuged again for 10 min at 13,000 rpm at 4 °C. After removing the supernatant, the sample was dried for 15 min at 37 °C with an open lid. Deionized and resin-base treated formamide (7.5 µl per slide) was added to the sample and shaken for 15 min at 1,000 rpm to loosen the pellet. As a final step in the probe preparation, an equal amount of hybridisation mix (7.5 µl per slide; 2X SSC, 10 % dextran sulfate, 25 mM sodium phosphate) was added to the sample, and shaken again for 15 min at 1,000 rpm. The probe was carefully added to the slides, covered with a coverslip and sealed with Fixogum to prevent evaporation. For probe hybridisation, the sample was denatured for 8 min at 75 °C and hybridised overnight at 37 °C in a hybridisation chamber. The following day, Fixogum was carefully removed, and slides were washed with freshly prepared Wash A buffer (50 % formamide pH 7.0, 2X SSC in ddH_2O) in a 42 °C shaking water bath for 10 min to remove the coverslip. After another 3 washes for 5 min with Wash A buffer, samples were washed with Wash B buffer (0.5X SSC in ddH_2O), pre-warmed at 60 °C, three times for 5 min at 42 °C. To block non-specific sites, slides were incubated with 4X SSC + 1 % BSA, pH 7.3, for 30 min at 37 °C in a humidified chamber. Avidin-FITC and AntiDig-Rhodamin were mixed in detection buffer (4X SSC + 1 % BSA, pH 7.3) and added to the slides for 30 min at 37 °C in a humidified chamber and protected from light. Slides were finally washed with Wash C buffer (4X SSC in ddH_2O, 0.1 % Tween-20, pH 7.3) three times for 5 min at 42 °C. Excess buffer was removed and slides were mounted with ProLong Gold Antifade Mountant with DAPI and sealed with nail polish. Images were acquired using a Zeiss ImagerM2 microscope.

2.2.4 Lentivirus production

Lentiviruses were produced by transient cotransfection of 2nd generation lentiviral packaging plasmids, psPAX.2 and pMD2.G, and transfer plasmids into HEK293T as packaging cell line. For transfection, polyethylenimine (PEI) (1 mg/ml) was used in a DNA:PEI ratio of 1:3. Briefly, one day before transfection, 5 x 10^6 HEK293T cells were seeded in a 10 cm dish in 6 ml medium. Two hours before transfection, the medium was replaced by 6 ml fresh medium. For transfection, cells were transfected with 16 µg DNA composing of 8 µg of lentiviral vector containing the transgene, 4 µg of packaging vector psPAX.2 and envelope vector pMD2.G in 250 µl total volume OptiMEM medium. After 15 min incubation at room temperature (RT), the transfection mix was dropwise added to the cells, carefully mixed, and incubated for 24 h at 37 °C. The medium was replaced by 5 ml fresh medium and incubated for another 48 h at 37 °C. For lentivirus concentration, viral supernatant was collected, filtered through a 45 µm syringe filter into SW41 centrifuge tubes, and spun down using an SW41 rotor for 90 min at 25,000 rpm at 4 °C. The viral pellet was resuspended in 100 µl OptiMEM, aliquoted, and stored at - 80 °C for later use.

To test lentivirus transduction efficiency and calculate the multiplicity of infection (MOI), viral titre was quantified in HEK293T cells and target cell line using pLKO.1-TurboGFP lentiviruses that were produced in the same batch as the corresponding lentiviruses for transduction. 8 x 10^4 cells were seeded in a 12-well plate 24 h before transduction. Serial dilutions of pure, 10^{-3}, 10^{-4}, and 10^{-5} diluted virus were transduced in 1 ml medium supplemented with 1 µg/ml polybrene. The medium was replaced 24 h after transduction, and GFP-positive cells were detected 72 h post-transduction at a BD FACSCantoII Analyzer. The quantification of the lentiviral titre in transduction units per microliter (TU/µl) was calculated using the following equation

$$Titre\left(\frac{TU}{\mu l}\right) = \left(N * \frac{p}{100} * D\right) * \frac{1}{V}$$

where *N* is the transduced cell number, *p* the percentage of GFP positive cells [%], *D* the dilution factor (10^3, 10^4, 10^5), and *V* the total volume of transduction.

2.2.5 ShRNA cloning and knockdown

Gene knockdown was carried out with constitutive shRNA lentivirus infection. For efficient GLI1 targeting, three different shRNA sequences targeting different sites of the gene locus were tested and knockdown efficiencies and phenotypes were compared (see Table 11 for shRNA sequences and targeting sites). Desalted shRNA sequences with compatible sticky ends were cloned into an AgeI and EcoRI digested pLKO.1-puro expression plasmid. For phosphorylation and annealing of the shRNA sequences, 5'-phosphate groups were added to the forward and reverse oligonucleotides by T4 polynucleotide kinase for 30 min at 37 °C followed by a heating step at 95°C for 5 min and cool down to RT. The annealed oligonucleotides were ligated into the vector backbone using the Quick Ligation™ Kit. The annealed duplexes were diluted 1:200 and 1 µl of the dilution was mixed with 50 ng of vector backbone. After 15 min incubation at RT, the ligation mix was transformed into competent Stbl3 bacteria cells by standard heat-shock transformation. Bacteria were grown on LB+Amp agar plates overnight at 37 °C. Single colonies were analysed for insertion of the shRNA sequences using Sanger sequencing with hU6 promoter primer (5’-GACTATCATATGCTTACCGT-3’).

For shRNA delivery and expression, lentiviruses were prepared, and target cells were transduced with lentiviral particles with an MOI of 3. Cells were plated one day before transduction and transduced in medium supplemented with 1 µg/ml polybrene. The transduction mix was removed 24 h post-transduction and replaced by new medium. Transduced cells were selected with 1 µg/ml puromycin for 48 h before knockdown validation and phenotypic analysis.

2.2.6 Reverse transcription quantitative PCR

Total RNA was collected and extracted with the RNAeasy Mini Kit according to the manufacturer's instructions. RNA concentrations were quantified on a Nanodrop 2000 spectrophotometer. 1 µg RNA was reverse-transcribed into cDNA using Quantitect Reverse Transcription Kit, following the manufacturer's instructions. Subsequent quantitative PCR was carried out on a Quantstudio5 Real-Time PCR system using primaQuant SYBR Green. 25 ng cDNA was analysed in a total reaction volume of 10 µl and measured in technical triplicates using the following thermocycling parameters: 50 °C for 2 min, 95 °C for 15 min followed by 40 cycles of 95 °C for 15 s and 60 °C for 1 min. The $2^{-\Delta\Delta Ct}$ method was used for the quantification of gene expression. For normalisation, GAPDH, RPS18, and β-actin were used as housekeeping genes. Gene-specific primer sequences are listed in Table 13.

2.2.7 Western Blotting analysis

Cell pellets were collected and resuspended in RIPA buffer supplemented with 0.05 % SDS and protease inhibitor. Samples were incubated on ice for 20 min; spun down for 20 min at 13,000 x g, and the supernatant was collected. Protein concentrations were quantified with bicinchoninic acid (BCA) assay against a BSA standard curve. For western blotting, the cell lysate samples were prepared in SDS sample buffer (containing NuPAGE® LDS Sample Buffer (4X) and NuPAGE® Sample Reducing Agent (10X)). Protein samples were reduced by boiling them for 5 min at 95 °C, and bands were separated by polyacrylamide gel electrophoresis on a Bolt® 4 - 12 % Bis-Tris Plus gel in MOPS buffer at 120 V. Spectra™ Multicolor High Range Protein Ladder or Spectra™ Multicolor Broad Range Protein Ladder was used as size references. Proteins were transferred on a PVDF membrane by standard wet method in transfer buffer with 20 % methanol at 200 mA for 10 min, 300 mA for 10 min, 400 mA for 10 min, 500 mA for 20 min, and 50 mA for 1 h. The membrane was blocked in 5 % low-fat milk in TBS-Tween-20 (0.1 %, TBS-T) for 1 h before overnight incubation with the primary antibody in 1 % low-fat milk in TBS-T at 4 °C. The following day, the membrane was washed with TBS-T three times for 10 min, followed by incubation with horseradish peroxidase (HRP)-conjugated secondary antibodies for 1 h at RT. After additional washing of the membrane with TBS-T three times for 10 min, protein bands were detected using Pierce™ ECL Western Blotting Substrate. Chemiluminescence was recorded on an ECL ChemoCam Imager using the ChemoStar software. Quantification of immunosignals was performed using the Image J software.

2.2.8 Development of CTCF CRISPR/Cas9 KO cell lines

CRISPR/Cas9 technology was used to create cell lines with disrupted CTCF binding sites (CTCF BS) upstream of the *GLI1* locus. The location of CTCF binding was mapped in a study by Flavahan et al., 2016 using CTCF ChIP-seq analysis of eleven primary tumours and four glioma cell lines. CTCF binding sites were predicted using the CTCFBSDB database (https://insulatordb.uthsc.edu/) using the genomic sequence with mapped CTCF ChIP-Seq signal as input. The input sequences of the three targeted CTCF peaks were 400 nt (peak 1), 340 nt (peak 2) and 435 nt (peak 3) in length, and the motif with the highest prediction score using the REN_20 matrix was used as sgRNA target site [198]. Single guide RNAs (sgRNAs) were designed to cut within CTCF BSs using the CRISPR target track available at the UCSC genome browser. SgRNA sequences are listed in Table 12. Oligo sequences targeting the CTCF BS and control sequences were cloned into lentiCRISPRv2-puro plasmid as described in the literature [199, 200]. Cas9 and sgRNAs were delivered to T778 and LN308 target cells by lentiviral transduction followed by puromycin selection (1 µg/ml puromycin) for 72 h. Monoclonal cell populations were created by serial dilution in 96-well plates, and single clones were expanded for 14 days in puromycin selection medium. Single-cell clones were only retrieved in T778 cells expressing sgCTCF for peak 2. Twelve monoclonal populations were screened by Sanger sequencing of genomic DNA to characterise indels and to identify clones with biallelic frameshift mutations.

2.2.9 CTCF chromatin immunoprecipitation

Chromatin immunoprecipitation followed by qPCR (ChIP-qPCR) was used to confirm the absence of CTCF binding at the target site. For ChIP, T778 cells were grown in 150 mm dishes until they reached roughly 80 - 90 % cell confluency and the medium was changed one day before collecting the cells. DNA was cross-linked by adding 16 % formaldehyde (w/v, methanol-free) to the culture medium to a final concentration of 1 % formaldehyde. Plates were incubated for 10 min at RT on a shaking rotor. To quench the formaldehyde and to terminate the cross-linking reaction, 0.125 M glycine was added, and plates were shaken at RT for 5 min. Cells were washed three times with ice-cold PBS and collected in PBS with 1X protease inhibitor using a cell scraper. Samples were divided into aliquots of 10^7 cells and collected by centrifugation at 3,000 rpm at 4 °C. For chromatin preparation, cells were lysed in 1 ml Farnham lysis buffer (5 mM HEPES pH 8.0, 85 mM KCl, 0.5 % NP-40) with 1X protease inhibitor for 10 min on ice. Samples were centrifuged for 5 min at 4,000 rpm and washed twice with 1 ml shearing buffer (0.1 % SDS, 1 mM EDTA, 10 mM Tris, pH 8.1) with 1X protease inhibitor to remove any residual salts. Each cell pellet containing 10^7 cells was resuspended in 433.3 µl shearing buffer and transferred to Covaris micro-tubes with AFA fibre (130 µl per micro-tube containing roughly 3 x 10^6 cells), avoiding any bubble formation in the tubes. Chromatin was sonicated using a Covaris S2 machine with the settings listed below in Table 20.

Table 20: Covaris S2 sonication settings for chromatin fragmentation of T778 cells.

Parameter	Setting
Time	6 min
Duty cycle	5 %
Intensity	4
Cycles per burst	200
Power mode frequency	Sweeping
Degassing mode	Continuous
AFA intensifier	No intensifier
Water level	12
Bath temperature limit	7 °C

After chromatin sonication, samples were mixed with 1 % Triton X-100 and 150 mM NaCl, and insoluble material was removed by centrifugation at 8,000 rpm. Aliquots of 5 x 10^6 cells were prepared in 550 µl volume, and 1 % volume was kept as an input sample. For immunoprecipitation, sheared chromatin was incubated with CTCF target antibody (1 µg per 10^6 cells) or mouse IgG overnight at 4 °C with gentle rotation. The following day, 30 µl Protein G-Dyna Beads were added to pull down protein-antibody complexes. The Dynabeads were washed once with shearing buffer and added to the samples. After 1.5 h incubation at 4 °C with gentle rotation, beads were recovered on a magnet and sequentially washed twice with Low Salt Wash Buffer (0.1 % SDS, 1 % Triton-100, 2 mM EDTA, 20 mM Hepes-KOH pH 7.9, 150 mM NaCl), once with High Salt Wash Buffer (0.1 % SDS, 1 % Triton X-100, 2 mM EDTA, 20 mM Hepes-KOH pH 7.9, 500 mM NaCl), LiCl Wash Buffer (100 mM Tris-HCl pH 7.5, 0.5 M LiCl, 1 % NP-40, 1 % Sodium Deoxycholate), and finally with TE buffer pH 8.1. Antibody-protein complexes were eluted in ChIP Elution Buffer (10 mM Tris, pH 8.0, 0.1 mM EDTA, 1 % SDS) and shaken for 30 min at 65 °C. For reverse-crosslinking, supernatant and input sample were mixed with 200 mM NaCl and 0.5 µg RNAse A and incubated overnight at 65 °C. Proteins were digested with 2 µl proteinase K for 2 h at 50 °C. DNA was purified using the QIAquick PCR purification kit according to the manufacturer's instructions and DNA concentrations were photometrically quantified on a Nanodrop 2000 spectrophotometer.

2.2.10 CTCF ChIP-qPCR

To measure the enrichment of CTCF at CTCF binding sites upstream of the *GLI1* locus, purified chromatin was subjected to qPCR. Two different primer pairs (ChIP_CTCF pr.1, ChIP_CTCF pr.2) were used, and negative and positive primers (Neg. Ctrl chr.11, Pos. Ctrl hH19-ICR, respectively) were included as controls. Primer sequences are listed in Table 13. Quantitative PCR reaction was performed as described in chapter 2.2.6. 2 µl chromatin was used as input for each reaction. The CTCF signal was quantified as fold enrichment relative to the sgCTRL sample.

2.2.11 Click-iT cell proliferation assay

After transduction with shRNA constructs, cells were seeded in 12-well plates and grown for 24 h. 10 µM 5-ethynyl-2'-deoxyuridine (EdU) was added to each well for 8h (T778) or 16 h (LN308 and U3071). Cells were harvested by trypsinisation and fixed with 4 % PFA for 15 min. Fixed cells were washed with 1 % BSA in PBS and permeabilised in 0.1 % Triton-X100 for 30 min at RT. After washing, Click-iT reaction was performed as indicated by the manufacturer with Azide-488. Proliferating cells were quantified by cytometric analysis at a FACS Canto II. 10,000 cells per condition were acquired, and data were further processed and analysed using the FlowJo software (Flowjo LLC, V10.7.0).

2.2.12 Cell viability assay

The drug response was measured by quantification of the number of metabolically active cells using the CellTiter-Glo® Luminescent Cell Viability assay. Cells were seeded in white 96-well plates at optimised cell densities and treated with inhibitors after 24 h with serial dilutions of the inhibitors. DMSO vehicle concentration and 10 % DMSO were used as negative and positive controls, respectively. Cells were incubated for 72 h at 37 °C. CellTiter-Glo assay was performed according to the manufacturers' instructions. Briefly, the plate and its contents were equilibrated to RT for 30 min. An equal amount of CellTiter-Glo substrate was added to each well, and cell lysis was induced for 2 min on a plate shaker. For stabilisation of the luminescent signal, the plate was incubated for 10 min at RT before luminescence was recorded on a Mithras plate reader. An integration time of 1 s was used, and luminescence was recorded at 560 nm. After subtraction of the background luminescent signal raw values were normalised to DMSO vehicle controls. GraphPad Prism software was used to fit a dose-response curve and calculate IC_{50} values.

2.2.13 Cell proliferation assay

To evaluate the effect of GLI1 inhibition on the growth rate of viable cells, total cell numbers were measured over 72 h upon inhibitor treatment. For each time point and concentration, 8×10^4 T778 or 1.2×10^5 LN308 cells were seeded in 6-well plates overnight. The following day, cells were treated with the indicated concentrations of inhibitor. Total cell numbers were measured before inhibitor treatment as baseline count and 24 h, 48 h, and 72 h post-treatment. Cells were harvested by trypsinisation, resuspended in an equal amount of medium and a trypan blue count was performed using a Vi-CELL XR 2.03 cell counter.

2.2.14 Cell apoptosis assay

Cell apoptosis was assessed using Annexin V and 7-AAD staining according to the manufacturer's instructions. Briefly, cells were seeded in 12-well plates overnight and treated with indicated concentrations of inhibitors for 72 h. Cells were harvested and washed once with PBS, resuspended in 100 µl Annexin V Binding Buffer, and transferred in a 5 ml FACS test tube. 5 µl FITC Annexin V and 5 µl 7-AAD Viability Staining Solution were added to each tube, including unstained and single staining samples. Samples were gently vortexed and incubated for 15 min at RT protected from light. 200 µl Annexin V Binding Buffer was added to each tube before cytometric analysis at a FACS LSR Fortessa. 10,000 cells per condition were acquired, and data were further processed and analysed using the FlowJo software (Flowjo LLC, V10.7.0).

2.2.15 Soft agar assay

The soft agar assay was used to measure anchorage-independent growth and the colony formation rate of LN308 glioblastoma cells upon inhibitor treatment. Cells were grown in a layer of 0.35 % soft agar on top of a layer of 0.5 % agar. The higher concentration of agar in the bottom layer prevents cells from attaching to the culture plate and allows transformed cells to form and grow as colonies. 1 % and 0.7 % agar were prepared by slowly dissolving SeaPlaque agarose in water using a microwave, and afterwards equilibrated to 40 °C in a water bath until use. For the bottom layer, equal amounts of 1 % agar and 2X growth spheroid medium (1:1 Neurobasal A:DMEM/F12 with 2X B-27, 2X N2, 20 ng/ml hEGF, and 20 ng/ml rhFGF) were mixed to give 0.5 % agar and 1X medium. Using a multichannel pipette with pre-warmed tips, 50 µl of the agar-medium mix was dispensed in 96-well plates without creating air bubbles. The plate was cooled down for 1 h or overnight at 4 °C. To plate the top layer of 0.35 % agar containing the cells, cells were harvested as described, and a single-cell suspension was prepared in pre-warmed 2X growth medium. The cell suspension was mixed with 0.7 % agarose, and 2,500 cells were seeded per well in 50 µl volume without touching the bottom agar layer. After the cell layer was solidified, a final layer of 50 µl 1X growth medium was added to the wells and incubated for 24 h at 37 °C. For inhibitor treatment, 4-fold concentrated drugs were prepared in 50 µl 1X growth medium and added to each well. Each compound concentration was measured in quintuplicates; DMSO was used as vehicle control. Cells were incubated for 14 d at 37 °C and inhibitors were replenished every 72 h. Therefore, the liquid layer was carefully removed from wells without displacing the agar layers and a 2-fold concentrated inhibitor in 2X growth medium was added to the cells. As a final readout after 14 d of inhibitor treatment, the CellTiter-Glo® 3D Cell Viability Assay was used to measure ATP content proportional to the number of viable cells and cell colonies. The liquid layer was removed from each well and an equal amount of 3D CellTiter-Glo® substrate was added. Efficient cell lysis was induced by mixing the contents on a shaking rotor for 5 min. Plates were incubated for 25 min at RT to stabilise the luminescent signal and luminescence at 560 nM was recorded at a Mithras LB 940 plate reader. Wells with displaced or destroyed agar layers were excluded from the analysis. Raw luminescence values from blank measurements were subtracted from the wells and DMSO vehicle control was used for normalisation.

2.2.16 γH2AX foci staining after irradiation

Cells were seeded on Comet slides in QuadriPERM plates at a density of 2.5 x 10^5 cells per slide and treated with inhibitor for 24 h. For each condition, three slides were seeded (without irradiation, 1 h sample, 24 h sample). DNA damage was induced by irradiating the cells with 2 Gy on a Gammacell® 40 Exactor (0.87 Gy/min dose rate) and kept at 37 °C until further processing. To check for DNA damage induction, one slide for each condition was briefly washed in PBS and fixed after 1 h in 4 % PFA for 15 min at RT. After fixation, slides were kept in PBS at 4 °C until the next day. The remaining slides (24 h samples, unirradiated samples) were fixed 24 h after irradiation. After washing in PBS, cells were permeabilised with 0.15 % Triton-X100 in PBS for 15 min and blocked in 1 % BSA + 0.15 % glycine in PBS for 30 min at RT. The primary antibody was diluted 1:1000 in PBS and incubated on the slides overnight at 4 °C in a humidified chamber. The following day, slides were washed in PBS, permeabilised and blocked for 10 min each at RT. The secondary antibody was diluted 1:1000 in PBS and applied to the slides for 1 h at RT in a humidified chamber protected from light. The following wash step for 10 min in PBS and permeabilisation step for 5 min in 0.15 % Triton-X100 in PBS were performed in a dark cuvette. Slides were mounted in ProLong Gold Antifade Mountant with DAPI and sealed with nail polish. Images were acquired using a Zeiss AxioImager.Z2 microscope equipped with a 40x objective. γH2AX foci were quantified in at least 500 nuclei per condition using the Metafer4 Systems software. Apoptotic and mitotic cells were excluded from the analysis.

2.2.17 RNA sequencing

Total RNA was extracted using the RNAeasy Mini Kit according to the manufacturer's instructions including on-column digestion of genomic DNA using the RNase-Free DNase Set. RNA concentration was quantified using Qubit HS Assay RNA Kit and RNA integrity was assessed with an Agilent BioAnalyzer. RIN values of all samples were above 9.7. Sequencing libraries were prepared by the DKFZ GPCF Core Facility. Samples were sequenced on a HiSeq 2000 v4 (50 bp Single Read for sequencing of shNT and shGLI1 knockdown samples for differential gene expression analysis, 125 bp Paired-End for sequencing of wildtype cells for fusion gene analysis). The standard QC analysis was conducted by DKFZ GPCF Core Facility. All samples had read counts of at least 53 MReads for sequencing of shNT and shGLI1 knockdown samples and 110 MReads for wildtype cells. All Q30 values were above 95 %. RNA sequencing analyses, including read count mapping, TPM value calculation, logFC quantification, and KEGG pathway analyses, were done by Dr Michael Fletcher, former post-doc in the division of Molecular Genetics, DKFZ Heidelberg.

2.2.18 Drug Screening

2.2.18.1 Primary Screen

In the primary screen, GLI1 and DNA repair inhibitors were tested as single compounds to evaluate their sensitivity and selectivity in different cell lines.

Preparation of assay plates

Individual compounds were tested in a concentration range from 5 to 25,000 nM in nine dilution steps with logarithmic distribution. 23 inhibitors were included in the drug screening, comprising of 4 direct GLI1 inhibitors, 2 SHH inhibitors, and 17 clinically relevant and established DNA repair inhibitors targeting different pathways and cell cycle checkpoints. The compounds used in the study are listed in Table 4. Staurosporine, a broad-spectrum inhibitor of protein kinases, and panobinostat, an HDAC inhibitor, were used as positive controls; vehicle concentration as a negative control. If not purchased as such, stock solutions of 10 mM in DMSO were prepared for all compounds except ATO. ATO was dissolved in 0.1 N NaOH + 0.1 % Triton X100 due to its insolubility in DMSO. Drug screening was performed in white 384-well microtiter plates and the inhibitors were dispensed using a D300(e) Digital Dispenser from Tecan in a randomized manner to avoid artefacts due to inhibitor positioning. ATO was dispensed at the end of the procedure to prevent evaporation of the compound. The two outer rows were omitted for inhibitor distribution to avoid evaporation-based edge effects. The DMSO concentration was normalised to 0.25% in each well. After compound dispersion, pre-dosed plates were sealed with parafilm and stored at - 80°C until cell seeding.

Cell seeding and viability readout

Before performing the assay, seeding density was optimised for each cell line individually to improve screening stability and ensure exponential growth of the cells during inhibitor exposure. The determination of optimal cell numbers for seeding was performed by titration of cells. Therefore, cells were harvested at 80 - 90 % confluency and seeded in a 384-well plate with clear bottom in a dilution series ranging from 50 to 7,000 cells per well in triplicates for each cell dilution. After 72 h, the optimal cell number was determined by optical evaluation of the cell confluency, and in addition, cell numbers were quantified based on the ATP content using a CellTiter-Glo® viability assay as described in section 2.2.12. Luminescence signal was plotted against seeded cell numbers. Dilutions at the upper end of the logarithmic growth phase with the lowest possible standard deviation amongst triplicates or dilutions at 80 - 90 % confluency by visual inspection were defined as optimal seeding densities. Table 21 summarises the seeding densities for the cell lines used in the study.

Table 21: Seeding densities for cell lines used in this study.

Cell line	Seeding density (384-well plate) [cells/well]	Seeding density (1536-well plate) [cells/well]
T778	1,000	200
T449	3,000	600
LN308	1,750	350
LN229	1,500	300
U3071	5,000	na
U3037	4,500	na

Compound plates were equilibrated to RT at least one hour before seeding. Cells were harvested as single-cell suspensions and diluted in growth medium according to the optimised cell densities. Cells were seeded in a final assay volume of 30 µl per 384-well using a MultiDrop Combi system to accurately disperse cell suspension. Plates were incubated for 72 h at 37 °C and 5 % CO_2. Cell viability was measured with the CellTiter-Glo viability assay as described in 2.2.12 using a Tecan^{TM} Spark microplate reader.

Data analysis

De-randomisation of drug responses, data organisation, and result collection was performed with a pipeline established at the group of Prof Dr Marc Remke, Paediatric Neuro-Oncogenomics, DKTK, UKD Düsseldorf. Raw luminescence values were normalised to the vehicle controls. Dose-response data were generated using a five-parametric logistic (5PL) curve fitting algorithm using GraphPad Prism 9.0.0 software.

For the evaluation of sensitivity and selectivity for all individual compounds, a differential drug sensitivity (dDSS) scoring approach was used as described in Yadav & Pemovska, et al. [201]. In this method, drug response parameters computed with the 5PL function including slope, IC_{50} value, bottom plateau of the drug-response curve as well as highest and lowest drug concentration were used as input parameters. Data were analysed using the DSS package in R and visualised using the ggplot package.

2.2.18.2 Secondary Screen

In the secondary screen, compounds were tested in combination using a 9 x 9 concentration matrix design. For each compound, concentration ranges were adjusted individually according to the results observed in the primary screen to ensure optimal evaluation of drug combination effects. The concentration ranges used in the secondary screen are listed in Table 22.

Table 22: Compound concentration ranges used in the secondary screen.

Compound	Lowest concentration [nM]	Highest concentration [nM]
GANT61	1,000	25,000
ATO	50	25,000
GlaB	32.5	5,000
JK184	5	1,000
CC-115	32.5	25,000
AZD6738	100	25,000
Berzosertib	50	25,000
AZD0156	50	25,000
GDC-0575	32.5	25,000
LY2606368	1	25,000
MK-1775	500	25,000
Belotecan	1	25,000
Doxorubicin	32.5	25,000

The combination screen was carried out as described for the primary screen with exceptions described in the following: The assay was performed in white 1536-well microtiter plates with 9 combinations per plate. Drug combinations were tested in four cell lines: T778, T449, LN308 and LN229. Both inhibitors (GLI1/SHH inhibitor and DNA repair inhibitor) were consecutively dispensed in each well, and the DMSO concentration was normalised to 0.5 %. Cell seeding densities were adjusted to the 1536-well format, and the used cell number per well and cell line are listed in Table 21. The final assay was performed in 4 µl volume per well. Due to reasons of feasibility, one biological replicate was performed to screen all combinations per cell line. Validation experiments were done as a follow-up to confirm the findings of the screening.

Drug combination responses were evaluated through quality control and analysed using the CombeneFit software [202]. For quantification of drug interaction, concentrations were included until single-agent responses reached their maximum responses (bottom plateau). A minimum of at least 6 x 6 concentrations were used in all calculations.

2.2.19 Toxicity studies of cerebral organoids

Cerebral organoids (COR) were generated in collaboration with Pavle Boscovic, graduate student in the division of Molecular Genetics, DKFZ Heidelberg. CORs were developed using induced pluripotent stem cells (iPSCs) according to the protocol described in Lancaster et al. [203]. Toxicity studies were performed to determine the maximum tolerable concentration of inhibitors and examine toxic effects on organoid tissue. CORs at the age of 40 – 50 d were maintained in a 24-well plate in 1 ml mature COR differentiation medium (1:1 mix of DMEM/F12 w/ HEPES and Neurobasal medium, 2.5 µg/ml hr-Insulin, 1X 2-Mercaptoethanol, 0.5X GlutaMAX, 0.5X MEM-NEAA, 1 % P/S, 0.4 mM VitC, supplemented with 0.5X N2 and 0.5X B-27 + VitA) and treated with different concentrations of inhibitors for 8 d. Due to the limited availability of CORs, one CORs was used for each tested concentration. Inhibitors and COR differentiation medium were replenished every 72 h (D1, D4, and D7). CORs were incubated at 37 °C on a shaking plate with 125 rpm. Toxic effects and COR integrity were visually monitored daily. Cell viability was quantified after 8 d of drug treatment using eBioscience^{TM} Viability Dye eFluor^{TM} e450. Therefore, CORs were carefully transferred to a 15 ml falcon tube with minimal excess of medium. CORs were dissociated for 30 min at 37 °C using trypsin accompanied with additional mechanical dissociation. Cell suspensions were transferred to FACS tubes by passing through a 70 µM filter. After collection of cells, cells were washed once with PBS and stained for 30 min at 4 °C with eBioscience^{TM} Viability Dye eFluor^{TM} e450 (1:1000 in PBS). After washing in PBS, cell viability was acquired at a FACS LSR Fortessa, and data were further processed and analysed using the FlowJo software (Flowjo LLC, V10.7.0).

2.2.20 Drug treatment studies of GLICO models

To establish LN308 cells stably expressing Firefly Luciferase, LN308 were transduced with pLenti-PGK-V5-LUC-Neo and were cultured under Neomycin selection for 14 d. For co-culture experiments, cerebral organoids were transferred to a 24-well plate with one organoid per plate and co-cultured with 1.0 x 10^5 luciferase-expressing LN308 cells for 24 h without agitation. Organoids were subsequently washed with PBS and transferred to a clean well with 1 ml organoid differentiation medium and allowed to grow on an orbital shaker for 8 days at 37 °C. Bioluminescent signals were measured at baseline after removal of unbound tumour cells (D0), followed by measurements every 72 h, and before treatment start. Luciferase levels were measured according to the protocol described in 2.2.21. GLICOs were treated with 250 nM GlaB, 5 nM LY2606368, or a combination of both, and inhibitors were replenished every 72 h. Vehicle control organoids were maintained in medium containing 0.1 % DMSO.

2.2.21 Bioluminescent imaging of GLICO models

For quantification of tumour growth in cerebral organoids, bioluminescent signal was measured using the IVIS® Lumina LT Series III (PerkinElmer). Before signal acquisition, GLICOs were incubated with 150 µg/ml D-luciferin for 30 min at RT. GLICO tumours containing parental LN308 cells without luciferase expression were used as negative controls. Using a black-walled 24-well plate, the bioluminescent signal was acquired with an integration time of 1 min and total flux per defined region was quantified using the Living Image® software.

2.2.22 EdU labelling and cell viability staining of GLICO models

For cell proliferation analysis of tumour cells in the GLICO model, GLICOs were incubated for 1.5 h with 10 µM EdU before harvesting. Organoids were dissociated using an optimised dissociation procedure with papain. Therefore, papain (300 Units/ml) was activated in activation buffer for 30 min at 37 °C and used with DNase I (1000 U/ml) in HBSS as organoid dissociation buffer. Cerebral organoids were washed twice with PBS and incubated in 500 µl dissociation buffer for 30 min at 37 °C on an orbital shaker. Single-cell suspension was obtained by triturating using a 1 ml pipettor and passing through a 70 µM filter. Cells were collected by centrifugation at 1,200 rpm for 5 min in the presence of ovomucoid protease inhibitor solution (10 mg/ml). Viable EdU$^+$ tumour cells were stained using a fixable viability dye and the Click-iT EdU Alexa Fluor 647 Flow Cytometry Assay Kit, followed by intracellular V5 staining. The V5 staining was used to discriminate LN308 tumour cells expressing V5-tagged luciferase from organoid cells. After dissociation and single-cell collection, cells were stained with eBioscience™ Viability Dye eFluor™ e780 (1:1000 in PBS) and incubated for 30 min at 4 °C in the dark. Cells were washed three times with PBS and fixed in IC Fixation buffer for 30 min at RT in the dark, followed by permeabilisation using 1X Permeabilisation buffer for 5 min at RT. After centrifugation, cells were washed once with 1 % BSA in PBS and stained according to the instructions of the Click-iT EdU Alexa Fluor 647 Flow Cytometry Assay Kit for 30 min at RT in the dark. After washing in 1 % BSA/PBS, cells were stained with 0.5 µg V5-PE antibody in 100 µl 1X Permeabilisation buffer for 30 min at RT in the dark, washed twice, and resuspended in PBS before FACS analysis at a BD FACS Fortessa. Data were further processed and analysed using the FlowJo software (Flowjo LLC, V10.7.0).

2.2.23 Embedding, cryosectioning, and immunofluorescent staining of organoid tissue

For organoid embedding, organoid tissues were washed twice with PBS before fixation for 1.5 h in methanol-free 4 % PFA at RT. Excess of PFA was removed by briefly washing in PBS. Organoids were subsequently incubated in 30 % sucrose at 4 °C overnight or until organoids sank to the bottom of the plate. Before the next step, 7.5 % gelatine solution in 10 % sucrose was pre-warmed at 37 °C. Organoids were transferred to the gelatine and incubated for 15 min at 37 °C. A drop of gelatine was added to an embedding mould, followed by the organoid and kept at 4 °C until the gelatine solidified. Embedding mould was filled up with the remaining gelatine and after solidification, the embedded organoid was snap-frozen in a dry ice/isobutene bath. Therefore, dry ice was added to isobutene and once the temperature reached - 20 °C, gelatine block was carefully removed from the embedding mould and added to the dry ice/isobutene mix until completely frozen. Snap-frozen tissue blocks were kept at - 80 °C until cryosectioning.

Organoid sections were prepared using a Leica CM1860 UV cryomicrotome. Therefore, organoid blocks were removed from the freezer and equilibrated to the cryostat temperature of - 26 to - 30 °C for 30 min. Organoids were cut in 15 µM thick sections and transferred onto Superfrost PLUS slides. Slides were dried at RT and stored at - 20 °C.

For immunofluorescent staining, slides were removed from the freezer and allowed to dry for 20 min at RT. Slides were washed with PBS-T for 10 min at 37 °C to completely remove the gelatine. Tissue was blocked and permeabilised in 5 % goat serum + 0.5 % TritonX100 in PBS for 1 h in a humidified chamber at RT. Primary antibody was diluted in the appropriate concentrations (see Table 6) in 1 % goat serum + 0.1 % TritonX100 and incubated on the slides for 2 h in a humidified chamber at RT, followed by overnight incubation at 4 °C. The following day, slides were washed three times for 10 min in PBS-T. Secondary antibody was prepared in 1 % goat serum + 0.1 % TritonX100 and incubated on the slides for 1 h in a humidified chamber at RT. Slides were washed again three times for 10 min in PBS-T. Excess of washing solution was wiped off and slides were air-dried for 5 min, mounted in mounting medium containing DAPI, sealed with nail polish, and stored at 4 °C until image acquisition at a Leica SP8 confocal microscope. Images were further processed using the Fiji, ImageJ software.

2.2.24 Statistical analysis

Statistical analyses and visualisations were performed using GraphPad Prism software or R. Student's t-test or Mann Whitney U test were used to calculate statistical differences between two groups with normal or non-normal distributed data sets, respectively. One-way analysis of variance (ANOVA) was used to determine differences between more than two groups, while two-way ANOVA was applied in experiments with two independent variables. Kruskal-Wallis test was applied as a nonparametric test to compare more than two independent samples. To examine linear correlation between expression of two genes or IC_{50} values, Pearson correlation was used. The statistical test applied in each analysis is stated in the corresponding figure legend. In boxplot visualisations, the ends of the box correspond to the 25th and 75th percentiles, and the whiskers show 1.5× the interquartile range (IQR) from the 25th and 75th percentiles. Outliers beyond 1.5× IQR are shown as points. A p-value threshold of 0.05 was used in all experiments to consider the statistical significance.

3 Results

3.1 Genetic alterations of *GLI1* in glioblastoma

3.1.1 *GLI1* fusion genes frequently occur in 12q-amplified tumours and are associated with strong overexpression

Intending to identify driving genetic alterations and improve treatment decisions based on a patient's molecular profile, a comprehensive multi-omic tumour characterisation becomes more and more a standard in clinical practice. In a previously published study from our group, 60 untreated primary tumours of adult glioblastoma were molecularly profiled using deep-coverage total RNA sequencing (RNA-seq), whole-genome bisulphite sequencing (WGBS), 450k array/EPIC methylation microarrays, whole-exome sequencing (WES), and chromatin immunoprecipitation followed by sequencing (ChIP-seq) of histone marks [204]. Besides many other analyses, the 450k and EPIC DNA methylation array data were used to analyse copy number states and identify chromosome amplifications, deletions, losses, and gains. These copy number aberrations (CNAs) represent changes in the copy number of either a gene or whole chromosome arms. Typical glioblastoma CNAs were identified, including amplification of *EGFR*, *PDGFRA*, *CDK4* and *MDM2 or MDM4*, gain of chromosomes 7, 19, and 20, focal deletion *of CDKN2A/B*, and loss of chromosome 10 [204]. Of the 60 profiled patients, 14 patients (23.3 %) harboured an amplification of the chromosome bands 12q13-15, covering the *CDK4* and *MDM2* oncogene loci. *CDK4* alone was amplified in 13 patients, *MDM2* in one patient, while both oncogenes were amplified in five patients. The transcriptional regulator *GLI1* is located 275 kb upstream of the *CDK4* locus. Among the 14 patients with 12q amplification, *GLI1* was co-amplified in six patients. In the other eight patients, it was located outside of the amplicon with a maximum distance of 200 kb to the amplicon boundary. Patient information relevant for the current study are depicted in Figure 8; a more detailed table of reported CNAs for each patient is provided in Supplementary material 1.

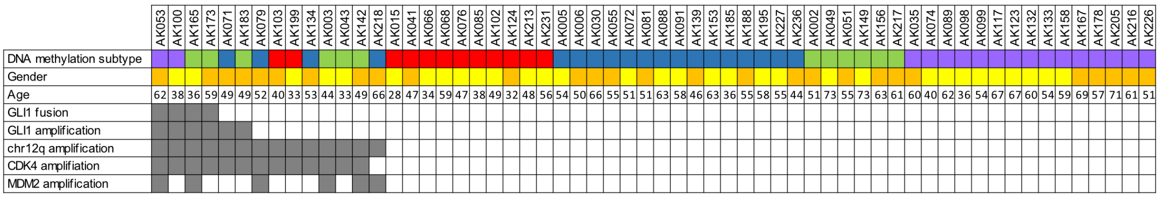

	AK053	AK100	AK165	AK173	AK071	AK183	AK079	AK103	AK199	AK134	AK003	AK043	AK142	AK218	AK015	AK041	AK066	AK068	AK076	AK085
DNA methylation subtype	🟪	🟪	🟩	🟩	🟦	🟩	🟦	🟥	🟥	🟦	🟩	🟩	🟩	🟦	🟥	🟥	🟥	🟥	🟥	🟥
Gender	🟧	🟨	🟨	🟧	🟧	🟧	🟧	🟧	🟨	🟧	🟨	🟨	🟧	🟧	🟨	🟧	🟨	🟨	🟨	🟨
Age	62	38	36	59	49	49	52	40	33	53	44	33	49	66	28	47	34	59	47	38
GLI1 fusion	⬛	⬛	⬛	⬛	⬜	⬜	⬜	⬜	⬜	⬜	⬜	⬜	⬜	⬜	⬜	⬜	⬜	⬜	⬜	⬜
GLI1 amplification	⬛	⬛	⬛	⬛	⬛	⬛	⬜	⬜	⬜	⬜	⬜	⬜	⬜	⬜	⬜	⬜	⬜	⬜	⬜	⬜
chr12q amplification	⬛	⬛	⬛	⬛	⬛	⬛	⬛	⬛	⬛	⬛	⬛	⬛	⬛	⬛	⬜	⬜	⬜	⬜	⬜	⬜
CDK4 amplifiation	⬛	⬛	⬛	⬛	⬛	⬛	⬛	⬛	⬛	⬛	⬛	⬛	⬛	⬜	⬜	⬜	⬜	⬜	⬜	⬜
MDM2 amplification	⬛	⬜	⬛	⬜	⬜	⬜	⬛	⬜	⬜	⬜	⬛	⬜	⬛	⬛	⬜	⬜	⬜	⬜	⬜	⬜

	AK102	AK124	AK213	AK231	AK005	AK006	AK030	AK055	AK072	AK081	AK088	AK091	AK139	AK153	AK185	AK188	AK195	AK227	AK236	AK002
DNA methylation subtype	🟥	🟥	🟥	🟥	🟦	🟦	🟦	🟦	🟦	🟦	🟦	🟦	🟦	🟦	🟦	🟦	🟦	🟦	🟦	🟩
Gender	🟨	🟧	🟨	🟨	🟨	🟧	🟧	🟧	🟨	🟧	🟨	🟨	🟧	🟨	🟨	🟧	🟨	🟨	🟧	🟧
Age	49	32	48	56	54	50	66	55	51	51	63	58	46	63	36	55	58	55	44	51
GLI1 fusion	⬜	⬜	⬜	⬜	⬜	⬜	⬜	⬜	⬜	⬜	⬜	⬜	⬜	⬜	⬜	⬜	⬜	⬜	⬜	⬜
GLI1 amplification	⬜	⬜	⬜	⬜	⬜	⬜	⬜	⬜	⬜	⬜	⬜	⬜	⬜	⬜	⬜	⬜	⬜	⬜	⬜	⬜
chr12q amplification	⬜	⬜	⬜	⬜	⬜	⬜	⬜	⬜	⬜	⬜	⬜	⬜	⬜	⬜	⬜	⬜	⬜	⬜	⬜	⬜
CDK4 amplifiation	⬜	⬜	⬜	⬜	⬜	⬜	⬜	⬜	⬜	⬜	⬜	⬜	⬜	⬜	⬜	⬜	⬜	⬜	⬜	⬜
MDM2 amplification	⬜	⬜	⬜	⬜	⬜	⬜	⬜	⬜	⬜	⬜	⬜	⬜	⬜	⬜	⬜	⬜	⬜	⬜	⬜	⬜

	AK049	AK051	AK149	AK156	AK217	AK035	AK074	AK089	AK098	AK099	AK117	AK123	AK132	AK133	AK158	AK167	AK178	AK205	AK216	AK226
DNA methylation subtype	🟩	🟩	🟩	🟩	🟩	🟪	🟪	🟪	🟪	🟪	🟪	🟪	🟪	🟪	🟪	🟪	🟪	🟪	🟪	🟪
Gender	🟨	🟧	🟨	🟧	🟧	🟧	🟨	🟨	🟨	🟨	🟨	🟨	🟨	🟨	🟨	🟧	🟧	🟧	🟧	🟧
Age	73	55	73	63	61	60	40	62	36	54	67	67	60	54	59	69	57	71	61	51
GLI1 fusion	⬜	⬜	⬜	⬜	⬜	⬜	⬜	⬜	⬜	⬜	⬜	⬜	⬜	⬜	⬜	⬜	⬜	⬜	⬜	⬜
GLI1 amplification	⬜	⬜	⬜	⬜	⬜	⬜	⬜	⬜	⬜	⬜	⬜	⬜	⬜	⬜	⬜	⬜	⬜	⬜	⬜	⬜
chr12q amplification	⬜	⬜	⬜	⬜	⬜	⬜	⬜	⬜	⬜	⬜	⬜	⬜	⬜	⬜	⬜	⬜	⬜	⬜	⬜	⬜
CDK4 amplifiation	⬜	⬜	⬜	⬜	⬜	⬜	⬜	⬜	⬜	⬜	⬜	⬜	⬜	⬜	⬜	⬜	⬜	⬜	⬜	⬜
MDM2 amplification	⬜	⬜	⬜	⬜	⬜	⬜	⬜	⬜	⬜	⬜	⬜	⬜	⬜	⬜	⬜	⬜	⬜	⬜	⬜	⬜

DNA methylation subtype:
🟥 IDH
🟦 MES
🟩 RTKI
🟪 RTKII

Gender:
🟧 female
🟨 male

Amplification/fusion:
⬛ detected
⬜ not detected

Figure 8: Patient information of HIPO016 cohort. 60 adult primary glioblastoma tumours were molecularly profiled in the HIPO016 study. Patient information on glioblastoma subtype based on 450k DNA methylation data, gender, age, relevant CNAs for this study, including chromosome 12q, *CDK4*, *MDM2* and *GLI1*, and occurrence of *GLI1* fusions are illustrated as a heat map. Additional information is provided in Supplementary material 1.

Genomic instability coexists with fusion transcripts and loci of chromosomal amplifications often serve as hot-spot regions for generating recurrent gene fusions [205]. It is of interest whether such recurrent fusions are passenger aberrations or potential driving events of tumorigenesis. Within the HIPO016 cohort, 4 out of 14 patients with 12q amplicon (28.6 %) harboured fusion transcripts associated with *GLI1* (Figure 9 A). The analysis of RNA expression revealed that only fusion-positive patients had an overexpression of *GLI1* compared to other patients in the cohort. The strong overexpression was independent of the 12q amplification status as *GLI1* was almost not expressed in 12q-amplified patients without *GLI1* fusion transcripts and patients with balanced 12q copy numbers (Figure 9 B). Of note, two patients with *GLI1* amplification without *GLI1* fusions (AK071 and AK188) did not show elevated *GLI1* RNA expression levels (Figure 9 C, labelled in red). CDK4 is located 275 kb downstream of the *GLI1* locus and in contrast to *GLI1*, amplification of *CDK4* was directly associated with its overexpression (Figure 9 C). These data suggest that *GLI1* fusion genes are often found in association with 12q amplification and are the main mechanism to drive GLI1 activation in glioblastoma while amplification alone is not sufficient to activate its expression.

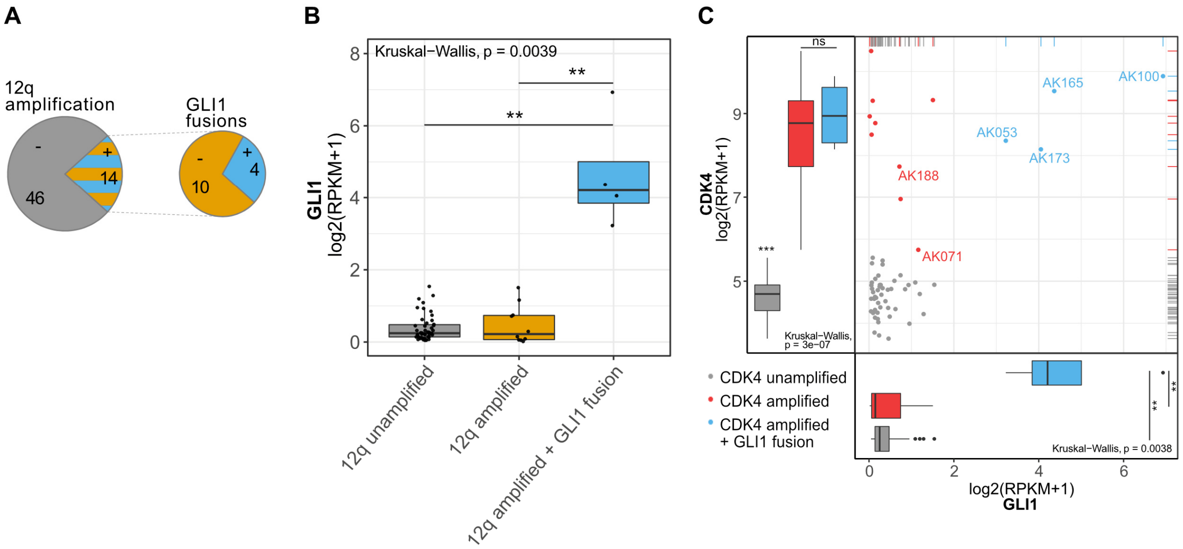

Figure 9: 12q amplification and *GLI1* expression in the HIPO016 cohort. A Overview of the number of patients with 12q amplification and *GLI1* fusion genes in the HIPO016 cohort (n=60 primary adult glioblastoma) is illustrated as a pie chart. *GLI1* fusion genes were exclusively found in 12q-amplified tumours. **B** *GLI1* RNA expression levels were compared between 12q-unamplified (n=48), 12q-amplified without *GLI1* fusion (n=8) and 12q-amplified with *GLI1* fusion (n=4) samples. **C** Scatterplot of *CDK4* and *GLI1* expression values for each patient coloured by 12q amplification/*GLI1* fusion gene status. Labelled tumours in red are tumours with amplification of *CDK4* and *GLI1* without detected *GLI1* fusion gene (*p<0.05, **<0.01, ***<0.001; ns, not significant; Kruskal-Wallis test with Dunn post-hoc test for multiple comparisons of groups).

3.1.2 Identification and validation of *GLI1* fusion transcripts in glioblastoma tumours of the HIPO016 cohort

High-confidence fusion transcripts presented in this work were detected by Dr Zhiqin Huang and Dr Yonghe Wu (former members of the division of Molecular Genetics, DKFZ Heidelberg) using the confFuse scoring algorithm pipeline [206]. Paired-end RNA-seq data from all 60 patients were used to identify fusion transcripts. A confidence score was assigned to each predicted fusion transcript, taking multiple parameters into account to eliminate false-positive predictions. As such, the number of split/spanning reads, read-through sequencing, alternative splicing between adjacent genes, artefacts, and location of the breakpoints were examined [206]. Fusion transcripts with a confidence score of ≥ 7 were considered biologically relevant with high confidence. In total, 898 fusion candidates (score ≥ 7) were identified, 531 of which were scored ≥ 8. In concordance with previous findings [158], chromosome 12 harboured the highest number of fusion candidates (n = 348, score ≥ 7), the majority of which located in chromosome bands 12q13-15. Mostly intrachromosomal but also interchromosomal *GLI1* fusion transcripts were detected in patients AK053, AK100, AK165, and AK173 (Table 23). Interchromosomal translocations with genes located on chromosome 17 and chromosome 18 were found in patient AK100. Fusion partners differ amongst patients and recurrent *GLI1* fusion partners were not detected. In addition to the confFuse software, fusion predictions were validated by the Arriba software tool, provided by the ODCF Core Facility at the German Cancer Research Centre. With the exception of the *GLI1-CPSF6* fusion in patient AK053, *KIAA1328-GLI1* in AK100, and *INHBE-GLI1* in AK173, all fusions were detected with both methods.

Table 23: *GLI1* fusion transcript prediction in patients of the HIPO016 cohort using the confFuse and Arriba software. Gene names and chromosome number for both fusion partners, number of spanning reads, confFuse prediction, confFuse score, Arriba prediction, and Arriba score are provided for each fusion event. na: not available.

Patient ID	Gene 1	Gene 2	Chrom 1	Chrom 2	Spanning reads	confFuse	confFuse Score	Arriba	Arriba score
AK053	CPSF6	**GLI1**	12	12	7	yes	9.5	yes	high
	GLI1	CPSF6	12	12	5	yes	9.5	no	na
AK100	RP11-58A17.4	**GLI1**	12	12	125	yes	9.5	yes	high
	ACACA	**GLI1**	17	12	29	yes	7.5	yes	high
	KIAA1328	**GLI1**	18	12	26	yes	6.5	no	na
	AATF	**GLI1**	17	12	83	yes	9.5	yes	high
	OS9	**GLI1**	12	12	17	yes	4	yes	medium
	GLI1	RP11-571M6.7	12	12	12	yes	3	yes	medium
AK165	DDIT3	**GLI1**	12	12	244	yes	8.5	yes	high
AK173	INHBE	**GLI1**	12	12	60	yes	3.5	yes	low

Experimental validation of all fusion transcripts with a confFuse score ≥ 7 was performed by Man Ka Hou, a master student in the division of Molecular Genetics, using standard PCR with primers flanking the predicted fusion breakpoints (Figure 10 A). Amplified products were subjected to Sanger sequencing to confirm the breakpoint and fusion partner prediction. All fusion transcripts except *ACACA-GLI1* in patient AK100 could be amplified from the genomic DNA of the corresponding patients (Figure 10 B). Multiple bands were often observed in the gel electrophoresis of the PCR products, most probably arising from different fusion breakpoints in individual copies of the focally amplified *GLI1* locus. When some of the higher molecular weight bands were Sanger-sequenced, an additional sequence of 15 - 20 bp length was identified to be trapped between the predicted fusion partners, further suggesting that *GLI1* fusion transcripts do not have a single breakpoint (Figure 10 C). In line with this assumption, a subsequent analysis that included fusion transcripts supported by fewer discordant and split reads identified multiple breakpoints of the same fusion transcripts (data not shown). Overall, the experimental validation of fusion transcripts proofed that the transcriptomic analysis correctly predicted fusion partners and the majority of breakpoints.

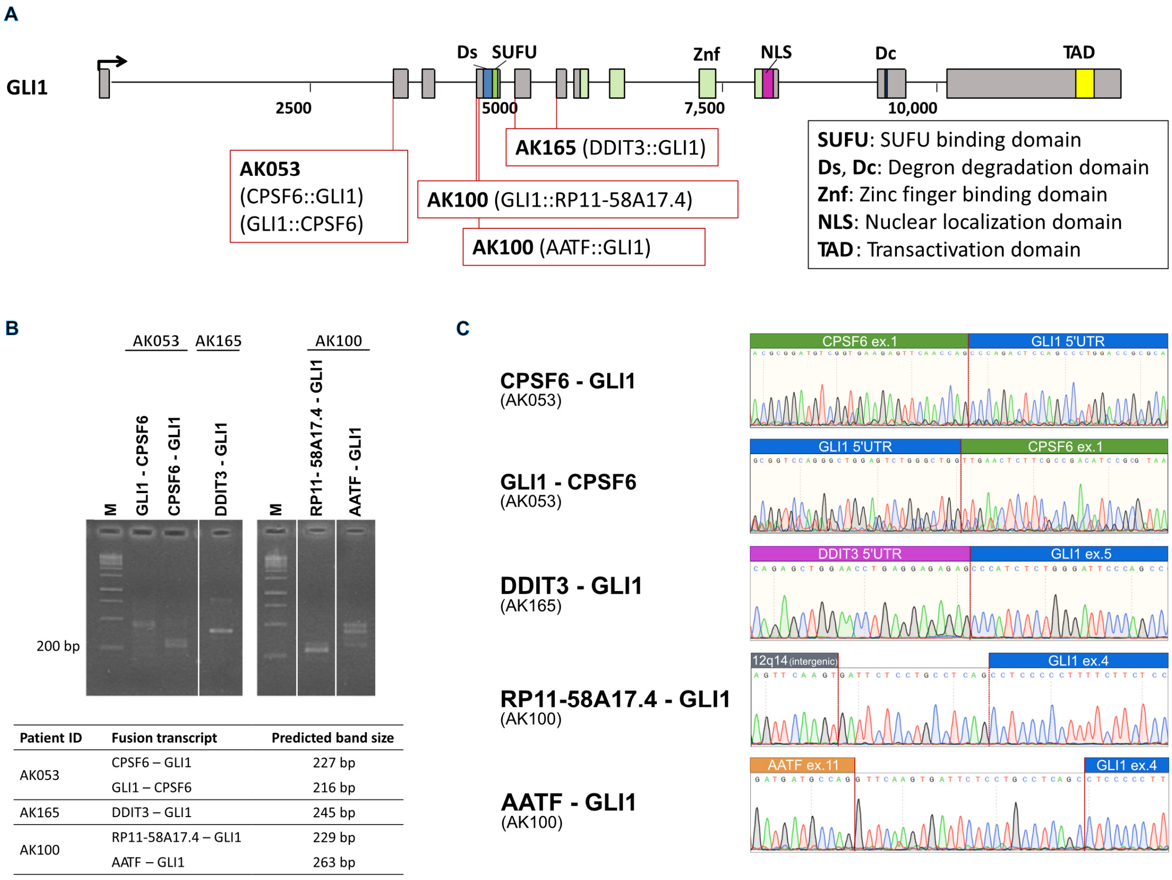

Patient ID	Fusion transcript	Predicted band size
AK053	CPSF6 – GLI1	227 bp
	GLI1 – CPSF6	216 bp
AK165	DDIT3 – GLI1	245 bp
AK100	RP11-58A17.4 – GLI1	229 bp
	AATF – GLI1	263 bp

Figure 10: Experimental validation of *GLI1* fusion transcripts found in the HIPO016 cohort. A Schematic representation of the genomic structure of the *GLI1* gene, its functional domains, and predicted breakpoints in the HIPO016 *GLI1* fusion-positive tumours. **B** Gel electrophoresis of PCR products amplified by the primers flanking the predicted genomic breakpoints, M Marker. The table below lists the fusion transcripts with their predicted amplicon size. **C** Chromatograms of validation PCR products analysed by Sanger sequencing. Red lines indicate the breakpoints. Fusion transcripts RP11-58A17.4–GLI1 and AATF–GLI1 in patient AK100 contain additional nucleotide sequences that cannot be mapped to either of the two fusion partners.

3.1.3 Amplification boundary coincides with *GLI1* breakpoint in fusion-positive tumours

Particular genome sequences are known to be fragile sites that are prone to break more often than others. These chromosome fragile sites (CFS) can impact the susceptibility towards genomic amplification and define the boundaries of amplicons [207, 208]. They are sensitive to chromosomal breakage due to replication stress and are often rearranged in cancer. To study the structure of amplicons and precisely reconstruct the position of the amplicon boundaries in tumours with *GLI1* fusions, copy number profiles were examined from the Illumina 450k/EPIC DNA methylation arrays. The review of whole-genome (Figure 11 left) and *GLI1* locus (Figure 11 right) copy number of the four patient tumours with *GLI1* fusion genes revealed common characteristics, including gains of chromosome 7 with focal amplification of *EGFR* in AK053 and AK100, and a loss of chromosome 10 in all samples. A gain of chromosome 19 was detected in AK053 and AK100, and losses of chromosomes 13 and 15 were found in AK053 and AK165. Additional focal losses within chromosomes 1, 3, 4, 8, 11, and 12 were prevalent in all patients, except AK100.

In chromosome region 12q13-15, *CDK4* was amplified in all four patients with *GLI1* fusion transcripts, and *MDM2* in patients AK053 and AK165. In patients AK053 and AK100, the individual probe intensities within the *GLI1* locus vary between the 5’ and 3’ ends of the gene. While a copy number neutral state was observed at the 5’ end, DNA methylation beta-value increased within the gene locus, suggesting that the amplicon boundary is located within the *GLI1* locus. An increase in DNA methylation was also observed in AK165, although less prominent than in AK053 and AK100. In patient AK173, the entire *GLI1* locus was amplified. These data suggest that the occurrence of *GLI1*-fusion transcripts is tightly associated with the amplification of *GLI1*, and amplicon boundaries within the locus promote the formation of gene fusions.

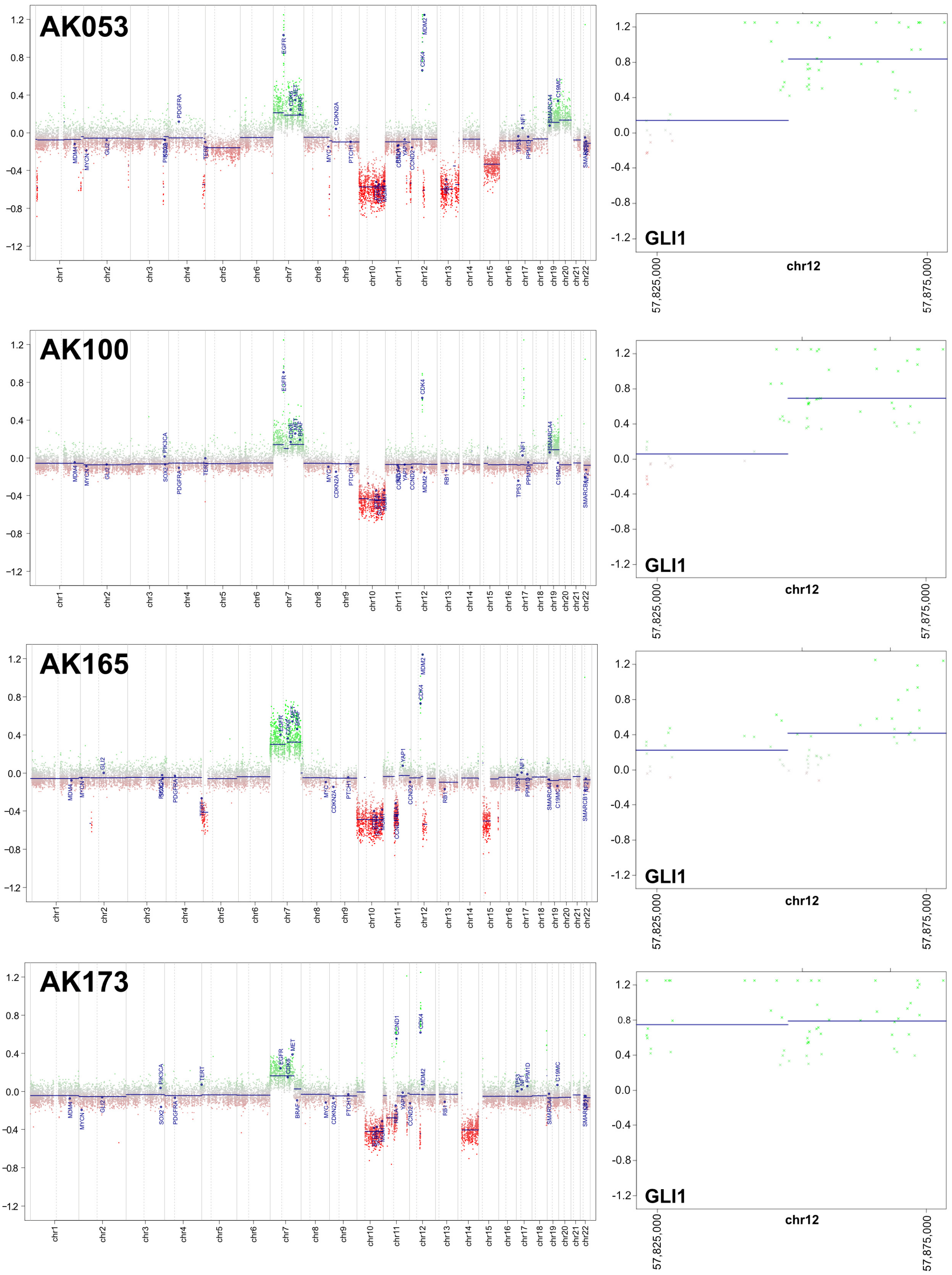

Figure 11: CNV plots based on 450k/EPIC methylation array analyses of patient tumours with *GLI1* fusion transcripts. Left: CNV plots of the complete genome. Individual chromosomes are separated by solid lines, centromere positions by dashed lines. Intensity values of each bin are plotted in coloured dots, segments are represented as blue lines. Known oncogenes and tumour suppressor genes are labelled. Right: CNV plots of *GLI1* locus. Intensity values of individual probes are plotted in coloured crosses, bins are shown as blue lines.

3.1.4 GLI1 target gene expression is upregulated in fusion-positive tumours of the HIPO016 cohort

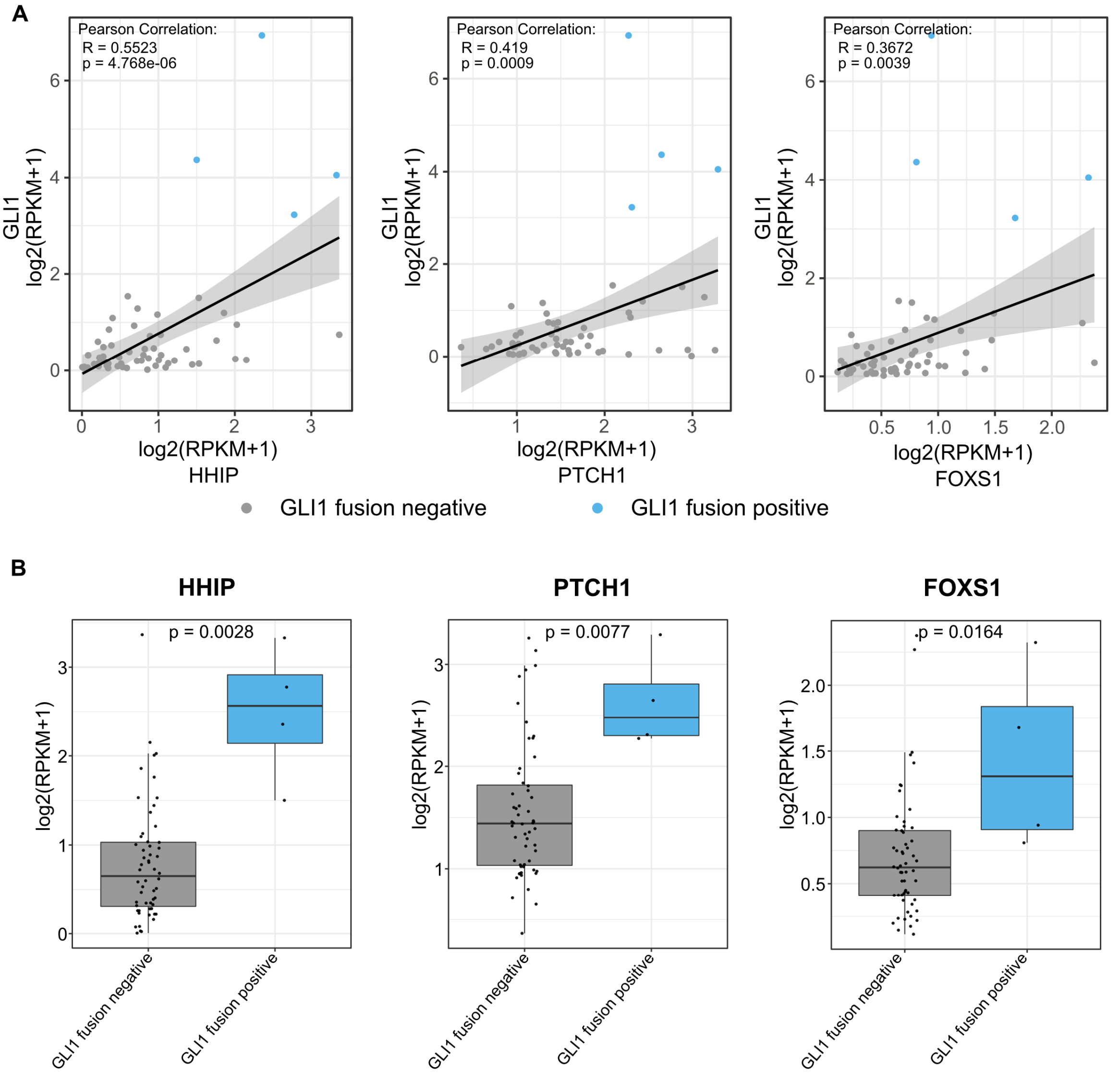

Figure 12: Expression of GLI1 target genes is upregulated in fusion-positive tumours. A Pearson correlation plots of *HHIP* (left), *PTCH1* (middle), and *FOXS1* (right) expression (x-axis) with *GLI1* expression (y-axis) for fusion-positive and fusion negative patients. **B** Expression levels of *HHIP* (left), *PTCH1* (middle), and *FOXS1* (right) in *GLI1* fusion-positive and fusion-negative patients (p-values are indicated in the graphs, Mann-Whitney U test).

GLI1 is an effector transcription factor controlling the expression of several target genes and regulating key cellular processes [209-213]. Direct GLI1 target genes include *HHIP*, *PTCH1* and *FOXS1*. HHIP and PTCH1 are components of the HH pathway undergoing Shh-regulated transcriptional feedback regulation [211]. FOXS1 is a member of the FOX gene family acting as a transcriptional repressor and its expression is correlated with *GLI1* expression. It has been shown that GLI1 directly binds to its promoter [210, 214]. Analysis of the HIPO016 cohort, comparing patients with and without *GLI1* fusion genes, showed RNA expression of the GLI1 target genes *HHIP*, *PTCH1*, and *FOXS1* positively correlated with the expression of *GLI1*, with Pearson correlations of

0.5523, 0.419, and 0.3672, respectively (Figure 12 A). Furthermore, target gene expression was significantly upregulated in *GLI1* fusion-positive vs. *GLI1* fusion-negative tumours (Figure 12 B).

These data indicate that the fusion-dependent upregulation of *GLI1* is associated with the upregulation of its direct target genes.

3.1.5 Detection of *GLI1* genomic rearrangements in additional glioblastoma cohorts

The detection and interpretation of genomic rearrangements have always been of great interest when profiling large cohorts of patient samples. To support the previous findings and evaluate the prevalence of *GLI1* fusion genes and *GLI1* expression in large patient cohorts, two additional glioblastoma cohorts, TCGA-GB and HIPO043, were surveyed. The TCGA-GB study was conducted by the TCGA consortium. It consists of 543 untreated primary glioblastoma samples with copy number, DNA methylation, protein, mRNA, and miRNA profiles, providing a detailed taxonomy of molecular features in glioblastoma. Whole-genome sequencing data is available for 42 tumours, RNA sequencing for 164 samples [157]. The HIPO043 study, supported by the collaborative research project ‘SYS-GLIO’ and part of the Heidelberg Center for Personalized Oncology (HIPO), analysed IDH^{wt} glioblastoma samples from 50 paired primary and recurrent tumour samples.

Of the TCGA-GB cohort samples with either RNA-sequencing or whole-genome sequencing data (n = 206), three tumours (1.5 %) had reported somatic rearrangement involving *GLI1*, all of which were intrachromosomal structural variants. Recurrent fusion events were not detected (Table 24). In both patients profiled by whole-genome sequencing, *GLI1* was fused to genes identified as targets of recurrent intragenic copy number breakpoints [157]. For the 50 glioblastomas of the HIPO043 cohort, RNA-sequencing data for fusion gene calling was available for 29 primary and relapsed tumour pairs (n = 58). The analysis with confFuse software was performed by Zhiqin Huang. A *GLI1* intrachromosomal fusion event with a structural variant was detected in one recurrent tumour (Table 24).

Table 24: Genomic rearrangements with GLI1 in TCGA and HIPO043 glioblastoma cohorts.

Cohort	Patient ID	Gene 1	Gene 2	Chrom 1	Chrom 2	Source	Prediction method
TCGA	TCGA-06-2570	**GLI1**	ARHGAP9	12	12	DNA - WGS	BreakDancer [215]
	TCGA-02-2485	**GLI1**	MARS	12	12	DNA - WGS	BreakDancer [215]
	TCGA-06-5859	DDIT3	**GLI1**	12	12	RNA	PRADA [216]
HIPO043	H043_63R6_T2	MARS	**GLI1**	12	12	RNA	confFuse
		INHBE	**GLI1**	12	12	RNA	confFuse

For copy number and mRNA expression analysis in the TCGA-GB cohort, 537 samples were used, for which both data sets were available. Amongst these tumours, 76 (14.2 %) had an amplification of the chromosome arm 12q, and in 36 patients, GLI1 was located within the amplified region, including the three patients with reported *GLI1* fusions (Figure 13 A). *GLI1* expression was quantified using Affymetrix U133A arrays and RNA levels compared between groups of patients with 12q-unamplified, 12q-amplified excluding the *GLI1* locus, and *GLI1*-amplified tumours. *GLI1*-amplified tumours with and without fusion genes were not differentiated since the RNA-sequencing and/or whole-genome sequencing analysis necessary for *GLI1* fusion prediction was not available for all samples. *GLI1* RNA expression was upregulated in tumours with *GLI1* amplification and the three patients with reported *GLI1* fusion genes were above the 75th percentile of tumours with *GLI1* amplification (Figure 13 B).

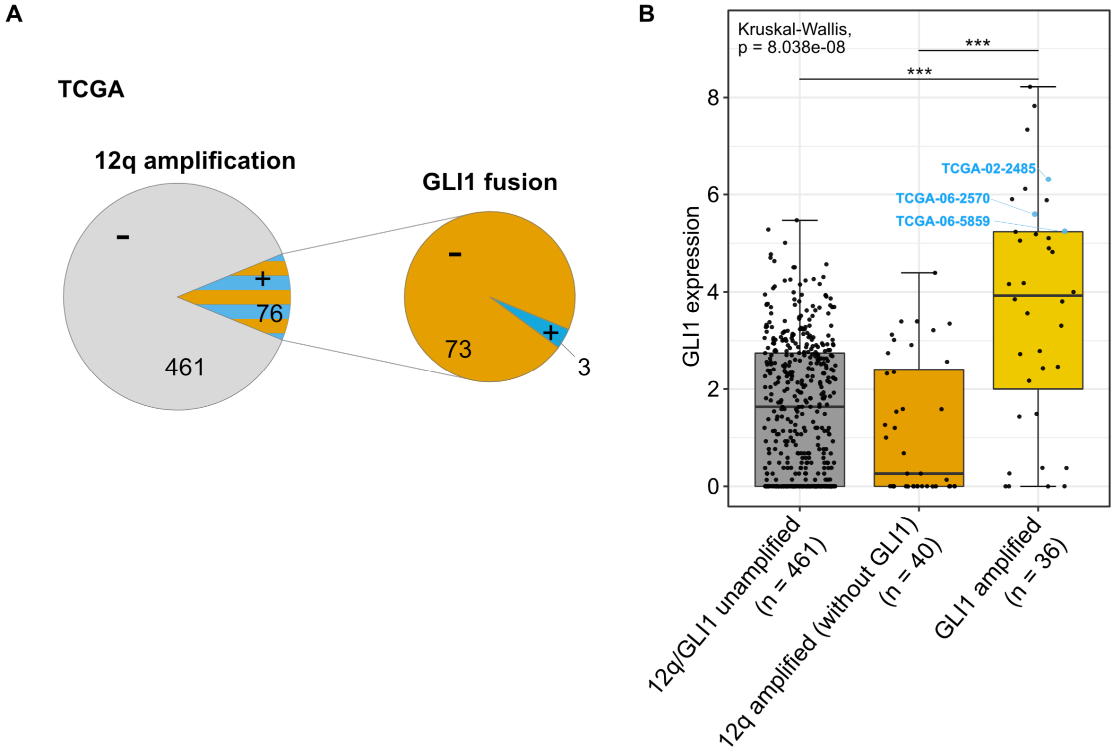

Figure 13: *GLI1* fusion events and RNA expression in the TCGA-GB cohort. A Overview of patient numbers with 12q amplification and *GLI1* fusion genes in the TCGA-GB cohort (n = 537 primary adult glioblastoma), illustrated as a pie chart. *GLI1* fusion genes were exclusively found in 12q-amplified tumours. **B** *GLI1* mRNA expression levels (Affymetrix U133a array platform) were compared between 12q-unamplified (n = 461), 12q-amplified without the *GLI1* locus (n = 40) and 12q-amplified with the *GLI1* locus (n = 36) samples (*p<0.05, **<0.01, ***<0.001, Kruskal-Wallis test with Dunn post-hoc test for multiple comparisons of groups).

GLI1 RNA expression levels were similar in the primary and recurrent tumours of the HIPO043 cohort, except for recurrent tumour H043-63R6 which showed a *GLI1*-fusion event and strong transcriptional upregulation (Figure 14). The DNA copy number profiles pointed to the expansion of a focal *CDK4* amplification in the primary tumour to include the *GLI1* locus in the recurrent tumour as the probable causal event for fusion gene formation and *GLI1* overexpression. (Supplementary material 3). These data suggest that DNA copy number amplification and associated structural rearrangement plays a vital role in *GLI1* upregulation and possibly glioblastoma progression.

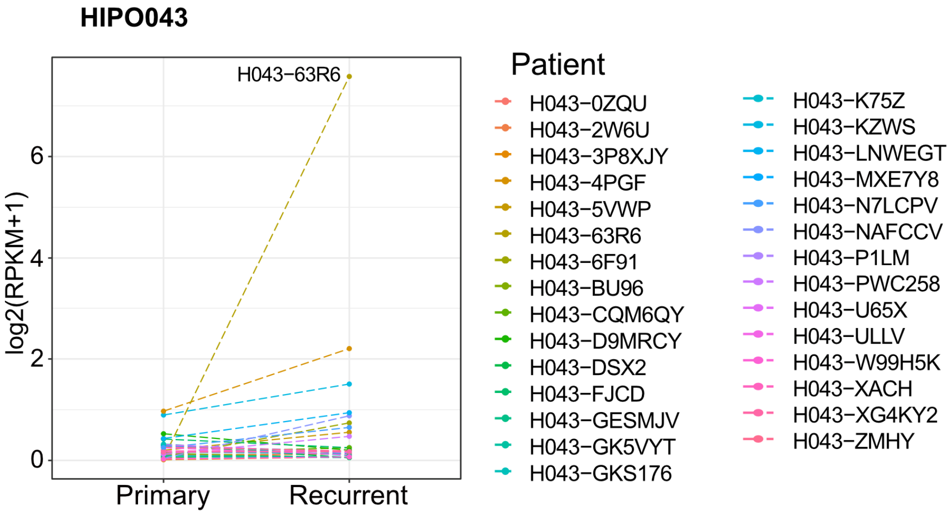

Figure 14: *GLI1* expression levels in glioblastoma tumours of the HIPO043 cohort. Expression levels of *GLI1* from RNA-seq analysis are shown for 29 matched primary and secondary tumours. The dotted lines connect the primary and recurrent tumours of individual patients.

3.2 Genetic alterations of *GLI1* in sarcoma

Soft-tissue sarcomas are a rare type of tumour arising in the supporting tissue of the body. Genomic analysis of adult soft-tissue sarcoma (HIPO028, H021, and K02K projects by Prof. Stefan Fröhling) revealed the presence of *GLI1* fusion transcripts in four patients diagnosed with dedifferentiated liposarcoma (DDLS), liposarcoma (not otherwise specified), and leiomyosarcoma. Intrachromosomal and interchromosomal high confidence fusion transcripts were identified with the confFuse or Arriba detection software (Table 25). The Arriba analysis was only performed on liposarcoma cases including WDLS and DDLS (n = 54), while all tumours within HIPO021 and HIPO028 (n = 270) were analysed with confFuse software. Consistent with the observation in glioblastoma, fusion-positive samples displayed high *GLI1* RNA expression levels with H028-NTAT and H028-YRZB as the two samples with the highest expression levels in the cohort (Figure 15 A).

Table 25: Detected genomic rearrangements with *GLI1* in the HIPO028 sarcoma cohort.

Patient ID	Diagnosis	Gene 1	Gene 2	Chrom 1	Chrom 2	Prediction	Confidence score
H028-NTAT	DDLS	MYRFL	**GLI1**	12	12	Arriba	high
H028-JSF3	LS	**GLI1**	PTPRQ	12	12	confFuse	9.5
H028-LXSA	LMS	MKL1	**GLI1**	22	12	confFuse	10
H028-YRZB	NOS	**GLI1**	ZFAND5	12	9	confFuse	9
		ZFAND5	GLI1	9	12	confFuse	9

LS liposarcoma, LMS leiomyosarcoma, NOS not otherwise specified

Sarcomas arise in various tissues and cell types and are therefore very heterogeneous in their molecular profile [79, 217]. For example, copy number gain and amplification of 12q13-15 have been identified as diagnostic and predictive markers for liposarcoma, especially WDLS and DDLS [218]. *GLI1* expression levels were systematically studied amongst the different sarcoma subtypes to identify groups with aberrant *GLI1* expression (Figure 15 B). High *GLI1* expression was found in different types of osteosarcoma, including GCTB, CSA, EWS, and CHORD and different soft-tissue subtypes, including ESS, LS, MPNST, PECOMA, ESS, SS, and ASA. Outliers with strong upregulation of *GLI1* were present in liposarcoma (LS and DDLS), MPNST, SCS, CCS, and sarcoma not otherwise specified, including patients with reported *GLI1* fusions. The amplification status of *GLI1* was analysed together with Dr Damian Stichel (postdoc, Clinical Cooperation Unit Neuropathology, Prof. Dr Andreas von Deimling) in a cohort of sarcomatous tumours based on DNA methylation data. Sarcoma subtypes with high *GLI1* expression often showed amplification of *GLI1* (Figure 15 C). In rhabdomyosarcoma, endometrial stromal sarcoma, high-grade osteosarcoma, and WDLS/DDLS, amplification of *GLI1* was detected in 12 % (22/187), 10 % (2/20), 4.5 % (15/331), and

2.9 % (11/381) of tumours, respectively. Even though many of these subtypes had small sample sizes, the analysis showed that *GLI1* is upregulated and frequently amplified in a subset of sarcoma tumours, indicating it as a potential therapeutic target.

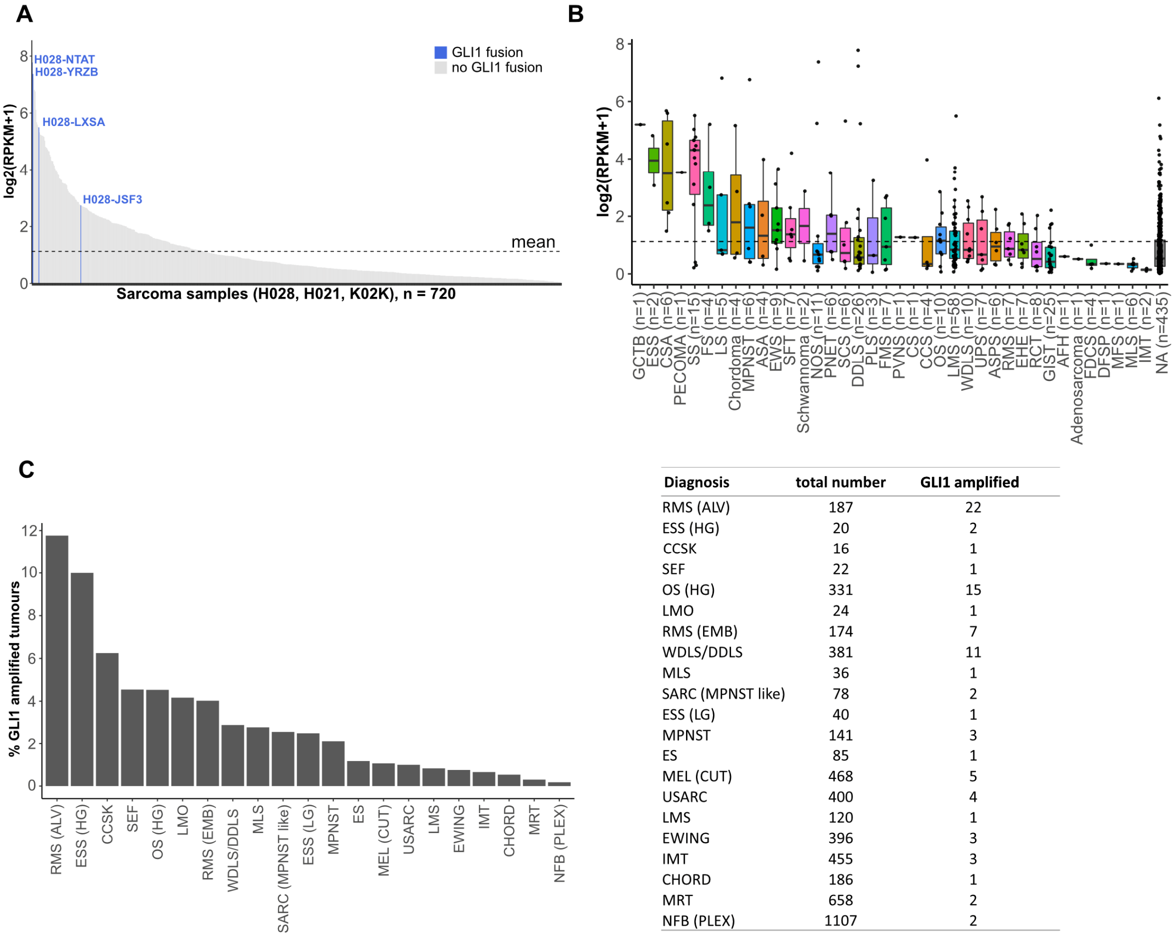

Diagnosis	total number	GLI1 amplified
RMS (ALV)	187	22
ESS (HG)	20	2
CCSK	16	1
SEF	22	1
OS (HG)	331	15
LMO	24	1
RMS (EMB)	174	7
WDLS/DDLS	381	11
MLS	36	1
SARC (MPNST like)	78	2
ESS (LG)	40	1
MPNST	141	3
ES	85	1
MEL (CUT)	468	5
USARC	400	4
LMS	120	1
EWING	396	3
IMT	455	3
CHORD	186	1
MRT	658	2
NFB (PLEX)	1107	2

Figure 15: *GLI1* expression and amplification in sarcoma tumours. A *GLI1* expression levels in sarcoma tumours of the H028, H021, and K02K cohorts (n=720). *GLI1* fusion-positive patients are labelled in blue. The mean expression level across all patients is indicated as a dashed line. **B** *GLI1* expression levels grouped based on sarcoma diagnosis. The mean expression level across all patients is indicated as a dashed line. **C** Frequency of *GLI1* amplification in sarcoma subtypes. The number of total and *GLI1*-amplified patients per group are listed in the table on the right. Abbreviations: GCTB, giant cell tumour of bone; ESS, endometrial stromal sarcoma, CSA, chondrosarcoma; PECOMA, Perivascular epithelioid cell sarcoma; SS, synovial sarcoma; FS, fibrosarcoma ; LS, liposarcoma; CHORD, chordoma; MPNST, malignant peripheral nerve sheath tumour; ASA, angiosarcoma; EWS, Ewing sarcoma; SFT, solitary fibrous tumour; NOS, not otherwise specified; PNET, primitive neuroectodermal tumor; SCS, spindle cell sarcoma; DDLS, dedifferentiated liposarcoma; PLS, primary lung sarcoma; FMS, fibromyxoid sarcoma; PVNS, pigmented villonodular synovitis; CCS, clear cell sarcoma; OS, osteosarcoma; LMS, leiomyosarcoma; WDLS, well-differentiated liposarcoma; UPS, undifferentiated pleomorphic sarcoma; ASPS, alveolar soft-part sarcoma; RMS, rhabdomyosarcoma; EHE, epithelioid hemangioendothelioma; RCT, round cell tumour; GIST, gastrointestinal stromal tumour; AFH, angiomatoid fibrous histiocytoma; FDCS, follicular dendritic cell sarcoma; DFSP, dermatofibrosarcoma protuberans; MFS, myxofibrosarcoma; MLS, myxoid liposarcoma; IMT, inflammatory myofibroblastic tumour; CCSK, clear cell sarcoma of the kidney; SEF, sclerosing epithelioid fibrosarcoma; LMO, leiomyoma; ES, epithelioid sarcoma; MEL (CUT), cutaneous melanoma, USARC, undifferentiated sarcoma; MRT, malignant rhabdoid tumour; MRT, malignant rhabdoid tumour; NA, not available, HG, high-grade. Descriptive analysis of expression levels, without statistical analysis due to different sample sizes.

3.3 Comparison of *GLI1* fusion frequency and implications for further study

The prevalence of *GLI1* structural variants differed amongst the reviewed glioblastoma cohorts with 4/60, 3/206, and 1/29 patients harbouring *GLI1* fusion events in the HIPO016, TCGA-GB, and HIPO043 cohorts, respectively. Besides cohort composition and age of the patients, a potential main reason for the varying frequencies might be differences in sequencing coverage and the associated performance of detection algorithms. At highly amplified chromosome regions, a large number of copies of the amplified gene are present in the sample, requiring sequencing at high depth to allow the distinction of the different gene transcripts and to identify discordant and junction spanning reads. In line with this assumption, the highest percentage of fusion-positive patients was detected in the HIPO016 cohort, which was sequenced at very high coverage (61.5 to 325,000,000 read counts per sample). In contrast, the average sequencing depth of the TCGA datasets across cancer types was much smaller with around 50 million reads per sample. The effect of sequencing coverage in the detection of fusion genes as potential confounding factors was not further addressed in this study.

3.4 Epigenetic alteration by CTCF binding site disruption controls *GLI1* expression

The CTCF insulator protein, together with numerous other chromatin and transcription factor proteins, organises the eukaryotic genome topology that is critical for gene regulation [219]. The disruption of CTCF binding sites, as well as genomic rearrangements, have been linked with alterations in gene expression within TADs that can cause oncogene activation [95, 220-222]. Examination of published CTCF ChIP-seq data [95] identified three CTCF peaks in the proximity of the *GLI1* gene locus (Figure 16). Additional CTCF binding was found between peak 1 and peak 2, but the ChIP-seq signal was much lower compared to the other three peaks. Peak 1 and peak 2 are located upstream of the GLI1 promoter, and peak 3 is placed between exons 1 and 2 in the 5' UTR. In two *GLI1*-fusion tumours of the HIPO016 cohort analysed by WGS, multiple breakpoints were mapped between peaks 2 and 3, and downstream of peak 3, prompting the question of whether the formation of gene fusions interfere with the genome topology and transcriptional regulation in this region.

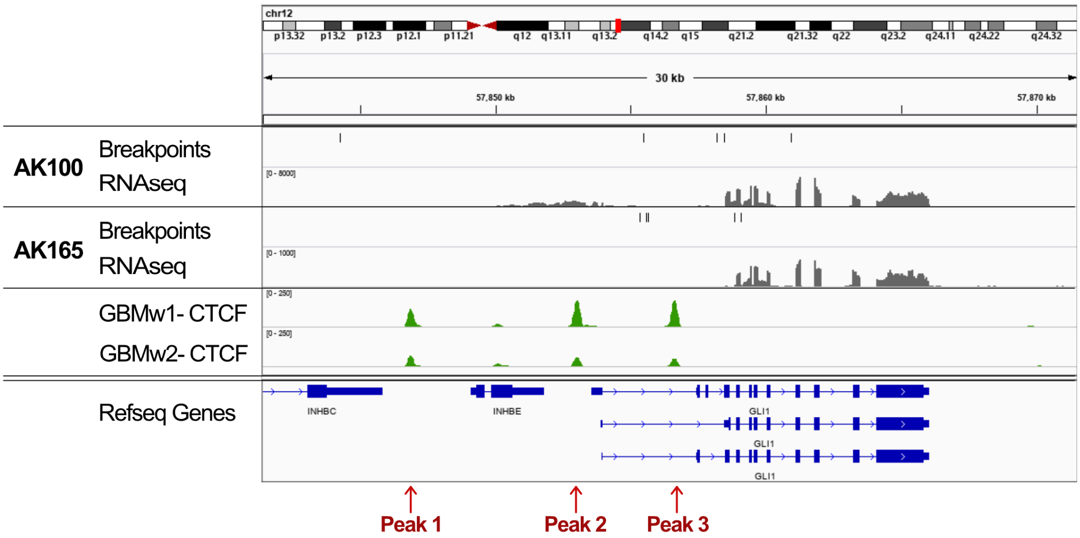

Figure 16: CTCF binding sites locate in proximity of the *GLI1* locus. Genomic view of the *GLI1* locus on chromosome 12 shows annotated RefSeq genes (blue, bottom), CTCF ChIPseq signals for two glioblastoma tumours as identified in Flavahan et al, 2016 [95] (green, middle), RNA-seq and breakpoint tracks of two glioblastoma tumours from the HIPO016 cohort. Red arrows indicate CTCF peaks that were subjected to CRISPR/Cas9 editing for CTCF binding site disruption.

To investigate whether the absence of CTCF binding due to genomic rearrangements affects the interaction of the *GLI1* promoter with regulatory elements, resulting in aberrant gene expression, individual CTCF peaks were disrupted using CRISPR/Cas9 technology in T778 liposarcoma and LN308 glioblastoma cells. The exact location of binding was predicted by CTCFBS core motif search with position weight matrices (PWM), and sgRNA sequences were designed to target the motif with the highest binding prediction score. Single-cell clones could be isolated only for T778 cells with the targeting of peak 2. Sanger sequencing of monoclonal populations revealed two clones (sgCTCF cl.1 and sgCTCF cl.10) with homozygous deletion of three nucleotides (Figure 17 A). The disruption of the CTCF binding site reduced the predicted binding *in silico* (Figure 17 B), and ChIP-qPCR analysis confirmed the absence of CTCF binding at the locus (Figure 17 C). Quantification of mRNA expression levels revealed an upregulation of *GLI1* and its target genes *PTCH1* and *CCND2* in both clones with disrupted CTCF binding. These cells also showed an increase in GLI1 expression on protein levels (Figure 17 E) and a higher proliferative capacity (Figure 17 F), pointing towards a link between this specific CTCF binding site and the regulation of *GLI1*. These data suggest a potential model of how disruption of local TAD boundaries by structural chromosome rearrangements can activate *GLI1* expression and regulate tumour cell function.

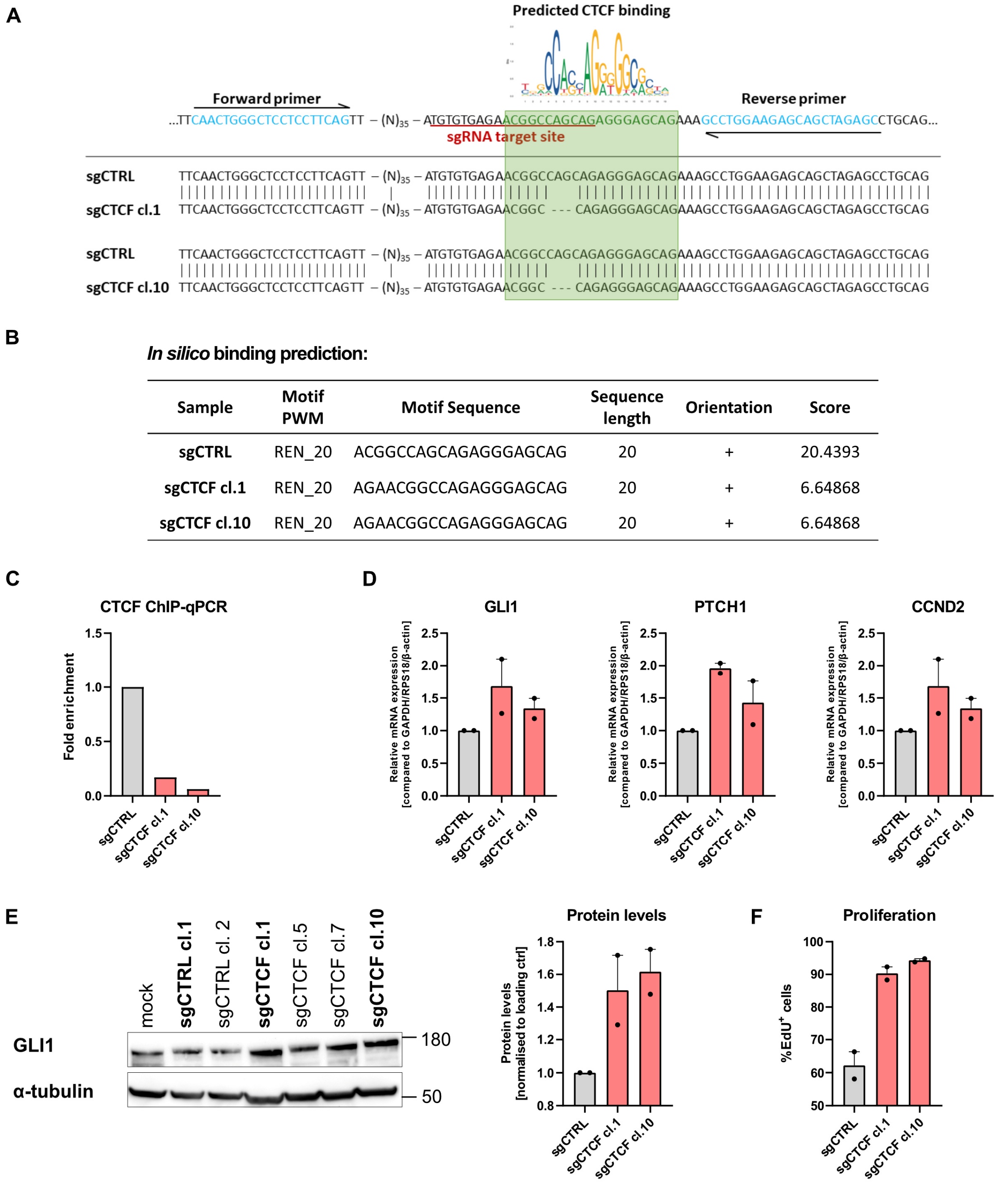

In silico binding prediction:

Sample	Motif PWM	Motif Sequence	Sequence length	Orientation	Score
sgCTRL	REN_20	ACGGCCAGCAGAGGGAGCAG	20	+	20.4393
sgCTCF cl.1	REN_20	AGAACGGCCAGAGGGAGCAG	20	+	6.64868
sgCTCF cl.10	REN_20	AGAACGGCCAGAGGGAGCAG	20	+	6.64868

Figure 17: CRISPR/Cas9 CTCF binding site disruption changes expression levels and cell proliferation. **A** Sanger sequencing and BLAST alignment of T778 sgCTCF cl.1, sgCTCF cl.10, and sgCTRL single-cell clones to verify the disruption of the CTCF binding site. Cl.1 and cl.10 show a deletion of three nucleotides within the predicted CTCF binding site. The scheme on top shows the predicted CTCF binding site (shaded in green), sgCTCF target site (underlined in red), and binding sites of ChIP-qPCR primers (blue). CTCF binding profile is depicted on top of the predicted binding site. The sequence logo was downloaded from the JASPAR database. **B** *In silico* prediction of CTCF binding in T778 sgCTRL, sgCTCF cl.1, and sgCTCF cl.10 cells. CTCF binding was scored using the position weight matrix of the REN_20 motif. **C** Quantification of CTCF binding site occupancy in T778 sgCTRL and sgCTCF cl. 1 and cl. 10 cells as fold enrichment by ChIP-qPCR. One biological replicate. **D** Relative mRNA expression levels of *GLI1*, *PTCH1*, and *CCND2* in T778 sgCTRL and sgCTCF cl.1 and cl.10 cells quantified by RT-qPCR show an upregulation in cells with disrupted CTCF binding site. Two biological replicates. **E** Western Blot analysis of GLI1 expression in T778 sgCTRL and sgCTCF clones. Clones used in RNA expression analyses and cell proliferation assay are depicted in bold. SgCTCF cl.5 and cl.7 represent cell clones with heterozygous editing of the CTCF binding site. Quantification of protein expression of two biological replicates. **F** Quantification of EdU$^+$ cells by Click-iT reaction in T778 sgCTRL and sgCTCF cl. 1 and cl. 10 cells reveals a higher proliferative capacity in sgCTCF cl.1 and cl.10 cells. Two biological replicates.

3.5 *In vitro* phenotypic analysis of GLI1 in glioblastoma and liposarcoma cell models

3.5.1 Characterisation of glioblastoma and liposarcoma cell lines

Deregulation of transcription factors modulates the expression of specific repertoires of target genes, thereby interfering with various cellular processes [223]. To study the phenotypic changes upon GLI1 knockdown and inhibition, glioblastoma and liposarcoma cell lines with *GLI1* copy number gains and high expression were used as model organisms. Copy number states were analysed by DNA FISH staining with BAC probes and DNA methylation-based copy number profiles for some of the cell lines; expression levels were assessed by RT-qPCR. The glioblastoma cell lines LN308 and U3071 (patient-derived) both showed amplification of *GLI1* by DNA FISH. While LN308 cells disclosed homogeneously staining regions for *GLI1*, the signal in U3071 cells was distributed across the cell nuclei indicating the presence of double minute chromosomes or amplified DNA across the genome (Figure 18 A). The amplification was associated with high mRNA expression levels compared to cell lines without *GLI1* amplification (Figure 18 B). The copy number profile of the U3071 cell line showed chromosome 12 amplification with multiple non-contiguous segments, including the genomic loci of *GLI1* and *CDK4* (Supplementary material 4). The LN229 and U3037 (patient-derived) cell lines were used as control glioblastoma cell lines which both were characterised, showing balanced *GLI1* copy number state and low *GLI1* RNA expression. To study the role of GLI1 in sarcoma, the liposarcoma cell lines T449 and T778, established from a primary and recurrent WDLS of the same patient, respectively, were used in the study. These two models further exemplified a potential role of GLI1 in tumour progression as amplification and upregulation of expression was only present in T778 cells (from tumour relapse). Amplicons of the two cell lines showed size variability with *CDK4* amplification in both cell lines, but T778 cells showed additional amplified DNA stretches, including the *GLI1* locus (Supplementary material 4). RNA-sequencing was performed for U3071 and T778 cell lines detecting several fusion transcripts with genes located on chromosome 12q13-15, but *GLI1* fusion transcripts were not detected. The described characteristics reflect the association of high *GLI1* expression associated with gain in copy numbers observed in patients and confirm their suitability as cell models for the study.

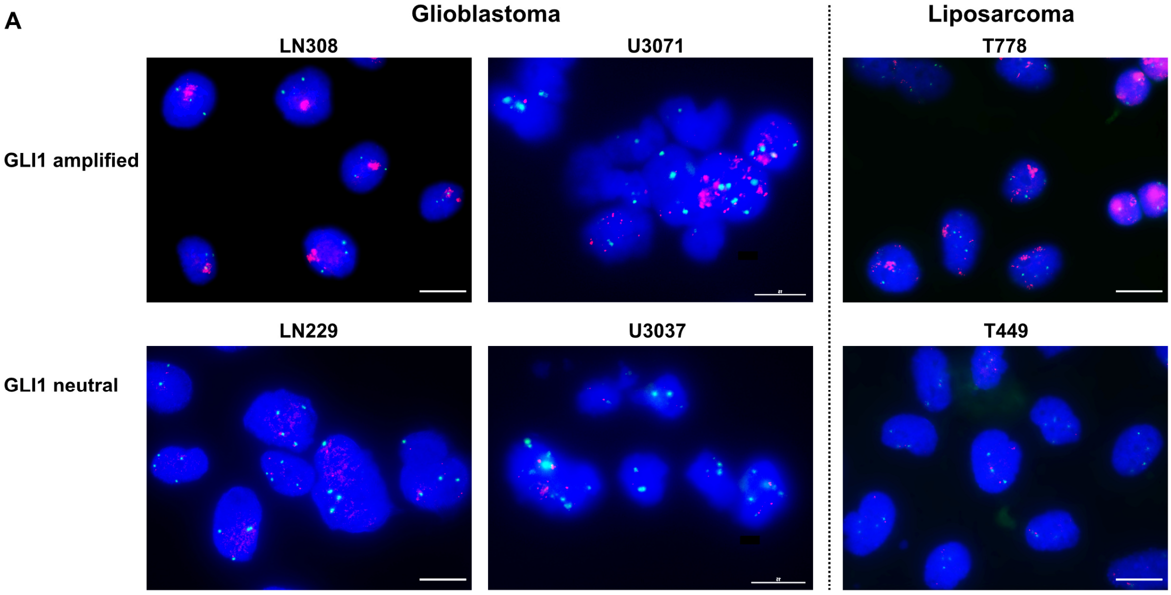

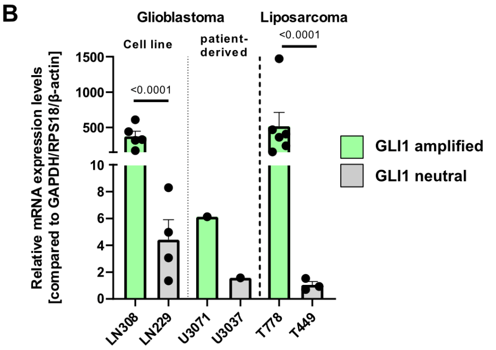

C

Tumour entity	Cell line	GLI1 expression	GLI1 CNA	CDK4 CNA	GLI1 fusion
Glioblastoma	U3071	high	amplified	amplified	negative
	U3037	low	neutral	amplified	negative
	LN308	high	amplified	amplified	na
	LN229	low	neutral	amplified	na
Liposarcoma	T778	high	amplified	amplified	negative
	T449	low	neutral	amplified	negative

Figure 18: Characterisation of glioblastoma and liposarcoma cell lines. A Example images of GLI1 DNA FISH staining of *GLI1*-amplified and *GLI1*-neutral glioblastoma and liposarcoma cell lines. red: *GLI1* locus probe, green: chromosome 12 centromere probe, scale bar 20 µM in images of LN308, LN229, T778, and T449 cell lines; 15 µM in images of U3071 and U3037 cell lines. **B** RT-qPCR analysis of *GLI1* mRNA expression levels in *GLI1*-amplified and *GLI1*-neutral glioblastoma and liposarcoma cell lines (mean ± SEM, p-values are indicated in the graph, unpaired Student's t-test on ΔCT values). **C** Overview of *GLI1*/*CDK4* CNA, *GLI1* expression, and presence of *GLI1* fusion transcripts in cell lines used for this study.

3.5.2 GLI1 knockdown and inhibition affects cell proliferation, anchorage-independent growth, and apoptosis

To assess the phenotypic changes upon GLI1 knockdown or inhibition, functional assays were performed upon shRNA knockdown with three different shRNAs and inhibition with the direct GLI1 inhibitor GlaB in glioblastoma and liposarcoma cell lines. Relative mRNA and protein expression levels were significantly reduced by 75 - 90 % in LN308 and T778 cell lines with all tested shRNAs, a comparable effect was observed in U3071 cells in one experiment (Figure 19 A + B). The effect of GLI1 knockdown on cell proliferation was analysed using the Click-iT technology, measuring cell proliferation by EdU incorporation in newly synthesised DNA. Adherent cell cultures were incubated for 8 h (T778) or 16 h (LN308 and U3071, due to slower cell growth) and the number of EdU^{+} cells was quantified by flow cytometry. As shown in Figure 19 C, GLI1 knockdown significantly inhibited cell proliferation with a stronger effect in glioblastoma cells compared to liposarcoma cells.

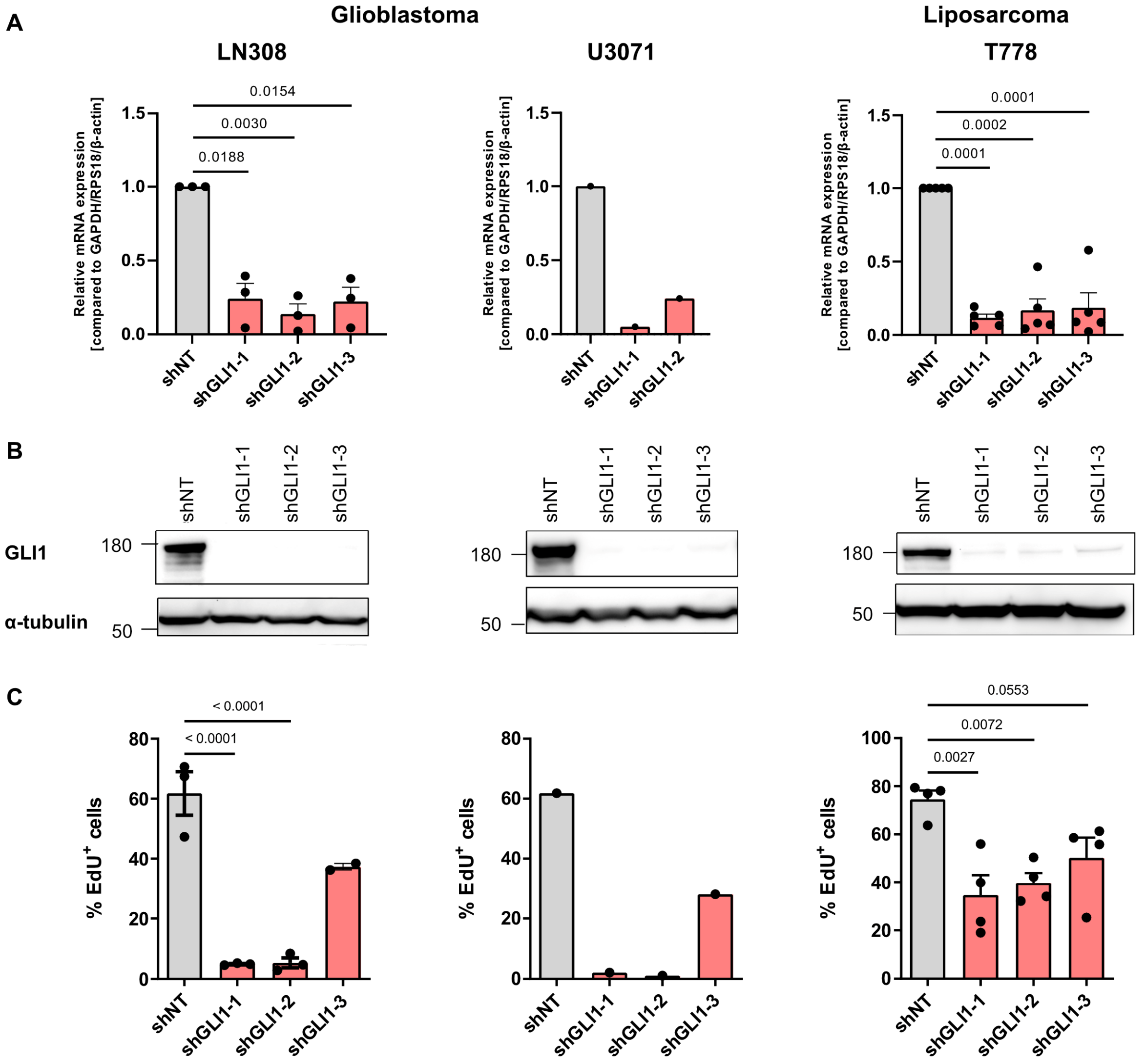

Figure 19: ShRNA knockdown of GLI1 decreases cell proliferation in glioblastoma and liposarcoma cell lines. A Relative *GLI1* mRNA expression levels in LN308 (left), U3071 (middle), and T778 (right) cell lines upon shRNA-mediated knockdown show a downregulation on RNA level between 70 - 90% (mean ± SEM, p-values are indicated in the graphs, one-way ANOVA with Dunnett's test for multiple comparisons of groups, one biological replicate experiment in U3071 cells). **B** Protein expression levels of GLI1 upon shRNA knockdown in LN308 (left), U3071 (middle), and T778 (right) cell lines. **C** Click-iT EdU incorporation assay in LN308 (left), U3071 (middle), and T778 (right) cell lines after depletion of GLI1 shows a decrease in proliferating (EdU$^+$) cells in shGLI1 cells compared to shNT control cells (mean ± SEM, p-values are indicated in the graphs, one-way ANOVA with Dunnett's test for multiple comparisons of groups, one biological replicate experiment in U3071 cells).

GlaB is a small-molecule inhibitor derived from the seeds of *Derris glabrescens* (*Leguminosae*) that has been shown to directly bind to GLI1, preventing its interaction with DNA [147]. In contrast to other GLI1 inhibitors, such as GANT61 and ATO, GlaB has proven promising potency in bioavailability and blood-brain barrier permeability in preclinical models of Hedgehog-dependent medulloblastoma and basal cell carcinoma [147, 148]. GlaB inhibitor was produced and provided by the group of Prof Bruno Botta, La Sapienza University in Rome, Italy. Glioblastoma and liposarcoma cells were treated with different concentrations of inhibitors, and total cell numbers were quantified after 24 h, 48 h, and 72 h to measure the growth rate of viable cells. GlaB significantly inhibited proliferation in a dose-dependent effect (Figure 20 A + B). After 72 h treatment with 250 nM GlaB, total cell numbers were reduced by 50 % and 44 % in LN308 and T778 cells, respectively. A GlaB concentration of 1000 nM decreased cell proliferation up to 83 % (LN308) and 78 % (T778). In addition, early and late apoptotic cells were quantified by Annexin V and 7-AAD staining after 72 h treatment with GlaB. A dose-dependent increase was observed in the percentage of early and late apoptotic cells in LN308, suggesting a pro-apoptotic role for GlaB at concentrations above 250 nM (Figure 20 C + D). The impact of GlaB on anchorage-independent growth and long-term survival was evaluated using the soft agar colony formation assay. This assay mimics the cellular environment seen in *vivo* and estimates the ability of tumour cells to survive and proliferate in a semi-solid matrix, both required for tumour growth and metastasis. LN308 cells were treated for 14 d with GlaB or JK184, an HH pathway inhibitor repressing GLI1-dependent transcriptional activity, and colony formation rate was examined using a CellTiter-Glo® 3D Assay. Anchorage-independent growth was hampered by inhibition with both GlaB and JK184. Cell colonies were detectable at the lowest concentrations, but only single cells remained in the matrix when treated with higher drug concentrations. The decrease in colony formation is unlikely to be a direct consequence of the onset of cell apoptosis. A concentration of 250 nM GlaB resulted in 95 % inhibition of colony formation but only a small increase in early and late apoptotic cell numbers. These data indicate that the long-term inhibitory effects of GlaB on anchorage-independent growth do not correlate with the extent of apoptosis up to 72 h after treatment.

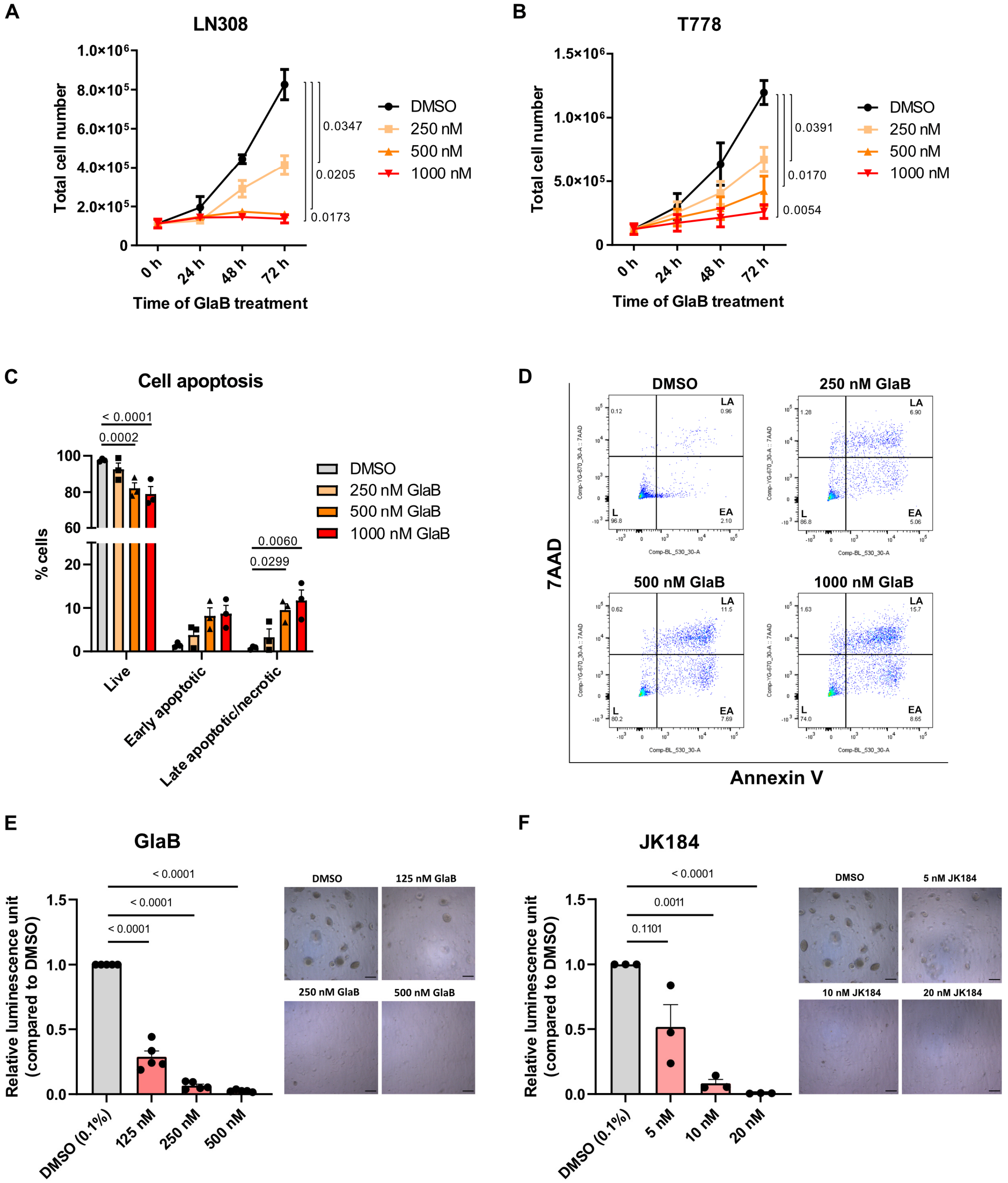

Figure 20: GLI1 inhibition impairs cell proliferation and anchorage-independent growth and induces apoptosis. A+B Trypan blue count was performed at the indicated times to measure total cell numbers and determine the growth rate of viable cells. Reduction in total cell numbers was observed upon treatment with different concentrations of GlaB inhibitor in LN308 (**A**) and T778 (**B**) cells (mean ± SEM, p-values are indicated in the graphs and represent significance at 72 h timepoint, two-way ANOVA followed by Dunnett's test for multiple comparisons of groups). **C** Quantitative distribution of LN308 cells as live, early apoptotic, and late apoptotic/necrotic cells after treatment with different concentrations of GlaB inhibitor (mean ± SEM, significant p-values are indicated in the graph, two-way ANOVA followed by Dunnett's test for multiple comparisons of groups). **D** Images of representative dot plots of apoptotic fractions in LN308 cells (L, live; EA, early apoptotic; LA, late apoptotic/necrotic). Apoptotic fractions were analysed by FITC-Annexin V and 7-AAD staining after 72 h treatment with GlaB at the indicated concentrations. **E+F** Anchorage-independent growth is reduced upon treatment with GlaB (**E**) and JK184 (**F**) inhibitors in LN308 cells. Example images are illustrated for each condition, scale bar 50 µM (mean ± SEM, p-values are indicated in the graphs, one-sample t-test).

3.5.3 RNA sequencing reveals downregulation of DNA repair pathways upon GLI1 knockdown

To gain mechanistic insights into the role of GLI1 in glioblastoma and liposarcoma cells, total RNA sequencing was performed upon GLI1 shRNA knockdown in T778 and U3071 cells. RNA sequencing analysis was done by Dr Michael Fletcher, a postdoc in the division of Molecular Genetics. Differentially expressed genes with logFC < -1.5 or logFC > 1.5 were identified in GLI1 knockdown groups compared to control groups for both cell lines (Figure 21 A). A total of 1007 and 295 genes were downregulated in T778 and U3071 cells, respectively, while 1057 and 214 genes, respectively, were upregulated. Comparing differentially expressed genes amongst both cell lines revealed an overlap of 57 commonly downregulated and 36 upregulated genes. This analysis suggests that both tumour entities share common transcriptional regulation upon GLI1 depletion but still show large tumour type-specific regulation. In Figure 21 B, the top 25 commonly down- and upregulated genes in both cell lines are listed. A full list of all commonly down- and upregulated genes upon GLI1 knockdown in glioblastoma and liposarcoma are provided in Supplementary material 5 and Supplementary material 6, respectively. *GLI1* itself and known GLI1 target genes such as *SOSTDC1* were found amongst the commonly downregulated genes [214]. The link between GLI1 and TGF-β signalling described in the literature could also be observed as *TGF-β* was upregulated in both cell lines [224-226].

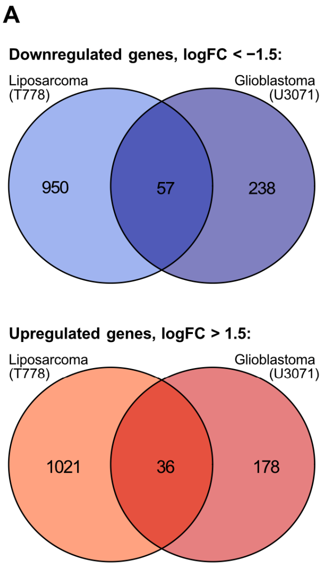

B

Downregulated genes:

Gene	Ensembl ID	logFC U3071	logFC T778
LITAF	ENSG00000189067	-3.2113	-4.3241
PTPRJ	ENSG00000149177	-2.8904	-2.6726
PCDHGC3	ENSG00000240184	-2.8733	-2.8243
RP11-93B14.5	ENSG00000232803	-2.8010	-2.5053
SLCO4A1	ENSG00000101187	-2.7168	-4.3309
SOSTDC1	ENSG00000171243	-2.6968	-5.1305
GLI1	ENSG00000111087	-2.6812	-6.0372
RP11-332K15.1	ENSG00000232524	-2.5435	-4.7631
GLTP	ENSG00000139433	-2.5330	-2.2164
KRT17	ENSG00000128422	-2.3731	-1.5081
IMPA2	ENSG00000141401	-2.3414	-2.3257
RASSF3	ENSG00000153179	-2.3397	-2.1777
HEXB	ENSG00000049860	-2.2780	-2.5300
RGS16	ENSG00000143333	-2.2662	-1.9730
RTN4R	ENSG00000040608	-2.2564	-1.5041
TMED10	ENSG00000170348	-2.1928	-1.5936
RAB21	ENSG00000080371	-2.1787	-2.1431
SLC39A6	ENSG00000141424	-2.1469	-1.6867
ERBB3	ENSG00000065361	-2.1190	-2.6365
HCN2	ENSG00000099822	-1.9783	-1.5472
CMTM4	ENSG00000183723	-1.9719	-2.3310
TUBG1	ENSG00000131462	-1.9459	-2.4097
LINC00639	ENSG00000259070	-1.9333	-1.9944
PAQR6	ENSG00000160781	-1.9084	-2.5540
SNORD66	ENSG00000212158	-1.8991	-1.9033

Upregulated genes:

Gene	Ensembl ID	logFC U3071	logFC T778
GUCY1A3	ENSG00000164116	3.1200	2.4338
MMP13	ENSG00000137745	2.5398	2.6802
RNU6-1098P	ENSG00000252581	2.5199	1.8205
RGS1	ENSG00000090104	2.4649	4.5150
SLC20A1	ENSG00000144136	2.2823	2.2277
ARPC3	ENSG00000111229	2.2410	2.0162
AC112721.2	ENSG00000222032	2.1826	4.7911
MMP1	ENSG00000196611	2.1124	1.9686
CMKLR1	ENSG00000174600	2.0339	5.5522
PLXNA4	ENSG00000221866	2.0210	2.2593
DDO	ENSG00000203797	1.9345	2.3682
RP11-399D6.2	ENSG00000234840	1.9148	4.2721
ACPP	ENSG00000014257	1.9065	1.8148
RP11-620J15.1	ENSG00000257953	1.8954	4.1122
LINC00702	ENSG00000233117	1.8943	2.7294
RP11-675F6.3	ENSG00000253361	1.8495	4.0041
AC005083.1	ENSG00000233834	1.8416	1.9776
SERPINE1	ENSG00000106366	1.8210	1.7370
SYT12	ENSG00000173227	1.7991	2.8512
AC112721.1	ENSG00000222022	1.7967	4.4926
TGFB1	ENSG00000105329	1.7914	1.6385
FABP4	ENSG00000170323	1.7823	2.9200
IL1RAP	ENSG00000196083	1.7715	1.7103
CTC-487M23.7	ENSG00000272389	1.7146	3.0531
Y_RNA	ENSG00000272110	1.7106	1.5688

Figure 21: Differentially expressed genes in glioblastoma and liposarcoma cell lines. A Venn diagrams depicting unique and shared downregulated (top) and upregulated genes (bottom) among liposarcoma T778 and glioblastoma U3071 cell lines, upon GLI1 shRNA knockdown. Downregulated: Genes with logFC < -1.5; upregulated: genes with logFC > 1.5. **B** Top 25 common downregulated (left) and upregulated (right) genes in T778 and U3071 cell lines. Genes are ranked based on logFC of shGLI1 vs. shNT in U3071 cells.

Gene ontology and KEGG pathway enrichment analysis were performed for differentially expressed genes identifying downregulated (Table 26) and upregulated pathways (Table 27) in liposarcoma and glioblastoma cell lines. Several pathways involved in glycan biosynthesis and glycosylation were upregulated in GLI1-deficient glioblastoma and liposarcoma cells, while otherwise, several DNA repair pathways, including homologous recombination, mismatch repair, nucleotide-excision repair, base excision repair, and DNA replication, were downregulated upon GLI1 knockdown.

Table 26: KEGG pathway analysis of differentially expressed genes identifies common DNA repair pathways downregulated in liposarcoma and glioblastoma cell lines. Lists of top 20 downregulated pathways upon GLI1 knockdown in liposarcoma (left) and glioblastoma (right). ES, enrichment score; NES, normalised enrichment score.

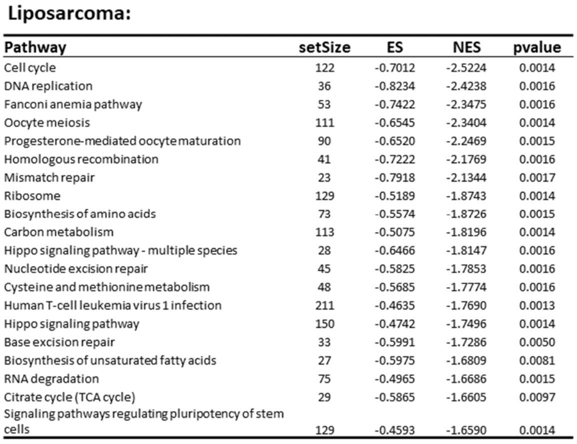

Liposarcoma:

Pathway	setSize	ES	NES	pvalue
Cell cycle	122	-0.7012	-2.5224	0.0014
DNA replication	36	-0.8234	-2.4238	0.0016
Fanconi anemia pathway	53	-0.7422	-2.3475	0.0016
Oocyte meiosis	111	-0.6545	-2.3404	0.0014
Progesterone-mediated oocyte maturation	90	-0.6520	-2.2469	0.0015
Homologous recombination	41	-0.7222	-2.1769	0.0016
Mismatch repair	23	-0.7918	-2.1344	0.0017
Ribosome	129	-0.5189	-1.8743	0.0014
Biosynthesis of amino acids	73	-0.5574	-1.8726	0.0015
Carbon metabolism	113	-0.5075	-1.8196	0.0014
Hippo signaling pathway - multiple species	28	-0.6466	-1.8147	0.0016
Nucleotide excision repair	45	-0.5825	-1.7853	0.0016
Cysteine and methionine metabolism	48	-0.5685	-1.7774	0.0016
Human T-cell leukemia virus 1 infection	211	-0.4635	-1.7690	0.0013
Hippo signaling pathway	150	-0.4742	-1.7496	0.0014
Base excision repair	33	-0.5991	-1.7286	0.0050
Biosynthesis of unsaturated fatty acids	27	-0.5975	-1.6809	0.0081
RNA degradation	75	-0.4965	-1.6686	0.0015
Citrate cycle (TCA cycle)	29	-0.5865	-1.6605	0.0097
Signaling pathways regulating pluripotency of stem cells	129	-0.4593	-1.6590	0.0014

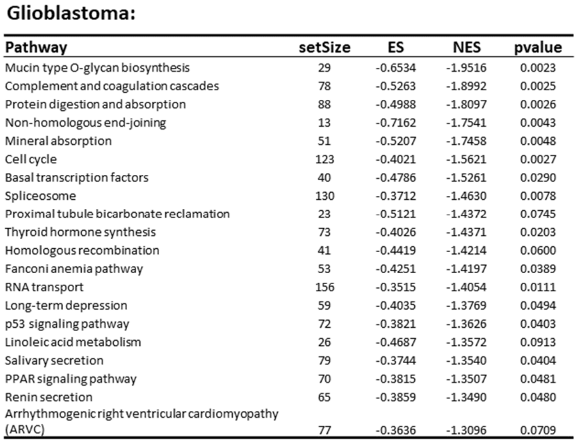

Glioblastoma:

Pathway	setSize	ES	NES	pvalue
Mucin type O-glycan biosynthesis	29	-0.6534	-1.9516	0.0023
Complement and coagulation cascades	78	-0.5263	-1.8992	0.0025
Protein digestion and absorption	88	-0.4988	-1.8097	0.0026
Non-homologous end-joining	13	-0.7162	-1.7541	0.0043
Mineral absorption	51	-0.5207	-1.7458	0.0048
Cell cycle	123	-0.4021	-1.5621	0.0027
Basal transcription factors	40	-0.4786	-1.5261	0.0290
Spliceosome	130	-0.3712	-1.4630	0.0078
Proximal tubule bicarbonate reclamation	23	-0.5121	-1.4372	0.0745
Thyroid hormone synthesis	73	-0.4026	-1.4371	0.0203
Homologous recombination	41	-0.4419	-1.4214	0.0600
Fanconi anemia pathway	53	-0.4251	-1.4197	0.0389
RNA transport	156	-0.3515	-1.4054	0.0111
Long-term depression	59	-0.4035	-1.3769	0.0494
p53 signaling pathway	72	-0.3821	-1.3626	0.0403
Linoleic acid metabolism	26	-0.4687	-1.3572	0.0913
Salivary secretion	79	-0.3744	-1.3540	0.0404
PPAR signaling pathway	70	-0.3815	-1.3507	0.0481
Renin secretion	65	-0.3859	-1.3490	0.0480
Arrhythmogenic right ventricular cardiomyopathy (ARVC)	77	-0.3636	-1.3096	0.0709

Table 27: KEGG pathway analysis of differentially expressed genes identifies common metabolic pathways upregulated in liposarcoma and glioblastoma cell lines. Lists of top 20 upregulated pathways upon GLI1 knockdown in liposarcoma (left) and glioblastoma (right). ES, enrichment score; NES, normalized enrichment score.

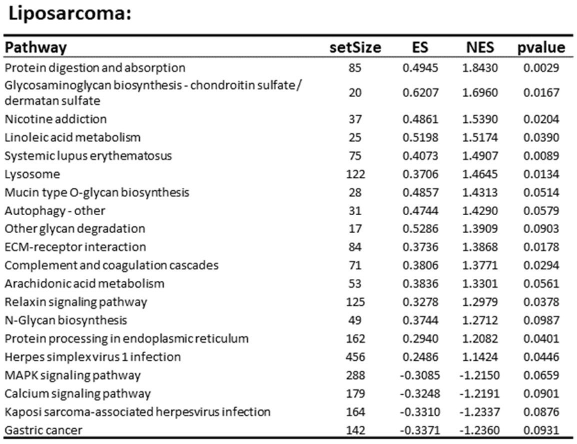

Liposarcoma:

Pathway	setSize	ES	NES	pvalue
Protein digestion and absorption	85	0.4945	1.8430	0.0029
Glycosaminoglycan biosynthesis - chondroitin sulfate / dermatan sulfate	20	0.6207	1.6960	0.0167
Nicotine addiction	37	0.4861	1.5390	0.0204
Linoleic acid metabolism	25	0.5198	1.5174	0.0390
Systemic lupus erythematosus	75	0.4073	1.4907	0.0089
Lysosome	122	0.3706	1.4645	0.0134
Mucin type O-glycan biosynthesis	28	0.4857	1.4313	0.0514
Autophagy - other	31	0.4744	1.4290	0.0579
Other glycan degradation	17	0.5286	1.3909	0.0903
ECM-receptor interaction	84	0.3736	1.3868	0.0178
Complement and coagulation cascades	71	0.3806	1.3771	0.0294
Arachidonic acid metabolism	53	0.3836	1.3301	0.0561
Relaxin signaling pathway	125	0.3278	1.2979	0.0378
N-Glycan biosynthesis	49	0.3744	1.2712	0.0987
Protein processing in endoplasmic reticulum	162	0.2940	1.2082	0.0401
Herpes simplex virus 1 infection	456	0.2486	1.1424	0.0446
MAPK signaling pathway	288	-0.3085	-1.2150	0.0659
Calcium signaling pathway	179	-0.3248	-1.2191	0.0901
Kaposi sarcoma-associated herpesvirus infection	164	-0.3310	-1.2337	0.0876
Gastric cancer	142	-0.3371	-1.2360	0.0931

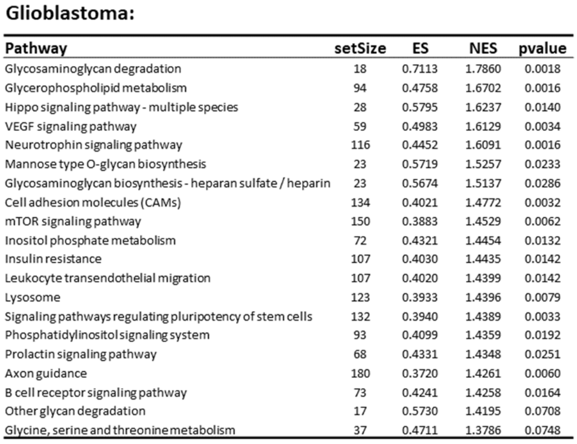

Glioblastoma:

Pathway	setSize	ES	NES	pvalue
Glycosaminoglycan degradation	18	0.7113	1.7860	0.0018
Glycerophospholipid metabolism	94	0.4758	1.6702	0.0016
Hippo signaling pathway - multiple species	28	0.5795	1.6237	0.0140
VEGF signaling pathway	59	0.4983	1.6129	0.0034
Neurotrophin signaling pathway	116	0.4452	1.6091	0.0016
Mannose type O-glycan biosynthesis	23	0.5719	1.5257	0.0233
Glycosaminoglycan biosynthesis - heparan sulfate / heparin	23	0.5674	1.5137	0.0286
Cell adhesion molecules (CAMs)	134	0.4021	1.4772	0.0032
mTOR signaling pathway	150	0.3883	1.4529	0.0062
Inositol phosphate metabolism	72	0.4321	1.4454	0.0132
Insulin resistance	107	0.4030	1.4435	0.0142
Leukocyte transendothelial migration	107	0.4020	1.4399	0.0142
Lysosome	123	0.3933	1.4396	0.0079
Signaling pathways regulating pluripotency of stem cells	132	0.3940	1.4389	0.0033
Phosphatidylinositol signaling system	93	0.4099	1.4359	0.0192
Prolactin signaling pathway	68	0.4331	1.4348	0.0251
Axon guidance	180	0.3720	1.4261	0.0060
B cell receptor signaling pathway	73	0.4241	1.4258	0.0164
Other glycan degradation	17	0.5730	1.4195	0.0708
Glycine, serine and threonine metabolism	37	0.4711	1.3786	0.0748

3.5.4 GLI1 inhibition causes DNA repair deficiency upon irradiation-induced DNA damage

Defects in DNA repair efficiency upon GLI1 depletion were verified by γH2AX immunofluorescence staining. The image acquisition was performed at the Metafer system available in the group of Prof Peter Schmezer under supervision by Dr Ali Bakr (DKFZ, Heidelberg). The number of γH2AX foci per cell is a direct biomarker for the actual double-stranded breaks (DSBs) within the cells. When DNA is damaged and forms DSBs, γH2AX is phosphorylated and thus recruits and localises DNA repair proteins to the site of damage for efficient and rapid DNA repair. The amount of DNA damage in LN308 and T778 cells was analysed under GlaB inhibitor treatment at baseline and upon DNA damage induction. DNA damage was induced by ionising irradiation with 2 Gy and quantified 1 h post-irradiation. DNA repair efficiency in control and treatment groups was evaluated after 24 h. A sample without irradiation was analysed to assess DNA damage at baseline. Extensive DNA damage was observed 1 h after irradiation in control and treatment groups, a control to confirm the activation of DNA repair response in all samples. 24 h post DNA damage induction, the number of γH2AX signals per cell and the proportion of cells with > 10 foci was significantly higher in GlaB treated vs. untreated LN308 cells (Figure 22 A - C). Similar effects were also observed in T778 cells in two experiments (Figure 22 D + E). Independent, γH2AX IF staining of cells with GLI1 shRNA knockdown corroborated these results (one replicate, data not shown). These data confirm that GLI1 inhibition results in defects in DNA repair response, as expected based on the downregulation of DNA repair pathways identified in RNA sequencing analyses.

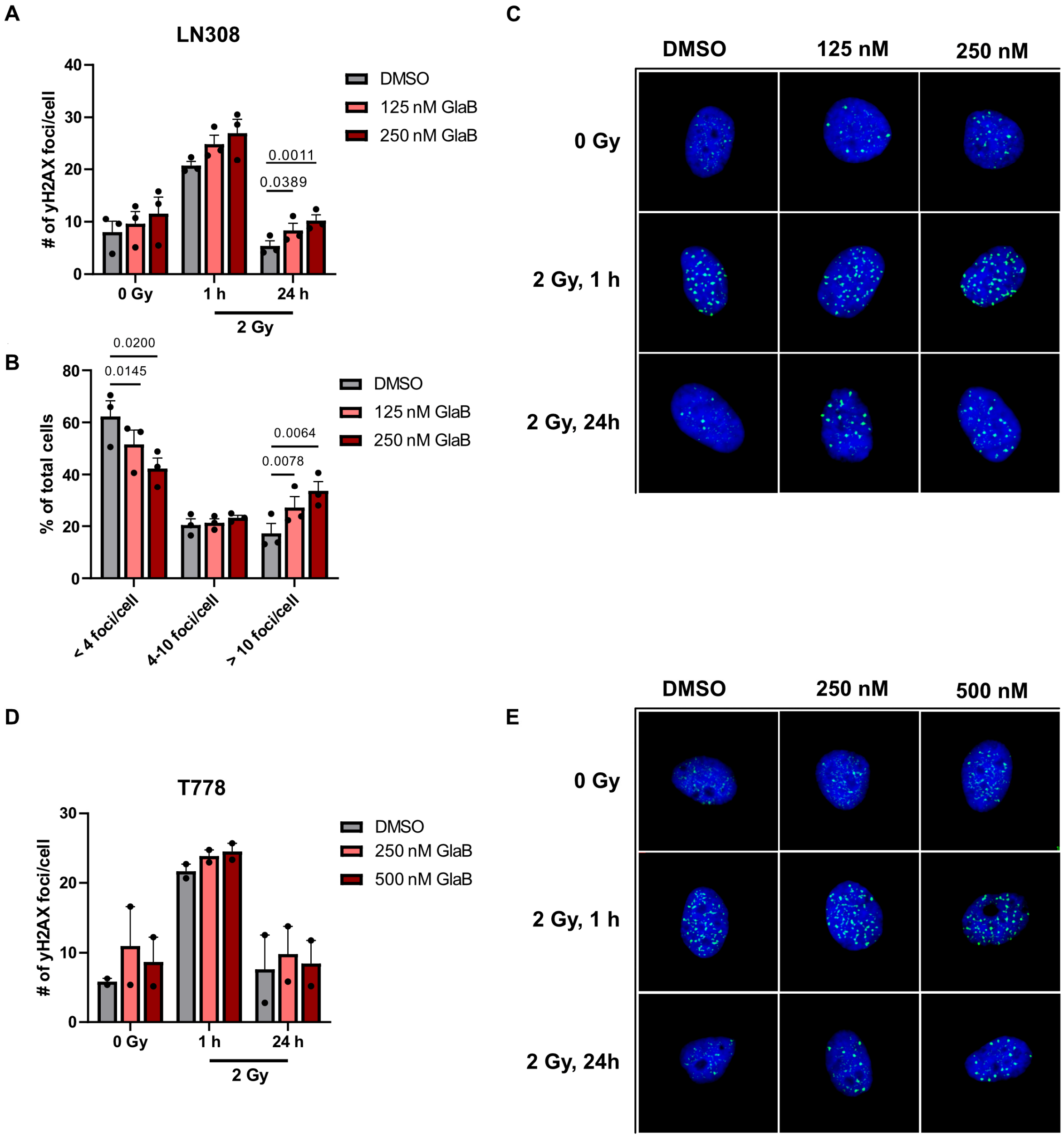

Figure 22: GLI1 inhibition impairs DNA repair efficiency. A Quantification of DNA damage induction and repair in LN308 cells upon treatment with GlaB inhibitor. DNA damage was induced by ionising radiation with 2 Gy and analysed 1 h and 24 h post-irradiation by γH2AX immunofluorescence staining. Baseline DNA damage was quantified in cells without exposure to irradiation. The number of γH2AX foci per cell was quantified in 500 cells per condition and experiment, and the mean was calculated for each biological replicate (mean ± SEM, significant p-values are indicated in the graphs, two-way ANOVA followed by Dunnett's test for multiple comparisons of groups). **B** Percentage of LN308 cells with < 4 foci/cell, 4 - 10 foci/cell, and > 10 foci/cell in control and treatment groups (mean ± SEM, significant p-values are indicated in the graphs, two-way ANOVA followed by Dunnett's test for multiple comparisons of groups). **C** Representative images of γH2AX staining in control DMSO, 125 nM, and 250 nM GlaB treated LN308 cells quantified in (A). **D** Quantification of DNA damage induction and repair efficiency in T778 cells upon treatment with GlaB inhibitor. The number of γH2AX foci per cell was quantified in 500 cells per condition per experiment, and the mean of two biological replicates was calculated. **E** Representative images of γH2AX staining in control DMSO, 125 nM, and 250 nM GlaB treated T778 cells quantified in (D).

3.6 Preclinical combination screening of GLI1 and DNA repair inhibitors

3.6.1 Screen setup

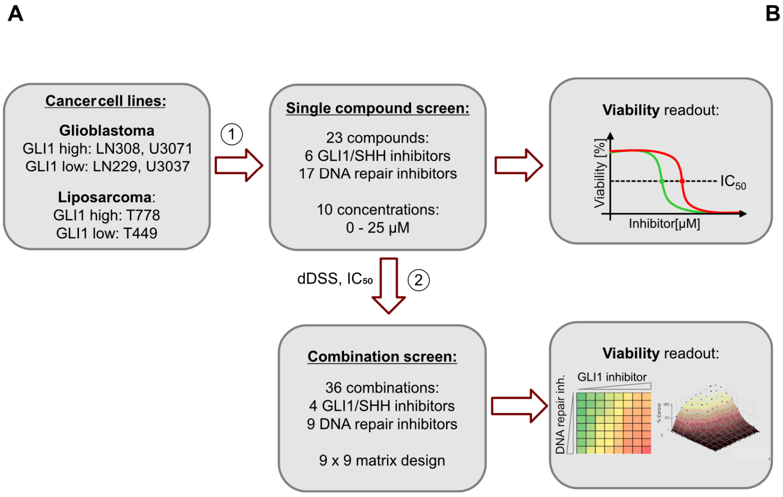

B

	Inhibitor class		Compound
GLI1/SHH inhibitors	GLI1 inhibitors		GANT58
			GANT61
			ATO
			GlaB
	SHH inhibitors		JK184
			BMS-833923
DNA repair inhibitors	Base excision repair	PARP inhibitor	Pamiparib
			Olaparib
			Veliparib
		APE1 inhibitor	Methoxyamine
	NHEJ repair	DNA-PKcs	CC-115
			Nedisertib
	HR repair	ATR inhibitor	AZD6738
			Berzosertib
	Checkpoint inhibitors	ATM inhibitor	AZD0156
		CHK1 inhibitors	GDC-0575
			MK-8776
			LY2606368
		WEE1 inhibitors	MK-1775
	Topoisomerase inhibitors	Topo I inhibitors	Belotecan
			Irinotecan
		Topo II inhibitors	Doxorubicin
			Etoposide

Figure 23: Screen setup of GLI1 and DNA repair inhibitors. A Schematic representation of the screening procedure. The screen was split into a primary and secondary screen. In the primary screen, compounds were tested individually to identify effective and selective drugs based on IC_{50} values and dDSS scores. The most promising candidates were tested afterwards in combination in the subsequent secondary screen. **B** List of inhibitors used in the primary screen grouped by their pathway and molecule targets.

DNA damage response defects promote tumorigenesis and provide therapeutic opportunities to eradicate cancer cells without affecting healthy cells [227]. The combination of chemotherapeutics potentiates the efficacy compared to a single agent therapy approach and decreases the chances of drug resistance. To explore whether patients with aberrant high GLI1 expression can benefit from a combined therapy of GLI1 and DNA repair inhibitors, a preclinical drug combination screen was performed in glioblastoma and liposarcoma cell lines (Figure 23). The drug screen was performed in collaboration with David Pauck and Dr Jasmin Bartl of the Paediatric Neuro-Oncogenomics group of Prof Dr Marc Remke at the university clinics in Düsseldorf and Heinrich-Heine-University Düsseldorf. The screen was divided into two parts (Figure 23 A). In the primary screen, GLI1/SHH inhibitors and DNA repair inhibitors were screened as single agents for their sensitivity and selectivity in glioblastoma cell lines U3071, LN308 (both $GLI1^{high}$) and LN229, U3037 (both $GLI1^{low}$), and liposarcoma cell lines T778 ($GLI1^{high}$) and T449 ($GLI1^{low}$). The following criteria for the selection of screening compounds were considered: gene expression analyses of RNA sequencing data identifying DNA repair pathways deregulated upon GLI1 depletion, (pre)clinical status of these compounds, and the potency of blood-brain-barrier penetrance. As such, compounds targeting Topoisomerase I and II, ATM, ATR, WEE1, CHK1, DNA-PKcs, APE1, and PARP proteins were included in the screening (see Figure 23 B for the complete list of inhibitors) and tested in 10 concentrations in the range of 5 to 25,000 nM. Compounds were ranked by their respective IC_{50} values (half-maximum inhibitory concentration) and their selective response for cell lines with high GLI1 expression was calculated using a published differential drug sensitivity score (dDSS) [201]. According to the individual sensitivity and selectivity of the drugs, the best performing candidates of

GLI1 and DNA repair inhibitors were used in the secondary screen and tested in combination in a 9 x 9 matrix design to evaluate drug combination effects. Cell seeding densities were optimised to improve screening stability and ensure exponential cell growth throughout the experiment. In both screenings, cell lines were expanded and grown in Heidelberg and transported to Düsseldorf where drug assay plates were prepared and cells seeded. Cell viability readouts after 72 h incubation were recorded by David Pauck, and drug response analyses were generated with a pipeline established by Dr Nan Qin, a postdoc in the group of Prof Dr Marc Remke.

3.6.2 Primary drug screen identifies drugs with high sensitivity and selectivity as single agents

The primary screen aimed to identify drugs with high sensitivity and selectivity in cell lines with high GLI1 expression compared to control cells with low GLI1 expression. Drug responses were assessed by cell viability based on metabolic activity. The effects on the inhibition of metabolic activity are represented in Figure 24 A + B for LN308 and T778, respectively. Among the tested GLI1/SHH inhibitors, JK184 and GlaB had the highest sensitivity in glioblastoma and liposarcoma cell lines with IC_{50} values of around 20 nM for JK184, and around 500 nM for GlaB (Figure 24 C + D). No response in the tested range of concentration was observed for the GLI1 inhibitor GANT58 in all cell lines. The effects towards BMS-833923, a Smoothened antagonist, were comparably low in all cell lines, confirming the assumption that GLI1 activation in $GLI1^{high}$ cell lines is independent of the canonical SHH pathway and inhibition of SMO has similar effects in all cell lines (Supplementary material 7). LN308 and T778 cells were susceptible to checkpoint inhibitors targeting CHK1, the ATR inhibitor Berzosertib, and the Topoisomerase II inhibitor Belotecan. Dose-response curves for all compounds and cell lines are illustrated in Supplementary material 7. Data from patient-derived glioblastoma cell lines U3071 and U3037 had to be excluded from further analysis as they showed little sensitivity to only a subset of compounds. This was likely due to technical problems caused by the laminin coating required for the monolayer culture of the cells. Therefore, the U3071 and U3037 cell lines were not used for the secondary drug screen and subsequent experiments.

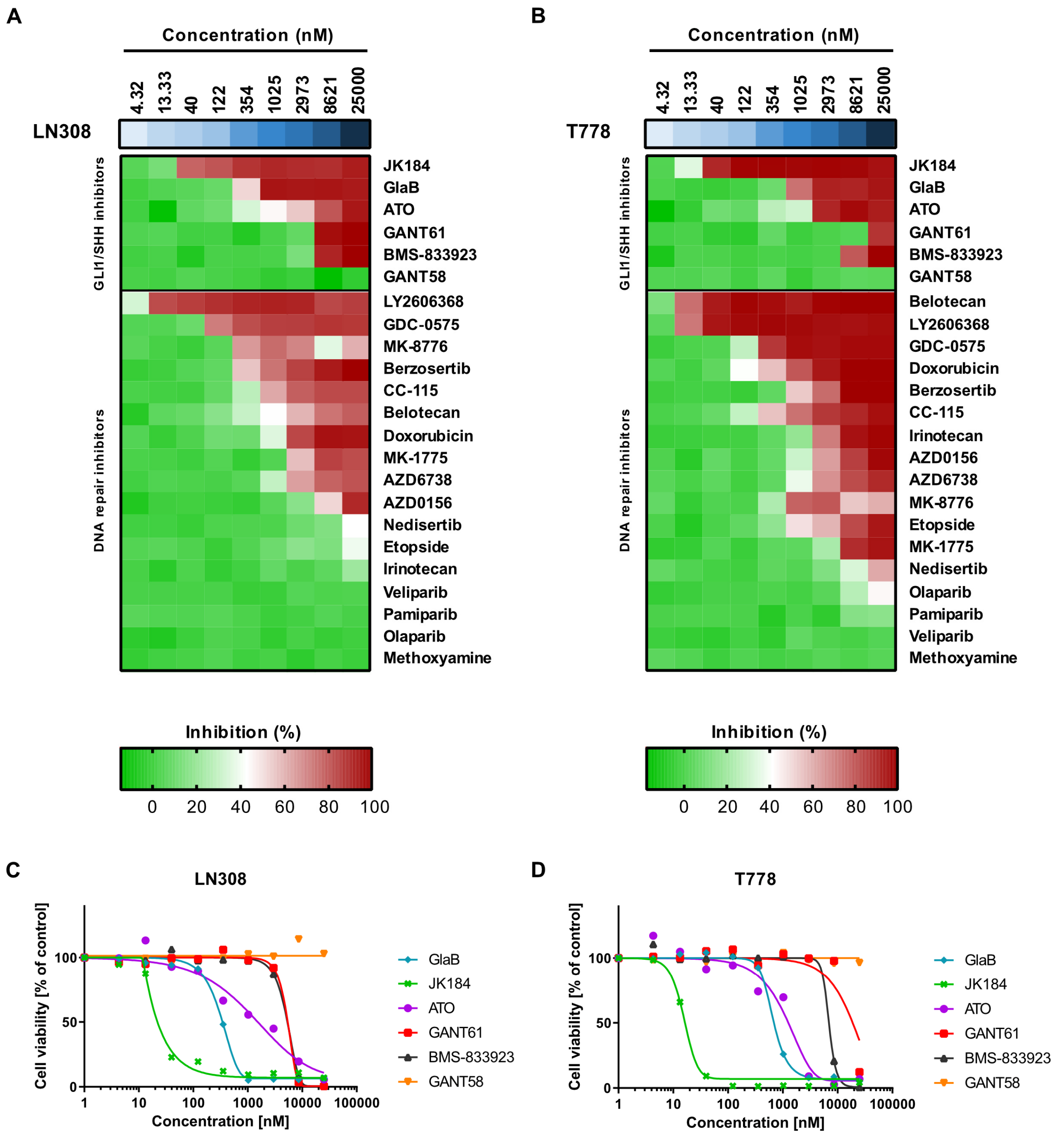

Figure 24: Inhibitor dose responses in cell lines with high GLI1 expression. A Heat map representing dose responses of GLI1/SHH and DNA repair inhibitors in LN308 glioblastoma cells measured as percentage inhibition of the metabolic activity. **B** Heat map representing the dose responses of GLI1/SHH and DNA repair inhibitors in T778 liposarcoma cells measured as percentage inhibition of the metabolic activity. **C** Dose-response curves of GLI1/SHH inhibitors in LN308 glioblastoma cells. **D** Dose-response curves of GLI1/SHH inhibitors in T778 liposarcoma cells.

To compare drug response patterns between GLI1^{high} and GLI1^{low} cells, drug selectivity was assessed by calculating a differential drug sensitivity score (dDSS) according to a published algorithm [201]. In this approach, dose-response parameters, including IC_{50} value, the slope at the calculated IC_{50} concentration, and minimum and maximum response (R_{min} and R_{max}) are estimated through logistic functions and used as input to calculate a DSS score for each compound and cell line. The dDSS scores were computed as the difference of DSS GLI1^{high} and DSS GLI1^{low} cells, permitting the identification of drugs with a positive dDSS as selective for cells with high GLI1 expression (Figure 25 A). Using this approach, selective drugs were identified for LN308 and T778 cells (Figure 25 B + C, respectively). As expected, GLI1/SHH inhibitors were highly selective, with the highest selectivity observed for JK184 and GlaB in both tumour entities (Figure 25 D + E). In addition, checkpoint inhibitors GDC-0575 and LY2606368 targeting CHK1 and MK1775 targeting WEE1 as well as ATR inhibitor Berzosertib showed high selectivity in LN308 cells. While unselective in glioblastoma, topoisomerase inhibitors were selective in liposarcoma T778 cells with the highest scores for Belotecan and Doxorubicin. Similar to glioblastoma, checkpoint inhibitors targeting CHK1 and ATR inhibitor Berzosertib showed a high selectivity in liposarcoma.

Stringent thresholds were applied to identify potent compounds in the primary screen and to select drugs for the secondary combination screen. The classification of a compound as a potent drug in its use as a single agent required a positive dDSS in both tumour entities and/or an IC_{50} value < 2000 nM. These criteria identified four GLI1 inhibitors (JK184, GlaB, GANT61, and ATO) and nine DNA repair inhibitors (CC-115, AZD6738, Berzosertib, AZD0156, GDC-0575, LY2606368, MK-1775, Belotecan, and Doxorubicin) as potent drugs that were used in the subsequent secondary screen.

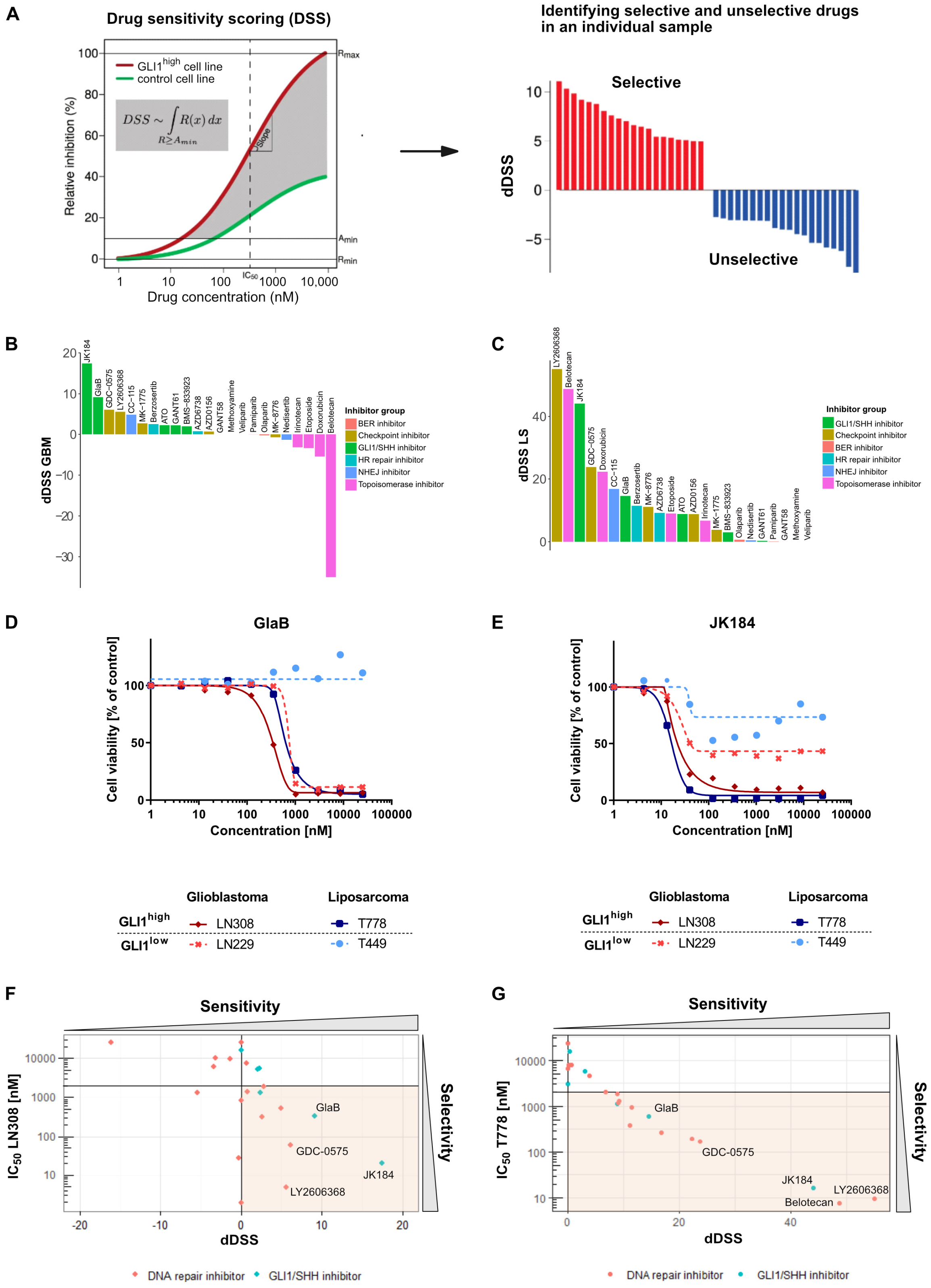

Figure 25: Drug sensitivity scoring identifies selective drugs in glioblastoma and liposarcoma cell models. A Schematic representation of the dDSS algorithm used to quantify selective response in cancer cells and classify selective and unselective drugs based on their dDSS. Dose-response parameters calculated by 5PL function include IC_{50} value, the slope at IC_{50} concentration, maximum and minimum response (R_{min} and R_{max}), and were used in DSS quantification in GLI1^{high} and GLI1^{low} control cells. Graph adapted from [201]. **B + C** dDSS scores of compounds coloured by their target group in glioblastoma (**B**) and liposarcoma (**C**) models. **D + E** Dose-response curve for GlaB (**D**) and JK184 (**E**) in glioblastoma and liposarcoma cell lines. Solid curves represent cell lines with high GLI1 expression, dashed curves represent cell lines with low GLI1 expression. **F + G** Scatterplot of IC_{50} values and dDSS in glioblastoma (**F**) and liposarcoma (**G**) cell models. Data points in orange shaded area define compounds with IC_{50} values < 2000 nM and dDSS > 0.

3.6.3 Secondary screen identifies synergistic drug combinations of GLI1 and DNA repair inhibitors

3.6.3.1 Dose-response data of the combination screen correlate with primary screen data

The top hits from the primary screen were selected for the combination screen to identify potent drug combinations with additive or synergistic interactions. Four GLI1 inhibitors (JK184, GlaB, GANT61, and ATO) and nine DNA repair inhibitors (CC-115, AZD6738, Berzosertib, AZD0156, GDC-0575, LY2606368, MK-1775, Belotecan, and Doxorubicin) were tested in 36 combinations in a matrix with 9 x 9 concentrations for each combination and cell line. The tested range of concentration was adjusted individually for each compound based on the dose-response data from the primary screen. The screen was performed in 1536-well plates to allow the screening of such a high number of combinations and concentrations. After 72 h incubation, metabolic activity was measured as a readout for cell viability and drug response data were analysed.

During the experiment, ATO had to be excluded from the combination screening as cross-reactivity between solvent and compounds were observed. While all other compounds were dissolved in DMSO, ATO has poor DMSO solubility and was instead dissolved in 0.1 N NaOH. For the combination screen, assay plates were prepared by adding both compounds that were to be tested in combination to the plates before cell seeding. As the solvent NaOH induced a chemical reaction with other compounds, ATO could not be used for further testing and analysis.

To evaluate the comparability of results from the primary screen in 384-well format with the results from the secondary screen in 1536-well format, IC_{50} values of both experiments were compared for each compound and cell line (Figure 26). In all four cell lines, IC_{50} values correlated with a Pearson correlation coefficient above 0.6. The highest correlation was achieved within T778 and LN308 cells with a Pearson correlation of 0.9973 and 0.9401, respectively. This quality control confirmed that the drug responses were similar in both formats and validated the suitability of 1536-well plates for the combination screening.

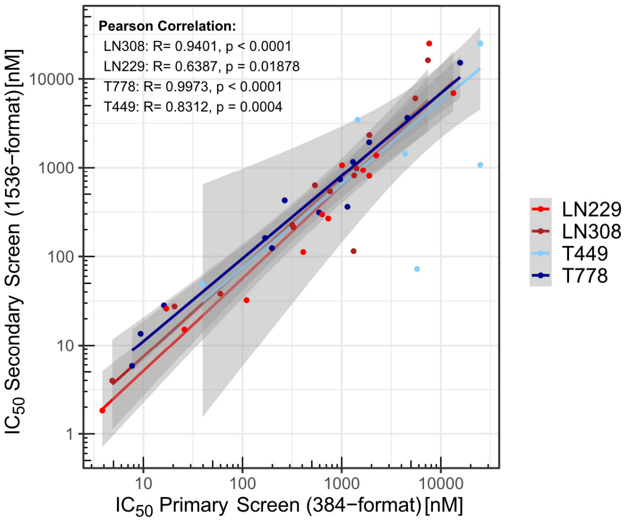

Figure 26: Correlation of IC_{50} values in 384-well format and 1536-well format. IC_{50} values were correlated (Pearson correlation) from the primary screen in 384-well format (x-axis) and secondary screen in 1536-well format (y-axis) for each compound and cell line. Pearson correlation coefficient (R) and p-values for each cell line are depicted in the graph.

3.6.3.2 Synergistic effects occur between GLI1 inhibitors and compounds targeting the ATR/CHK1 pathway

To identify potent drug interactions of GLI1 and DNA repair inhibitors, dose-response data for all combinations and cell lines were analysed using the Combenefit software. A drug interaction score was calculated for all combinations representing the sum of synergy and antagonism observed across the concentration matrix, with a positive score indicating a synergistic interaction between the compounds. Synergistic effects were identified in cell lines with high GLI1 expression (Figure 27 A, left graph) while GLI1^{low} cell lines showed almost no synergistic interactions (Figure 27 A, right graph). The results identified additive or synergistic interactions between GLI1/SHH inhibitors with the CHK1 inhibitors LY2606368 (Figure 27 B, top) and GDC-0575 (Supplementary material 8 A), as well as with the ATR inhibitor Berzosertib (Supplementary material 8 B). In contrast, LY2606368 resulted in an antagonistic interaction in GLI1 low expressing T449 cells when combined with GANT61, JK184 or GlaB (Figure 27 B, bottom). Similar results were also observed in glioblastoma but with lower synergistic interactions between the compounds (Supplementary material 9 Supplementary material 10).

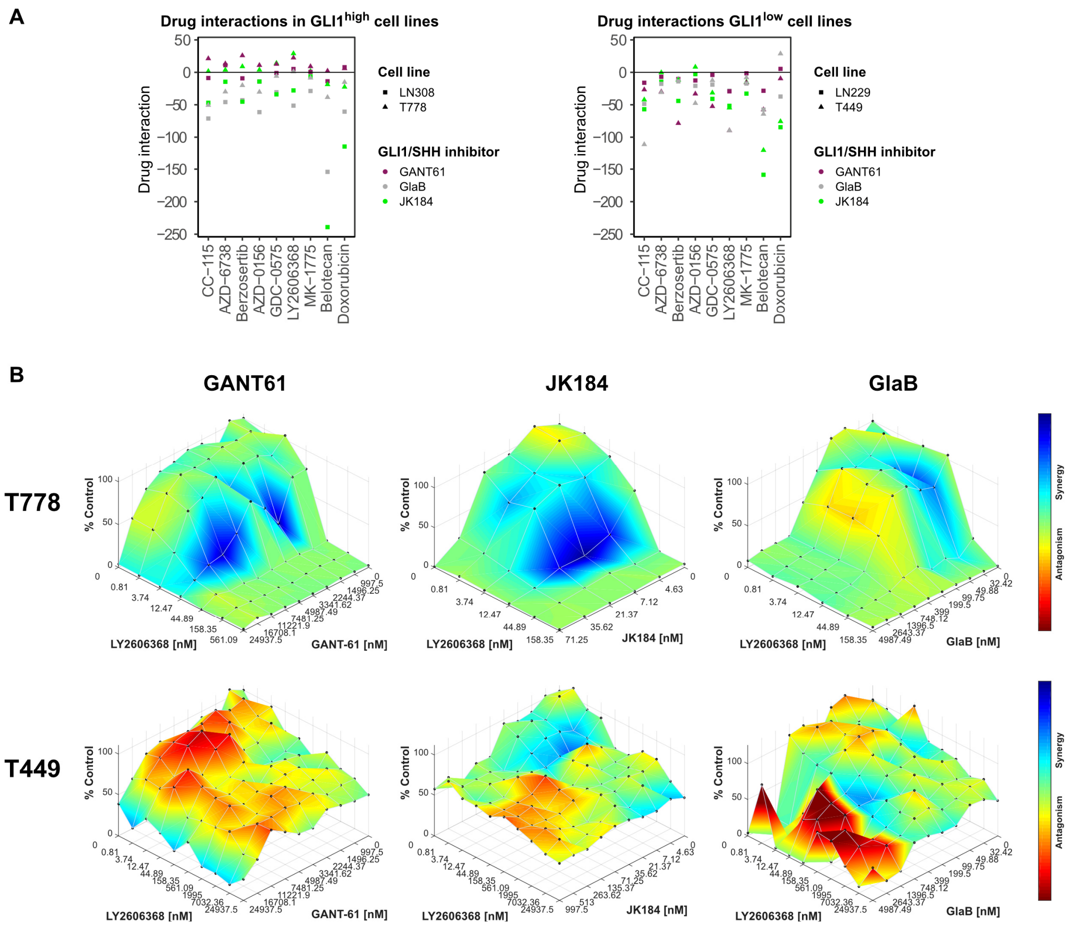

Figure 27: Drug interaction profiles across GLI1/SHH and DNA repair inhibitor combinations. A Drug interaction scores in cell lines with high GLI1 expression (LN308, T778; left graph) and in cell lines with low GLI1 expression (LN229, T449; right graph), summarising the drug interactions amongst all tested combinations. For each DNA repair inhibitor, drug interaction scores with all three GLI1/SHH inhibitors, GANT61, JK184, and GlaB, in both cell lines are shown. **B** Bliss surface plots show synergistic and antagonistic drug interactions between GLI1 inhibitors and CHK1 inhibitor LY2606368 in T778 and T449 cell lines. Synergy and antagonism are mapped on the dose-response data of metabolic activity. Only one technical replicate was performed in the experiment. Plots were generated using the Combenefit software.

3.6.4 Validation of drug screening results

As follow up of the combination screening, validation experiments were performed to confirm the findings of the screening approach. In the validation experiments, GLI1 inhibitors JK184 and GlaB were tested in combination with CHK1 inhibitor LY2606368 in 96-well format on the T778 and LN308 cell lines in a 9 x 9 matrix design. Both cell lines revealed additive effects upon combination treatment with GlaB and LY2606368 (Figure 28). Similar results were obtained when LY2606368 was combined with JK184, showing synergistic interaction in LN308 cells at IC_{50} concentrations (Supplementary material 11).

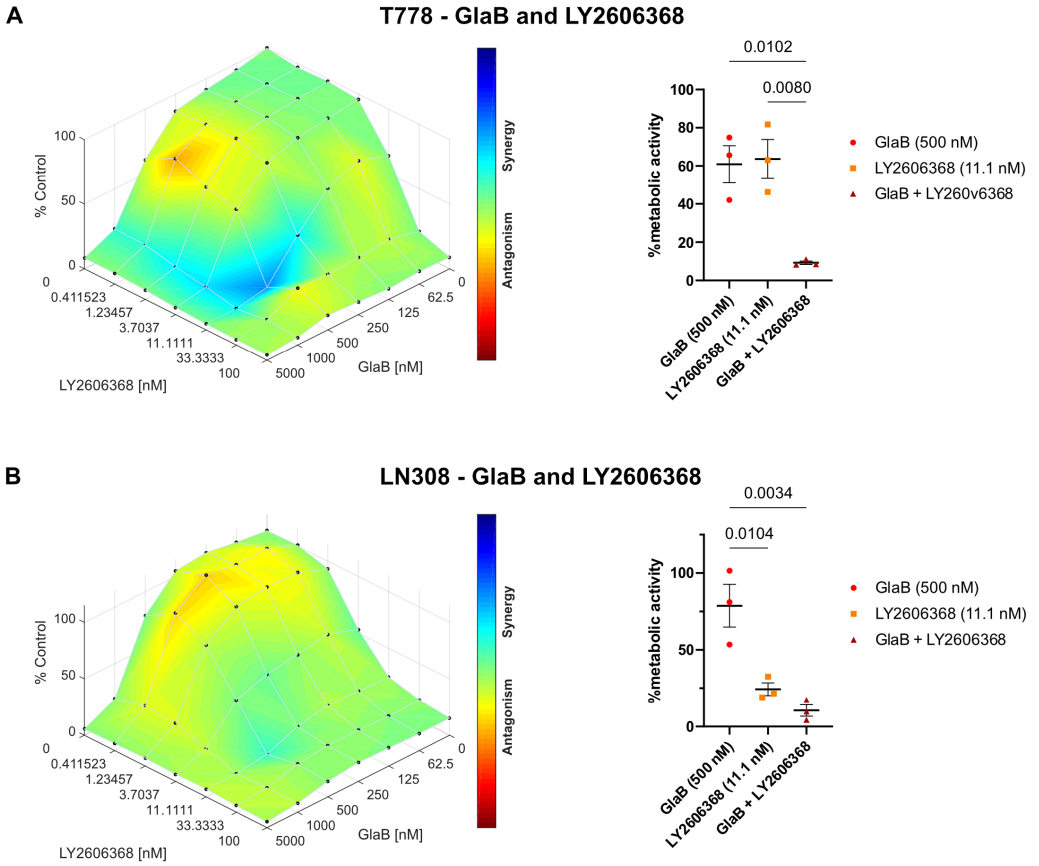

Figure 28: Additive effects in T778 and LN308 cells upon combination treatment with GlaB and LY2606368. Bliss surface plots for T778 (**A**) and LN308 (**B)** cells upon combination treatment with GlaB and LY2606368. Synergy and antagonism were mapped on the dose-response surface generated by the average of the metabolic activity values at each data point as percentages of the DMSO control for three biological replicates. Plots were generated using the Combenefit software. Dot plots on the right show the metabolic activity compared to DMSO control at concentrations resulting in the highest synergy score (GlaB, 500 nM; LY2606368 11.11 nM) (mean ± SEM, significant p-values are indicated in the graphs, one-way ANOVA followed by Tukey's test for multiple comparisons of groups).

3.6.4.1 Combination treatment inhibits long-term tumour cell proliferation rather than cell apoptosis in vitro

As a next step, long-term anchorage-independent growth was tested in LN308 cells treated with single agents and a combination of GlaB and LY2606368. Since in single-agent experiments anchorage-independent growth was affected already at low concentrations, three different concentrations below the IC_{50} value of GlaB were tested in combination with 0.1 nM LY2606368. Treatments with GLI1 and CHK1 inhibition alone decreased the ability of tumour cells to form colonies and the effect was further potentiated by combining the drugs (Figure 29 A). When cells were treated with 50 nM GlaB in combination with 0.1 nM LY2606368, the clonogenic potential in soft agar was significantly reduced by 23 % compared to the single treatment. Short-term proliferation was also reduced upon combination treatment with GlaB and LY2606368 for 72 h (Figure 29 B), while cell apoptosis experiments showed only a minor increase in early and late apoptotic cells (Figure 29 C). These data indicate that the inhibition of GLI1 and CHK1 have a long-term effect on tumour cells by preventing their proliferation capacity.

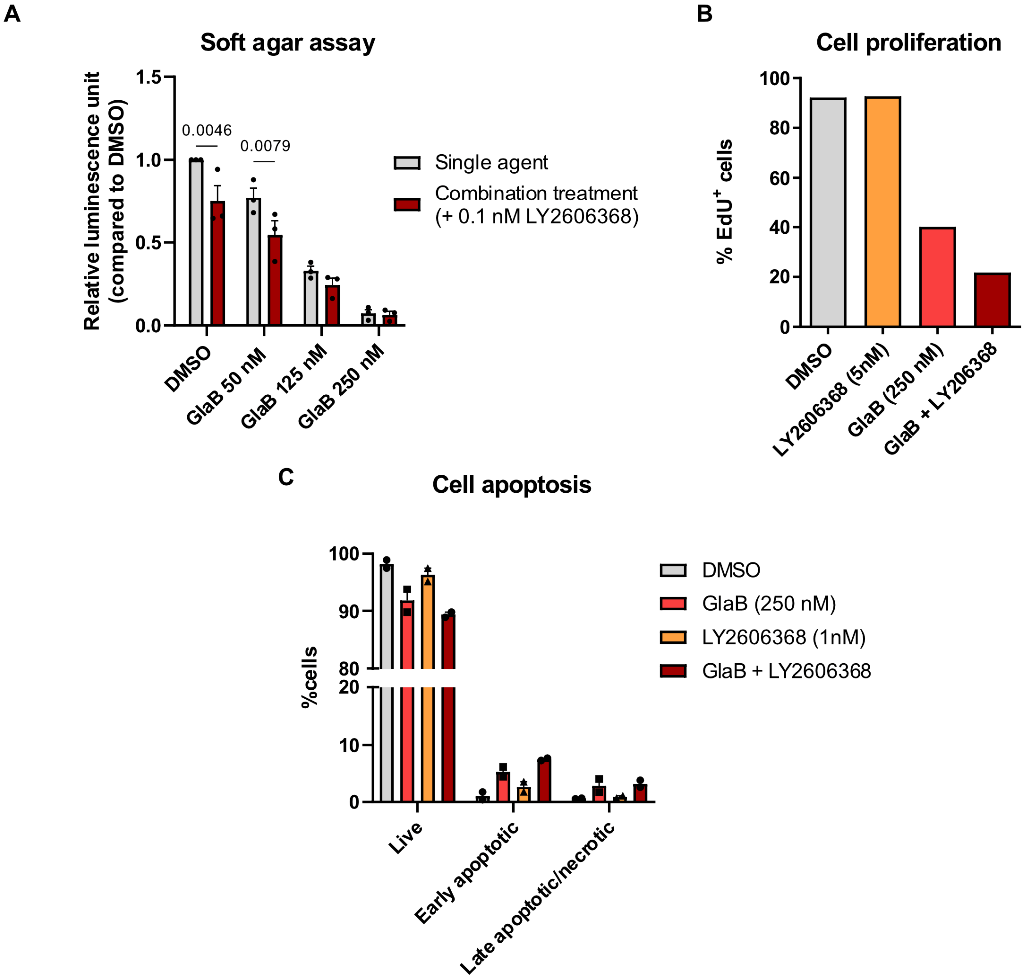

Figure 29: Inhibition of long- and short-term proliferation in LN308 cells upon combination treatment with GlaB and LY2606368. A Soft agar colony formation assay in LN308 cells upon single and combination treatment with GlaB and LY2606368 for 14 d. (mean ± SEM, significant p-values are indicated in the graph, two-way ANOVA followed by Holm-Šídák test for multiple comparisons of groups). **B** Click-iT EdU incorporation assay in LN308 cells upon single and combination treatment with GlaB and LY2606368 for 72 h. One biological replicate. **C** Quantification of live, early apoptotic, and late apoptotic/necrotic LN308 cells upon treatment with GlaB and LY2606368 for 72 h (mean ± SEM, two biological replicates).

3.6.4.2 Combination treatment inhibits tumour growth in a cerebral organoid model

Evaluation of maximum tolerable drug concentrations

Cerebral organoids (CORs) have emerged as a novel and robust preclinical tool to study neurological disorders, including brain tumours, and provide an alternative tool for effective antitumour drug screening. Single agents and combination treatment were tested on CORs to investigate the effects on tumour growth. CORs were established from iPSCs by Pavle Boskovic (graduate student, Molecular Genetics, DKFZ Heidelberg) and morphologically characterised by SOX2 and TUJ1 staining marking neural progenitors and neurons, respectively (Figure 30 A). In a first step, a toxicity study was performed to assess the neurotoxicity of the compounds and to identify the optimal tolerable concentration of inhibitors for the subsequent treatment study. GlaB and LY2606368 were tested on CORs for 8 d in three different concentrations as well as a combination of both. In organoids treated with 1000 nM and 2000 nM GlaB cell integrity became distorted already after 96 h of treatment and showed large amounts of cell debris after 8 d (Figure 30 B). Cell viability of organoids was evaluated at the end of inhibitor treatment and revealed a dose-dependent increase in toxic effects on organoid tissue (Figure 30 C). Treatment at the lowest concentrations of LY2606368 did not affect cell viability while the highest concentration, as well as GlaB and combination treatment, revealed a strong increase in the percentages of dead cells, indicating that these concentrations were not tolerable for the subsequent treatment study. As a conclusion from this toxicity study, the maximal tolerable concentration for GlaB was below 500 nM and LY2606368 could be tolerated at 5 nM concentration. For the subsequent GLICO treatment study, concentrations of 250 nM GlaB and 5 nM LY2606368 were used as single agents and in combination.

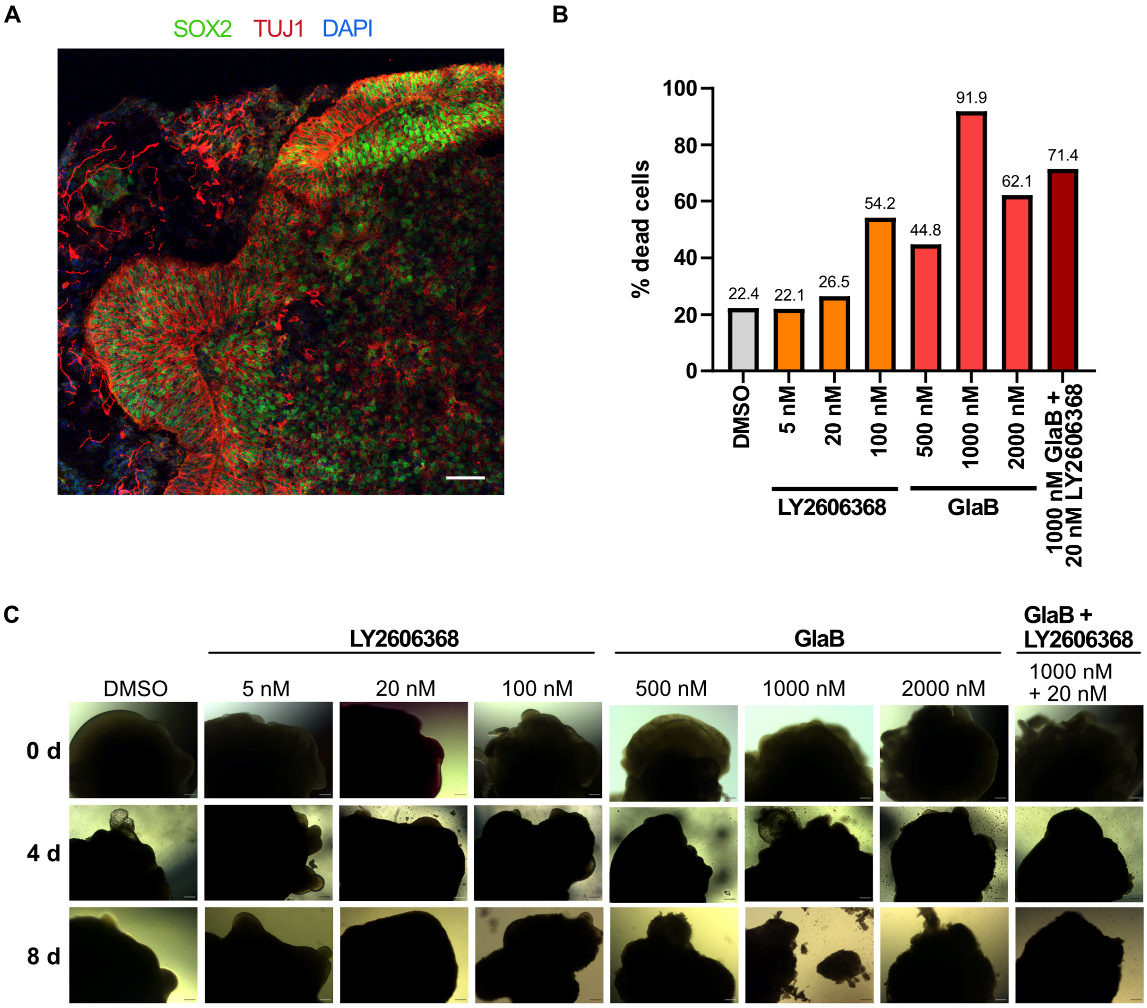

Figure 30: Evaluation of toxicity effects in cerebral organoids upon drug treatment. A Representative image of immunofluorescent staining of a 45-day old organoid tissue with SOX2, TUJ1, and DAPI. Scale bar 50 µM. **B** Quantification of dead cells after 8 d of inhibitor treatment. One cerebral organoid was assessed per treatment condition. **C** Images of cerebral organoids before and after 4 and 8 d of treatment with different concentrations of GlaB, LY2606368, and GlaB + LY2606368 combination, scale bar 100 µM.

Combination treatment study in a GLICO model

In the second step, GlaB and LY2606368 inhibitors were tested as single agents and in combination in a glioblastoma cerebral organoid (GLICO) model. V5-tagged luciferase-expressing LN308 glioblastoma cells grown as spheroids were co-cultured with cerebral organoids for 8 d to allow the tumour cells to invade the organoids and to form a tumour. Subsequently, the organoid tumours were treated with inhibitors for 14 days (Figure 31 A). Tumour growth was monitored by bioluminescence imaging, showing a reduction of tumour growth in the GlaB and combination treatment groups compared to the DMSO control group (Figure 31 B + C). LY2606368 alone had little effect at treatment start but considerably reduced tumour growth after 8 days of inhibitor treatment. At the endpoint of the treatment study, tumour content, viability and proliferative capacity of tumour cells were quantified. Tumour load was evaluated by FACS staining of $V5^+$ tumour cells, confirming that the organoids of the combination treatment group contained the fewest tumour cells, exceeding the effects of the single treatment groups (Figure 31 D). The analysis of cell viability within tumour cells revealed that the percentage of dead cells was increased in the combination treatment group. In contrast, no differences were observed in the overall viability of all cells (organoid cells and tumour cells), indicating that the inhibitor concentrations didn’t have any adverse effects on the organoid tissue (Figure 31 F). Furthermore, the percentage of EdU^+ tumour cells was reduced in the combination treatment group, confirming the decreased proliferative capacity of these cells (Figure 31 G). These data are in line with the *in vitro* studies (Figure 20, Figure 28, and Figure 29) and underline the therapeutic potential of a combination treatment with GLI1 and CHK1 inhibitors in tumours with *GLI1* overexpression.

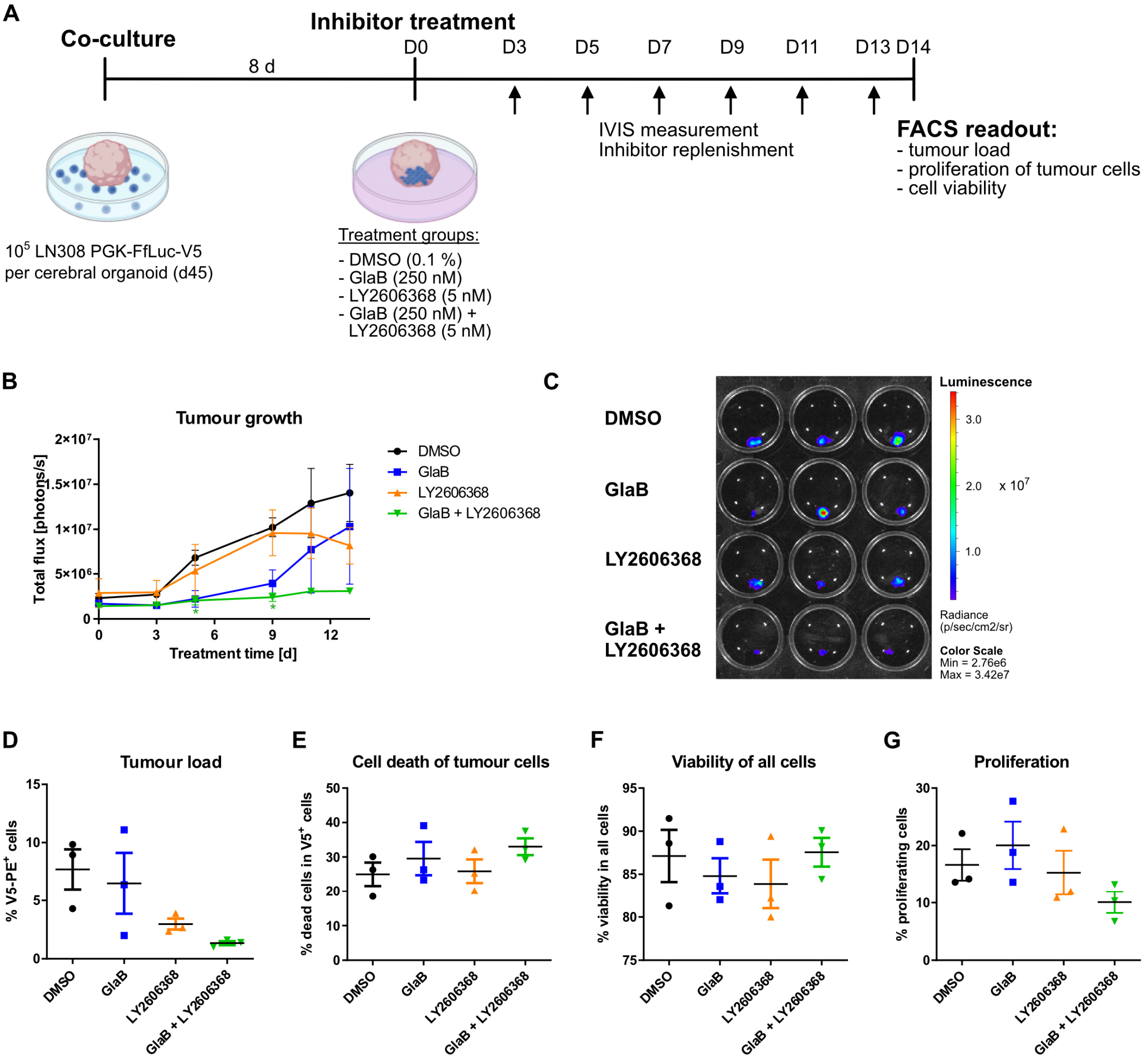

Figure 31: Inhibitor treatment study in LN308 GLICO model. A Experimental setup and treatment schedule of the LN308 GLICO model with GlaB, LY2606368, and GlaB + LY2606368 combination treatment. **B** Luminescent intensity of photons emitted from each organoid was quantified before treatment start, at D3, followed by measurements every 48 h. D7 was not included in the analysis due to failure in the measurement resulting in low luminescent intensity in all samples. 3 organoids per treatment group (mean ± SEM, two-way ANOVA followed by Holm-Šídák test for multiple comparisons of groups; * $p < 0.05$, at D5 and D9 significant reduction in tumour load comparing DMSO and GlaB + LY2606368). **C** IVIS image at D13 post-treatment start. **D** Quantification of $V5^+$ tumour cells at the endpoint of the study (mean ± SEM, one-way ANOVA followed by Tukey's test for multiple comparisons of groups, no significance detected). **E** Quantification of non-viable tumour cells at the endpoint of the study (mean ± SEM, one-way ANOVA followed by Tukey's test for multiple comparisons of groups, no significance detected). **F** Quantification of viable cells at the endpoint of the study (mean ± SEM, one-way ANOVA followed by Tukey's test for multiple comparisons of groups, no significance detected). **G** Quantification of proliferative tumour cells at the endpoint of the study. EdU^+ $V5^+$ tumour cells were quantified by Click-iT reaction followed by V5 staining (mean ± SEM, one-way ANOVA followed by Tukey's test for multiple comparisons of groups, no significance detected).

4 Discussion

With the advances in next-generation sequencing and the rising number of large-scale tumour profile datasets, the field of oncology has witnessed substantial changes in the way cancer patients are managed, moving from a “one-size-fits-all” approach towards precision medicine in which cancer patients are treated based on their specific genomic aberrations [228, 229]. These comprehensive genomic analyses can accelerate the identification of cancer driver genes and the development of specific therapies that improve the clinical outcome of cancer patients. Glioblastoma and certain types of sarcoma are characterised by extensive intratumoral heterogeneity, high rates of chemoresistance, and tumour relapse [230-232]. Effective targeted treatment modalities are still sparse despite recent insights into deregulated core signalling pathways and subclassification advances [79, 81, 156, 157, 204].

In the thesis work presented here, I aimed to explore the potential use of the oncogene GLI1 as a therapeutic target in patients with aberrant GLI1 expression. As GLI1 is often activated independent of the upstream HH signalling pathway, different non-canonical activation mechanisms of GLI1 were analysed in glioblastoma and sarcoma cohorts. The obtained results contributed to the understanding that *GLI1* transcription is upregulated by the formation of gene fusions and genomic amplification or the disruption of a nearby CTCF binding site. Furthermore, functional evidence from glioblastoma and liposarcoma cell line and organoid models was provided, supporting GLI1 as a therapeutic target. The potency of GLI1 inhibition can be additionally increased when combined with inhibitors targeting the CHK1/ATR axis.

4.1 Oncogenic activation of GLI1 in 12q-amplified glioblastoma and sarcoma tumours

Structural variation plays a vital role in tumorigenesis and cancer evolution. The majority of tumours are aneuploid, harbouring an abnormal set of chromosomes [233, 234]. While some tumours are more susceptible to genomic instability than others, a recent PCAWG study of 2559 tumours across 38 cancers showed that almost all patients (2429/2559) had at least one somatic copy number alteration. Copy number gains were frequently associated with the upregulation of oncogene expression [18, 26]. Transcriptomic, genomic, and epigenomic profiling of 60 primary adult tumours in our research group identified typical glioblastoma hotspots of genomic gains and losses, including the amplification of chromosome band 12q13-15 in 23 % of tumours (14/60) associated with a high frequency of genomic rearrangements. Besides the well-established oncogenes *CDK4* and *MDM2* in this chromosome region, *GLI1* was co-amplified in almost half the patients (6/14) and formed fusion genes in four patients. The overall high number of structural rearrangements on chromosome arm 12q is consistent with findings on the somatic glioblastoma landscape by the TCGA network, in which structural variations in this region were found in 26 % (11/42) of whole genomes and 12q-associated fusion transcripts in 15 % (25/164) of transcriptomes [157]. As a follow-up to this study, the authors defined chromosome band 12q14-15 as a breakpoint-enriched region (BER) with a shattered chromosome pattern, suggesting local chromosomal instability. The 12q14-15 BER was identified in 5 % of *IDH*-wildtype glioblastoma and was associated with adverse survival [158]. While *TP53* mutations were significantly fewer in these tumours possibly due to TP53 degradation by MDM2, the potential impact of other genes within the 12q14-15 BER was not the subject of this study.

The emerging complexity and the vast number of detected gene fusions in cancer genomes inevitably raise the central question of whether fusion genes are a cause or effect of tumorigenesis. There is an ongoing debate whether the large number of chromosome aberrations in tumours is noise and purely reflect the consequence of chromosomal instability [235, 236] or pathogenetically meaningful in carcinogenesis [60]. However, there is little controversy that balanced rearrangements can represent early driver mutations with distinct characteristics and are pathognomonic for certain cancers [237]. These reciprocal translocations typically result either in the deregulation of a normal gene or in the creation of a gene hybrid made up of parts from two genes. For instance, the reciprocal translocation t(9;22)(q34;q11) generates the Philadelphia chromosome encoding for the BCR-ABL1 hybrid protein, which is detected in more than 90 % of CML patients [64]. There are numerous examples of cancer-relevant fusion genes, resulting in transcriptional regulation without generating a hybrid protein. The formation of gene fusions of the *MYC* oncogene with regulatory elements of the immunoglobulin family confers transcriptional deregulation to *MYC* in Burkitt lymphoma [238-240]. *FGFR3*-*TACC3* fusions resulting from tandem duplication and insertion on chromosome 4 have been detected in several tumour entities, including glioblastoma, with a reported prevalence ranging from 1.2 – 8.3 % [70, 71, 241]. The tyrosine kinase domain of FGFR3 becomes constitutively active through fusion with the TACC domain of TACC3 and clinical trials in fusion-positive patients provide first evidence of response to FGFR inhibition [242]. The majority of gene fusions are associated with amplification or deletion at the DNA level. Large-scale analyses have shown that 82 % of gene fusions in cancer transcriptomes were associated with structural variants [61, 62], suggesting that they occur due to chromosome instability. As too much chromosomal instability, however, can also be disadvantageous to tumour cells, only chromosome aberrations will be propagated that are selectively favoured. If key genes such as oncogenes are affected, a major clone can be selected driving tumour progression and cancer evolution. Additionally, chromosome breakpoints preferentially occur in gene-rich regions in cancer [243], suggesting that chromosome rearrangements can affect other genes in addition to the ones clearly associated with tumour pathogenesis. It is thus of great interest to clearly distinguish pathogenetically important fusion genes from secondary non-consequential abnormalities.

Analyses of the *GLI1* fusion transcripts in glioblastoma tumours revealed that the fusion genes differed in their fusion partners and genomic breakpoints. Most fusions occurred intrachromosomally and retained the gene regions encoding the functional protein domains necessary for DNA binding and transcriptional activation. Two additional isoforms of *GLI1* have been reported in the literature. One has an N-terminal deletion of 128-amino acids (*GLI1ΔN*) [244], and the other represents a truncated form (*tGLI1*) resulting from alternative splicing with a loss of 41 codons from exon 3 and 4, preferentially expressed in tumour tissue [245]. However, the comparison of the detected gene fusions did not reveal sequence consensus with the described isoforms. The identified *GLI1* genomic rearrangements with multiple transcript partners and breakpoints are very likely caused by DNA double-strand breaks and subsequent fusion as a result of genomic amplification. This is additionally supported by the fact that the amplification boundary often coincides within the *GLI1* locus. The presence of multiple breakpoints and fusion partners can be explained by the initiation of mechanisms that drive genomic amplification. Once the formation of double minute chromosomes and breakage fusion bridge cycles are initiated, the accumulation of gene copies and random breakage of the genome is expected [246].

High *GLI1* expression was tightly associated with the presence of *GLI1* fusion transcripts in the HIPO016 cohort, suggesting a mechanistic role of the chromosome 12q13 rearrangement. The upregulation of *GLI1* expression was independent of the amplification of *CDK4*, located 275 kb downstream of the *GLI1* locus, as *GLI1* fusion-negative tumours with *CDK4* amplification did not show an increase in *GLI1* expression. The activity of GLI1 in these tumours was confirmed by target gene expression analysis. The upregulation of the *GLI1* target genes *PTCH1*, *HHIP*, and *FOXS1* indicated that GLI1 is functionally active in these tumours, exerting its role as a transcription factor. Two additional glioblastoma cohorts, TCGA-GB and HIPO043, were subjected to *GLI1* expression and fusion gene analysis, and *GLI1* fusion genes associated with strong transcriptional upregulation were detected in three TCGA tumours (3/206 tumours, 1.5 %) and one recurrent tumour in HIPO043 (1/29, 3.4 %), supporting the results obtained from the HIPO016 cohort. Two low-grade gliomas in the TCGA cohort were also found to harbour *GLI1* fusion genes, but as the focus of this study was on high-grade glioblastoma, these cases were not considered for further analysis. The acquisition of a *GLI1* fusion and associated upregulation in expression in the recurrent glioblastoma tumour in HIPO043 illustrated a potential role of GLI1 in glioblastoma progression. As the primary tumour harboured only a focal amplification of the *CDK4* locus, structural variation was gained by the expansion of the amplified regions over the *GLI1* locus, probably causing the formation of a *GLI1* fusion gene as a secondary structural rearrangement.

The overall frequency of *GLI1* fusions in the TCGA cohort was much lower compared to the HIPO016 cohort. Several factors might explain this difference. First, the detection of fusion genes from RNA sequencing data highly depends on the detection algorithm. Deep-sequencing technologies are very sensitive, allowing the detection of rare events, but they are also error-prone. Fusion gene detection can be confounded by factors induced either already during library preparation of the sequencing samples or the bioinformatics analyses. Over the last decade, multiple software algorithms have been developed to detect candidate fusion transcripts accurately. The detection of gene fusions from RNA-seq analysis can be done either by read-mapping to identify discordant and junction-spanning reads or by *de novo* fusion transcript assembly that identifies chimeric transcripts after the assembly of read counts into longer transcripts. Errors in the reference genome assembly or read count mapping due to high similarities of genes are only two examples of factors that can increase the number of false-positive fusion transcripts. Comparisons of different methods show that they highly differ in sensitivity and selectivity, resulting in different numbers of detected fusion transcripts [247]. Two detection methods, Arriba and confFuse, were therefore applied to call fusion transcripts with high confidence. Even though Arriba was shown to be amongst the most accurate and fastest detection methods, experimental validation of the bioinformatics prediction of fusion transcripts is indispensable.

Second, the performance of the detection methods additionally depends on the sequencing coverage of the samples. High sequencing coverage is an essential factor to detect fusion genes in amplified regions because of the very high DNA copy number. The TCGA cohort samples were sequenced at considerably lower coverage than those of the HIPO016 cohort. Thus, fusion genes in the 12q13 amplification region could have been missed due to low sequencing coverage. In addition, gene expression was determined by microarray for about one-third of the TCGA-GB samples, precluding fusion gene calling. Some of these tumours had very high *GLI1* expression but whether fusion genes are present cannot be answered as RNA-seq data is missing to identify fusion genes. Furthermore, fusion transcripts will not be detected if no chimeric mRNA is formed. This is for example the case when the chromosome rearrangement results in enhancer or promoter hijacking.

In addition to the fusion of two coding sequences and genomic amplification, the structural reorganisation of chromatin can lead to significant gene expression changes and oncogenic activation [92, 95]. In this study, functional evidence was provided that the disruption of a CTCF binding site upstream of the *GLI1* locus induces transcriptional upregulation of *GLI1* and its target genes in T778 cells, ultimately resulting in a higher proliferative capacity of the cells. Whether this reorganisation results in the interaction with an otherwise distal enhancer, in the loss of insulator repression, or any other mechanism has yet to be determined. It also needs to be addressed whether the disruption of the CTCF binding site alone is sufficient to drive GLI1 expression or whether concurrent genomic amplification is necessary for this effect. It can be speculated that the amplification and formation of gene fusions at the *GLI1* locus reshapes the structural organisation of the tumour, which affects the gene expression. Given that tumour cells are genomically unstable, it is very likely that disruption of TAD domains are frequent events in cancer that can change the transcriptome on a large scale and possibly even drive tumorigenesis.

Furthermore, the amount of protein present in the cell is controlled by its degradation and translational synthesis. The binding of microRNA to mRNA sequences can affect post-transcriptional mRNA stability or translation. Analyses of miRNA expression in medulloblastoma have revealed a set of 34 miRNAs downregulated in GLI1^{high} tumours. Of these, miR-324-5p was able to target *GLI1* 3’ UTR and suppress GLI1 functionally [248]. Thus, *GLI1*-amplified or fusion-positive tumours might lose miRNA binding sites, which would otherwise induce a rapid turnover of *GLI1* mRNA, resulting in increased GLI1 activity. Additionally, GLI1 binding sites were identified in the first intron 5’ of the GLI1 TSS, promoting positive feedback of GLI1 transcription [115]. Besides miRNA binding and self-regulation, GLI1 stability is controlled internally by encoded degradation sequences that serve as recognition sites for the proteasomal machinery. The removal of these sites has been shown to stabilise GLI1 and accelerate BCC tumour induction [249]. In the *DDIT3*-*GLI1* fusion of patient AK165, the D_s degradation sequence is lost, and GLI1 proteins thus may not be targeted for degradation.

The relevance of fusion-associated upregulation of *GLI1* was additionally studied in sarcoma tumours. Four *GLI1* fusion-positive tumours, diagnosed as leiomyosarcoma and liposarcoma, with strong upregulation of RNA expression were found within the NCT MASTER cohort. Both tumour entities frequently show amplification of chromosome band 12q13-15. A systematic analysis of *GLI1* expression across the cohort revealed additional tumours with strong upregulation in *GLI1* RNA expression. Whether these tumours carry fusion genes cannot be fully answered since fusion gene calling could only be performed on a subset of the cohort. Additionally, the analysis of the NCT MASTER cohort was performed on samples enrolled in the study until August 2018 (n=720), including only samples from Heidelberg. An updated analysis with all currently registered and analysed samples of the NCT MASTER cohort (n=2750) is ongoing and will provide a more precise estimate of *GLI1* aberrations in sarcoma, especially for very rare subtypes that were previously represented with only very few samples per group in the presented analysis. The list of *GLI1* fusions in sarcoma can be further expanded by individual cases reported in the literature [177]. First clinical examples were described in pericytomas, a perivascular soft tissue sarcoma, with t(7;12) translocations of *GLI1* with the ubiquitously expressed *ACTB* (β-actin) [250]. Other examples include cases of *ACTB*-*GLI1* fusion in the bone [251] and skin [252], *MALAT*-*GLI1* fusion in gastric tumours [253], *PTCH1*-*GLI1* fusion in a primary ovarian tumour [254], and head and neck neoplasm [255]. These tumours showed characteristic monomorphic nested epithelioid morphology with frequent S100 positivity and metastatic potential [256]. Additional soft tissue tumours with similar morphologic characteristics were found to show *GLI1* amplification but lacked the expression of *GLI1* fusion transcripts with either of the reported genes, *ACTB*, *MALAT*, and *PTCH1* [257]. Taken together, the examples reported in the literature and present in the NCT MASTER cohort prove GLI1 as an interesting target in specific subsets of sarcomatous tumours.

4.2 Validation of GLI1 as a therapeutic target in glioblastoma and sarcoma cell models

Genomic amplification, fusion genes, and their associated deregulated expression are important drivers in tumorigenesis [13, 14, 62]. Owing to their low expression in healthy tissue and their implication in key cellular mechanisms attributed to the hallmarks of cancer, they represent ideal therapeutic targets for cancer therapy [183]. The oncogene GLI1 is the transcriptional effector protein downstream of the Hedgehog/GLI signalling pathway, initially found as an amplified gene in human glioma [106, 113]. Its relevance in other tumour entities was shortly afterwards described, including basal cell carcinoma, SHH-driven medulloblastoma, and cancers of breast, lung, colon, stomach, ovarian, and pancreas. However, the targeting of GLI1 in a clinical setting has failed so far due to the lack of potent inhibitors.

The glioblastoma and liposarcoma cell models used to study the phenotypic effects of GLI1 depletion and inhibition *in vitro* showed amplification of *GLI1* with associated high RNA expression. However, fusion genes were not detected in the GLI1 coding sequence of T778 (liposarcoma) or U3071 cells (glioblastoma, patient-derived); LN308 cells were not subjected to high-coverage RNA-sequencing. As discussed above, fusion gene analysis can be confounded by several factors, and additional epigenetic mechanisms can drive *GLI1* expression. Thus, it became apparent that it is not relevant to study the tumorigenic function of individual fusion genes but instead solely focus on aberrant GLI1 expression for the further course of the work.

Data presented in this study indicate the potential of GLI1 as a therapeutic target for several reasons. First, depletion and inhibition of GLI1 in cell lines affect fundamental cellular mechanisms. In constitutive shRNA knockdown experiments, cell proliferation was significantly decreased in all three tested cell line models, LN308, U3071, and T778. The natural small-molecule inhibitor GlaB, which prevents DNA binding of GLI1, showed dose-dependent anti-proliferative and pro-apoptotic effects on tumour cells. GlaB treatment decreased the percentage of EdU^+ cells but increased early and late apoptotic cell fractions. These observations are in line with previously reported effects of GlaB on GLI1-dependent *in vitro* and *in vivo* medulloblastoma and basal cell carcinoma growth [147]. GlaB additionally reduced the clonogenic potential of LN308 cells, grown under stem-cell conditions, in an anchorage-independent environment. A second inhibitor, JK184, additionally confirmed the reduction in anchorage-independent growth. Both inhibitors drastically reduced the clonogenic potential at concentrations below the IC_{50} values observed *in vitro*. Active HH/GLI1 signalling is essential for the proliferation and maintenance of cancer stem cells (CSCs) by upregulation of genes involved in self-renewal and dedifferentiation [258, 259]. Therefore, targeting GLI1 could be an efficient treatment strategy to overcome disease progression, drug resistance to conventional therapies, and tumour spread [260]. In mammary carcinoma, CSCs secrete SHH to stimulate paracrine HH signalling in cancer-associated fibroblasts (CAFs). In turn, CAFs produce growth factors such as ACTIVIN A, NOV, IGF-1, and LIF, that regulate CSC proliferation and self-renewal. Treatment with a Hedgehog inhibitor effectively reduced tumour stroma, CSC content, and delayed breast cancer formation [261]. Hedgehog signalling additionally retains CSCs in their dormant state in tumours through upregulation of the polycomb gene Bmi-1, which acts as a transcriptional repressor on cell cycle regulator genes, including $p16^{INK4A}$ and p19 ARF [262]. Studies in $CD133^+$-expressing glioma stem cells (GSCs) showed the important role of the HH pathway also in the perivascular niche in glioma. SHH-expressing endothelial cells localise to GSCs, activate HH signalling in perivascular glioma cells, and promote their GSC-like phenotype through VEGF stimulation [263]. In addition, histological evaluation of glioma specimens revealed that Shh expression in endothelial cells and GLI1 expression in perivascular glioma cells correlated with tumour grade. High-grade glioma showed higher GLI1 expression than low-grade glioma, which indicated a worse prognosis [263]. Consistent with the literature, the inhibition of GLI1 transcriptional activity with GlaB and JK184 interferes with the long-term proliferation and sphere formation of glioma-stem like cells, highlighting its rationale as a therapeutic strategy to target cancer stem cells.

Second, direct targeting of GLI1 represents a promising complementary treatment strategy for cancer patients with aberrant HH signalling better than the currently used SMO-inhibitor therapies. Patients with mutations in *PTCH1* and consequential constitutive activation of the HH pathway through SMO have been shown to initially respond to the SMO inhibitor vismodegib with tumour regression [264]. However, frequent acquisition of secondary *SMO* mutations occurs in basal cell carcinoma and medulloblastoma. These mutations prevent the binding of vismodegib to SMO, conferring resistance towards SMO inhibition [131, 265]. Patients harbouring such mutations could benefit from treatment targeting GLI transcription factors directly. This is beneficial as therapy response does not rely on any of the upstream pathway regulators and mutations in *GLI1* occur at a very low frequency [266]. Furthermore, tumours with activation of GLI1 independent of the upstream HH pathway require specific therapy against GLI1, as they are in any case insensitive to inhibitors that affect the upstream HH signalling cascade. Consistent with the literature, treatment of T778 cells with erismodegib, another FDA-approved SMO inhibitor, in an *in vitro* experiment did not affect their proliferative capacity (data not shown). As targeting GLI1 allows the inhibition of both canonical and non-canonical signalling, it represents a treatment approach with superior anticancer effects compared to inhibition of Hh components upstream of GLI1.

Third, GLI1 has low expression levels in healthy cells, suggesting that the specific targeting of tumour cells with aberrant GLI1 expression could show high efficacy with limited cytotoxic side effects for the patients [267].

4.3 GLI1 as a regulator of the DNA damage response and glycosylation

RNA sequencing analysis of GLI1 shRNA knockdown and control cells provided mechanistic insights into the role of GLI1 in glioblastoma and liposarcoma models with high GLI1 expression. Differential gene expression analysis revealed tumour type-specific regulation, but a substantial fraction of genes that were differentially regulated between knockdown and control cells were shared between glioblastoma and liposarcoma. For example, upregulation of TGF-β expression upon GLI1 knockdown was observed in both cancers, consistent with the previously reported crosstalk between the TGF-β and HH signalling pathways [268]. Whether the upregulation of TGF-β is a direct response to the proliferation inhibition or a mechanism compensating GLI1 loss by upregulating the TGF-β signalling axis was not addressed in this study. However, the upregulation of the MAPK pathway further indicates that compensatory mechanisms take place upon GLI1 inhibition.

Several pathways regulating glycan metabolism such as glycosaminoglycan biosynthesis, glycerophospholipid metabolism, N-glycan biosynthesis, mannose-type O-glycan biosynthesis, or glycan degradation, were upregulated in liposarcoma and glioblastoma upon GLI1 depletion. The glycosylation pattern of a cell is unique for each cell type, regulating diverse cellular functions, and abnormal glycosylation in cancer stem cells has been attributed with stemness maintenance,tumorigenesis, drug resistance, and metastasis [269, 270]. The finding of aberrant O-glycosylation in this study is consistent with the literature on breast cancer cells and melanoma, reporting co-regulation of O-glycosylation by the SOX2/GLI1 transcriptional complex in melanoma metastasis [271]. Furthermore, O-linked N-acetylglucosamine (O-GlcNAc) modification of GLI1/2 directly affects their transcriptional activity in hyperglycemic conditions of breast cancer cells [272]. The glycosyltransferase GALNT1 mediates the glycosylation and activation of SHH in cancer stem cells of bladder cancer, promoting self-renewal and bladder tumorigenesis [273]. While unchanged in glioblastoma, GALNT1 expression is upregulated in liposarcoma upon GLI1 depletion; other glycotransferases such as GALNT10, 15, and 18 are upregulated in both cancers. N-linked glycosylation plays a pivotal role in neuronal differentiation [274] and is required for Smo trafficking [275]. The upregulation of the KEGG pathways ‘ECM receptor interaction’ and ‘cell adhesion molecules (CAMs)’ presumably promote a migratory phenotype, de-differentiation of tumour cells into CSCs, and help to establish favourable conditions that can serve as a niche for CSCs. In line with these studies, the upregulation of glycosylation pathways detected in GLI1-deficient glioblastoma and liposarcoma cell lines, as observed in this study, will likely affect stem cell characteristics in these cells and regulate survival and proliferation. These findings suggest the analysis of CSC-specific glycosyltransferase function and patterns as a means to identify new therapeutic targets and strategies to erase CSCs.

The observed downregulation of several DNA-repair and cell cycle regulation pathways was striking in GLI1-deficient glioblastoma and liposarcoma cells. Downregulated pathways included homologous recombination (HR), nucleotide-excision repair, base-excision repair, DNA replication, p53 signalling pathway, and cell cycle, indicating a global role for GLI1 in DNA damage response rather than the regulation of a specific DNA repair pathway. Cells with a deficiency in these pathways are generally more sensitive towards DNA-damaging agents and become senescent or undergo apoptosis if the damage remains unrepaired. Following DNA damage, the DNA damage response (DDR) signal is induced by phosphorylation of Ser139 of γH2AX, sensed by ATM and ATR kinases, and propagated to their downstream targets CHK1 and CHK2. These cell-cycle checkpoint components promote either DNA repair by homologous recombination, non-homologous end-joining, and other repair pathways or regulate cell cycle progression through CDK activity [276]. The observed role of GLI1 in DNA damage response is consistent with a study in human keratinocytes, in which GLI1 and GLI2 promoted apoptosis resistance upon UV-induced genotoxic stress [277]. Human colon carcinoma cells have provided the first evidence that inhibition of GLI1 with GANT61 increases DNA damage, inducing cell cycle arrest at G1–S and early S-phase, and cell death [278]. Treatment with DNA topoisomerase 1 inhibitor camptothecin induced DNA damage through replication stress and phosphorylation of CHK1. In this process, a potential role for GLI1 was proposed through transcriptional regulation of the Bid protein that ultimately promotes ATR-mediated signalling [279]. Deficiency in S-phase cell-cycle checkpoint will tolerate cell cycle progression of cells with unrepaired DNA damage, resulting in mitotic defects and cell death [280].

The proposed function of GLI1 in DNA damage response is further supported by evidence linking the upregulation of glycan-related pathways with DNA damage response [281]. For instance, DNA replication, mitosis, cytokinesis, and DNA damage response are regulated by O-GlcNAcylation, the post-translational modification of serine and threonine residues with O-linked N-acetylglucosamine [282, 283]. Moreover, phosphoproteomic analyses revealed that proteins regulating mitosis and cytokinesis, and many DDR proteins, including CHK1, are O-GlcNAcylated [284]. Additionally, O-GlcNAcylation fluctuates during cell cycle stages, regulating the stability and levels of cyclin A, B, and D [285]. Furthermore, increased O-GlcNAc levels were observed upon UV irradiation of cells [286], and γH2AX is O-GlcNAcylated at Ser139 upon DNA damage [287]. Whether O-GlcNAc controls DNA repair pathway responses to different types of DNA damage, and what role GLI1 might play in this regulation, has yet to be investigated. However, a deeper understanding of glycobiology in cancer can pave the way to new clinical therapies.

4.4 Identification of novel drug combinations in a preclinical drug screening

Even though the suppression of one gene can initially reduce tumour growth and induce regression, tumours typically compensate for the loss of this gene, and the tumour can recur. The combination of two or more compounds co-targeting multiple molecular mechanisms can provide benefits in the treatment of cancer patients and overcome the risks of drug resistance [184, 288]. This study used medium-throughput drug screening to systematically study the interaction of drug combinations, including compounds targeting the activity of GLI1 and DNA damage/cell cycle checkpoint regulators.

As anticipated, GLI1 inhibitors showed high sensitivity and selectivity as single agents in glioblastoma and liposarcoma models with high GLI1 expression, while they were less active in control cell lines with low GLI1 expression. As a nice proof-of-principle of the dDSS algorithm and the insensitivity to inhibition of the upstream HH pathway, BMS-833923, a Smoothened inhibitor, showed only effects at very high inhibitor concentrations with no difference between GLI1^{high} and GLI1^{low} cell lines. GlaB and JK184 were the most potent compounds amongst the tested GLI1/SHH inhibitors, with IC_{50} values of around 20 nM for JK184 and 500 nM for GlaB. JK184 is an imidazopyridine derivative with inhibitory effects of GLI1 transcriptional activity [289]. The exact mechanism of action has yet to be elucidated, but it has been shown to inhibit alcohol dehydrogenase 7 (Adh7) and microtubule assembly that, in turn, can regulate GLI1 function [290]. The described low pharmacokinetic profile and poor stability of JK184 might be overcome by improving its formulation. Encapsulation in polymeric micelles has been shown to prolong circulation time and increase the plasma concentration in pancreatic tumour models [291]. The potency to cross the blood-brain barrier has yet to be tested to prove its potency as a therapeutic drug in brain tumours.

The *in vitro* models used in the screen recapitulate the strong GLI1 activity observed in fusion-positive glioblastoma and liposarcoma tumours. However, they might still not fully represent the patient situation due to their long-term culture of the cell lines and associated acquired adaptations. Alternatively, primary patient-derived cell cultures can be used to profile drug sensitivities at the individual level and to accelerate the translation of *ex vivo* screening results into the clinics, providing a direct benefit for cancer patients [292]. For this reason, the patient-derived glioblastoma cell lines, U3071 and U3037, were included in the primary screening. However, the limitation in the expansion of the cells and culture requirements did not allow their use in the secondary screen to test drug combinations on a large scale.

Drug interactions in this study were scored using the Bliss independence method. It is a widely accepted model to measure drug synergy under the assumption that the two drugs in combination are non-interacting and targeting independent biological pathways [293]. The screening data provided the first hint that targeting the oncogene GLI1 in combination with members of the ATR/CHK1 pathway has a beneficial effect in patients with aberrant GLI1 expression. The most substantial synergistic effect was observed when the GLI1 inhibitors GlaB and JK184 were combined with the CHK1 inhibitors LY2606368 and GDC-0575, or the ATR inhibitor Berzosertib. Interestingly, previous reports have described that PTCH1 haploinsufficiency and associated GLI1 activation in mice impairs the ATR/CHK1 pathway upon radiation of the cerebellum, resulting in S-phase checkpoint defects and spontaneous development of medulloblastoma [294]. Besides its regulation of the G2/M checkpoint upon phosphorylation by ATR, CHK1 also phosphorylates BRCA2 and RAD51 proteins in response to DNA damage [295]. In line with these reports, simultaneous repression of GLI1 and CHK1 most likely blocks cell proliferation by defects in DNA damage response, replication stress accumulation, and cell cycle progression attenuation. Additional examples of synergistic drug interactions by interfering with non-canonical activation of Hedgehog signalling have been reported in the literature. A study in relapsed/refractory AML patients showed that the cell cycle regulation of GLI1 through its crosstalk with the PI3K/AKT pathway reduces drug sensitivity to the antimetabolite cytarabine (Ara-C), and the combined use of GLI1 and CDK4/6 inhibitors has a synergistic effect on Ara-c chemosensitivity [296]. Furthermore, non-canonical activation of GLI1 by the SOX2-BRD4 transcriptional complex in metastatic melanoma can be overcome by combinatorial treatment within this axis [297].

A significant limitation of the synergy scoring was represented by the used drug concentration range. The concentration matrices for all compounds were designed to fit the varying sensitivities of all cell models. As the responses in GLI1^{high} and GLI1^{low} expressing cells were very different for several compounds, especially towards GLI1/SHH inhibitors, the tested range of concentrations was not ideal for quantifying synergy for all combinations. In cell lines with a strong response towards these compounds, it would have been beneficial to test a range of lower concentrations according to the individual dose-response evaluated in the single-agent screen to characterise the drug interaction more accurately. This would have allowed a more accurate characterisation of drug interactions. Nevertheless, the applied screening approach, which was intended to provide a general idea of drug interaction between GLI1 and DNA repair inhibitors, successfully identified potent drug combinations for further validation.

4.5 Combined targeting of GLI1 and the ATR/CHK1 axis as a potential treatment for patients with aberrant GLI1 activity

The enhanced treatment effect of LY2606368, when combined with GlaB or JK184, was validated in matrix experiments followed by phenotypic assays studying proliferation and apoptosis upon treatment. For the evaluation of drug combination treatment, it is of interest to investigate whether and to what extent the treatment interferes with long-term proliferation and tumour cell survival. This is particularly important, since clinically relevant concentrations of inhibitors may not be sufficient to induce apoptosis but rather affect long-term tumour cell survival. The combination of GlaB and LY2606368 augmented the reduction in clonogenic potential compared to their use as single agents, while the effects on apoptosis were only marginal. These data indicate that reduction in proliferation, rather than cell death, is the major determinant for the long-term consequences of the drug treatment, an effect that is likely to be reflected in the clinical setting. Interestingly, the effects on cell death were stronger when LY2606368 was combined with JK184, which might be explained by the mitosis inhibitory function of JK184. If JK184, as proposed, interferes with microtubule assembly [290], it will generally stall mitosis and favour cell apoptosis. However, more importantly, this aspect raises concern about possible side effects of JK184, as it will also affect healthy proliferating cells in addition to interfering with GLI1-dependent cell proliferation.

Organoids are robust preclinical models to assess the neurotoxicity of chemical compounds and can help to predict the effectiveness of a specific compound in a patient [298, 299]. Before testing the drugs on tumour models, the initial toxicity study performed in cerebral organoid tissue determined drug doses with minimal toxicity for the organoid tissue. Based on these results, the concentrations used in the GLICO model was chosen and did not show any side effects on healthy tissue as quantified in the overall viability of organoid tissue after treatment. Moreover, the treatment study provided evidence that the combination of GlaB and LY2606368 reduces tumour growth by increasing apoptosis and decreasing the proliferative capacity of the tumour cells. The response in the combination treatment group was consistent in all organoids, whereas it varied in organoids treated with GLI1 inhibitor GlaB and CHK1 inhibitor LY2606368 alone. While the tumour initially regressed upon GlaB treatment in all organoids, one out of three regained proliferative capacity, resulting in a high tumour load at the end of the treatment, comparable to the tumour load in the control group. This suggests a potential compensation mechanism and the development of treatment resistance. Even though these results have yet to be confirmed in a larger set of samples to support further the claim that the drug combination of GlaB and LY2606368 can prevent resistance to individual agents, these results are indicative of patients' responsiveness to the proposed drug combination.

The GLICO organoid model provided a first estimate of the potential *in vivo* efficacy of the identified combination treatment. However, although organoids recapitulate many molecular features and characteristics of the human brain, the GLICO model still cannot replace *in vivo* testing due to several reasons. First, the model does not contain an immune system and thus cannot reproduce the immunosuppressive characteristics of the glioblastoma microenvironment [300]. Second, pharmacokinetic and pharmacodynamics studies to evaluate the stability and plasma-protein binding of pharmacologic compounds are difficult to interpret in models that are unhinged from the rest of the organism [301]. Third, the model does not contain a functional blood-brain barrier, which would be required to evaluate compounds for their use within the brain and to study their potency to traffic from the blood vessel into the central nervous system. These limitations illustrate that *in vivo* testing of the combination is inevitable as a further step. In collaboration with the groups of Prof. Bruno Botta and Prof Lucia Di Marcotullio from the University of Rome, the combination of GlaB and LY2606368 is currently tested in an LN308 orthotopic mouse model. As the compounds have not been tested in combination before, an initial toxicity study with different drug concentrations was performed to evaluate potential toxicities. No adverse effects were observed at the tested concentrations (25 mg/kg GlaB, 5 mg/kg LY2606368), providing a sound basis for the subsequent study of *in vivo* treatment efficacy in mice. The results of this study will enable a more profound conclusion on the efficacy of simultaneous targeting of GLI1 and CHK1 in tumours with aberrant GLI1 expression.

5 Conclusion

This study revealed that oncogenic *GLI1* fusion gene formation and transcriptional activation are frequent events in glioblastoma and soft-tissue sarcoma with amplification of chromosome bands 12q13-15. GLI1 knockdown and pharmacological inhibition reduced DNA-repair pathway activity and tumour-cell proliferation in cell line and organoid models. Preclinical drug screening combining GLI1 and DNA repair inhibitors indicated the concurrent targeting of the SHH/GLI1 and ATR/CHK1 axes as a precision-therapy approach for tumours with aberrant GLI1 expression. These findings potentially can be transferred to other cancers with high GLI1 expression or SHH-pathway activation. In future studies, it will be interesting to explore whether the observed combinatorial effect can be further enhanced when combined with radiotherapy or DNA-damaging compounds.

6 References

1. Hanahan, D. and R.A. Weinberg, *Hallmarks of cancer: the next generation.* Cell, 2011. **144**(5): p. 646-74.

2. Martincorena, I. and P.J. Campbell, *Somatic mutation in cancer and normal cells.* Science, 2015. **349**(6255): p. 1483-9.

3. Iyer, M.K., et al., *The landscape of long noncoding RNAs in the human transcriptome.* Nat Genet, 2015. **47**(3): p. 199-208.

4. Huarte, M., *The emerging role of lncRNAs in cancer.* Nat Med, 2015. **21**(11): p. 1253-61.

5. DiStefano, J.K., *The Emerging Role of Long Noncoding RNAs in Human Disease.* Methods Mol Biol, 2018. **1706**: p. 91-110.

6. Wang, L.H., et al., *Loss of Tumor Suppressor Gene Function in Human Cancer: An Overview.* Cell Physiol Biochem, 2018. **51**(6): p. 2647-2693.

7. Chang, E.H., et al., *Human genome contains four genes homologous to transforming genes of Harvey and Kirsten murine sarcoma viruses.* Proc Natl Acad Sci U S A, 1982. **79**(16): p. 4848-52.

8. Gabay, M., Y. Li, and D.W. Felsher, *MYC activation is a hallmark of cancer initiation and maintenance.* Cold Spring Harb Perspect Med, 2014. **4**(6).

9. Zhan, T., N. Rindtorff, and M. Boutros, *Wnt signaling in cancer.* Oncogene, 2017. **36**(11): p. 1461-1473.

10. Sattler, M. and J.D. Griffin, *Molecular mechanisms of transformation by the BCR-ABL oncogene.* Semin Hematol, 2003. **40**(2 Suppl 2): p. 4-10.

11. Prior, I.A., F.E. Hood, and J.L. Hartley, *The Frequency of Ras Mutations in Cancer.* 2020. **80**(14): p. 2969-2974.

12. Haluska, F.G., Y. Tsujimoto, and C.M. Croce, *Oncogene activation by chromosome translocation in human malignancy.* Annu Rev Genet, 1987. **21**: p. 321-45.

13. Lockwood, W.W., et al., *DNA amplification is a ubiquitous mechanism of oncogene activation in lung and other cancers.* Oncogene, 2008. **27**(33): p. 4615-4624.

14. Pon, J.R. and M.A. Marra, *Driver and Passenger Mutations in Cancer.* 2015. **10**(1): p. 25-50.

15. Stratton, M.R., P.J. Campbell, and P.A. Futreal, *The cancer genome.* Nature, 2009. **458**(7239): p. 719-724.

16. Martínez-Jiménez, F., et al., *A compendium of mutational cancer driver genes.* Nature Reviews Cancer, 2020. **20**(10): p. 555-572.

17. Kandoth, C., et al., *Mutational landscape and significance across 12 major cancer types.* Nature, 2013. **502**(7471): p. 333-339.

18. Campbell, P.J., et al., *Pan-cancer analysis of whole genomes.* Nature, 2020. **578**(7793): p. 82-93.

19. Davies, H., et al., *Mutations of the BRAF gene in human cancer.* Nature, 2002. **417**(6892): p. 949-954.

20. Minamoto, T., M. Mai, and Z. Ronai, *K-ras mutation: early detection in molecular diagnosis and risk assessment of colorectal, pancreas, and lung cancers--a review.* Cancer Detect Prev, 2000. **24**(1): p. 1-12.

21. Beaupre, D.M. and R. Kurzrock, *RAS and leukemia: from basic mechanisms to gene-directed therapy.* J Clin Oncol, 1999. **17**(3): p. 1071-9.

22. Albertson, D.G., *Gene amplification in cancer.* Trends Genet, 2006. **22**(8): p. 447-55.

23. Albertson, D.G., et al., *Chromosome aberrations in solid tumors.* Nat Genet, 2003. **34**(4): p. 369-76.

24. Feuk, L., A.R. Carson, and S.W. Scherer, *Structural variation in the human genome.* Nat Rev Genet, 2006. **7**(2): p. 85-97.

25. Lichter, P., *Multicolor FISHing: what's the catch?* Trends in Genetics, 1997. **13**(12): p. 475-479.

26. Li, Y., et al., *Patterns of somatic structural variation in human cancer genomes.* Nature, 2020. **578**(7793): p. 112-121.

27. Sanders, A.D., et al., *Single-cell analysis of structural variations and complex rearrangements with tri-channel processing.* Nat Biotechnol, 2020. **38**(3): p. 343-354.

28. Turner, K.M., et al., *Extrachromosomal oncogene amplification drives tumour evolution and genetic heterogeneity.* Nature, 2017. **543**(7643): p. 122-125.

29. Verhaak, R.G.W., V. Bafna, and P.S. Mischel, *Extrachromosomal oncogene amplification in tumour pathogenesis and evolution.* Nat Rev Cancer, 2019. **19**(5): p. 283-288.

30. Cox, D., C. Yuncken, and A.I. Spriggs, *Minute Chromatin Bodies in Malignant Tumours of Childhood.* Lancet, 1965. **1**(7402): p. 55-8.

31. Deshpande, V., et al., *Exploring the landscape of focal amplifications in cancer using AmpliconArchitect.* Nat Commun, 2019. **10**(1): p. 392.

32. deCarvalho, A.C., et al., *Discordant inheritance of chromosomal and extrachromosomal DNA elements contributes to dynamic disease evolution in glioblastoma.* Nat Genet, 2018. **50**(5): p. 708-717.

33. Campbell, P.J., et al., *Identification of somatically acquired rearrangements in cancer using genome-wide massively parallel paired-end sequencing.* Nat Genet, 2008. **40**(6): p. 722-9.

34. Seol, J.H., E.Y. Shim, and S.E. Lee, *Microhomology-mediated end joining: Good, bad and ugly.* Mutat Res, 2018. **809**: p. 81-87.

35. Glenfield, C. and H. Innan, *Gene Duplication and Gene Fusion Are Important Drivers of Tumourigenesis during Cancer Evolution.* 2021. **12**(9): p. 1376.

36. Reams, A.B. and J.R. Roth, *Mechanisms of gene duplication and amplification.* Cold Spring Harbor perspectives in biology, 2015. **7**(2): p. a016592-a016592.

37. Kinsella, M. and V. Bafna, *Combinatorics of the breakage-fusion-bridge mechanism.* J Comput Biol, 2012. **19**(6): p. 662-78.

38. Gisselsson, D., et al., *Chromosomal breakage-fusion-bridge events cause genetic intratumor heterogeneity.* 2000. **97**(10): p. 5357-5362.

39. Xing, R., et al., *Whole-genome sequencing reveals novel tandem-duplication hotspots and a prognostic mutational signature in gastric cancer.* Nat Commun, 2019. **10**(1): p. 2037.

40. Duijf, P.H., N. Schultz, and R. Benezra, *Cancer cells preferentially lose small chromosomes.* Int J Cancer, 2013. **132**(10): p. 2316-26.

41. Santarius, T., et al., *A census of amplified and overexpressed human cancer genes.* Nature Reviews Cancer, 2010. **10**(1): p. 59-64.

42. Borg, A., et al., *ERBB2 amplification in breast cancer with a high rate of proliferation.* Oncogene, 1991. **6**(1): p. 137-43.

43. Peiró, G., et al., *Analysis of HER-2/neu amplification in endometrial carcinoma by chromogenic in situ hybridization. Correlation with fluorescence in situ hybridization, HER-2/neu, p53 and Ki-67 protein expression, and outcome.* Modern Pathology, 2004. **17**(3): p. 277-287.

44. Oliner, J.D., A.Y. Saiki, and S. Caenepeel, *The Role of MDM2 Amplification and Overexpression in Tumorigenesis.* Cold Spring Harbor perspectives in medicine, 2016. **6**(6): p. a026336.

45. Ito, M., et al., *Comprehensive Mapping of p53 Pathway Alterations Reveals an Apparent Role for Both SNP309 and MDM2 Amplification in Sarcomagenesis.* 2011. **17**(3): p. 416-426.

46. Tuna, M., C.I. Amos, and G.B. Mills, *Molecular mechanisms and pathobiology of oncogenic fusion transcripts in epithelial tumors.* Oncotarget, 2019. **10**(21): p. 2095-2111.

47. Lobo, I., *Chromosome Abnormalities and Cancer Cytogenetics.* Nature Education, 2008. **1**(1): p. 68.

48. Luijten, M.N.H., J.X.T. Lee, and K.C. Crasta, *Mutational game changer: Chromothripsis and its emerging relevance to cancer.* Mutat Res Rev Mutat Res, 2018. **777**: p. 29-51.

49. Stephens, P.J., et al., *Massive genomic rearrangement acquired in a single catastrophic event during cancer development.* Cell, 2011. **144**(1): p. 27-40.

50. Voronina, N., et al., *The landscape of chromothripsis across adult cancer types.* Nature Communications, 2020. **11**(1): p. 2320.

51. Cortés-Ciriano, I., et al., *Comprehensive analysis of chromothripsis in 2,658 human cancers using whole-genome sequencing.* Nature Genetics, 2020. **52**(3): p. 331-341.

52. Shen, M.M., *Chromoplexy: a new category of complex rearrangements in the cancer genome.* Cancer cell, 2013. **23**(5): p. 567-569.

53. Baca, S.C., et al., *Punctuated evolution of prostate cancer genomes.* Cell, 2013. **153**(3): p. 666-677.

54. Nacu, S., et al., *Deep RNA sequencing analysis of readthrough gene fusions in human prostate adenocarcinoma and reference samples.* BMC Med Genomics, 2011. **4**: p. 11.

55. Akiva, P., et al., *Transcription-mediated gene fusion in the human genome.* Genome Res, 2006. **16**(1): p. 30-6.

56. Parra, G., et al., *Tandem chimerism as a means to increase protein complexity in the human genome.* Genome Res, 2006. **16**(1): p. 37-44.

57. McCartney, A.M., et al., *Gene Fusions Derived by Transcriptional Readthrough are Driven by Segmental Duplication in Human.* Genome Biol Evol, 2019. **11**(9): p. 2678-2690.

58. Nowell, P.C., *The minute chromosome (Phl) in chronic granulocytic leukemia.* Blut, 1962. **8**: p. 65-6.

59. Rowley, J.D., *Letter: A new consistent chromosomal abnormality in chronic myelogenous leukaemia identified by quinacrine fluorescence and Giemsa staining.* Nature, 1973. **243**(5405): p. 290-3.

60. Mertens, F., et al., *The emerging complexity of gene fusions in cancer.* Nat Rev Cancer, 2015. **15**(6): p. 371-81.

61. Calabrese, C., et al., *Genomic basis for RNA alterations in cancer.* Nature, 2020. **578**(7793): p. 129-136.

62. Yoshihara, K., et al., *The landscape and therapeutic relevance of cancer-associated transcript fusions.* Oncogene, 2015. **34**(37): p. 4845-54.

63. Gao, Q., et al., *Driver Fusions and Their Implications in the Development and Treatment of Human Cancers.* Cell Reports, 2018. **23**(1): p. 227-238.e3.

64. Stam, K., et al., *Evidence of a new chimeric bcr/c-abl mRNA in patients with chronic myelocytic leukemia and the Philadelphia chromosome.* N Engl J Med, 1985. **313**(23): p. 1429-33.

65. Clarke, M., et al., *Infant High-Grade Gliomas Comprise Multiple Subgroups Characterized by Novel Targetable Gene Fusions and Favorable Outcomes.* Cancer Discov, 2020. **10**(7): p. 942-963.

66. Ota, K., et al., *Induction of PD-L1 Expression by the EML4-ALK Oncoprotein and Downstream Signaling Pathways in Non-Small Cell Lung Cancer.* Clin Cancer Res, 2015. **21**(17): p. 4014-21.

67. Marzec, M., et al., *Oncogenic kinase NPM/ALK induces through STAT3 expression of immunosuppressive protein CD274 (PD-L1, B7-H1).* Proc Natl Acad Sci U S A, 2008. **105**(52): p. 20852-7.

68. Storlazzi, C.T., et al., *Biallelic somatic inactivation of the NF1 gene through chromosomal translocations in a sporadic neurofibroma.* Int J Cancer, 2005. **117**(6): p. 1055-7.

69. Duro, D., et al., *Inactivation of the P16INK4/MTS1 gene by a chromosome translocation t(9;14)(p21-22;q11) in an acute lymphoblastic leukemia of B-cell type.* Cancer Res, 1996. **56**(4): p. 848-54.

70. Parker, B.C., et al., *The tumorigenic FGFR3-TACC3 gene fusion escapes miR-99a regulation in glioblastoma.* J Clin Invest, 2013. **123**(2): p. 855-65.

71. Singh, D., et al., *Transforming fusions of FGFR and TACC genes in human glioblastoma.* Science, 2012. **337**(6099): p. 1231-5.

72. Zhang, Y., et al., *Chimeric transcript generated by cis-splicing of adjacent genes regulates prostate cancer cell proliferation.* Cancer Discov, 2012. **2**(7): p. 598-607.

73. Ye, C.J., Z. Sharpe, and H.H. Heng, *Origins and Consequences of Chromosomal Instability: From Cellular Adaptation to Genome Chaos-Mediated System Survival.* Genes (Basel), 2020. **11**(10).

74. Kanwal, R. and S. Gupta, *Epigenetic modifications in cancer.* Clin Genet, 2012. **81**(4): p. 303-11.

75. Wajed, S.A., P.W. Laird, and T.R. DeMeester, *DNA methylation: an alternative pathway to cancer.* Annals of surgery, 2001. **234**(1): p. 10-20.

76. Van Tongelen, A., A. Loriot, and C. De Smet, *Oncogenic roles of DNA hypomethylation through the activation of cancer-germline genes.* Cancer Lett, 2017. **396**: p. 130-137.

77. Aran, D. and A. Hellman, *DNA methylation of transcriptional enhancers and cancer predisposition.* Cell, 2013. **154**(1): p. 11-3.

78. Su, J., et al., *Homeobox oncogene activation by pan-cancer DNA hypermethylation.* Genome biology, 2018. **19**(1): p. 108-108.

79. Koelsche, C., et al., *Sarcoma classification by DNA methylation profiling.* Nat Commun, 2021. **12**(1): p. 498.

80. Sturm, D., et al., *Hotspot mutations in H3F3A and IDH1 define distinct epigenetic and biological subgroups of glioblastoma.* Cancer Cell, 2012. **22**(4): p. 425-37.

81. Noushmehr, H., et al., *Identification of a CpG island methylator phenotype that defines a distinct subgroup of glioma.* Cancer Cell, 2010. **17**(5): p. 510-22.

82. Esteller, M., *Cancer epigenomics: DNA methylomes and histone-modification maps.* Nat Rev Genet, 2007. **8**(4): p. 286-98.

83. Turner, B.M., *Reading signals on the nucleosome with a new nomenclature for modified histones.* Nat Struct Mol Biol, 2005. **12**(2): p. 110-2.

84. Hahn, M.A., et al., *Loss of the polycomb mark from bivalent promoters leads to activation of cancer-promoting genes in colorectal tumors.* Cancer Res, 2014. **74**(13): p. 3617-3629.

85. Peng, Y. and C.M. Croce, *The role of MicroRNAs in human cancer.* Signal Transduction and Targeted Therapy, 2016. **1**(1): p. 15004.

86. Wang, X., et al., *Regulation of let-7 and its target oncogenes (Review).* Oncol Lett, 2012. **3**(5): p. 955-960.

87. Johnson, C.D., et al., *The let-7 microRNA represses cell proliferation pathways in human cells.* Cancer Res, 2007. **67**(16): p. 7713-22.

88. Johnson, S.M., et al., *RAS Is Regulated by the let-7 MicroRNA Family.* Cell, 2005. **120**(5): p. 635-647.

89. Dou, H., et al., *Decreased plasma let-7c and miR-152 as noninvasive biomarker for non-small-cell lung cancer.* International journal of clinical and experimental medicine, 2015. **8**(6): p. 9291-9298.

90. Ghanbari, R., et al., *Simultaneous Underexpression of let-7a-5p and let-7f-5p microRNAs in Plasma and Stool Samples from Early Stage Colorectal Carcinoma.* Biomarkers in cancer, 2016. **7**(Suppl 1): p. 39-48.

91. Kadauke, S. and G.A. Blobel, *Chromatin loops in gene regulation.* Biochimica et biophysica acta, 2009. **1789**(1): p. 17-25.

92. Valton, A.L. and J. Dekker, *TAD disruption as oncogenic driver.* Curr Opin Genet Dev, 2016. **36**: p. 34-40.

93. Dixon, J.R., et al., *Topological domains in mammalian genomes identified by analysis of chromatin interactions.* Nature, 2012. **485**(7398): p. 376-80.

94. Akdemir, K.C., et al., *Disruption of chromatin folding domains by somatic genomic rearrangements in human cancer.* Nature Genetics, 2020. **52**(3): p. 294-305.

95. Flavahan, W.A., et al., *Insulator dysfunction and oncogene activation in IDH mutant gliomas.* Nature, 2016. **529**(7584): p. 110-4.

96. Northcott, P.A., et al., *Enhancer hijacking activates GFI1 family oncogenes in medulloblastoma.* Nature, 2014. **511**(7510): p. 428-34.

97. Tomlins, S.A., et al., *Recurrent fusion of TMPRSS2 and ETS transcription factor genes in prostate cancer.* Science, 2005. **310**(5748): p. 644-8.

98. Tomlins, S.A., et al., *Urine TMPRSS2:ERG fusion transcript stratifies prostate cancer risk in men with elevated serum PSA.* Sci Transl Med, 2011. **3**(94): p. 94ra72.

99. Druker, B.J., *Translation of the Philadelphia chromosome into therapy for CML.* Blood, 2008. **112**(13): p. 4808-17.

100. Capdeville, R., et al., *Glivec (STI571, imatinib), a rationally developed, targeted anticancer drug.* Nature Reviews Drug Discovery, 2002. **1**(7): p. 493-502.

101. Solomon, B. and J.C. Soria, *The continuum of care for ALK-positive NSCLC: from diagnosis to new treatment options - an overview.* Ann Oncol, 2016. **27 Suppl 3**: p. iii1-iii3.

102. Hong, D.S., et al., *Larotrectinib in patients with TRK fusion-positive solid tumours: a pooled analysis of three phase 1/2 clinical trials.* Lancet Oncol, 2020. **21**(4): p. 531-540.

103. Cocco, E., M. Scaltriti, and A. Drilon, *NTRK fusion-positive cancers and TRK inhibitor therapy.* Nature Reviews Clinical Oncology, 2018. **15**(12): p. 731-747.

104. Dean, L. and M. Kane, *Trastuzumab Therapy and ERBB2 Genotype*, in *Medical Genetics Summaries*, V.M. Pratt, et al., Editors. 2012, National Center for Biotechnology Information (US): Bethesda (MD).

105. von Minckwitz, G., et al., *Adjuvant Pertuzumab and Trastuzumab in Early HER2-Positive Breast Cancer.* 2017. **377**(2): p. 122-131.

106. Kinzler, K.W., et al., *Identification of an amplified, highly expressed gene in a human glioma.* Science, 1987. **236**(4797): p. 70-3.

107. Kinzler, K.W., et al., *The GLI gene is a member of the Kruppel family of zinc finger proteins.* Nature, 1988. **332**(6162): p. 371-4.

108. Kinzler, K.W. and B. Vogelstein, *The GLI gene encodes a nuclear protein which binds specific sequences in the human genome.* Mol Cell Biol, 1990. **10**(2): p. 634-42.

109. Dahmane, N. and A. Ruiz i Altaba, *Sonic hedgehog regulates the growth and patterning of the cerebellum.* Development, 1999. **126**(14): p. 3089-100.

110. Zhu, H. and H.-W. Lo, *The Human Glioma-Associated Oncogene Homolog 1 (GLI1) Family of Transcription Factors in Gene Regulation and Diseases.* Current genomics, 2010. **11**(4): p. 238-245.

111. Sasaki, H., et al., *Regulation of Gli2 and Gli3 activities by an amino-terminal repression domain: implication of Gli2 and Gli3 as primary mediators of Shh signaling.* 1999. **126**(17): p. 3915-3924.

112. Huntzicker, E.G., et al., *Dual degradation signals control Gli protein stability and tumor formation.* 2006. **20**(3): p. 276-281.

113. Hui, C.C. and S. Angers, *Gli proteins in development and disease.* Annu Rev Cell Dev Biol, 2011. **27**: p. 513-37.

114. Wheway, G., L. Nazlamova, and J.T. Hancock, *Signaling through the Primary Cilium.* 2018. **6**(8).

115. Taylor, R., et al., *Regulation of GLI1 by cis DNA elements and epigenetic marks.* DNA Repair, 2019. **79**: p. 10-21.

116. Chai, J.Y., et al., *The Role of Smoothened-Dependent and -Independent Hedgehog Signaling Pathway in Tumorigenesis.* Biomedicines, 2021. **9**(9).

117. Avery, J.T., R. Zhang, and R.J. Boohaker, *GLI1: A Therapeutic Target for Cancer.* 2021. **11**(1833).

118. Kenney, A.M. and D.H. Rowitch, *Sonic hedgehog Promotes G1 Cyclin Expression and Sustained Cell Cycle Progression in Mammalian Neuronal Precursors.* 2000. **20**(23): p. 9055-9067.

119. Li, Z.J., et al., *Evasion of p53 and G2/M checkpoints are characteristic of Hh-driven basal cell carcinoma.* Oncogene, 2014. **33**(20): p. 2674-2680.

120. Regl, G., et al., *Activation of the BCL2 Promoter in Response to Hedgehog/GLI Signal Transduction Is Predominantly Mediated by GLI2.* 2004. **64**(21): p. 7724-7731.

121. Epstein, E.H., *Basal cell carcinomas: attack of the hedgehog.* Nature reviews. Cancer, 2008. **8**(10): p. 743-754.

122. Kimura, H., et al., *Gli1 is important for medulloblastoma formation in Ptc1+/- mice.* Oncogene, 2005. **24**(25): p. 4026-36.

123. Clement, V., et al., *HEDGEHOG-GLI1 Signaling Regulates Human Glioma Growth, Cancer Stem Cell Self-Renewal, and Tumorigenicity.* Current Biology, 2007. **17**(2): p. 165-172.

124. Khatib, Z.A., et al., *Coamplification of the CDK4 gene with MDM2 and GLI in human sarcomas.* Cancer Res, 1993. **53**(22): p. 5535-41.

125. Bermudez, O., et al., *Gli1 mediates lung cancer cell proliferation and Sonic Hedgehog-dependent mesenchymal cell activation.* PLoS One, 2013. **8**(5): p. e63226.

126. Yang, Z., et al., *Gli1, a potential regulator of esophageal cancer stem cell, is identified as an independent adverse prognostic factor in esophageal squamous cell carcinoma.* J Cancer Res Clin Oncol, 2017. **143**(2): p. 243-254.

127. Fei, D.L., et al., *Hedgehog signaling regulates bladder cancer growth and tumorigenicity.* Cancer research, 2012. **72**(17): p. 4449-4458.

128. Villani, R.M., et al., *Patched1 Inhibits Epidermal Progenitor Cell Expansion and Basal Cell Carcinoma Formation by Limiting Igfbp2 Activity.* 2010. **3**(10): p. 1222-1234.

129. Jayaraman, S.S., et al., *Mutational Landscape of Basal Cell Carcinomas by Whole-Exome Sequencing.* Journal of Investigative Dermatology, 2014. **134**(1): p. 213-220.

130. Taylor, M.D., et al., *Mutations in SUFU predispose to medulloblastoma.* 2002. **31**(3): p. 306-310.

131. Yauch, R.L., et al., *Smoothened mutation confers resistance to a Hedgehog pathway inhibitor in medulloblastoma.* Science, 2009. **326**(5952): p. 572-4.

132. Po, A., et al., *Noncanonical GLI1 signaling promotes stemness features and in vivo growth in lung adenocarcinoma.* Oncogene, 2017. **36**(32): p. 4641-4652.

133. Rajurkar, M., et al., *The activity of Gli transcription factors is essential for Kras-induced pancreatic tumorigenesis.* Proc Natl Acad Sci U S A, 2012. **109**(17): p. E1038-47.

134. Yao, Y., et al., *GLI1 overexpression promotes gastric cancer cell proliferation and migration and induces drug resistance by combining with the AKT-mTOR pathway.* Biomed Pharmacother, 2019. **111**: p. 993-1004.

135. Kebenko, M., et al., *ErbB2 signaling activates the Hedgehog pathway via PI3K–Akt in human esophageal adenocarcinoma: Identification of novel targets for concerted therapy concepts.* Cellular Signalling, 2015. **27**(2): p. 373-381.

136. Rimkus, T.K., et al., *Targeting the Sonic Hedgehog Signaling Pathway: Review of Smoothened and GLI Inhibitors.* Cancers (Basel), 2016. **8**(2).

137. Robarge, K.D., et al., *GDC-0449-a potent inhibitor of the hedgehog pathway.* Bioorg Med Chem Lett, 2009. **19**(19): p. 5576-81.

138. Pan, S., et al., *Discovery of NVP-LDE225, a Potent and Selective Smoothened Antagonist.* ACS Med Chem Lett, 2010. **1**(3): p. 130-4.

139. Peer, E., S. Tesanovic, and F. Aberger, *Next-Generation Hedgehog/GLI Pathway Inhibitors for Cancer Therapy.* 2019. **11**(4): p. 538.

140. Pietrobono, S., S. Gagliardi, and B. Stecca, *Non-canonical Hedgehog Signaling Pathway in Cancer: Activation of GLI Transcription Factors Beyond Smoothened.* Frontiers in genetics, 2019. **10**: p. 556-556.

141. Calcaterra, A., et al., *Chemical, computational and functional insights into the chemical stability of the Hedgehog pathway inhibitor GANT61.* Journal of Enzyme Inhibition and Medicinal Chemistry, 2018. **33**(1): p. 349-358.

142. Agyeman, A., et al., *Mode and specificity of binding of the small molecule GANT61 to GLI determines inhibition of GLI-DNA binding.* Oncotarget, 2014. **5**(12): p. 4492-503.

143. Lauth, M., et al., *Inhibition of GLI-mediated transcription and tumor cell growth by small-molecule antagonists.* Proceedings of the National Academy of Sciences of the United States of America, 2007. **104**(20): p. 8455-8460.

144. Kim, J., et al., *Arsenic antagonizes the Hedgehog pathway by preventing ciliary accumulation and reducing stability of the Gli2 transcriptional effector.* Proc Natl Acad Sci U S A, 2010. **107**(30): p. 13432-7.

145. Beauchamp, E.M., et al., *Arsenic trioxide inhibits human cancer cell growth and tumor development in mice by blocking Hedgehog/GLI pathway.* J Clin Invest, 2011. **121**(1): p. 148-60.

146. Au, W.-Y., et al., *Determinants of cerebrospinal fluid arsenic concentration in patients with acute promyelocytic leukemia on oral arsenic trioxide therapy.* Blood, 2008. **112**(9): p. 3587-3590.

147. Infante, P., et al., *Gli1/DNA interaction is a druggable target for Hedgehog-dependent tumors.* EMBO J, 2015. **34**(2): p. 200-17.

148. Infante, P., et al., *Glabrescione B delivery by self-assembling micelles efficiently inhibits tumor growth in preclinical models of Hedgehog-dependent medulloblastoma.* Cancer Lett, 2021. **499**: p. 220-231.

149. Ostrom, Q.T., et al., *CBTRUS Statistical Report: Primary Brain and Other Central Nervous System Tumors Diagnosed in the United States in 2012-2016.* Neuro Oncol, 2019. **21**(Suppl 5): p. v1-v100.

150. Tan, A.C., et al., *Management of glioblastoma: State of the art and future directions.* CA Cancer J Clin, 2020. **70**(4): p. 299-312.

151. Stupp, R., et al., *Radiotherapy plus concomitant and adjuvant temozolomide for glioblastoma.* N Engl J Med, 2005. **352**(10): p. 987-96.

152. Lee, S.Y., *Temozolomide resistance in glioblastoma multiforme.* Genes Dis, 2016. **3**(3): p. 198-210.

153. Zhang, J., M.F. Stevens, and T.D. Bradshaw, *Temozolomide: mechanisms of action, repair and resistance.* Curr Mol Pharmacol, 2012. **5**(1): p. 102-14.

154. Parker, N.R., et al., *Molecular heterogeneity in glioblastoma: potential clinical implications.* Front Oncol, 2015. **5**: p. 55.

155. Louis, D.N., et al., *The 2007 WHO classification of tumours of the central nervous system.* Acta Neuropathol, 2007. **114**(2): p. 97-109.

156. Verhaak, R.G., et al., *Integrated genomic analysis identifies clinically relevant subtypes of glioblastoma characterized by abnormalities in PDGFRA, IDH1, EGFR, and NF1.* Cancer Cell, 2010. **17**(1): p. 98-110.

157. Brennan, C.W., et al., *The somatic genomic landscape of glioblastoma.* Cell, 2013. **155**(2): p. 462-77.

158. Zheng, S., et al., *A survey of intragenic breakpoints in glioblastoma identifies a distinct subset associated with poor survival.* Genes Dev, 2013. **27**(13): p. 1462-72.

159. Hui, A.B.-Y., et al., *Detection of Multiple Gene Amplifications in Glioblastoma Multiforme Using Array-Based Comparative Genomic Hybridization.* Laboratory Investigation, 2001. **81**(5): p. 717-723.

160. Mao, X. and R.A. Hamoudi, *Molecular and cytogenetic analysis of glioblastoma multiforme.* Cancer Genet Cytogenet, 2000. **122**(2): p. 87-92.

161. Becher, O.J., et al., *Gli Activity Correlates with Tumor Grade in Platelet-Derived Growth Factor–Induced Gliomas.* 2008. **68**(7): p. 2241-2249.

162. Takezaki, T., et al., *Essential role of the Hedgehog signaling pathway in human glioma-initiating cells.* Cancer Sci, 2011. **102**(7): p. 1306-12.

163. Melamed, J.R., et al., *Investigating the role of Hedgehog/GLI1 signaling in glioblastoma cell response to temozolomide.* Oncotarget, 2018. **9**(43): p. 27000-27015.

164. Liu, Y.J., et al., *Combination therapy with micellarized cyclopamine and temozolomide attenuate glioblastoma growth through Gli1 down-regulation.* Oncotarget, 2017. **8**(26): p. 42495-42509.

165. Doyle, L.A., *Sarcoma classification: an update based on the 2013 World Health Organization Classification of Tumors of Soft Tissue and Bone.* Cancer, 2014. **120**(12): p. 1763-74.

166. WHO Classification of Tumours, *WHO Editorial Board WHO Classification of Tumours: Soft Tissue and Bone Tumours, 5th Ed. 978-92-8324502-5 (IARC)*. Vol. 3. 2020.

167. Weidema, M.E., et al., *DNA Methylation Profiling Identifies Distinct Clusters in Angiosarcomas.* Clin Cancer Res, 2020. **26**(1): p. 93-100.

168. Watson, S., et al., *Transcriptomic definition of molecular subgroups of small round cell sarcomas.* J Pathol, 2018. **245**(1): p. 29-40.

169. Trama, A., et al., *Soft tissue sarcoma in Italy: From epidemiological data to clinical networking to improve patient care and outcomes.* Cancer Epidemiol, 2019. **59**: p. 258-264.

170. RARECAREnet, P.J.D.a.i.h.w.r.e.r., *Information Network on Rare Cancers.* 2014.

171. Linch, M., et al., *Systemic treatment of soft-tissue sarcoma-gold standard and novel therapies.* Nat Rev Clin Oncol, 2014. **11**(4): p. 187-202.

172. Cancer Genome Atlas Research Network. Electronic address, e.d.s.c. and N. Cancer Genome Atlas Research, *Comprehensive and Integrated Genomic Characterization of Adult Soft Tissue Sarcomas.* Cell, 2017. **171**(4): p. 950-965 e28.

173. Roberts, W.M., et al., *Amplification of the gli Gene in Childhood Sarcomas.* 1989. **49**(19): p. 5407-5413.

174. Khatib, Z.A., et al., *Coamplification of the CDK4 Gene with MDM2 and GLI in Human Sarcomas.* 1993. **53**(22): p. 5535-5541.

175. Stein, U., et al., *GLI Gene Expression in Bone and Soft Tissue Sarcomas of Adult Patients Correlates with Tumor Grade.* 1999. **59**(8): p. 1890-1895.

176. Yoon, J.W., et al., *Up-regulation of GLI1 in vincristine-resistant rhabdomyosarcoma and Ewing sarcoma.* BMC Cancer, 2020. **20**(1): p. 511.

177. Mertens, F., C.R. Antonescu, and F. Mitelman, *Gene fusions in soft tissue tumors: Recurrent and overlapping pathogenetic themes.* 2016. **55**(4): p. 291-310.

178. Lee, A.T.J., et al., *Clinical and Molecular Spectrum of Liposarcoma.* J Clin Oncol, 2018. **36**(2): p. 151-159.

179. Italiano, A., et al., *Clinical and biological significance of CDK4 amplification in well-differentiated and dedifferentiated liposarcomas.* Clin Cancer Res, 2009. **15**(18): p. 5696-703.

180. Johannessen, C.M., et al., *COT drives resistance to RAF inhibition through MAP kinase pathway reactivation.* Nature, 2010. **468**(7326): p. 968-72.

181. Emery, C.M., et al., *MEK1 mutations confer resistance to MEK and B-RAF inhibition.* Proc Natl Acad Sci U S A, 2009. **106**(48): p. 20411-6.

182. Nazarian, R., et al., *Melanomas acquire resistance to B-RAF(V600E) inhibition by RTK or N-RAS upregulation.* Nature, 2010. **468**(7326): p. 973-7.

183. Felsher, D.W., *Cancer revoked: oncogenes as therapeutic targets.* Nature Reviews Cancer, 2003. **3**(5): p. 375-379.

184. Bayat Mokhtari, R., et al., *Combination therapy in combating cancer.* Oncotarget, 2017. **8**(23): p. 38022-38043.

185. Mukherjee, B., et al., *EGFRvIII and DNA double-strand break repair: a molecular mechanism for radioresistance in glioblastoma.* Cancer Res, 2009. **69**(10): p. 4252-9.

186. Ghosh, D., S. Nandi, and S. Bhattacharjee, *Combination therapy to checkmate Glioblastoma: clinical challenges and advances.* Clin Transl Med, 2018. **7**(1): p. 33.

187. Wang, H., et al., *Combination therapy in a xenograft model of glioblastoma: enhancement of the antitumor activity of temozolomide by an MDM2 antagonist.* J Neurosurg, 2017. **126**(2): p. 446-459.

188. Lesueur, P., et al., *Radiosensitization Effect of Talazoparib, a Parp Inhibitor, on Glioblastoma Stem Cells Exposed to Low and High Linear Energy Transfer Radiation.* Sci Rep, 2018. **8**(1): p. 3664.

189. Lesueur, P., et al., *Poly-(ADP-ribose)-polymerase inhibitors as radiosensitizers: a systematic review of pre-clinical and clinical human studies.* Oncotarget, 2017. **8**(40): p. 69105-69124.

190. Li, E.X., et al., *[Effect of modified MAID regimen for patients with advanced soft tissue sarcoma].* Ai Zheng, 2006. **25**(8): p. 1048-51.

191. Pant, A., J.R. Lurain, and J.C. Schink, *Mesna, doxorubicin, ifosfamide, and dacarbazine (MAID) chemotherapy for treatment of metastatic or recurrent uterine leiomyosarcoma.* 2012. **30**(15_suppl): p. e15523-e15523.

192. Hensley, M.L., et al., *Gemcitabine and docetaxel in patients with unresectable leiomyosarcoma: results of a phase II trial.* J Clin Oncol, 2002. **20**(12): p. 2824-31.

193. Hensley, M.L., *Update on gemcitabine and docetaxel combination therapy for primary and metastatic sarcomas.* Curr Opin Oncol, 2010. **22**(4): p. 356-61.

194. Zöllner, S.K., et al., *Inhibition of the oncogenic fusion protein EWS-FLI1 causes G(2)-M cell cycle arrest and enhanced vincristine sensitivity in Ewing's sarcoma.* Sci Signal, 2017. **10**(499).

195. Ziebarth, J.D., A. Bhattacharya, and Y. Cui, *CTCFBSDB 2.0: a database for CTCF-binding sites and genome organization.* Nucleic Acids Res, 2013. **41**(Database issue): p. D188-94.

196. Bao, L., M. Zhou, and Y. Cui, *CTCFBSDB: a CTCF-binding site database for characterization of vertebrate genomic insulators.* Nucleic Acids Res, 2008. **36**(Database issue): p. D83-7.

197. Fornes, O., et al., *JASPAR 2020: update of the open-access database of transcription factor binding profiles.* Nucleic Acids Res, 2020. **48**(D1): p. D87-D92.

198. Kim, T.H., et al., *Analysis of the vertebrate insulator protein CTCF-binding sites in the human genome.* Cell, 2007. **128**(6): p. 1231-45.

199. Sanjana, N.E., O. Shalem, and F. Zhang, *Improved vectors and genome-wide libraries for CRISPR screening.* Nat Methods, 2014. **11**(8): p. 783-784.

200. Shalem, O., et al., *Genome-scale CRISPR-Cas9 knockout screening in human cells.* Science, 2014. **343**(6166): p. 84-87.

201. Yadav, B., et al., *Quantitative scoring of differential drug sensitivity for individually optimized anticancer therapies.* Sci Rep, 2014. **4**: p. 5193.

202. Di Veroli, G.Y., et al., *Combenefit: an interactive platform for the analysis and visualization of drug combinations.* Bioinformatics, 2016. **32**(18): p. 2866-8.

203. Lancaster, M.A. and J.A. Knoblich, *Generation of cerebral organoids from human pluripotent stem cells.* Nat Protoc, 2014. **9**(10): p. 2329-40.

204. Wu, Y., et al., *Glioblastoma epigenome profiling identifies SOX10 as a master regulator of molecular tumour subtype.* Nat Commun, 2020. **11**(1): p. 6434.

205. Sanchez-Vega, F., et al., *Oncogenic Signaling Pathways in The Cancer Genome Atlas.* Cell, 2018. **173**(2): p. 321-337 e10.

206. Huang, Z., et al., *confFuse: High-Confidence Fusion Gene Detection across Tumor Entities.* Front Genet, 2017. **8**: p. 137.

207. Gajduskova, P., et al., *Genome position and gene amplification.* Genome Biol, 2007. **8**(6): p. R120.

208. Coquelle, A., et al., *Expression of fragile sites triggers intrachromosomal mammalian gene amplification and sets boundaries to early amplicons.* Cell, 1997. **89**(2): p. 215-25.

209. Shahi, M.H., et al., *Regulation of sonic hedgehog-GLI1 downstream target genes PTCH1, Cyclin D2, Plakoglobin, PAX6 and NKX2.2 and their epigenetic status in medulloblastoma and astrocytoma.* BMC Cancer, 2010. **10**: p. 614.

210. Wang, S., et al., *FOXS1 is regulated by GLI1 and miR-125a-5p and promotes cell proliferation and EMT in gastric cancer.* Sci Rep, 2019. **9**(1): p. 5281.

211. Vokes, S.A., et al., *Genomic characterization of Gli-activator targets in sonic hedgehog-mediated neural patterning.* Development, 2007. **134**(10): p. 1977-89.

212. Vokes, S.A., et al., *A genome-scale analysis of the cis-regulatory circuitry underlying sonic hedgehog-mediated patterning of the mammalian limb.* Genes Dev, 2008. **22**(19): p. 2651-63.

213. Katoh, Y. and M. Katoh, *Hedgehog target genes: mechanisms of carcinogenesis induced by aberrant hedgehog signaling activation.* Curr Mol Med, 2009. **9**(7): p. 873-86.

214. Diao, Y., et al., *Identification of novel GLI1 target genes and regulatory circuits in human cancer cells.* Mol Oncol, 2018. **12**(10): p. 1718-1734.

215. Chen, K., et al., *BreakDancer: an algorithm for high-resolution mapping of genomic structural variation.* Nat Methods, 2009. **6**(9): p. 677-81.

216. Torres-Garcia, W., et al., *PRADA: pipeline for RNA sequencing data analysis.* Bioinformatics, 2014. **30**(15): p. 2224-6.

217. Marino-Enriquez, A. and J.V. Bovee, *Molecular Pathogenesis and Diagnostic, Prognostic and Predictive Molecular Markers in Sarcoma.* Surg Pathol Clin, 2016. **9**(3): p. 457-73.

218. Creytens, D., et al., *Characterization of the 12q amplicons in lipomatous soft tissue tumors by multiplex ligation-dependent probe amplification-based copy number analysis.* Anticancer Res, 2015. **35**(4): p. 1835-42.

219. Rowley, M.J. and V.G. Corces, *Organizational principles of 3D genome architecture.* Nat Rev Genet, 2018. **19**(12): p. 789-800.

220. Lupianez, D.G., et al., *Disruptions of topological chromatin domains cause pathogenic rewiring of gene-enhancer interactions.* Cell, 2015. **161**(5): p. 1012-1025.

221. Hnisz, D., et al., *Activation of proto-oncogenes by disruption of chromosome neighborhoods.* Science, 2016. **351**(6280): p. 1454-1458.

222. Akdemir, K.C., et al., *Disruption of chromatin folding domains by somatic genomic rearrangements in human cancer.* Nat Genet, 2020. **52**(3): p. 294-305.

223. Lee, T.I. and R.A. Young, *Transcriptional regulation and its misregulation in disease.* Cell, 2013. **152**(6): p. 1237-51.

224. Javelaud, D., M.J. Pierrat, and A. Mauviel, *Crosstalk between TGF-beta and hedgehog signaling in cancer.* FEBS Lett, 2012. **586**(14): p. 2016-25.

225. Dennler, S., et al., *Induction of sonic hedgehog mediators by transforming growth factor-beta: Smad3-dependent activation of Gli2 and Gli1 expression in vitro and in vivo.* Cancer Res, 2007. **67**(14): p. 6981-6.

226. Dennler, S., et al., *Cloning of the human GLI2 Promoter: transcriptional activation by transforming growth factor-beta via SMAD3/beta-catenin cooperation.* J Biol Chem, 2009. **284**(46): p. 31523-31.

227. Dietlein, F., L. Thelen, and H.C. Reinhardt, *Cancer-specific defects in DNA repair pathways as targets for personalized therapeutic approaches.* Trends Genet, 2014. **30**(8): p. 326-39.

228. Malone, E.R., et al., *Molecular profiling for precision cancer therapies.* Genome Medicine, 2020. **12**(1): p. 8.

229. Yates, L.R., et al., *The European Society for Medical Oncology (ESMO) Precision Medicine Glossary.* Ann Oncol, 2018. **29**(1): p. 30-35.

230. Patel, A.P., et al., *Single-cell RNA-seq highlights intratumoral heterogeneity in primary glioblastoma.* Science, 2014. **344**(6190): p. 1396-401.

231. Sottoriva, A., et al., *Intratumor heterogeneity in human glioblastoma reflects cancer evolutionary dynamics.* Proc Natl Acad Sci U S A, 2013. **110**(10): p. 4009-14.

232. Korber, V., et al., *Evolutionary Trajectories of IDH(WT) Glioblastomas Reveal a Common Path of Early Tumorigenesis Instigated Years ahead of Initial Diagnosis.* Cancer Cell, 2019. **35**(4): p. 692-704 e12.

233. Lens, S.M.A. and R.H. Medema, *Cytokinesis defects and cancer.* Nature Reviews Cancer, 2019. **19**(1): p. 32-45.

234. Duijf, P.H.G., N. Schultz, and R. Benezra, *Cancer cells preferentially lose small chromosomes.* 2013. **132**(10): p. 2316-2326.

235. Bakhoum, S.F. and L.C. Cantley, *The Multifaceted Role of Chromosomal Instability in Cancer and Its Microenvironment.* Cell, 2018. **174**(6): p. 1347-1360.

236. Kalyana-Sundaram, S., et al., *Gene fusions associated with recurrent amplicons represent a class of passenger aberrations in breast cancer.* Neoplasia (New York, N.Y.), 2012. **14**(8): p. 702-708.

237. Mitelman, F., F. Mertens, and B. Johansson, *Prevalence estimates of recurrent balanced cytogenetic aberrations and gene fusions in unselected patients with neoplastic disorders.* Genes Chromosomes Cancer, 2005. **43**(4): p. 350-66.

238. Dalla-Favera, R., et al., *Human c-myc onc gene is located on the region of chromosome 8 that is translocated in Burkitt lymphoma cells.* Proc Natl Acad Sci U S A, 1982. **79**(24): p. 7824-7.

239. Taub, R., et al., *Translocation of the c-myc gene into the immunoglobulin heavy chain locus in human Burkitt lymphoma and murine plasmacytoma cells.* Proc Natl Acad Sci U S A, 1982. **79**(24): p. 7837-41.

240. Erikson, J., et al., *Translocation of an immunoglobulin kappa locus to a region 3' of an unrearranged c-myc oncogene enhances c-myc transcription.* Proc Natl Acad Sci U S A, 1983. **80**(24): p. 7581-5.

241. Bao, Z.S., et al., *RNA-seq of 272 gliomas revealed a novel, recurrent PTPRZ1-MET fusion transcript in secondary glioblastomas.* Genome Res, 2014. **24**(11): p. 1765-73.

242. Tabernero, J., et al., *Phase I Dose-Escalation Study of JNJ-42756493, an Oral Pan-Fibroblast Growth Factor Receptor Inhibitor, in Patients With Advanced Solid Tumors.* J Clin Oncol, 2015. **33**(30): p. 3401-8.

243. Mitelman, F., et al., *Cancer chromosome breakpoints cluster in gene-rich genomic regions.* 2019. **58**(3): p. 149-154.

244. Shimokawa, T., et al., *Novel human glioma-associated oncogene 1 (GLI1) splice variants reveal distinct mechanisms in the terminal transduction of the hedgehog signal.* J Biol Chem, 2008. **283**(21): p. 14345-54.

245. Lo, H.W., et al., *A novel splice variant of GLI1 that promotes glioblastoma cell migration and invasion.* Cancer Res, 2009. **69**(17): p. 6790-8.

246. Tanaka, H. and T. Watanabe, *Mechanisms Underlying Recurrent Genomic Amplification in Human Cancers.* Trends in cancer, 2020. **6**(6): p. 462-477.

247. Haas, B.J., et al., *Accuracy assessment of fusion transcript detection via read-mapping and de novo fusion transcript assembly-based methods.* Genome Biology, 2019. **20**(1): p. 213.

248. Ferretti, E., et al., *Concerted microRNA control of Hedgehog signalling in cerebellar neuronal progenitor and tumour cells.* The EMBO journal, 2008. **27**(19): p. 2616-2627.

249. Huntzicker, E.G., et al., *Dual degradation signals control Gli protein stability and tumor formation.* Genes Dev, 2006. **20**(3): p. 276-81.

250. Dahlén, A., C. Fletcher, and F. Mertens, *Activation of the GLI oncogene through fusion with the beta-actin gene (ACTB) in a group of distinctive pericytic neoplasms: pericytoma with t(7;12).* 2004. **164**: p. 1645-1653.

251. Bridge, J.A., et al., *Pericytoma with t(7;12) and ACTB-GLI1 fusion arising in bone.* Human Pathology, 2012. **43**(9): p. 1524-1529.

252. Rollins, B.T., D.S. Cassarino, and M. Lindberg, *Primary cutaneous epithelioid mesenchymal neoplasm with ACTB-GLI1 fusion: a case report.* J Cutan Pathol, 2021.

253. Spans, L., et al., *Recurrent MALAT1–GLI1 oncogenic fusion and GLI1 up-regulation define a subset of plexiform fibromyxoma.* 2016. **239**(3): p. 335-343.

254. Alwaqfi, R.R., et al., *PTCH1-GLI1 Fusion–Positive Ovarian Tumor: Report of a Unique Case With Response to Tyrosine Kinase Inhibitor Pazopanib %J Journal of the National Comprehensive Cancer Network.* 2021. **19**(9): p. 998-1004.

255. Xu, B., et al., *Head and Neck Mesenchymal Neoplasms With GLI1 Gene Alterations: A Pathologic Entity With Distinct Histologic Features and Potential for Distant Metastasis.* 2020. **44**(6): p. 729-737.

256. Antonescu, C.R., et al., *A Distinct Malignant Epithelioid Neoplasm With GLI1 Gene Rearrangements, Frequent S100 Protein Expression, and Metastatic Potential: Expanding the Spectrum of Pathologic Entities With ACTB/MALAT1/PTCH1-GLI1 Fusions.* Am J Surg Pathol, 2018. **42**(4): p. 553-560.

257. Agaram, N.P., et al., *GLI1-amplifications expand the spectrum of soft tissue neoplasms defined by GLI1 gene fusions.* Mod Pathol, 2019. **32**(11): p. 1617-1626.

258. Po, A., et al., *Hedgehog controls neural stem cells through p53-independent regulation of Nanog.* Embo j, 2010. **29**(15): p. 2646-58.

259. Clement, V., et al., *HEDGEHOG-GLI1 signaling regulates human glioma growth, cancer stem cell self-renewal, and tumorigenicity.* Curr Biol, 2007. **17**(2): p. 165-72.

260. Ayob, A.Z. and T.S. Ramasamy, *Cancer stem cells as key drivers of tumour progression.* Journal of Biomedical Science, 2018. **25**(1): p. 20.

261. Valenti, G., et al., *Cancer Stem Cells Regulate Cancer-Associated Fibroblasts via Activation of Hedgehog Signaling in Mammary Gland Tumors.* Cancer Res, 2017. **77**(8): p. 2134-2147.

262. Liu, S., et al., *Hedgehog signaling and Bmi-1 regulate self-renewal of normal and malignant human mammary stem cells.* Cancer research, 2006. **66**(12): p. 6063-6071.

263. Yan, G.-N., et al., *Endothelial cells promote stem-like phenotype of glioma cells through activating the Hedgehog pathway.* 2014. **234**(1): p. 11-22.

264. Von Hoff, D.D., et al., *Inhibition of the hedgehog pathway in advanced basal-cell carcinoma.* N Engl J Med, 2009. **361**(12): p. 1164-72.

265. Pricl, S., et al., *Smoothened (SMO) receptor mutations dictate resistance to vismodegib in basal cell carcinoma.* Molecular oncology, 2015. **9**(2): p. 389-397.

266. Sharpe, H.J., et al., *Genomic analysis of smoothened inhibitor resistance in basal cell carcinoma.* Cancer cell, 2015. **27**(3): p. 327-341.

267. Baldo, B.A. and N.H. Pham, *Adverse reactions to targeted and non-targeted chemotherapeutic drugs with emphasis on hypersensitivity responses and the invasive metastatic switch.* Cancer Metastasis Rev, 2013. **32**(3-4): p. 723-61.

268. Javelaud, D., M.J. Pierrat, and A. Mauviel, *Crosstalk between TGF-β and hedgehog signaling in cancer.* FEBS Lett, 2012. **586**(14): p. 2016-25.

269. Khan, T. and H. Cabral, *Abnormal Glycosylation of Cancer Stem Cells and Targeting Strategies.* Front Oncol, 2021. **11**: p. 649338.

270. Barkeer, S., et al., *Glycosylation of Cancer Stem Cells: Function in Stemness, Tumorigenesis, and Metastasis.* Neoplasia, 2018. **20**(8): p. 813-825.

271. Pietrobono, S., et al., *ST3GAL1 is a target of the SOX2-GLI1 transcriptional complex and promotes melanoma metastasis through AXL.* Nature Communications, 2020. **11**(1): p. 5865.

272. Das, S., et al., *O-GlcNAcylation of GLI transcription factors in hyperglycemic conditions augments Hedgehog activity.* Laboratory investigation; a journal of technical methods and pathology, 2019. **99**(2): p. 260-270.

273. Li, C., et al., *GALNT1-Mediated Glycosylation and Activation of Sonic Hedgehog Signaling Maintains the Self-Renewal and Tumor-Initiating Capacity of Bladder Cancer Stem Cells.* 2016. **76**(5): p. 1273-1283.

274. Kimura, K., et al., *Glycoproteomic analysis of the changes in protein N-glycosylation during neuronal differentiation in human-induced pluripotent stem cells and derived neuronal cells.* Scientific Reports, 2021. **11**(1): p. 11169.

275. Marada, S., et al., *Functional Divergence in the Role of N-Linked Glycosylation in Smoothened Signaling.* PLoS Genet, 2015. **11**(8): p. e1005473.

276. Jackson, S.P. and J. Bartek, *The DNA-damage response in human biology and disease.* Nature, 2009. **461**(7267): p. 1071-1078.

277. Harrison, W., et al., *The oncogenic GLI transcription factors facilitate keratinocyte survival and transformation upon exposure to genotoxic agents.* Oncogene, 2014. **33**(19): p. 2432-2440.

278. Mazumdar, T., et al., *Blocking Hedgehog survival signaling at the level of the GLI genes induces DNA damage and extensive cell death in human colon carcinoma cells.* Cancer research, 2011. **71**(17): p. 5904-5914.

279. Tripathi, K., et al., *Gli1 protein regulates the S-phase checkpoint in tumor cells via Bid protein, and its inhibition sensitizes to DNA topoisomerase 1 inhibitors.* J Biol Chem, 2014. **289**(45): p. 31513-25.

280. Palle, K., et al., *Aberrant GLI1 Activation in DNA Damage Response, Carcinogenesis and Chemoresistance.* Cancers (Basel), 2015. **7**(4): p. 2330-51.

281. Liu, C. and J. Li, *O-GlcNAc: A Sweetheart of the Cell Cycle and DNA Damage Response.* Front Endocrinol (Lausanne), 2018. **9**: p. 415.

282. Drougat, L., et al., *Characterization of O-GlcNAc cycling and proteomic identification of differentially O-GlcNAcylated proteins during G1/S transition.* Biochimica et Biophysica Acta (BBA) - General Subjects, 2012. **1820**(12): p. 1839-1848.

283. Fong, J.J., et al., *β-N-Acetylglucosamine (O-GlcNAc) Is a Novel Regulator of Mitosis-specific Phosphorylations on Histone H3*.* Journal of Biological Chemistry, 2012. **287**(15): p. 12195-12203.

284. Zhong, J., et al., *Quantitative phosphoproteomics reveals crosstalk between phosphorylation and O-GlcNAc in the DNA damage response pathway.* 2015. **15**(2-3): p. 591-607.

285. Slawson, C., et al., *Perturbations in O-linked β-N-Acetylglucosamine Protein Modification Cause Severe Defects in Mitotic Progression and Cytokinesis*.* Journal of Biological Chemistry, 2005. **280**(38): p. 32944-32956.

286. Zachara, N.E., et al., *Dynamic O-GlcNAc Modification of Nucleocytoplasmic Proteins in Response to Stress: A SURVIVAL RESPONSE OF MAMMALIAN CELLS*.* Journal of Biological Chemistry, 2004. **279**(29): p. 30133-30142.

287. Chen, Q. and X. Yu, *OGT restrains the expansion of DNA damage signaling.* Nucleic Acids Research, 2016. **44**(19): p. 9266-9278.

288. Al-Lazikani, B., U. Banerji, and P. Workman, *Combinatorial drug therapy for cancer in the post-genomic era.* Nature Biotechnology, 2012. **30**(7): p. 679-692.

289. Lee, J., et al., *A Small-Molecule Antagonist of the Hedgehog Signaling Pathway.* 2007. **8**(16): p. 1916-1919.

290. Cupido, T., et al., *The Imidazopyridine Derivative JK184 Reveals Dual Roles for Microtubules in Hedgehog Signaling.* 2009. **48**(13): p. 2321-2324.

291. Zhang, N., et al., *Biodegradable polymeric micelles encapsulated JK184 suppress tumor growth through inhibiting Hedgehog signaling pathway.* Nanoscale, 2015. **7**(6): p. 2609-2624.

292. Crystal, A.S., et al., *Patient-derived models of acquired resistance can identify effective drug combinations for cancer.* Science, 2014. **346**(6216): p. 1480-6.

293. Zhao, W., et al., *A New Bliss Independence Model to Analyze Drug Combination Data.* J Biomol Screen, 2014. **19**(5): p. 817-21.

294. Leonard , J.M., et al., *Sonic Hedgehog signaling impairs ionizing radiation–induced checkpoint activation and induces genomic instability.* Journal of Cell Biology, 2008. **183**(3): p. 385-391.

295. Bahassi, E.M., et al., *The checkpoint kinases Chk1 and Chk2 regulate the functional associations between hBRCA2 and Rad51 in response to DNA damage.* Oncogene, 2008. **27**(28): p. 3977-85.

296. Zhou, C., et al., *GLI1 reduces drug sensitivity by regulating cell cycle through PI3K/AKT/GSK3/CDK pathway in acute myeloid leukemia.* Cell Death & Disease, 2021. **12**(3): p. 231.

297. Pietrobono, S., et al., *Targeting non-canonical activation of GLI1 by the SOX2-BRD4 transcriptional complex improves the efficacy of HEDGEHOG pathway inhibition in melanoma.* Oncogene, 2021. **40**(22): p. 3799-3814.

298. Schwartz, M.P., et al., *Human pluripotent stem cell-derived neural constructs for predicting neural toxicity.* 2015. **112**(40): p. 12516-12521.

299. Sun, N., et al., *Applications of brain organoids in neurodevelopment and neurological diseases.* Journal of Biomedical Science, 2021. **28**(1): p. 30.

300. DeCordova, S., et al., *Molecular Heterogeneity and Immunosuppressive Microenvironment in Glioblastoma.* Front Immunol, 2020. **11**: p. 1402.

301. Lee, M.W., et al., *Current methods in translational cancer research.* Cancer and Metastasis Reviews, 2021. **40**(1): p. 7-30.

A Supplementary Information

List of supplementary material

Supplementary material 1: Summary of HIPO016 patient data. 142
Supplementary material 2: Structural rearrangement plots of *GLI1* fusion-positive tumours. 144
Supplementary material 3: CNV plots of H043-63R6 primary and recurrent tumours. 145
Supplementary material 4: CNV plots of glioblastoma and liposarcoma cell lines. 146
Supplementary material 5: Common downregulated genes in U3071 glioblastoma and T778 liposarcoma cell lines upon GLI1 knockdown. 147
Supplementary material 6: Common upregulated genes in U3071 glioblastoma and T778 liposarcoma cell lines upon GLI1 knockdown. 149
Supplementary material 7: Dose-response curves of all compounds tested in the primary screen. 151
Supplementary material 8: Bliss surface plots of GLI1/SHH inhibitors and DNA repair inhibitors. 155
Supplementary material 9: Bliss surface plots of GLI1/SHH inhibitors and CHK1 inhibitors in glioblastoma. 156
Supplementary material 10: Bliss surface plots of GLI1/SHH inhibitors and ATR inhibitor in glioblastoma. 157
Supplementary material 11: Combination treatment of JK184 and LY2606368 in T778 and LN308 cells. 158
Supplementary material 12: Cell apoptosis in T778 cells upon single and combination treatment with JK184 and LY2606368. 159

Supplementary material 1: Summary of HIPO016 patient data. Information on age, sex, DNA-methylation subtype, OS, PFS, *IDH1/2* mutation status, copy number status of individual chromosomes and genes from 60 adult primary glioblastoma tumours, analysed in the HIPO016 cohort. OS: overall survival, PFS: progression-free survival. Adapted from Wu et al., 2020 [204].

Sample ID	**diagnosis**	**WHO grade**	**survival status**	**OS (months)**	**progression**	**PFS (months)**	**DNA-methylation subtype**	**IDH1 mutaton status**	**IDH2 mutation status**	**chr7 gain**	**chr10 loss**	**chr10q loss**	**chr19 gain**	**chr20 gain**	**EGFR amplification**	**PTEN deletion**	**MDM2 amplification**	**MDM4 amplification**	**PDGFRA amplification**	**CDKN2A/B deletion**	**CDK4 amplification**	**GLI1 amplification**	**GLI1 fusion gene**
AK015	primary glioblastoma	IV	alive	24	0	24	IDH	R132H	wt	0	0	0	0	0	0	0	0	0	0	0	0	0	0
AK041	primary glioblastoma	IV	alive	27	0	27	IDH	R132H	wt	0	0	0	0	0	0	0	0	0	0	0	0	0	0
AK066	primary glioblastoma	IV	alive	32	0	32	IDH	R132H	wt	1	0	0	0	0	0	0	0	0	0	0	0	0	0
AK068	primary glioblastoma	IV	alive	12	0	12	IDH	R132H	wt	0	0	0	0	0	0	0	0	0	0	1	0	0	0
AK076	primary glioblastoma	IV	alive	22	0	22	IDH	R132H	wt	0	0	1	0	0	0	0	0	0	0	0	0	0	0
AK085	primary glioblastoma	IV	alive	22	1	16	IDH	R132H	wt	0	0	0	0	0	0	0	0	0	0	0	0	0	0
AK102	primary glioblastoma	IV	alive	58	0	58	IDH	R132H	wt	0	0	0	0	0	0	0	0	0	0	1	0	0	0
AK103	primary glioblastoma	IV	alive	44	0	44	IDH	R132H	wt	0	0	1	0	0	1	0	0	0	0	0	1	0	0
AK124	primary glioblastoma	IV	alive	64	0	64	IDH	R132H	wt	0	0	1	0	0	0	0	0	0	0	0	0	0	0
AK199	primary glioblastoma	IV	alive	62	0	62	IDH	R132H	wt	0	0	1	0	0	0	0	0	0	0	0	1	0	0
AK213	primary glioblastoma	IV	alive	67	1	48	IDH	R132H	wt	1	0	0	0	0	0	0	0	0	0	0	0	0	0
AK231	primary glioblastoma	IV	dead	8	1	4	IDH	R132H	wt	0	0	1	0	0	0	0	0	0	0	0	0	0	0
AK005	primary glioblastoma	IV	dead	8	1	6	MES	wt	wt	0	1	0	0	0	0	0	0	1	0	0	0	0	0
AK006	primary glioblastoma	IV	dead	12	1	8	MES	wt	wt	1	0	0	0	0	0	0	0	1	0	0	0	0	0
AK030	primary glioblastoma	IV	dead	4	1	3	MES	wt	wt	0	0	0	0	0	0	0	0	0	0	0	0	0	0
AK055	primary glioblastoma	IV	dead	8	1	6	MES	wt	wt	1	1	0	0	0	1	0	0	0	0	1	0	0	0
AK071	primary glioblastoma	IV	dead	18	1	14	MES	wt	wt	1	1	0	0	0	1	0	0	0	0	1	1	1	0
AK072	primary glioblastoma	IV	dead	5	1	3	MES	wt	wt	1	1	0	0	0	1	1	0	0	0	1	0	0	0
AK079	primary glioblastoma	IV	dead	7	1	3	MES	wt	wt	0	1	0	0	0	0	0	1	0	0	0	1	0	0
AK081	primary glioblastoma	IV	dead	6	1	3	MES	wt	wt	1	1	0	0	0	1	0	0	1	0	0	0	0	0
AK088	primary glioblastoma	IV	dead	12	1	3	MES	wt	wt	1	0	0	0	1	0	0	0	0	0	1	0	0	0
AK091	primary glioblastoma	IV	dead	7	1	3	MES	wt	wt	1	1	0	0	0	1	0	0	0	0	1	0	0	0
AK134	primary glioblastoma	IV	dead	12	1	8	MES	wt	wt	0	1	0	0	0	0	0	0	0	0	0	1	0	0
AK139	primary glioblastoma	IV	dead	9	1	14	MES	wt	wt	1	1	0	0	0	0	0	0	0	0	1	0	0	0
AK153	primary glioblastoma	IV	dead	8	1	5	MES	wt	wt	0	0	0	0	0	0	0	0	0	0	0	0	0	0
AK185	primary glioblastoma	IV	alive	11	0	11	MES	wt	wt	1	0	0	0	0	1	0	0	1	0	0	0	0	0
AK188	primary glioblastoma	IV	alive	14	0	14	MES	wt	wt	0	1	0	0	0	1	0	0	0	0	0	0	0	0
AK195	primary glioblastoma	IV	dead	13	1	10	MES	wt	wt	1	0	0	0	0	0	0	0	0	0	0	0	0	0
AK218	primary glioblastoma	IV	dead	6	1	3	MES	wt	wt	1	1	0	0	0	0	0	1	0	1	1	0	0	0
AK227	primary glioblastoma	IV	alive	10	0	10	MES	wt	wt	1	0	0	0	0	0	0	0	0	0	0	0	0	0

Continued from the previous page

Sample ID	diagnosis	WHO grade	survival status	OS (months)	progression	PFS (months)	DNA-methylation subtype	IDH1 mutaton status	IDH2 mutation status	chr7 gain	chr10 loss	chr10q loss	chr19 gain	chr20 gain	EGFR amplification	PTEN deletion	MDM2 amplification	MDM4 amplification	PDGFRA amplification	CDKN2A/B deletion	CDK4 amplification	GLI1 amplification	GLI1 fusion gene
AK236	primary glioblastoma	IV	dead	12	1	8	MES	wt	wt	0	0	0	0	0	0	0	0	0	0	0	0	0	0
AK002	primary glioblastoma	IV	dead	19	1	15	RTK I	wt	wt	0	0	1	0	0	0	0	0	0	1	1	0	0	0
AK003	primary glioblastoma	IV	dead	20	1	17	RTK I	wt	wt	0	1	0	0	0	0	0	1	0	1	0	1	0	0
AK043	primary glioblastoma	IV	alive	22	0	22	RTK I	wt	wt	0	0	0	0	0	0	0	0	0	1	0	1	0	0
AK049	primary glioblastoma	IV	dead	6	1	3	RTK I	wt	wt	1	1	0	0	0	0	0	0	1	0	1	0	0	0
AK051	primary glioblastoma	IV	dead	12	1	8	RTK I	wt	wt	0	1	0	0	0	0	1	0	0	0	1	0	0	0
AK142	primary glioblastoma	IV	alive	3	0	3	RTK I	wt	wt	1	1	0	0	0	1	0	1	0	0	0	1	0	0
AK149	primary glioblastoma	IV	dead	14	1	10	RTK I	wt	wt	1	1	0	0	0	0	1	0	0	1	1	0	0	0
AK156	primary glioblastoma	IV	dead	11	1	6	RTK I	wt	wt	0	1	0	0	0	0	0	0	0	0	1	0	0	0
AK165	primary glioblastoma	IV	alive	12	0	10	RTK I	wt	wt	1	1	0	0	0	0	0	1	0	0	0	1	1	1
AK173	primary glioblastoma	IV	dead	6	1	3	RTK I	wt	wt	1	0	1	0	0	0	0	0	0	0	0	1	1	1
AK183	primary glioblastoma	IV	alive	12	0	12	RTK I	wt	wt	0	1	0	0	0	0	0	0	0	0	0	1	1	0
AK217	primary glioblastoma	IV	NA	NA	NA	NA	RTK I	wt	wt	0	0	0	0	0	0	0	0	0	1	1	0	0	0
AK035	primary glioblastoma	IV	dead	7	1	4	RTK II	wt	wt	1	1	0	0	1	1	0	0	0	0	1	0	0	0
AK053	primary glioblastoma	IV	dead	10	1	4	RTK II	wt	wt	1	1	0	1	1	1	0	1	0	0	0	1	1	1
AK074	primary glioblastoma	IV	alive	10	0	10	RTK II	wt	wt	1	1	0	1	1	1	0	0	0	0	0	0	0	0
AK089	primary glioblastoma	IV	dead	11	1	6	RTK II	wt	wt	1	1	0	1	0	1	0	0	0	0	1	0	0	0
AK098	primary glioblastoma	IV	dead	22	1	16	RTK II	wt	wt	1	1	0	1	0	1	0	0	0	0	1	0	0	0
AK099	primary glioblastoma	IV	dead	14	1	10	RTK II	wt	wt	1	1	0	1	1	1	0	0	0	0	0	0	0	0
AK100	primary glioblastoma	IV	alive	32	1	22	RTK II	wt	wt	1	1	0	1	0	1	0	0	0	0	0	1	1	1
AK117	primary glioblastoma	IV	dead	7	1	5	RTK II	wt	wt	1	1	0	1	1	1	0	0	0	0	1	0	0	0
AK123	primary glioblastoma	IV	dead	6	1	3	RTK II	wt	wt	0	1	0	1	1	1	0	0	0	0	1	0	0	0
AK132	primary glioblastoma	IV	NA	NA	NA	NA	RTK II	wt	wt	1	1	0	0	0	0	0	0	0	1	1	0	0	0
AK133	primary glioblastoma	IV	dead	12	1	8	RTK II	wt	wt	0	1	0	1	0	1	0	0	0	0	1	0	0	0
AK158	primary glioblastoma	IV	dead	12	1	4	RTK II	wt	wt	1	1	0	1	1	1	0	0	1	0	1	0	0	0
AK167	primary glioblastoma	IV	dead	6	1	3	RTK II	wt	wt	0	1	0	0	0	0	0	0	0	0	0	0	0	0
AK178	primary glioblastoma	IV	dead	8	1	6	RTK II	wt	wt	1	1	0	1	0	1	0	0	0	0	1	0	0	0
AK205	primary glioblastoma	IV	dead	4	1	2	RTK II	wt	wt	0	1	0	0	0	1	0	0	0	0	1	0	0	0
AK216	primary glioblastoma	IV	dead	12	1	7	RTK II	wt	wt	1	1	0	0	0	0	1	0	0	0	0	0	0	0
AK226	primary glioblastoma	IV	dead	12	1	8	RTK II	wt	wt	1	1	0	1	1	1	0	0	0	0	1	0	0	0

Supplementary material 2: Structural rearrangement plots of *GLI1* fusion-positive tumours. Genomic breakpoints and structural rearrangements are detected from whole-genome sequencing (WGS) data using the SOPHIA algorithm. Genomic breakpoints in chromosome 12 identified in WGS data confirm the breakpoints in RNA-seq data-derived fusion transcripts. SOPHIA analysis from all HIPO016 samples was performed by Dr Umut Toprak (DKFZ, Heidelberg). The figure depicts only tumours with detected *GLI1* fusion genes.

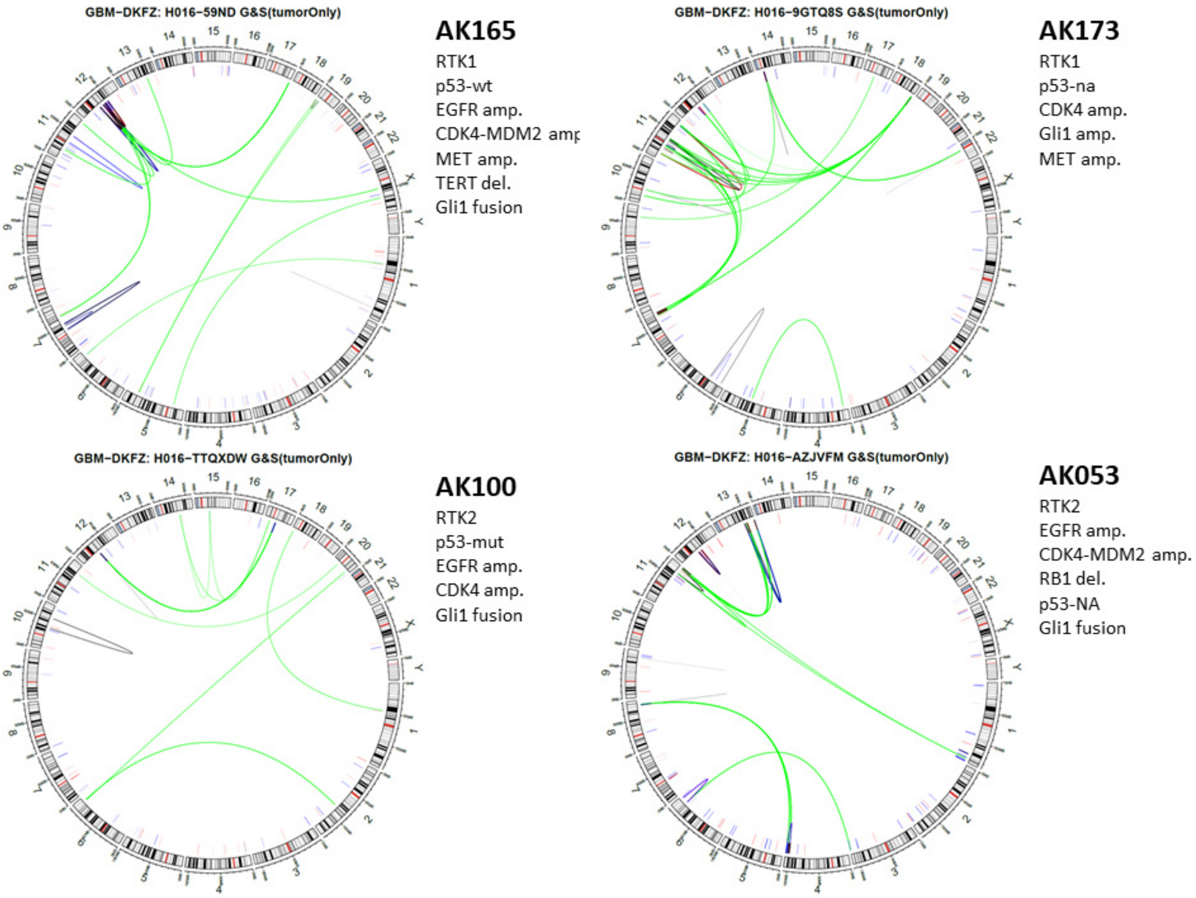

Supplementary material 3: CNV plots of H043-63R6 primary and recurrent tumours. A + B CNV plots derived from 450k/EPIC array DNA methylation for glioblastoma primary (A) and recurrent tumour (B) of patient H043-63R6 from the HIPO043 cohort. The DNA copy number profiles in chromosome 12 show a focal *CDK4* amplification in the primary tumour that is expanded in the recurrent tumour, including also the *GLI1* locus. **C** DNA methylation β-values at the GLI1 and CDK4 loci in the primary and recurrent tumour of patient H043-63R6.

A

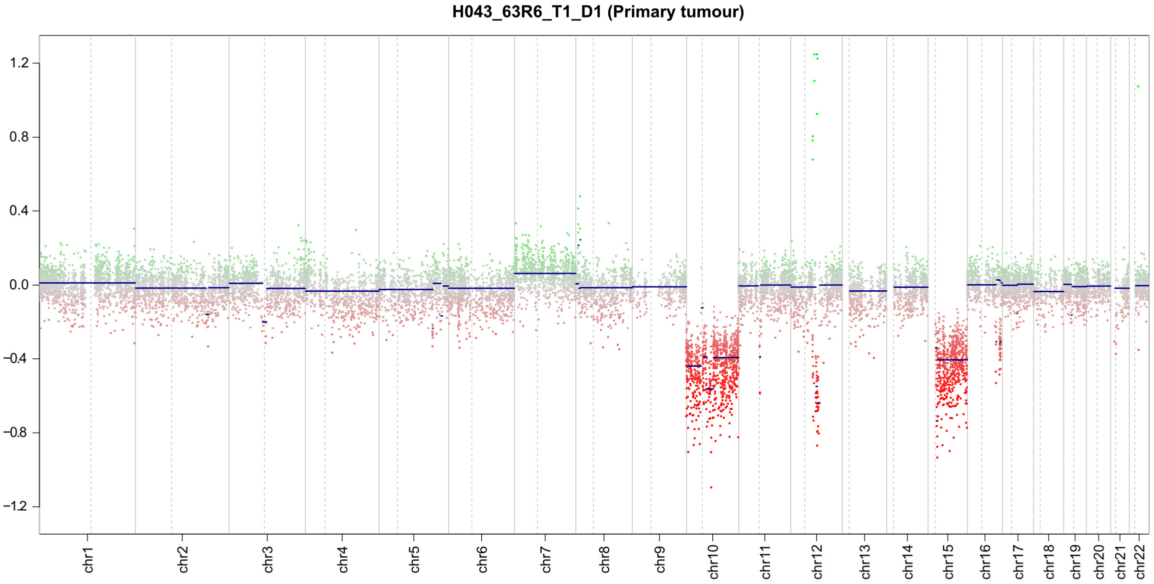

B

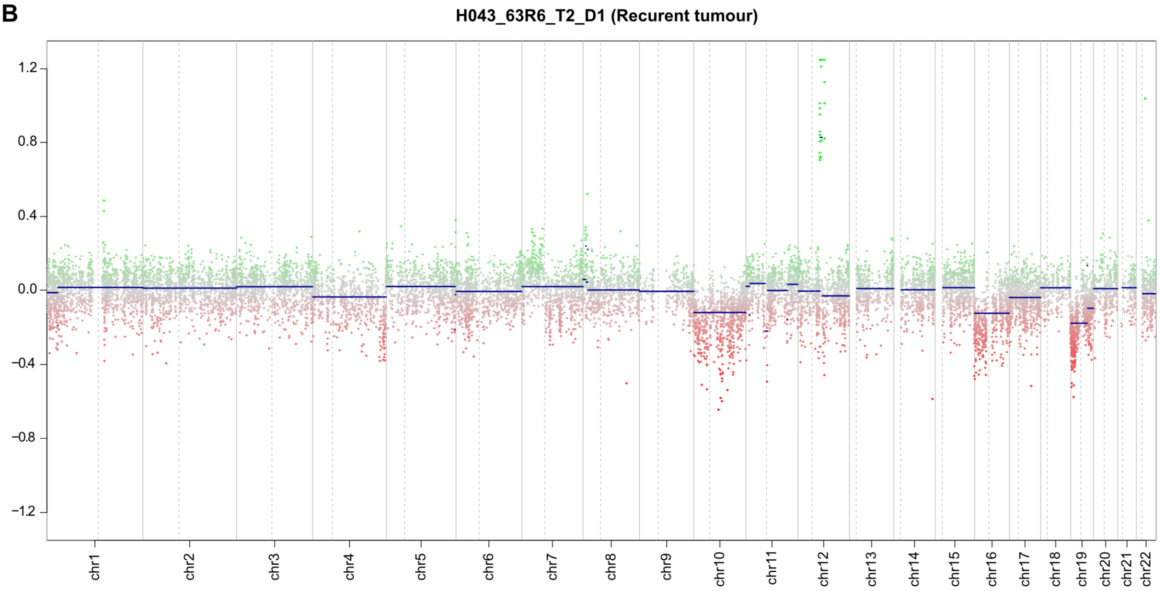

C

Locus	Primary tumour H043-63R6_T1	Recurrent tumour H043-63R6_T2
Chr12:57850000 – 57900000 (GLI1)	-0.296	0.861
Chr12:58100000 – 58150000 (CDK4)	0.784	0.986

Supplementary material 4: CNV plots of glioblastoma and liposarcoma cell lines. CNV plots derived from 450k/EPIC array DNA methylation for patient-derived glioblastoma cell lines U3071 and U3037, and liposarcoma cell lines T778 (WDLS, tumour recurrence) and T449 (WDLS, primary tumour).

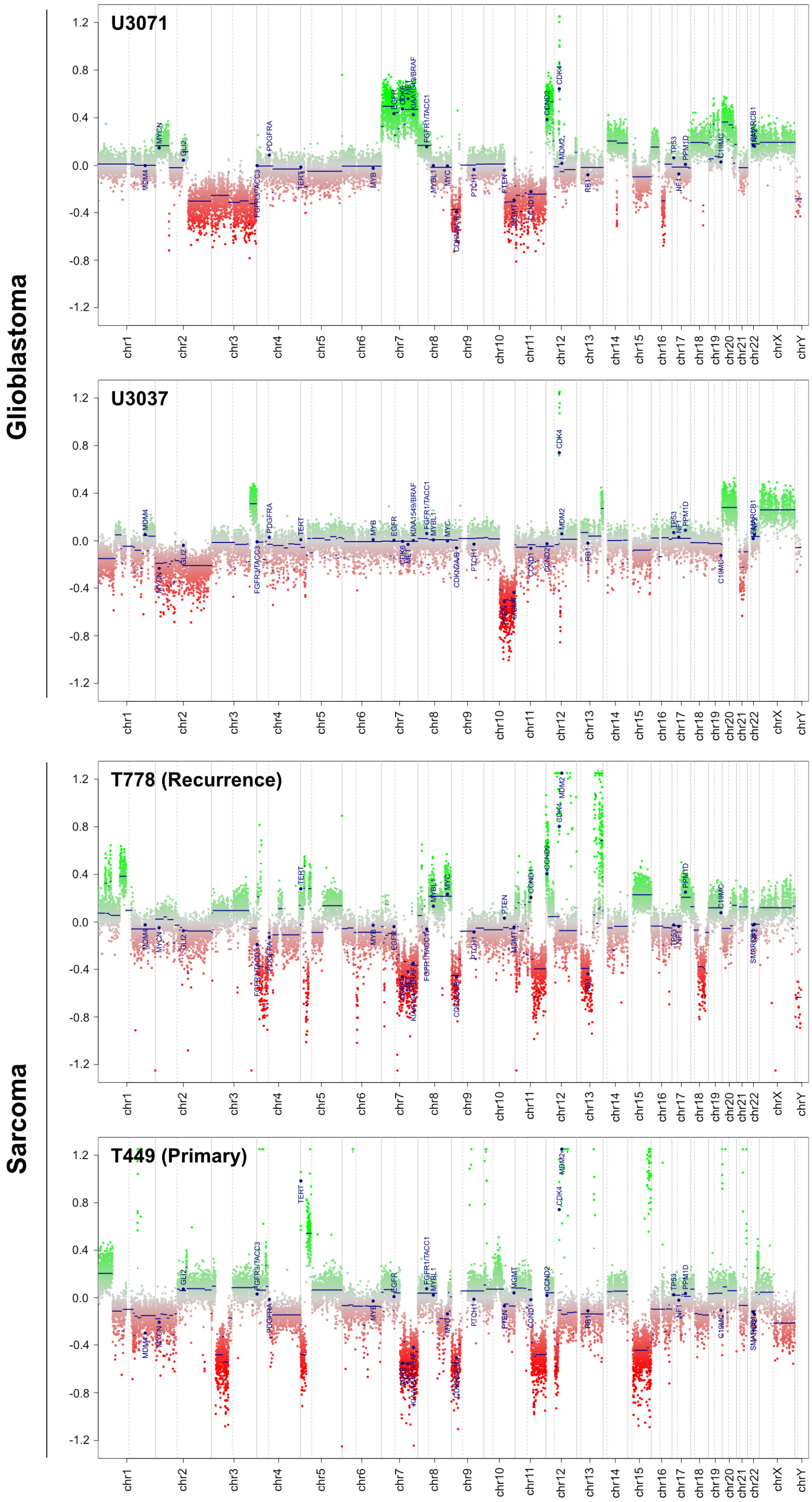

Supplementary material 5: Common downregulated genes in U3071 glioblastoma and T778 liposarcoma cell lines upon GLI1 knockdown. Genes with logFC < -1.5, ranked based on logFC of shGLI1 vs. shNT in U3071 cells.

Gene name	Ensembl gene	U3071 logFC (shGLI1 vs. shNT)	T778 logFC (shGLI1 vs. shNT)
LITAF	ENSG00000189067	-3.211286727	-4.324050975
PTPRJ	ENSG00000149177	-2.890390087	-2.672634619
PCDHGC3	ENSG00000240184	-2.873298162	-2.824261823
RP11-93B14.5	ENSG00000232803	-2.800953056	-2.505295678
SLCO4A1	ENSG00000101187	-2.716818519	-4.33085666
SOSTDC1	ENSG00000171243	-2.696767541	-5.130464777
GLI1	ENSG00000111087	-2.681205701	-6.037224557
RP11-332K15.1	ENSG00000232524	-2.543537076	-4.763090602
GLTP	ENSG00000139433	-2.533026245	-2.216429781
KRT17	ENSG00000128422	-2.373113283	-1.508051527
IMPA2	ENSG00000141401	-2.341437384	-2.325745692
RASSF3	ENSG00000153179	-2.339654976	-2.177725278
HEXB	ENSG00000049860	-2.278022193	-2.530011553
RGS16	ENSG00000143333	-2.266157413	-1.97295303
RTN4R	ENSG00000040608	-2.256396294	-1.504076355
TMED10	ENSG00000170348	-2.192766503	-1.593573313
RAB21	ENSG00000080371	-2.178669664	-2.143148126
SLC39A6	ENSG00000141424	-2.146853437	-1.686682671
ERBB3	ENSG00000065361	-2.118963156	-2.636479084
HCN2	ENSG00000099822	-1.978271252	-1.547158452
CMTM4	ENSG00000183723	-1.971882154	-2.330955543
TUBG1	ENSG00000131462	-1.945854167	-2.40972959
LINC00639	ENSG00000259070	-1.933274256	-1.994363386
PAQR6	ENSG00000160781	-1.908381366	-2.554047371
SNORD66	ENSG00000212158	-1.899110233	-1.903315384
SOX8	ENSG00000005513	-1.893351942	-2.558915377
PRKCD	ENSG00000163932	-1.865852983	-1.643168547
AC005702.3	ENSG00000265638	-1.864289694	-2.159814211
PTPLAD1	ENSG00000074696	-1.850333191	-2.097228235
SMIM14	ENSG00000163683	-1.832481449	-1.928595404
MTMR12	ENSG00000150712	-1.817870219	-1.710015728
EDEM1	ENSG00000134109	-1.816791618	-2.102667244
NIPSNAP3A	ENSG00000136783	-1.777410451	-1.67001299
PPIAP9	ENSG00000219797	-1.762096884	-1.77341133

Gene name	Ensembl gene	U3071 logFC (shGLI1 vs. shNT)	T778 logFC (shGLI1 vs. shNT)
ERLIN1	ENSG00000107566	-1.743259268	-2.47126631
RP11-599J14.2	ENSG00000256673	-1.718546582	-2.107818627
SLC29A4	ENSG00000164638	-1.716142388	-1.568364046
MCCC2	ENSG00000131844	-1.708619871	-1.569439474
SLC7A5	ENSG00000103257	-1.706982229	-2.052729845
RP11-598P20.3	ENSG00000254198	-1.703021813	-2.309794688
FREM1	ENSG00000164946	-1.698790132	-4.934029844
CSF1	ENSG00000184371	-1.688277414	-1.978757774
ANKRD9	ENSG00000156381	-1.685966298	-1.933873436
WBP1L	ENSG00000166272	-1.643732225	-1.744551463
C11orf96	ENSG00000187479	-1.634596685	-4.364486557
FOXO3	ENSG00000118689	-1.626219253	-1.680629395
SAT1	ENSG00000130066	-1.625822309	-2.895185557
FSTL3	ENSG00000070404	-1.61847222	-1.7065482
PELI1	ENSG00000197329	-1.601604114	-1.79161325
HIST2H2AC	ENSG00000184260	-1.585055766	-1.912347122
RAB4A	ENSG00000168118	-1.571948985	-1.852033424
SOCS1	ENSG00000185338	-1.568819102	-3.109742489
DIRAS1	ENSG00000176490	-1.554909239	-2.365078001
SHISA5	ENSG00000164054	-1.554217892	-1.571943651
RP11-343B18.2	ENSG00000259676	-1.536705826	-1.664721788
RP11-161M6.2	ENSG00000260807	-1.53464567	-2.466869021
RP11-861E21.1	ENSG00000267108	-1.512168858	-1.702359658

Supplementary material 6: Common upregulated genes in U3071 glioblastoma and T778 liposarcoma cell lines upon GLI1 knockdown. Genes with logFC > 1.5, ranked based on logFC of shGLI1 vs. shNT in U3071 cells.

Gene name	Ensembl gene	U3071 logFC (shGLI1_vs._shNT)	T778 logFC (shGLI1_vs._shNT)
GUCY1A3	ENSG00000164116	3.119979465	2.4337778
MMP13	ENSG00000137745	2.539817554	2.680194197
RNU6-1098P	ENSG00000252581	2.51985426	1.820549815
RGS1	ENSG00000090104	2.464855619	4.514998038
SLC20A1	ENSG00000144136	2.282297044	2.227735227
ARPC3	ENSG00000111229	2.240956833	2.016249201
AC112721.2	ENSG00000222032	2.182587162	4.791105274
MMP1	ENSG00000196611	2.112372523	1.968624891
CMKLR1	ENSG00000174600	2.033882013	5.552245622
PLXNA4	ENSG00000221866	2.021007114	2.259341321
DDO	ENSG00000203797	1.934536196	2.368213759
RP11-399D6.2	ENSG00000234840	1.914827902	4.272109678
ACPP	ENSG00000014257	1.906452294	1.814826958
RP11-620J15.1	ENSG00000257953	1.895447949	4.112191875
LINC00702	ENSG00000233117	1.894272141	2.729408033
RP11-675F6.3	ENSG00000253361	1.849546194	4.004090401
AC005083.1	ENSG00000233834	1.841570974	1.977593242
SERPINE1	ENSG00000106366	1.820992717	1.737004577
SYT12	ENSG00000173227	1.799149093	2.851184932
AC112721.1	ENSG00000222022	1.796691878	4.492606685
TGFB1	ENSG00000105329	1.791406818	1.638479762
FABP4	ENSG00000170323	1.782305824	2.920043367
IL1RAP	ENSG00000196083	1.771529733	1.710302893
CTC-487M23.7	ENSG00000272389	1.714630684	3.053148082
Y_RNA	ENSG00000272110	1.71057656	1.5688352
ZCCHC5	ENSG00000179300	1.684804035	1.860507323
VASN	ENSG00000168140	1.671608339	3.064155252
FAM196B	ENSG00000204767	1.658419794	2.83779624
Y_RNA	ENSG00000252965	1.652720677	1.773368444
RP11-588K22.2	ENSG00000260244	1.63569755	2.513061115
SYNJ2BP	ENSG00000213463	1.616781915	1.774230758
GALNT10	ENSG00000164574	1.60459071	2.07187835
KITLG	ENSG00000049130	1.586722306	1.995667849
FAS	ENSG00000026103	1.542654833	1.999496385

Gene name	Ensembl gene	U3071 logFC (shGLI1_vs._shNT)	T778 logFC (shGLI1_vs._shNT)
RP11-332H14.1	ENSG00000272861	1.514866763	2.018137694
ISLR	ENSG00000129009	1.511172609	3.156704128
RP11-399D6.2	ENSG00000234840	1.914827902	4.272109678
ACPP	ENSG00000014257	1.906452294	1.814826958

Supplementary material 7: Dose-response curves of all compounds tested in the primary screen. For each tested compound, dose-response curves are shown for glioblastoma cell lines, LN308 and U3071 (high GLI1 expression) and U3037 and LN229 (low GLI1 expression), and liposarcoma cell lines, T778 (high GLI1 expression) and T449 (low GLI1 expression). Response curves of cell lines with high GLI1 expression are depicted as solid curves, cell lines with low GLI1 expression as dashed curves. Inhibitors are grouped according to their targeted molecule/pathways.

GLI1 inhibitors:

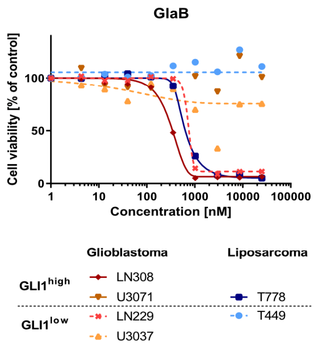

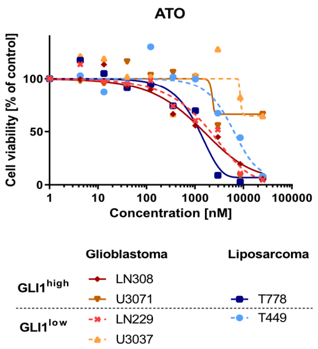

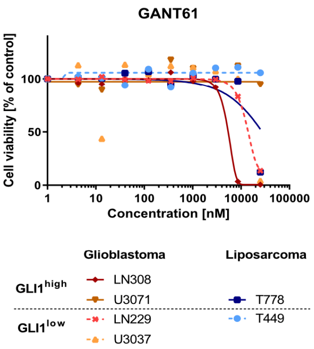

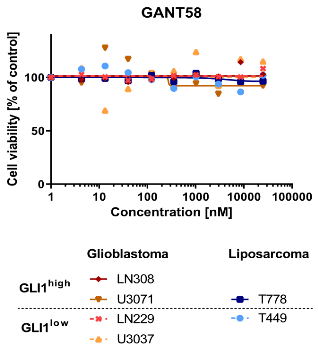

SHH inhibitors:

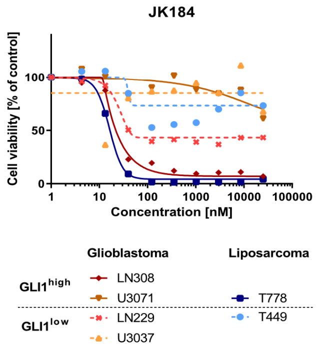

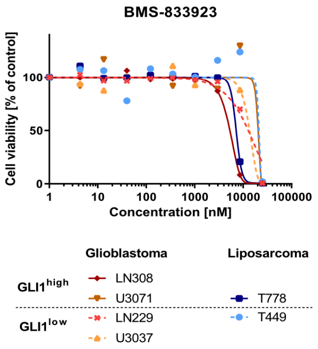

Continued from the previous page

Base excision repair inhibitors:

PARP inhibitors:

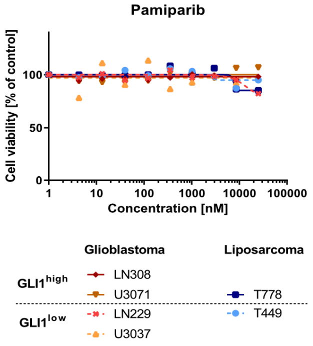
Pamiparib

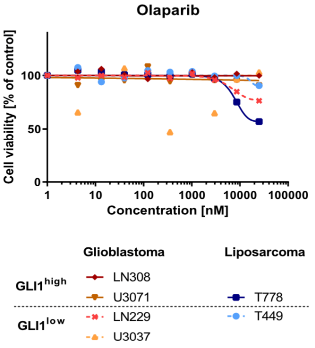
Olaparib

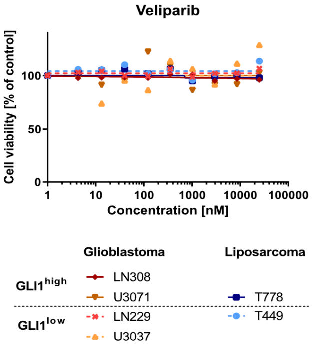
Veliparib

APE1 inhibitor:

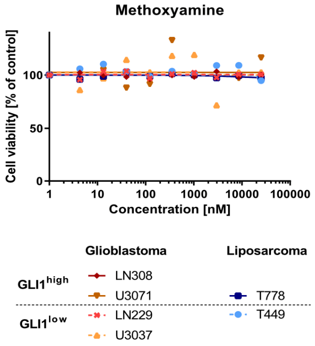
Methoxyamine

Homologous recombination repair inhibitors:

ATR inhibitors:

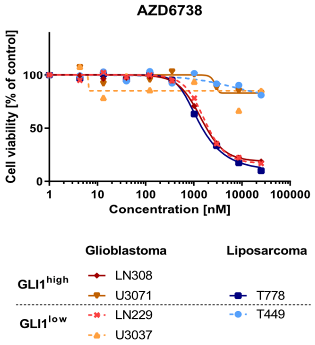
AZD6738

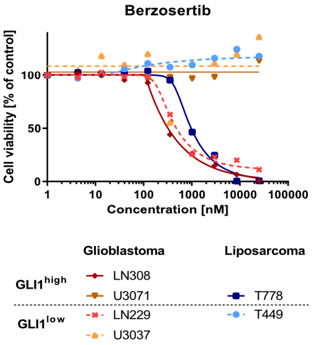
Berzosertib

Non-homologous end joining repair inhibitors:

DNA-PKc inhibitors:

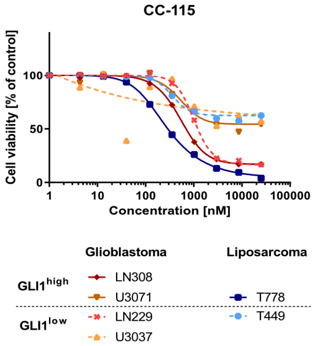
CC-115

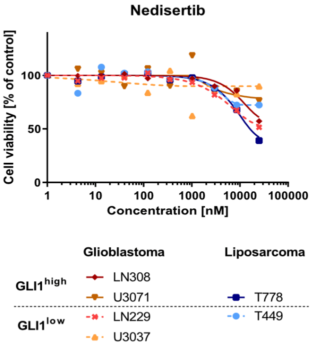
Nedisertib

Continued from the previous page

Checkpoint inhibitors:

CHK1 inhibitors:

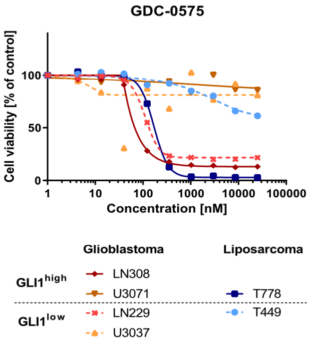

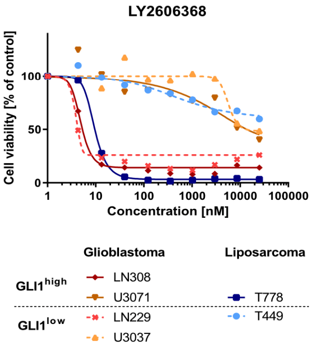

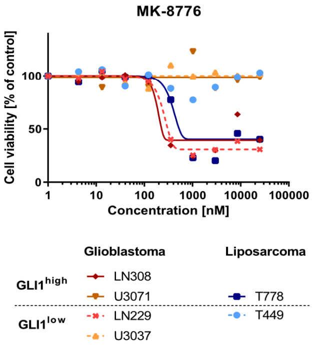

ATM inhibitor:

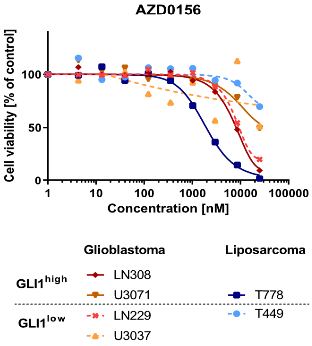

WEE1 inhibitor:

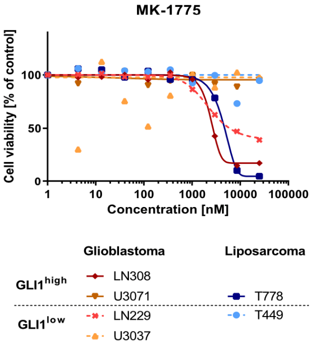

Topoisomerase inhibitors:

Topoisomerase I inhibitors:

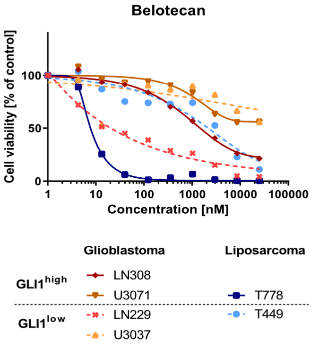

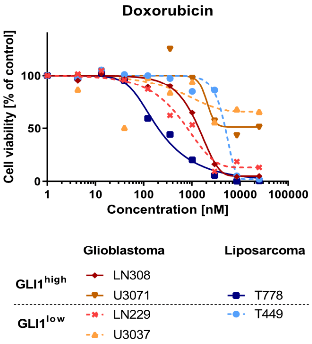

Topoisomerase II inhibitors:

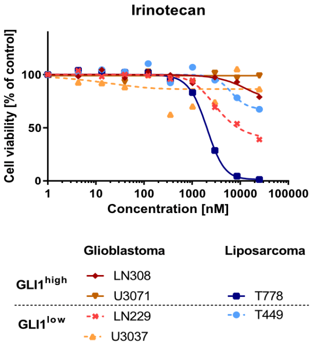

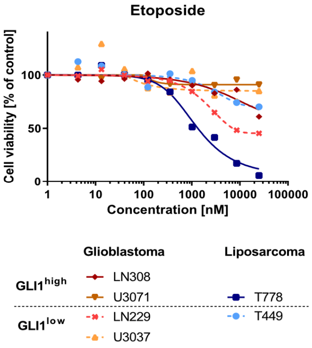

Continued from the previous page

Positive controls

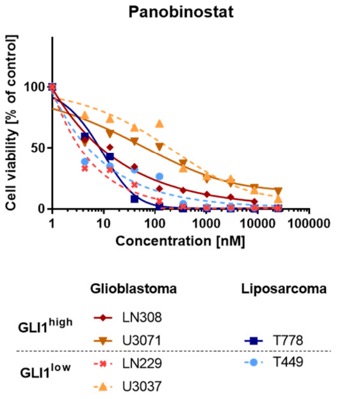

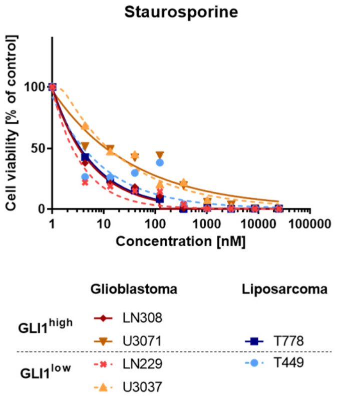

Supplementary material 8: Bliss surface plots of GLI1/SHH inhibitors and DNA repair inhibitors. Bliss surface plots showing synergistic and antagonistic drug interactions between GLI1 inhibitors and CHK1 inhibitor GDC-0575 (**A**) or ATR inhibitor Berzosertib (**B**) in T778 and T449 cell lines. Synergy and antagonism are mapped on the dose-response data of metabolic activity. One biological replicate was used for the analysis. Plots were generated using the Combenefit software.

A Combination: GLI1/SHH inhibitors + GDC-0575

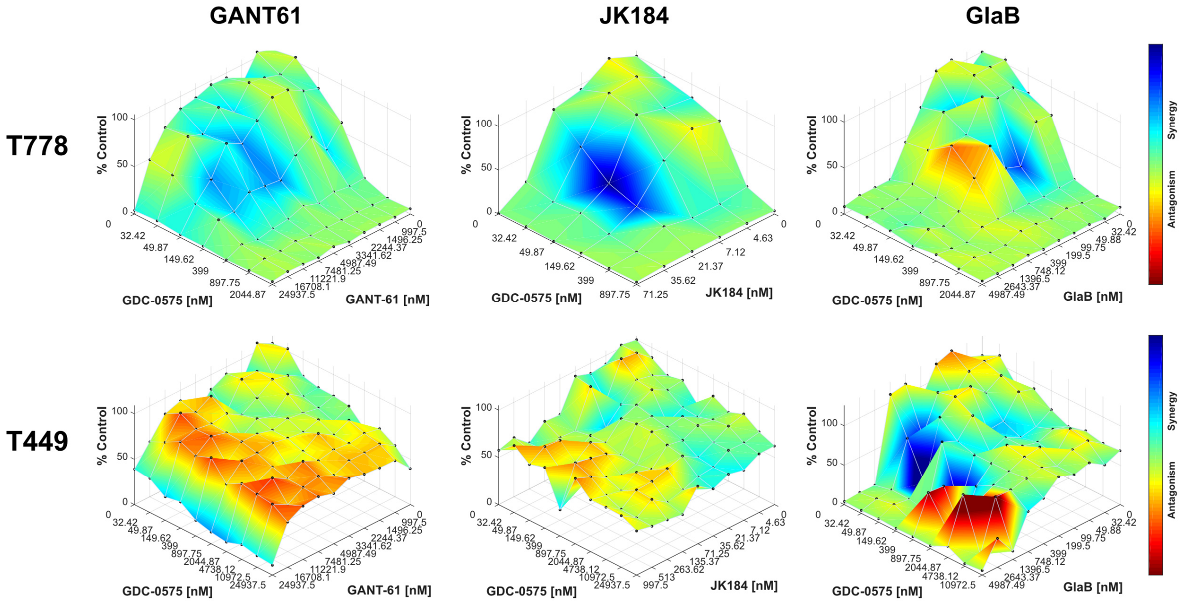

B Combination: GLI1/SHH inhibitors + Berzosertib

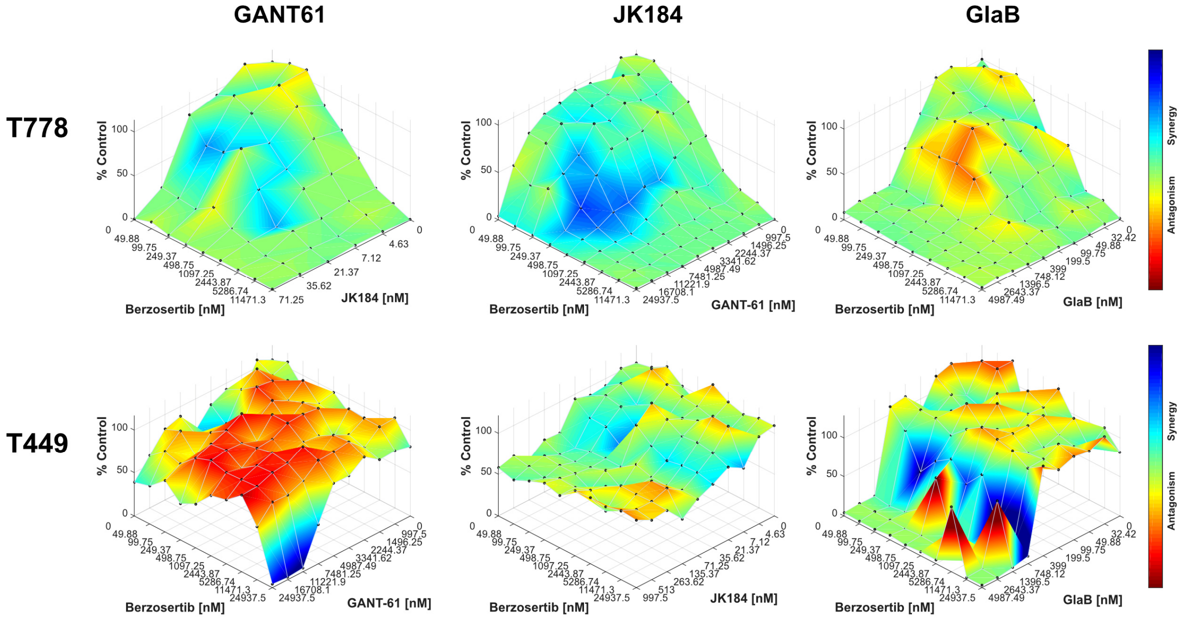

Supplementary material 9: Bliss surface plots of GLI1/SHH inhibitors and CHK1 inhibitors in glioblastoma. Bliss surface plots showing synergistic and antagonistic drug interactions between GLI1 inhibitors and CHK1 inhibitor LY2606368 (**A**) and GDC-0575 (**B**) in LN308 and LN229 cell lines. Synergy and antagonism are mapped on the dose-response data of metabolic activity. One biological replicate was used for the analysis. Plots were generated using the Combenefit software.

A LY2606368

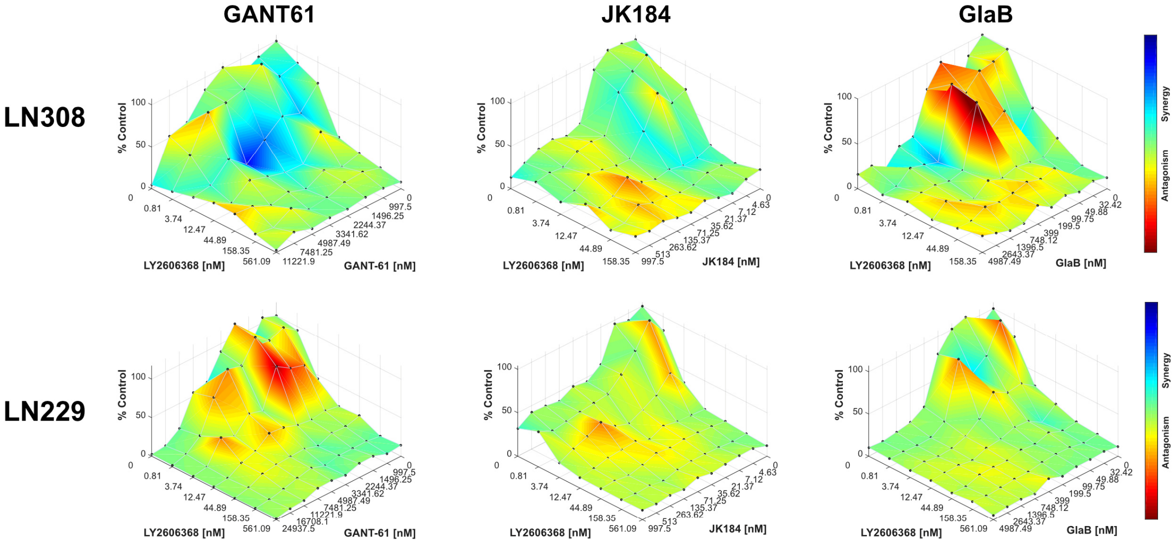

B GDC-0575

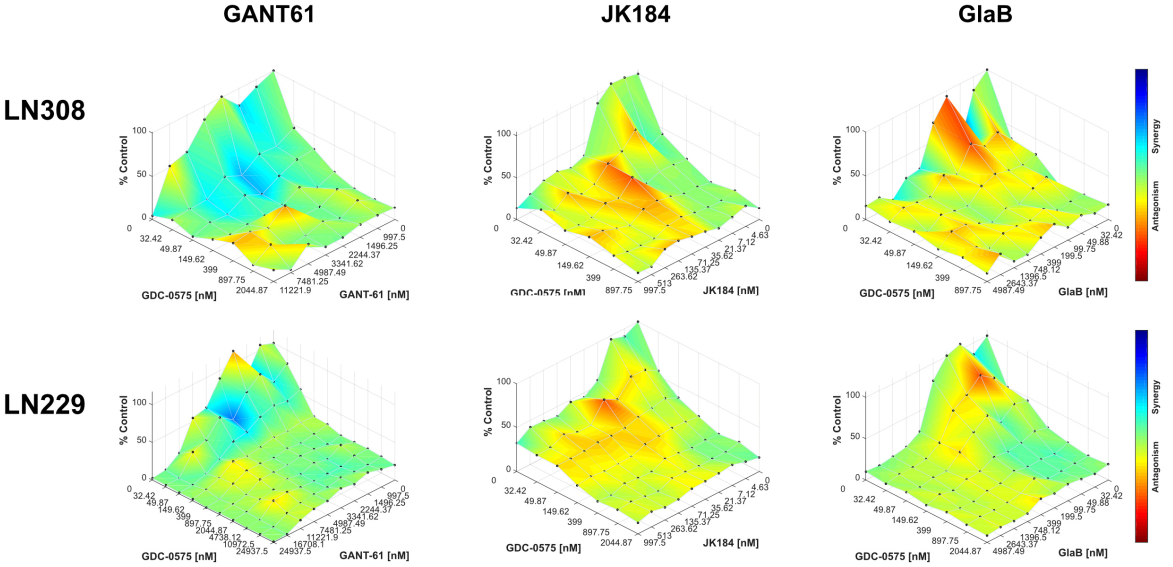

Supplementary material 10: Bliss surface plots of GLI1/SHH inhibitors and ATR inhibitor in glioblastoma. Bliss surface plots showing synergistic and antagonistic drug interactions between GLI1 inhibitors and ATR inhibitor Berzosertib in LN308 and LN229 cell lines. Synergy and antagonism are mapped on the dose-response data of metabolic activity. One biological replicate was used for the analysis. Plots were generated using the Combenefit software.

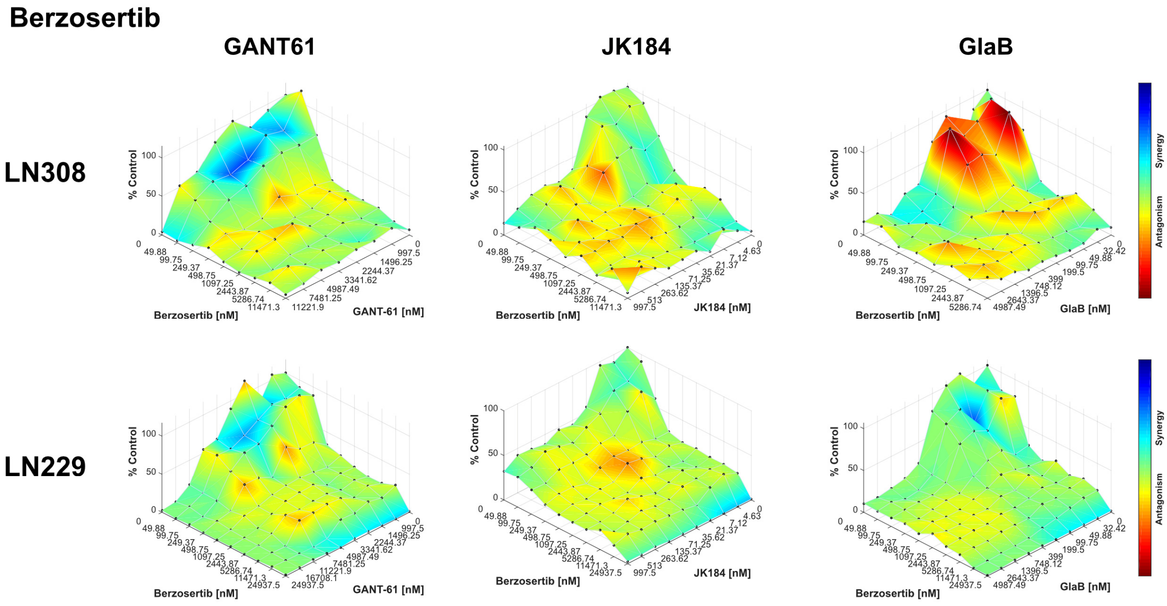

Supplementary material 11: Combination treatment of JK184 and LY2606368 in T778 and LN308 cells. Bliss surface plots for T778 (**A**) and LN308 (**B)** cells upon combination treatment with JK184 and LY2606368. Synergy and antagonism were mapped on the dose-response surface generated by the average of the metabolic activity values at each data point compared to DMSO control for three biological replicates. Plots were generated using the Combenefit software. Dot plots on the right show the metabolic activity compared to DMSO control at concentrations resulting in the highest synergy score (T778: JK184 1 nM; LY2606368 4 nM, LN308: JK184 1 nM; LY2606368 2.22 nM) (mean ± SEM, significant p-values are indicated in the graphs, one-way ANOVA followed by Tukey's test for multiple comparisons of groups).

A

T778 - GlaB and LY2606368

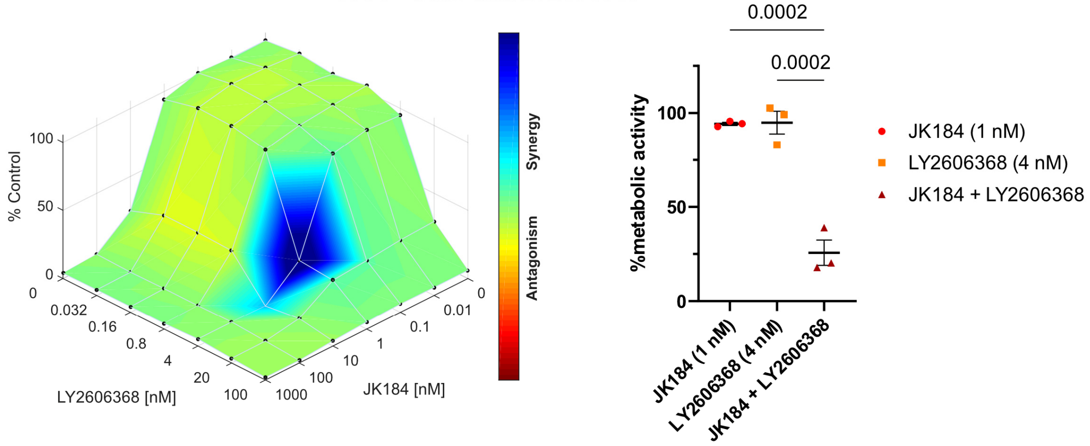

B

LN308 - GlaB and LY2606368

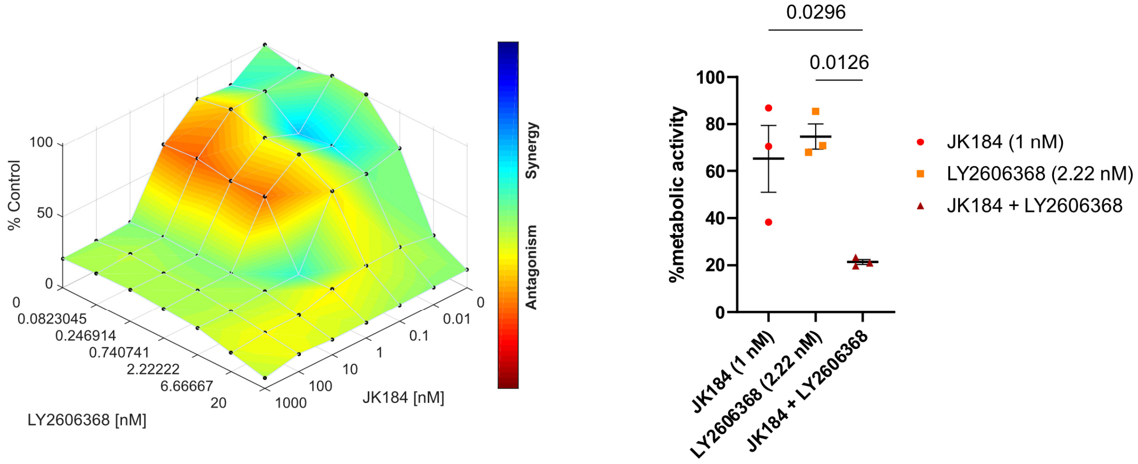

Supplementary material 12: Cell apoptosis in T778 cells upon single and combination treatment with JK184 and LY2606368. Quantification of live, early apoptotic, and late apoptotic/necrotic T778 cells upon treatment with JK184 and LY2606368 for 72 h (mean ± SEM, significant p-values are indicated in the graphs, two-way ANOVA followed by Tukey's test for multiple comparisons of groups).

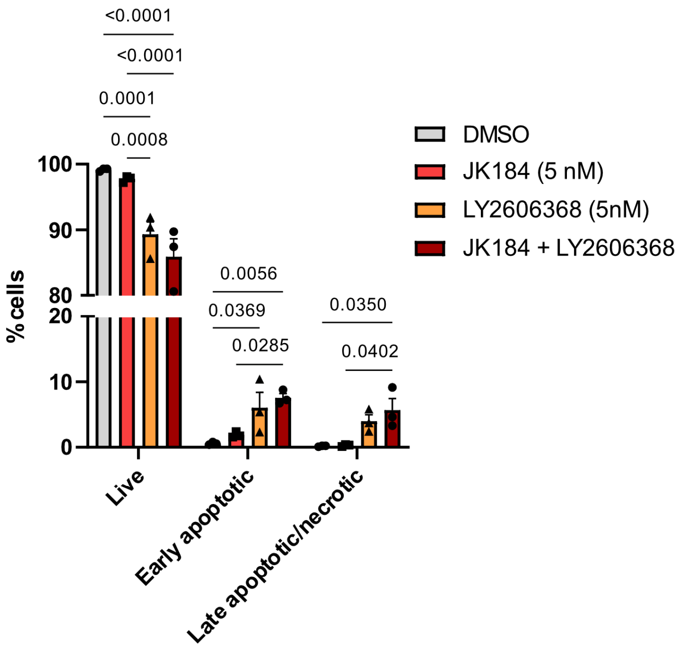

B Publications

Wu Y, Fletcher M, Gu Z, Wang Q, Costa B, Bertoni A, Man KH, Schlotter M, Felsberg J, **Mangei J**, Barbus M, Gaupel AC, Wang W, Weiss T, Eils R, Weller M, Liu H, Reifenberger G, Korshunov A, Angel P, Lichter P, Herrmann C, Radlwimmer B. Glioblastoma epigenome profiling identifies SOX10 as a master regulator of molecular tumour subtype. *Nat Commun* **11,** 6434 (2020).

C Acknowledgements

Already Steve Jobs knew that *“great things […] are not done by one person. They're done by a team of people."* The work in this thesis would not have been possible without the valuable guidance and contribution of the team behind it and whom I would like to acknowledge.

First and foremost, I would like to thank my supervisor Dr Bernhard Radlwimmer for his support throughout my PhD studies. He guided and encouraged me in my scientific and personal development and kept reminding me to believe and trust in myself. In his group, I was able to develop independently and implement my ideas but was always supported in establishing excellent collaborations that were indispensable for the progress of the study.

Furthermore, I would like to express my deep gratitude to Prof Dr Peter Lichter for giving me the opportunity to conduct my PhD studies in his laboratories. I am extremely thankful for his mentorship and advice that he was always willing to provide. His friendly nature is the basis for the warm working atmosphere in the division.

It was a great pleasure to work with Dr Michael Fletcher, Dr Yonghe Wu, Zhiqin Huang and everyone involved in the analysis of the HIPO016 study and bringing the GLI1 project to life. I highly acknowledge all your expertise and valuable input, which was essential for the development and success of the project.

At the same time, I would like to further extend my special thanks to our collaborators Prof Dr Marc Remke and his research team in the University Clinics Düsseldorf, especially David Pauck, Dr Jasmin Bartl, Lena Blümel, and Dr Nan Qi, not only for a very fruitful collaboration on the preclinical drug screen but also for hosting me in Düsseldorf to perform my experiments and providing a fun working environment that I will always keep in good memory. Of equal importance was the help of Prof Dr Stefan Fröhling, Dr Priya Chudrasama, Dr Sebastian Uhrig, and Dr Damian Stichel for the work on sarcoma tumours and the analysis of the NCT MASTER cohort. I additionally want to thank Dr Ali Bakr in Prof Dr Peter Schmezer’s research group for his continuous support and answers on DNA repair-related questions, as well as our collaborators in Rome, Prof Dr Bruno Botta, Dr Paola Infante, and Prof Lucia Di Marcotullio for sharing material and joining forces in the inhibitor studies.

I would like to offer my special thanks to Prof Dr Karsten Rippe and Prof Dr Andreas von Deimling for their valuable scientific input, supervision and support as first referee of my PhD thesis and members of my TAC committee. Furthermore, I sincerely thank Prof Dr Christian Schaaf and Dr Sevin Turcan for their willingness to evaluate this work and participate in my thesis examination committee.

Many thanks also go to the teams of the DKFZ core facilities for setting up and maintaining high-standard facilities and providing valuable support. I would like to especially point out the help of the Sequencing Core Facility, Microscopy Facility, and Flow Cytometry Core Facility.

Many thanks go to all current and former group members Liliana Francois Martin del Campo, Pavle Boskovic, Matthew Man Ka Hou, Theresa Schmid, Petra Schroeter, Magdalena Schlotter, Yuan Peng, Yonghe Wu, Michael Fletcher, Anne Jenseit, Niclas Kneisel, Achim Stephan, Ann-Christin Gaupel, Lidia Silva, Jeanette Kappenberger, and Michaela Kirchgäßner for the collaborative spirit, always being supportive, cheering me up at any time, and keep reminding me how important it is to have a good team.

I would also like to especially thank Petra Schroeter, Magdalena Schlotter, Andrea Wittmann, and Frauke Devens for their excellent technical assistance and support throughout my PhD studies. Additionally, I would like to further thank Verena Kalter, Sybille Ohl, Gabriele Müller, Frederic Bethke, Laura Puccio, and Achim Stephan for any help in technical questions and lab-related issues, Michael Hain and his team for IT support, and Jasmin Müller for her immediate help and patience with any question I had.

Furthermore, I am especially thankful to all members of the B060, B062, and B06x divisions. Thank you for creating such a great atmosphere to work in! I am extremely grateful to have met so many wonderful people in the lab that have become true friends. Thank you Mona Göttmann, Tolga Lokumcu, Umar Khalid, Michael Persicke, Laura Llao Cid, Laura von Soosten, Theresa Schmid, Mariana Coelho, Elena Wittmann, Jonas Bub, Himanshu Soni, Marie Bordas, Felix Schmitt-Hofer, Alexander Sommerkamp, and Emma Philipps for making every day to a fun day! I don’t know what I would have done without your friendship, the funny moments and great times during the working time, coffee/ice and after-work breaks, also and especially in stressful times during my PhD.

I won’t forget all the funny sports events and quality times I spent with my TriGirls, Britta Ismer and Sonja Krausert, and also with Laura Llao Cid, Liliana Francois Martin del Campo, Mona Göttmann, Laura von Soosten, Benjamin Schwalm, Norman Mack, Kati Ernst, Britta Statz, David Jones, Barbara Worst, and Daniel Haag. If it was on the water, in the boat, in the mud, in the Waldpark Neckarau, on the road bikes, the Philosopher’s path, at Unisport, or on the mountains, it was always so much fun and helped me to forget the stress, switch off and recharge myself with new energy.
Britta and Sonja, thank you for our friendship, for always being there for me, and thank you for challenging me with all the competitions that we did together. I wouldn’t have done it without you and I am looking forward to many more to come! You two are truly inspiring in what you achieve!

Special thanks also go to everyone I have met outside the B06x division in my time at BioContact e.V., the KiTZ club, the Social Events Team, Welcome Team, and Retreat Team. Thank you, Bianca Kuhn, for all the lunch breaks and your motivating words during the thesis writing time!

Finally and most importantly, I would like to thank my boyfriend Christian, my parents, and my sister for their love and unwavering support. You are always there for me, you shape me as a person, support me in everything I want to do, and you provide me with food packages whenever possible. You know how I feel without asking and you know what I need to make me happy. I could not have imagined myself doing it without you and I cannot describe in words how important you are to me.
I love you!